Topological Signatures and Quenches in One Dimensional Fermionic Systems

(Article begins on next page)

17 May 2023

Doctoral Dissertation
Doctoral Program in Physics (35th cycle)

Topological Signatures and Quenches in One Dimensional Fermionic Systems

By

Lorenzo Rossi

******

Supervisor(s):
Prof. Fabrizio Dolcini

Doctoral Examination Committee:
Prof. Matteo Rizzi, *Referee*, University of Cologne
Prof. Fabio Taddei, *Referee*, Istituto di Nanoscienze - CNR, Pisa.
Prof. Roberta Citro, *External Member*, Università degli Studi di Salerno
Prof. Mario Collura, *External Member*, SISSA
Prof. Luca F. Tocchio, *Internal Member*, Politecnico di Torino

Politecnico di Torino
2023

Declaration

I hereby declare that, the contents and organization of this dissertation constitute my own original work and does not compromise in any way the rights of third parties, including those relating to the security of personal data.

Lorenzo Rossi
2023

Acknowledgements

While the writing of this Thesis was undoubtedly a pain (very instructive indeed, yet still a pain), it is instead a great pleasure to write these acknowledgments and to thank all the persons who made these three years of graduate school a very enjoyable period, notwithstanding a global pandemic (and the need to write this Thesis). Thus, letting aside the scientific part of the PhD for a moment, I would like to acknowledge the people behind this work. In doing so, I cannot resist the temptation to use given names. Although I certainly dislike formalities, this choice should not disguise the utmost respect for each person mentioned here. On the contrary, it represents the beautiful feeling of familiarity that I felt in my Department and in the entire community. An attitude I deeply appreciate.

Without further ado, I would like to first thank Fabrizio. I believe that the overall quality of a PhD experience is mostly determined by the supervisor and I have always felt very lucky with him. His dedication, work ethic, and precision, while keeping humanity and well-being as essential conditions, have been a constant point of reference. Many sincere thanks are due to Fausto as well. Recalling the many interactions we had, I find that the fun he has from research, his availability and his willingness to really get his hands dirty with the projects of a newcomer PhD student are truly remarkable.

During the PhD I also had the fortune to collaborate with several other people, both from my Department and from different Institutions. The collaboration with Niccolò, Fabio, and Maura from the University of Genova, which started in the inauspicious days of the first covid-19 lock-down, was instrumental to keep an eye open to the outside world during those gloomy days. It was then a real pleasure to finally meet in person, almost two years later, at the very nice School they organized in Santa Margherita Ligure. Unfortunately, I haven't been equally lucky with Leonid. It is a real pity that he had to write his Master Thesis remotely and he could not join the group afterwards. It was very pleasant and profitable to work with him. Once the pandemic was over, I had also the fantastic opportunity to spend some visiting periods in a few research centers. Thus, I would like to really thank Giuseppe and Mario for hosting me in their research groups in

Sissa, Trieste. Their warm hospitality and the many lively discussions we had are sincerely acknowledged. I only regret that other duties prevented me to start a joint project. Many thanks also to Thomas, for inviting me for a short visit in Luxembourg and for showing me the city around with enthusiasm. The visiting period in Würzburg is greatly acknowledged as well. I am very thankful to Björn for hosting me in his group and for finding the time to carefully introduce me to all the different research themes and group members, notwithstanding his incredibly tight schedule. Then, a double thanks goes to Jan, for being such a nice and thoughtful host during my two visits in Dresden and for his tireless commitment during our collaboration. Finally, I would like to thank other members of the research group at Politecnico. In particular, Luca B. for his contributions to a joint project that, unfortunately, did not make it into the Thesis and for sharing with me his experience and advice about the research world. I am also in debt with Luca T. and Rita for the nice and informative conversations we had throughout the years.

Lastly, yet most importantly, these years would not have been full of so many good memories without all the nice people and the new friends met. To all of them, yet to each one of them in their own specific way, my love, my deep gratitude for the unique gems of humanity I received from them and my regret for not having enough lives to collect them all.

Abstract

This thesis in devoted to the theoretical analysis of the topological and out of equilibrium properties of one dimensional fermionic systems. After discussing the experimental signatures of topological bound states in spin-orbit coupled nanowires, we investigate transport phenomena in Dirac materials heterojunction. Furthermore, by analyzing the dynamical effects of quantum quenches, we predict the relaxation to a Generalized Gibbs Ensemble in an integrable system and its observability through optical measurement. We highlight the role of symmetries in both protecting and hiding topological states in a quenched topological insulator and we explore how a time dependent magnetic flux piercing a one dimensional insulating ring can generate a non linear current and dynamical quantum phase transitions. Finally, we show that the Berry phase of a quenched band insulator builds up a quantized response to a constant magnetic flux and we prove that the quantization is dictated by a dynamical topological invariant.

Contents

Chapter 1

Introduction

In this introductory Chapter we shall briefly review the ideas that provide the conceptual basis for this Thesis. While doing so, we shall also try to yield a bird's-eye view on recent achievements and open questions lying at the heart of the present research field, in order to set this work into a broader perspective. Then, an overview of the content of the Thesis is reported.

1.1 Topological phases of matter

Topological phases of matter [1, 2, 3, 4] are quantum phases of matter at zero temperature that cannot be identified by a local order parameter and by Landau's theory of spontaneous symmetry breaking [5]. In particular, different topological phases might share the same symmetries and the same local properties. Nonetheless, they display different global properties and can be identified and classified according to different topological features. Moreover, topological phases typically manifest peculiar observable signatures at the boundaries of the system.

Besides the intrinsic interest in understanding this new paradigm, topological phases are under the spotlight of research because their peculiar properties might enable technological breakthroughs, as we briefly describe here below. For definiteness, we shall outline the essential features of topological phases of matter by focusing on the family of remarkable phenomena related to the quantum Hall effect.

1.1.1 The integer quantum Hall effect and symmetry protected topological phases

In 1980 von Klitzing, Dorda and Pepper [6] reported that when a constant magnetic field of 18 Tesla is applied perpendicular to the inversion layer of a MOSFET at a temperature of 1.5 Kelvin, the Hall resistance develops a step like behaviour as a function of the gate potential and the plateau values are equal to $h/e^2\nu$, where ν is an integer. According to our current understanding the explanation of this phenomenon, called integer quantum Hall effect, goes as follows [7]. At low temperatures, the conducting electrons in the inversion layer of the MOSFET can be described as a Fermi gas living in a two dimensional (2D) world. When a strong magnetic field is applied, the single particle eigenstates then become the highly degenerate and equally spaced Landau levels (LL) [8]. Thus, if the Fermi energy is such that an integer number ν of LL are completely filled, the system turns out to be gapped. However, even though it is in a gapped state, the system is not in a trivial insulating phase and two remarkable and related features arise. The Hall conductivity computed in the bulk is found to be equal to $\sigma_H = \nu e^2/h$ [9, 10, 11] and deeply related to a topological invariant [12]. Furthermore, if the analysis is carried on a large but finite system, ν chiral edge modes propagating along the boundaries appear and are found to be responsible for the observed experimental results [9, 13, 14].

A couple of comments are thus in order. First, we recognize a clear example of a characteristic feature of topological phases, the so called bulk-boundary correspondence [1]: A topological property computed in the bulk (i.e. the Hall conductance) is linked to a property at the boundaries (i.e. the chiral modes)[1]. Second, the integer quantum Hall effect has found important applications almost since its discovery: The measured value of the Hall conductance is incredibly precise and independent of experimental details. It has thus been instrumental to improve the accuracy of the International System of Units, as already suggested in the original paper by von Klitzing *et al.* [6]. Moreover, chiral modes are a concrete example of perfectly conducting wires. The possibility to exploit such perfect wires in electronic devices would drastically reduce energy consumption and detrimental heating effects, suggesting an immediate application for this topological phase of matter.

Unfortunately, two massive obstacles prevent the everyday use of the chiral edge modes of the integer quantum Hall phase as the standard conducting channels for our electronics: the need for an intense magnetic field and cryogenic temperatures. However, Haldane

---

[1]The universal features of such correspondence have now been framed in the language of quantum field theory anomalies [15]

proposed in 1988 a model [16] where the same topological phase of the integer quantum Hall effect at $\nu = 1$ is realized in a 2D lattice system without the need of an external magnetic field (even though time reversal has to be locally broken). This model, that describes what is now called a quantum anomalous Hall or Chern insulator phase, would thus suggest that the first obstacle might be overcome. Yet Haldane's result was not fully appreciated[2] until the works of Kane and Mele [17, 18] and Zhang and coworkers [19, 20, 21] that in the years 2005-2006 predicted the existence of a novel topological phase called quantum spin Hall. Differently from the integer and anomalous quantum Hall phase, the quantum spin Hall phase is stable as long as time reversal symmetry is preserved and thus belongs to the family of symmetry protected topological (SPT) phases [4]. Roughly, it can be thought of as two independent copies of the quantum anomalous Hall phase, one for each spin degree of freedom of the charge carriers, as it exhibits a pair of perfectly conducting channels at its boundaries, characterized by opposite spin and velocity. These channels where experimentally observed for the first time in HgTe quantum wells in 2007 [22], giving a boost to the research in topological phases of matter. Still, measurements had to be performed at very low temperatures (below 10 K) and the reason lies in the relative weak spin-orbit interaction [23]: The quantum spin Hall phase exists only if the energy gap is produced by spin-orbit interaction and the gap has to be large compared to thermal energy in order to have a stable phase. It is thus an ongoing challenge for material science to find platforms where spin-orbit interaction is enhanced and the topological gap is sufficiently robust at room temperature[3] to enable technological applications [25, 26]. In this respect, impressive theoretical and experimental progress has been made since 2005: Topological insulators, namely the 3D analogue of the quantum spin Hall phase, were predicted in 2007 [27, 28, 29] and experimentally observed in 2008 [30], the quantum anomalous Hall phase was finally observed in 2013 [31] and a complete classification of SPT phases of non-interacting fermions has been recently achieved [3].

1.1.2 The fractional quantum Hall effect and topologically ordered phases

We can now leave these impressive developments and go back to 1982 in order to follow the evolution of a different, yet related, research area. Once again, the starting point is the

---

[2]It is interesting to notice that, according to the Scopus database, Haldane's paper was cited 53 times in the years 1989-2004 and 2987 times in the years 2005-2020

[3]A room temperature observation of the integer quantum Hall effect was instead reported in 2007 by exploiting a single layer of graphene [24], yet an intense magnetic field was needed.

quantum Hall effect. Indeed, in 1982, Tsui, Stormer and Gossard [32], by performing Hall measurements in very clean samples, reported the existence of an additional plateau in the Hall conductance at filling fraction $\nu = 1/3$. This was the first experimental realization of a fractional quantum Hall phase. While the integer quantum Hall phase, as well as all the other topological phases that we have described until now, can be understood in terms of non-interacting fermionic quasi-particles, the gap that stabilizes the fractional Hall phase is due to the electron-electron interactions, that break the extensive degeneracy of partially filled LL. Moreover, the quasi-particle excitations above the $\nu = 1/3$ fractional quantum Hall ground state are quite peculiar: They carry $1/3$ of electric charge, as first theoretically understood by Laughlin [33] [4], and obey fractional statistics [36, 37], providing the first experimental evidence of anyonic particles [38, 39, 40]. In particular, since such Laughlin quasi-particles are well localized in real space and the energy of the system does not depend on their relative position (as long as they are sufficiently far apart), one can (at least in principle) adiabatically exchange two of them. Upon this adiabatic operation, the wave function of the entire system is found to acquire a non trivial phase $e^{\mp i\pi/3}$ (the sign corresponds to the clockwise/anti-clockwise braiding of the two quasi-particles) that is neither the one characteristic for bosons, i.e. $+1$, nor the one characteristic for fermions, i.e. -1. Nonetheless, the exchange of two quasi-particles can be accounted for by a single phase, thus the anyons of the $\nu = 1/3$ fractional quantum Hall phase are called Abelian[5].

However, after the first discovery by Tsui *et al.*, it has been found that many other stable phases at different fractional fillings exist and some of them are believed to support even more exotic quasi-particles excitations. For instance, in the $\nu = 5/2$ fractional quantum Hall phase, experimentally discovered in 1987 [43], the excited state consisting of a given number of quasi-particles fixed in well defined and separated positions is not described by a unique wavefuntion [44]. Because of this degeneracy, upon a braiding of two quasi-particles, the wavefunction of the system can transform according to a non trivial unitary matrix and the anyons are thus called non-Abelian [45][6].

From our current understanding [4], all the fractional quantum Hall phases belong to the class of topological phases displaying topological order. At variance with SPT phases, topologically ordered phases are not protected by any symmetry and, besides supporting

---

[4]A direct observation of the fractional charge was instead reported in 1997 by two independent groups, exploiting shot-noise measurements through a quantum point contact [34, 35]

[5]A direct observation of this Abelian anyonic statistics was recently reported [41], complementing indirect observations based on shot-noise measurements [42]

[6]Evidence of the fractionally charged quasi-particles of the $\nu = 5/2$ quantum Hall phase, believed to carry a quarter of the electron charge, was reported in 2008, by similar means of the 1997 experiments [46].

anyonic excitations, have very peculiar properties such as ground state degeneracy on a toroidal geometry [11, 47] and long-range entanglement [48, 49].

1.1.3 Topological quantum computation and Majorana zero modes

Interest in non-Abelian anyons was further spurred by Kitaev who, in 1997, pointed out that a universal quantum computer could be realized by encoding and processing quantum information in the braiding of non-Abelian anyons [50]. Kitaev's proposal followed shortly after the ground breaking work by Shor [51], who proved that quantum computation can outperform its classical counterpart in some specific tasks and kickstarted the "quantum computer rush". Shor had also proven in 1996 that quantum computation can be performed fault-tolerantly [52], i.e. in the presence of slightly imperfect logical operations and some degree of decoherence, however Kitaev noticed that the precision needed for a robust quantum computation was unmatched in any known platform and suggested a novel approach that, in his words, "*is fault-tolerant by its physical nature*" [50]. Indeed, even though it is an unsolved challenge to experimentally control non-Abelian anyons[7], the power of Kitaev's proposal is believed to lie in the robust topological protection of quantum information. The idea goes as follows: As long as anyons are stable and their positions under control[8], it is extremely unlikely that information gets spoiled by some noise, since it should be strong enough to unbraid the anyons. Moreover, all the information is encoded in states that are energetically degenerate, preventing unwanted dephasing. For these reasons, the information stored in the topological braiding patterns is believed to be immune to decoherence and the field of topological quantum computation has been growing ever since [56].

Moreover, three years later, Kitaev proposed "*another (theoretically, much simpler) way to construct decoherence-protected degrees of freedom in one dimensional systems*" [57]. This second proposal is based on a 1D SPT phase, protected by charge conjugation symmetry and known as topological superconductive phase. We can sketch the model in

---

[7]Two independent groups recently reported the first observation of the topologically ordered phase predicted to appear in the ground state of the toric code (or surface code - depending on the topology of the underlying two dimensional lattice). Such model, first introduced by Kitaev in his 1997 paper [50, 53], is exactly soluble and supports topological order and anyonic excitations. Yet, the anyons are Abelian and cannot provide a physical basis for universal quantum computation. The result is nevertheless remarkable and it is interesting to notice that the two experiments were based on very different physical platforms, namely a quantum processor composed of 25-31 superconducting qubits [54] and an array of 19-24 optically controlled neutral atoms [55].

[8]Within an implementation with fractional quantum Hall phases, the standard proposal would be to use an STM tip as a tool for localizing and moving anyons around [56].

order to introduce the useful concept of Majorana operators and gain a concrete example of a SPT phase. The system is composed by spinless fermions hopping on a 1D lattice, in the presence of superconducting pairing (induced by proximity with a bulk superconductor). Following Kitaev's original paper, the Hamiltonian reads

$$H = \sum_j \left[-w(a_j^\dagger a_{j+1} + a_{j+1}^\dagger a_j) - \mu \left(a_j^\dagger a_j - \frac{1}{2} \right) + \Delta a_j a_{j+1} + \Delta^* a_{j+1}^\dagger a_j^\dagger \right]$$

where w is the hopping amplitude, μ is the chemical potential and Δ is the superconducting pairing. Exploiting the Bogolioubov-De Gennes formalism [58] and periodic boundary conditions (PBC), the Hamiltonian can be diagonalized and the excitation spectrum in the bulk is found to be $\epsilon(q) = \sqrt{(2w \cos q + \mu)^2 + 4|\Delta|^2 \sin^2 q}$, for $-\pi \leq q \leq \pi$. Thus, supposing that $|\Delta| \neq 0$ and $w > 0$, we can treat μ as a parameter and identify three gapped phases, namely $\mu < -2w$, $|\mu| < 2w$ and $\mu > 2w$, separated by two critical points at $\mu = \pm 2w$. Even though all three phases share the same symmetries, it turns out that the phase realized for $|\mu| < 2w$ is topologically non-trivial, while for $|\mu| > 2w$ the system is in the same, topologically trivial, phase. This topological distinction can be understood by computing a $\mathbf{Z}_2$ topological invariant out of the single particle bulk eigenstates with PBC [3], however the peculiar nature of the topopological phase becomes manifest by simply looking at the properties of the system with open boundary conditions (OBC). Indeed, we can sit in a specific point of the topological parameter region[9], namely $\mu = 0$, $w = |\Delta|$, and write the Hamiltonian in terms of Majorana operators. These can be formally defined as

$$c_{2j-1} = e^{i\theta/2}a_j + H.c. \qquad c_{2j} = \frac{e^{i\theta/2}a_j - H.c.}{i} \qquad j = 1, \ldots, L$$

where $e^{i\theta} = \Delta/|\Delta|$ and L is the number of sites of the chain. By construction, these operators are Hermitian, satisfy the algebra $\{c_l, c_m\} = 2\delta_{lm}$, for $l, m = 1, \ldots, 2L$, and are such that $\frac{i}{2}c_{2j-1}c_{2j} = a_j^\dagger a_j - \frac{1}{2}$. With this choice, the Hamiltonian reads $H = iw \sum_{j=1}^{L-1} c_{2j}c_{2j+1}$ and, by simply re-arranging the Majorana operators into a new set of fermionic modes $\tilde{a}_j = \frac{1}{2}(c_{2j} + ic_{2j+1})$, for $j = 1, \ldots, L-1$, the Hamiltonian turns out to be in a diagonal form $H = 2w \sum_{j=1}^{L-1} \left(\tilde{a}_j^\dagger a_j - \frac{1}{2} \right)$. At first sight, we have just consistently recovered the spectrum of bulk excitations, previously computed with PBC. Yet it seems that there is a missing eigenmode, since j runs from 1 to $L-1$ only. In fact, for the present choice of parameters, the Majorana operators c_1 and c_{2L} do not appear in the Hamiltonian. Therefore, we can define a boundary fermionic mode $a_B = \frac{1}{2}(c_1 + ic_{2L})$ and conclude that

---

[9]We are (legitimately) assuming that the topological property of the system cannot change unless a critical point is touched.

the system with OBC has two degenerate ground states $|\psi_0\rangle$ and $|\psi_1\rangle$. Both states host zero bulk excitations, i.e. $\tilde{a}_j|\psi_{0,1}\rangle = 0 \,\forall j = 1, \ldots, L-1$, however $|\psi_1\rangle$ hosts a fermion in the boundary mode while $|\psi_0\rangle$ does not. These two states are perfectly degenerate, since there is no cost in placing a fermion in the boundary mode. Moreover, even though we picked a peculiar point in the parameter space, one can show that the zero energy boundary mode survives in the whole topological region $|\mu| < 2w$ of an infinite chain[10]. In contrast, the chain does not sustain a boundary mode when the system lies in the topologically trivial phase. A close look at this zero energy eigenmode reveals its peculiar nature: It has support half on one end of the chain and half on the opposite end. We can thus think about it as a fermionic excitation split into two, physically separated, Majorana modes. Since the boundary mode has vanishing energy, the underlying Majorana modes are commonly known as Majorana zero modes (MZMs).

We are now in the position to understand Kitaev's argument as to why the doubly degenerate ground state of a (sufficiently long) topological superconducting chain realizes "*a reliable quantum memory*" [57]. Since $|\psi_0\rangle$ and $|\psi_1\rangle$ are degenerate there is no dephasing error. Moreover, since fermionic parity is preserved in the model, the state of the system cannot flip between $|\psi_0\rangle$ and $|\psi_1\rangle$, unless a bulk excitation is simultaneously produced - and this event is suppressed by the bulk excitation gap[11].

Notwithstanding many works devoted in the early 2000s to topological quantum computation and to the search for MZMs in different platforms [56, 64], the theoretical importance of this model was not fully recognized until 2010[12], when two different groups [65, 66] independently proposed to realize a 1D topological superconductive phase in a semiconductor-superconductor heterostructure, *de facto* proposing a concrete implementation of Kitaev's model [67]. The success of this proposal lied in the (theoretically) simple set up. Indeed, all the elementary building blocks were readily available at the time: a ballistic semiconductor nanowire with strong spin-orbit interaction, a tunable magnetic field - together with some gates controlling the chemical potential of the nanowire - and a conventional superconductor. A huge effort was thus devoted to experimentally demonstrate the realization of topological superconductivity in these platforms, together

---

[10]The degeneracy between $|\psi_0\rangle$ and $|\psi_1\rangle$ is lifted for a finite chain, however the energy gap is exponentially suppressed with system size

[11]This analysis, performed for an isolated system, has to be double checked against more realistic situations, where the effects of a bath are taken into account. Tunneling processes [59] from the environment may in fact spoil the system's fermionic parity and the qubit coherence [60, 61, 62]. At the same time, if under control, they might provide a useful tool to manipulate and measure the state of the qubit [63].

[12]According to the Google Scholar database, there are 21 entries citing Kitaev's paper in the years 2000-2009 and 3010 entries citing it in the years 2010-2019.

with the appearance of MZMs at the two ends of the wire. Just two years later, in 2012, the first positive experimental report appeared [68]. Moreover, while Kitaev originally proposed his model only as a decoherence-free quantum memory, Alicea *et al.* [67] proposed in 2011 to use a network of wires as a platform where multiple MZMs could be hosted and information processed in their braiding. A network of nanowires thus emerged as one of the most promising platforms for realizing a topological quantum computer. The scientific quest then merged with an entrepreneurial one in 2016, when Microsoft hired Leo Kouwenhoven and Charles Marcus, leading experimentalists in the field, in order to unambiguously prove the existence of MZMs and realize a scalable quantum computer [69]. At the same time, more and more refined theoretical schemes were proposed, addressing possible sources of errors and simplifying the physical mechanisms needed to process information [70]. Nonetheless, the experimental demonstration of MZMs turned out to be difficult to establish conclusively, as many of their experimental signatures can be mimicked by different phenomena [71]. Yet, important optimistic results were claimed at a rapid pace [72, 73, 74, 75, 76] until 2021, when Ref.[75] was retracted and the authors had to apologize for "*insufficient scientific rigour*". Shortly after, Ref.[74] was retracted too and an Editorial Concern was expressed for Ref.[76]. The last episode of this open quest is brand new, since in 2022, after a change in the experimental strategy, the Microsoft Team announced that success in the identification of topological superconductivity was eventually reached [77]. It is almost obvious to add that this claim is still under debate [78].

1.2 Quench dynamics

In the previous Section we dealt with many-body quantum systems at equilibrium, possibly in their ground state(s) at zero temperature, or with a finite number of excitations at most. Moreover, the dynamical processes involved, say, in the braiding operations of anyonic excitations were treated in the adiabatic limit, hence effectively described in an equilibrium framework. Now, we would like instead to explore the behaviour of many-body quantum systems far from an equilibrium state. In its full generality this is a formidable task and, in order to make some progress, we need to focus on some specific protocols used to generate the out of equilibrium configuration. In this section we briefly review one of them, namely the quantum quench protocol [79, 80, 81]. In its most essential formulation, a quantum quench can be stated in very simple terms: an isolated system is prepared in the ground state $|\psi_i\rangle$ of a given initial Hamitonian H_i and then, at time $t = 0$, the

Hamiltonian is suddenly changed to a different final one H_f, e.g. by some abrupt change of parameters. Thus, assuming that the two Hamiltonians do not commute, the system is suddenly kicked out of equilibrium and its state has a non-trivial unitary evolution dictated by $|\psi(t)\rangle = \exp\{-iH_f t/\hbar\}|\psi_i\rangle$ for $t \geq 0$. This sudden quench protocol, and slight variations thereof, has been used as a theoretical tool to investigate the relaxation dynamics in many-body isolated quantum systems at least since the 1970s [82, 83, 84], and it became a flourishing area of research in the early 2000s [85, 86, 87] mainly due to the experimental advances in ultra-cold atoms [88]. Indeed, some ground breaking experiments in 2001-2002 [89, 90, 91] showed for the first time the impressive potential of optical lattices in manipulating the properties of Bose-Einstein condensates, in particular proving the experimental capability to tune the system across a superfluid-Mott quantum phase transition [90, 92]. Even though this first generation of experiments was mainly concerned with the exploration of the equilibrium phase diagram of the system, the possibility to tune the Hamiltonian parameters in time opened the door to the analysis of dynamical phenomena. In fact, besides the possibility to control the lattice geometry and to tune atom interactions by Feshbach resonances [93], the long coherence time and almost perfect isolation from the environment designated ultra-cold atomic gases as perfect set-ups to study the unitary evolution after a quantum quench [94]. It is worth pointing out, though, that ultrafast pump-probe experiments on solid state devices witnessed amazing experimental advances in the same years [95, 96], offering an alternative platform for studying quantum quenches on different time scales. Intense and ultrafast laser pulses can surgically excite some desired degrees of freedom, while their dynamics can be probed shortly after, when the target degrees of freedom are still effectively decoupled from the environment and display a unitary evolution [97, 98]. Even though short-lived, it is thus possible to generate and observe quenched states with highly non trivial properties, such as, e.g., high temperature superconductivity [99, 100].

1.2.1 Thermalization in isolated quantum systems

With the aid of ultra-cold atoms some fundamental and venerable questions could be experimentally probed, such as the thermalization mechanism for isolated many-body quantum systems [101, 102, 103, 104, 105]. Indeed, a conundrum emerges in the attempt to explain the undoubted success of thermal states in the description of many-body quantum systems: If we consider an isolated system, i.e. we include in our description all the degrees of freedom of the thermodynamic universe, and we initialize it in a pure, out of

equilibrium state, e.g. with a quench protocol, how can it reach a thermal state, given that the dynamics is linear and unitary?

Already 1929, Von Neumann proposed a proof of the ergodic theorem for quantum mechanical systems [106], however the research on the subject gained momentum only in 2008, after the numerical simulations by Rigol, Dunjko and Olshanii [107] that explicitly demonstrated the approach to thermalization (for a few body observables) of a quenched generic system, providing numerical evidence to support the eigenstate thermalization hypothesis (ETH) [108], proposed a decade earlier by Deutsch [109] and, independently, Srednicki [110]. In a nutshell, the ETH states that the expectation values of a local observable over the energy eigenstates of a generic many-body Hamiltonian are a smooth function of the energy, i.e. $\langle \psi_E | \hat{O} | \psi_E \rangle = O(E)$ with $O(E)$ a smooth function. Therefore, the expectation value of any local observable on any (reasonable) quenched state converges in time to the expectation value over a properly defined microcanonical ensemble. Indeed, the initial state can be expanded on the final energy eigenstates $|\psi_i\rangle = \sum_E c_i(E)|\psi_E\rangle$, where the normalized coefficients $c_i(E)$, i.e. $\sum_E |c_i(E)|^2$ are typically not negligible only on a finite energy window ΔE. Then, because of dephasing and the absence of degeneracy for a generic Hamiltonian, the long time expectation value of any local observable converges to the diagonal ensemble prediction $\langle \hat{O} \rangle(t) \xrightarrow[t \to +\infty]{} \sum_E |c_i(E)|^2 O(E)$. Moreover, the latter has to be equal to the microcanonical expectation value $\sum_{E \in \Delta E} |\Delta E|^{-1} O(E)$. Indeed, since $O(E)$ is a smooth function of energy, one can very well approximate $\sum_E |c_i(E)|^2 O(E) \approx O(\bar{E}) \approx \sum_{E \in \Delta E} |\Delta E|^{-1} O(E)$, where $\bar{E}$ is the central value of the energy window ΔE. We can thus conclude that thermalization happens at the quantum level because each single energy eigenstate of a generic many-body Hamiltonian has local properties similar to the ones of a thermal state.

Additionally, assuming the ETH to work for any local observable, we can find an elegant solution to the initial conundrum: We can focus on a finite subsystem A of the thermodynamic universe U and define the reduced density matrix $\rho_A(t) = \text{Tr}_B\{|\psi(t)\rangle\langle\psi(t)|\}$, by tracing out all the degrees of freedom of the complement subsystem $B = U - A$. The expectation value of all observables having support in A can then be computed via the reduced density matrix $\rho_A(t)$, according to $\langle O_A \rangle(t) = \text{Tr}_A\{O_A \rho_A(t)\}$. Therefore, since the ETH guarantees that the expectation value of all local observables in A converges in time to the equilibrium value, we can conclude that the state of subsystem A, encoded in the reduced density matrix $\rho_A(t)$, converges in time to a thermal equilibrium state. Since this result holds for any subsystem A we have solved the conundrum: Even though the state of the whole thermodynamic universe remains pure, its long time local properties -

that are the only meaningful one in a thermodynamic system - are captured by a mixed thermal state. The local thermal entropy is thus only due to the entanglement entropy, dynamically accumulated, between the subsystem and the rest of the universe [111].

Yet, even though thermalization is expected to occur in a generic system, the time scales necessary for such equilibration cannot be straightforwardly derived from the ETH and non-trivial phenomena can occur, such as prethermalization [112, 113, 114, 115, 116, 117], when the system reaches, on a fast time scale, a long lived non thermal state, before thermalization is eventually approached at much longer times.

1.2.2 Preventing thermalization

Once the general mechanism for thermalization in a many-body quantum system is understood, one may wonder whether there are ways to prevent it[13]. For instance, it would be a disaster for quantum computation if the quantum information locally stored in an array of qubits were always irremediably spread in the whole system, due to an exponentially fast thermalization. Hence, besides exploring schemes where quantum information is stored in a non local fashion, such as in the braiding patterns of topological quantum computation, a lot of work has been devoted to characterizing systems where information is locally preserved.

Integrable models were the first class of systems able to preserve an extensive amount of local information that got under the spotlight of research [119, 120, 121]. The historical starting point is the 2006 experimental work by Kinoshita, Wenger and Weiss [118], where trapped 1D Bose particles, prepared in an out of equilibrium state, "*do not noticeably equilibrate even after thousands of collisions*". Indeed, the authors further add that "*Our results are probably explainable by the well-known fact that a homogeneous 1D Bose gas with point-like collisional interactions is integrable*". This experimental work stimulated a lot of theoretical effort and, just a year later, Rigol, Dunjko, Yurovsky and Olshanii theoretically addressed the relaxation dynamics in integrable systems, proposing an interpretation in terms of a generalized Gibbs ensemble (GGE) [122]. Given that integrable systems possess and infinite number of local constants of motion $\hat{I}_\alpha$ in convolution $[\hat{I}_\alpha, \hat{I}_\beta] = 0$, the correct statistical ensemble capturing their long time behaviour has to take all these local conserved quantities into account. Therefore, Rigol *et al.* proposed a relaxation towards a GGE density matrix $\rho_{GGE} \propto \exp\{-\sum_a \lambda_\alpha \hat{I}_\alpha\}$, where the Lagrangian multipliers λ_α are

---

[13]Historically, it was somehow the other way around: The failure of thermalization demonstrated in the experimental work by Kinoshita *et al.* [118] prompted theoretical, as well as experimental, investigations on the thermalization mechanism.

fixed by the expectation values of the constants of motion on the initial state. Even though the precise identification of the correct conserved charges might not be trivial [123, 124, 125, 126], many theoretical and numerical works have established the GGE as the correct description for the late time properties of integrable systems, at least in a prethermal regime [120, 115], i.e. as long as the integrability-breaking perturbations, that unavoidably occur in any realistic implementation, can be neglected [127]. Yet, finding experimental evidence of relaxation towards a GGE is demanding and very sophisticated measurements were employed in the only successful detection reported in 2015 [128].

Another class of systems where thermalization is believed to fail and information is believed to be locally retained is the one characterized by many-body localization (MBL) [129, 130]. The conceptual starting point is, apparently, very far from integrability, as it involves the highly disordered Anderson insulator [131, 132, 133, 134]. Indeed, it is well known, since the 1958 work by Anderson [131], that any finite amount of disorder in a 1D system of non-interacting particles is enough to exponentially localize the eigenfunctions and turn the system into an insulating phase. Less conclusive results were known about the robustness of localization against particle interactions and in the mid 2000s some seminal papers provided strong evidence in support of if [135, 136, 137], giving birth to the research on MBL. Systems supporting MBL are believed to display an infinite number of local conserved quantities, that can be roughly understood as the generalization, to the interacting case, of the number operators associated to the single particle localized eigenstates of an Anderson insulator. Thus, an unexpected link between systems displaying MBL and integrability can be formulated and the failure of thermalization in both systems can be understood on similar grounds [138]. Even though evidence for MBL was experimentally reported in a quasirandom optical lattice in 2015 [139], recent works have questioned whether MBL is a stable phase in the thermodynamic limit and a conclusive answer has not been found yet [140].

Finally, in the last five years, many other mechanisms preventing thermalization, at least on a finite time window, have been proposed and discovered, such as confinement of the quasi-particle excitations [141, 142, 143], quantum many-body scars and Hilbert space fragmentation [144, 145, 146, 147, 148, 149, 150, 151, 152], local symmetries in lattice gauge theories [144, 153] and kinetically constrained models [154, 155, 156].

1.2.3 Topology out of equilibrium

We started this Chapter by focussing on the equilibrium (zero temperature) properties of topological phases of matter. However, having by now some acquaintance with non equilibrium protocols, it becomes natural to elaborate on topological features beyond the equilibrium setting. For instance, with applications in topological quantum computing in mind, a first step might involve the discussion of diabatic corrections in braiding operations [157, 158, 159, 160, 161, 162], since they limit the speed of computations and they may pose severe limitations to the stability and efficiency of the process. Yet, given that in the last ten years many topological models have been successfully simulated with ultra-cold atoms in optical lattices [163, 164, 165, 166, 167, 168, 169, 170, 171, 172, 173, 174] one is allowed to take even more radical approaches and ask about the behaviour of topological phases in quench protocols. In particular, what happens if a system is quenched between two topologically different phases? On general ground, since time evolution is a local unitary transformation and any two gapped state connected by such a transformation belong to the same phase [175], bulk topological invariants cannot change after a quantum quench [176, 177, 178, 179]. The same argument can also be understood from a different perspective: While local order parameters are expected to thermalize after a quench - or, at least, to have a non trivial relaxation -, topological invariants, being global features, can reasonably evade this fate. Nonetheless, the standard connections between topological invariants and physical properties of the system, such as Hall response, are not guaranteed to hold in a dynamical framework [180, 181, 182, 183] and, if the system has boundaries, topological edge modes might not be dynamically stable [184, 178, 185]. Furthermore, if the topological phase is of the SPT kind, even bulk topological properties can undergo a sudden melting [186, 187]. Indeed, a general mechanism, recently proposed by McGinley and Cooper, can mine the dynamical robustness of topological phases [188, 189]. The idea, dubbed "*dynamically induced symmetry breaking*" is very simple, though far reaching: An antinunitary operator, e.g. time reversal, that commutes with a given Hamiltonian (and thus is a symmetry of the system) does not commute with the time evolution operator generated by the same Hamiltonian, because of the complex exponential. Therefore, even if both the initial state of the system and the quenched Hamiltonian are symmetric under an antinunitary operator, the state can - and in general will - be no longer symmetric at later times. Hence, whenever a topological phase is protected by an antiunitary symmetry, its robustness can get immediately spoiled after the quench [190].

1.3   Organization of the Thesis

The rest of the Thesis is organized in two parts. In the first half we will deal with systems at or close to equilibrium.

In particular, in Ch.2 we will discuss equilibrium properties of semiconductor nanowires with strong spin-orbit coupling. We will show that some observable features, known as orthogonal spin density peaks - originally proposed as unique fingerprints of MZMs - can be mimicked by topologically trivial nanowires. Indeed, such peculiar spin density peaks might appear as a consequence of an inhomogenous spin-orbit interaction, without the need of any superconductive pairing. Additional caution is thus needed in the interpretation of experimental results about MZMs. Furthermore, we will thoroughly discuss the existence of topologically trivial bound states that arise as a consequence of the interplay between an inhomogeneous spin-orbit profile and an applied magnetic field.

In Ch.3 we will instead propose a different application of spin-orbit coupled nanowires by studying a transport phenomenon dubbed "Dirac paradox". Similarly to the most famous Klein-paradox [191, 192], describing massless Dirac particles that cannot be trapped by a scalar potential because of their helical nature, the Dirac paradox involves massless Dirac modes that, due to their helicity, can neither be reflected nor transmitted across an interface. After discussing the paradox in its full generality, we will show that, by the same token the Klein paradox has found a direct test in a solid state platform [193], the Dirac paradox could be observed with the aid of spin-orbit coupled nanowires, providing a novel insight into helical states and their properties.

Then, in the second half of the Thesis, we will discuss different realizations of quench dynamics.

In Ch.4 we will study a local quench, i.e. a sudden application of a local attractive potential, on a 1D Fermi gas. Focusing on an implementation with semiconducting nanowires, we will show that the system quickly relaxes to a GGE distribution that can be detected by measuring the absorption spectrum of the system, similarly to what is routinely done in pump-probe experiments. Indeed, the out of equilibrium distribution approached after the quench entails a population inversion that generates a negative absorption, i.e. a stimulated emission of radiation, in a well defined photon frequency range, providing a direct evidence of the GGE state.

In Ch.5 we will instead analyze the quench dynamics of a paradigmatic 1D topological insulator, namely the Su-Schrieffer-Heeger (SSH) model, recently realized in ultra-cold

atoms platforms. We will first show a general theorem: Because of charge conjugation symmetry, the expectation values of all real-space local observables are constrained to their equilibrium values, even when a quench is performed between the two, topologically different, phases of the model. In particular, this implies that no real space signatures of the topological edge modes appear after a quench. However, we will subsequently suggest different strategies to evade the hypothesis of the theorem and observe the dynamical formation/melting of the edge modes.

In Ch.6 we will focus again on the SSH model, yet with a different perspective. In fact, we will study the effects of a flux quench, i.e. a sudden suppression of the magnetic flux threading a ring-shaped 1D system, on an insulating state. We will show that, despite a vanishing Drude weight and a finite commutator between the Hamiltonian and the current operator, the flux quench induces a finite stationary current in the SSH model, that scales cubically with the initial flux. Moreover, even though the system is always gapped, the flux quench may also induce dynamical quantum phase transitions in the system, i.e. singularities in the Loschmidt echo.

Lastly, in Ch.7 we will show how a novel dynamical notion of topological phase emerges in a quench protocol. While only SPT phases are allowed in 1D systems at equilibrium, we will show that a dynamical topological invariant, that is not symmetry protected, naturally arises in a 1D quenched system when the space-time scaling limit is taken, namely when both time and system size tend to infinity while their ratio is kept constant. Furthermore, such topological invariant leaves a clear signature in the time dependent Berry phase of the system: when a constant magnetic flux pierces the system, the Berry phase develops a staircase behaviour in time, whose plateaus are in a one to one correspondence with the dynamical topological invariant, realizing a dynamical analog of the integer quantum Hall phases.

A summary of the main results of the Thesis is finally reported in Ch.8, together with an outline of possible future developments.

Chapter 2

Majorana-like localized spin density without bound states

The content of this Chapter is based on the published papers [194, 195]

2.1   Introduction

While in theoretical models a topological phase is characterized by a well specified range of parameters in the Hamiltonian, when it comes to finding an experimental evidence of such phase in a given material, the challenging question is "how to distinguish signatures of a topological from a trivial bound state?" As a general criterion, a topological bound state is stable to perturbations that do not close the gap of the topological phase, while a trivial bound state is not. However, because in a given experimental setup the actual parameter range characterizing the topological phase is not known a priori and/or may be relatively narrow, the search for such stable signatures is in general not a trivial task. In Nanowires (NWs) with strong Rashba spin-orbit coupling (RSOC) exposed to a magnetic field and proximized superconducting films, the presence of Majorana quasi-particles (MQPs) has been predicted[66, 65]. Although various experimental signatures compatible with such exotic states have been observed[68, 196, 197, 198, 199, 73, 72, 200], a smoking gun evidence has not been found yet. Indeed it has been pointed out that some observed data, like the zero bias peak in the conductance [68, 197, 198, 200], may also be caused by Kondo effect [201], disorder [202, 203] or inhomogeneities [204]. This controversy has recently spurred further investigations, which pointed out that in the topological phase also trivial bound states may be present [204, 205, 206, 207, 208, 209, 210]. Furthermore,

a quite recent analysis [211], carried out on a nanowire with homogeneous RSOC and with inhomogeneous magnetic field, showed that at the interface between two magnetic domains with opposite magnetization directions, bound states appear that are unrelated to the Jackiw-Rebbi topological states.

A more clear evidence of topological bound states requires a spatially resolved analysis. This was done, for instance, in ferromagnetic atomic chains deposited on a superconductor [212], where the combined use of spatially resolved spectroscopic and spin-polarized measurements showed that zero-bias conductance peaks are due to states localized at the ends of the chain. Yet, the smoking gun enabling one to identify such states with MQPs is their disappearance in the normal state, when superconductivity is suppressed. As far as NWs are concerned, it has been pointed out that MQPs in the topological phase exhibit an *orthogonal* spin density, i.e., a component perpendicular to both the magnetic and spin-orbit fields, localized at the NW ends [213, 214, 215]. In order to identify a topological phase in a given system, it is thus particularly important to understand whether and when the *topologically trivial* phase may exhibit observables that are spatially localized at the interfaces and that may mistakenly be interpreted as a topological signature. So far, this aspect has been analyzed far less than the topological bound states.

In this Chapter we aim to address this issue. Specifically, we consider the case of a RSOC NW exposed to a uniform magnetic field, and we analyze the spatial profile of charge and spin densities at the interface between two regions with different values of RSOC, as sketched in Fig.2.1(a). Such type of interfaces emerge quite naturally in any realistic setup, since metallic electrodes or gates are typically deposited on top of a portion of the NW, thereby altering the underneath structure inversion asymmetry characterizing the very RSOC. Furthermore, the recent advances in various gating techniques[216, 217, 218, 219, 220, 221], including gate-all-around approaches, allow a large tunability of the RSOC constant, possibly even changing the RSOC sign [222, 223, 224, 225, 226, 218, 227, 228, 229, 230, 231, 232, 233].

Importantly, on both sides of the interface, the NW that we consider is in the *topologically trivial phase*, since no superconducting coupling is included. Furthermore, as the gap depends only on the strength of the magnetic field, it never closes at the interface if a uniform magnetic field is applied. Thus, under these conditions the existence of bound states of topological origin is ruled out a priori.

Our analysis unveils various noteworthy aspects. In the first instance, a bound state may appear at the interface. Importantly such interface bound state, while being not topological, is *not* a customary interface state merely arising from the inhomogeneity of the RSOC. Indeed it can only exist if an external magnetic field is applied orthogonally to the RSOC field, and if its intensity fulfills specific conditions with respect to the two spin-orbit energies characterizing the two NW regions. The conditions of existence and the robustness of the bound state are analyzed in details in terms of different values of RSOC across the interface, including the smoothening length characterizing the crossover between these two values and the presence of a magnetic field component parallel to the RSOC field direction.

Secondly, we find for realistic values of chemical potential and temperature that the orthogonal spin density exhibits a peak pinned at the interface. Despite the NW is in the topologically trivial phase, such peak is relative robust to other parameter variations. In fact, we show that it persists even when the bound state is absent, indicating that in such case also the continuum states locally modify their spin-texture to maintain such effect. A similar phenomenon, where bulk states reorganize themselves to compensate for the existence of edge modes, will be described for the Su-Schrieffer-Heeger model in Ch.5.

Furthermore, by considering the case of two interfaces, we show that an additional kind of bound states may emerge, only due to a non monotonic RSOC profile. However, independently of the presence of either kinds of bound states, the peaks of the orthogonal spin density are opposite at the two ends of the inner NW region, similarly to what occurs for MQPs in the topological phase.

These results imply that a localized orthogonal spin-density can neither be taken as a unique signature of a MQP, nor of a topologically trivial bound state. However, we argue that it can represent a useful way to indirectly detect spin current differences. Indeed, while the detection of a bulk equilibrium spin current, which emerges in a homogeneous NW from the correlations between spin and velocity induced by the magnetic and spin-orbit fields [234], has been elusive so far, any *variation* of equilibrium spin current occurring at the interface is precisely related to the orthogonal spin-density peak predicted here.

The Chapter is organized as follows. In Sec. 2.2 we introduce the model and describe the involved energy scales. In Sec. 2.3 we present the results concerning the interface bound state, discussing first the case of a sharp RSOC interface profile and a magnetic field applied along the NW axis. Then we analyze the more realistic case of a finite smoothening length and we address the effect of a magnetic field component parallel to the

spin-orbit field direction[1]. In Sec. 2.4 we investigate the spatial profile of the charge and spin densities, and analyze specifically the bound state contribution to them. In Sec. 2.5 we discuss the origin of the spin density profiles in terms of the equilibrium spin current induced in the system by the interplay of the RSOC and the magnetic field. In Sec. 2.6 we extend our analysis to the case of two interfaces, we show that a different kind of bound states might emerge and we demonstrate how a magnetic field can be used to tune the charge equilibrium properties of the system. Then in Sec. 2.7 we propose some possible experimental realizations and, finally, in Sec. 2.8 we draw our conclusions.

2.2 The model for a SOC interface

2.2.1 Nanowire Hamiltonian

Let x denote the longitudinal axis of a NW deposited on a substrate. The NW is characterized by a RSOC, which is assumed to take two different values α_L and α_R on the left and on the right side of an interface, respectively [see Fig.2.1 (a)-(b)]. This inhomogeneity in the RSOC profile $\alpha(x)$ may result e.g. from the presence of a gate covering only one portion of the NW, or from two different gate voltage values applied to top/bottom gates or to the substrate. The crossover between α_L and α_R occurs over a smoothening length λ_s. Denoting by z the direction of the spin-orbit field $\mathbf{h}^{SO}$, i.e., the effective "magnetic" field generated by the RSOC [see Fig.2.1(a)], the NW Hamiltonian in the effective mass approximation [235] is

$$\hat{\mathcal{H}} = \int \hat{\Psi}^\dagger(x)\, H(x)\, \hat{\Psi}(x)\, dx \quad , \tag{2.1}$$

where

$$H(x) = \frac{p_x^2}{2m^*}\sigma_0 - \frac{\{\alpha(x), p_x\}}{2\hbar}\sigma_z - \mathbf{h}\cdot\boldsymbol{\sigma} \quad . \tag{2.2}$$

Here $\hat{\Psi}(x) = (\hat{\Psi}_\uparrow(x),\, \hat{\Psi}_\downarrow(x))^T$ is the electron spinor field, with $\uparrow,\downarrow$ corresponding to spin projections along z, $p_x = -i\hbar\partial_x$ is the momentum operator, m^* the NW effective mass, σ_0 the 2×2 identity matrix, and $\boldsymbol{\sigma} = (\sigma_x, \sigma_y, \sigma_z)$ are the Pauli matrices. For definiteness, we take the location of the interface at $x = 0$. The anticommutator in Eq.(2.2) is necessary since p_x does not commute with the inhomogeneous RSOC $\alpha(x)$ [236, 237]. The last term

---

[1]Note that a component of the magnetic field along a direction orthogonal to both the nanowire and the spin-orbit field can be re-absorbed in the magnetic field component along the nanowire, via a global unitary transformation. We can thus set it to zero without loss of generality.

in Eq.(2.2), where $\mathbf{h} = g\mu_B \mathbf{B}/2$, describes the Zeeman coupling with an external uniform magnetic field $\mathbf{B} = (B_x, 0, B_z)$ applied in the substrate plane, with μ_B denoting the Bohr magneton and g the NW Landé factor. It is useful to decompose the magnetic energy vector as $\mathbf{h} = h_x \mathbf{i}_x + h_z \mathbf{i}_z$, where h_x and h_z denote the components parallel and perpendicular to the nanowire axis x, i.e., perpendicular and parallel to the Rashba spin-orbit field direction z, respectively [see Fig.2.1(a)]. Although for most of our analysis we shall focus on the case of the magnetic field directed along the nanowire axis x, we shall also discuss the effects of the component h_z parallel to $\mathbf{h}^{SO}$.
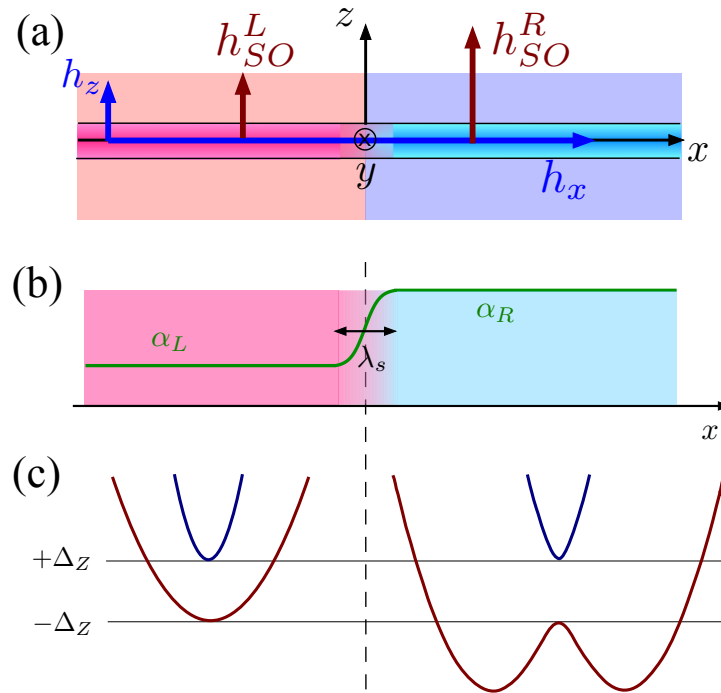
Fig. 2.1 (a) Top view of a Rashba nanowire deposited on a substrate: the Rashba effective magnetic field h^{SO} is directed along z, whereas an actual magnetic field, externally applied in the substrate plane, has components in the x-z substrate plane. The NW contains an interface between two regions with different RSOC values. (b) The spatial profile of the RSOC across the interface of the NW, ranging from the bulk values α_L to α_R over a smoothening lengthscale λ_s. (c) Examples of electronic bands related to the bulks of the two interface sides, the left-hand side in the Zeeman dominated regime, and the right-hand side in the Rashba-dominated regime.

2.2.2 Energy scales

In order to describe the results about the inhomogeneous RSOC profile at the interface, it is first worth pointing out the energy scales involved in the problem.

The homogeneous NW

Let us start by briefly summarizing the case of a homogeneous profile $\alpha(x) \equiv \alpha$ in Eq.(2.2), for an infinitely long NW. In such case the Hamiltonian (2.2) commutes with p_x, and the spectrum reads [234, 236, 237]

$$E_\pm(k) = \varepsilon_k^0 \pm \sqrt{h_x^2 + (\alpha k + h_z)^2} \quad , \tag{2.3}$$

where $\varepsilon_k^0 = \hbar^2 k^2/2m^*$ is the customary parabolic spectrum in the absence of RSOC and magnetic field. The spectrum (2.3) describes two bands separated by a minimal gap $2\Delta_Z$, where the quantity

$$\Delta_Z = |h_x| \tag{2.4}$$

shall be henceforth called the magnetic gap energy. Moreover, the RSOC α identifies the spin-orbit wavevector

$$k_{SO} = \frac{m^*|\alpha|}{\hbar^2} \quad , \tag{2.5}$$

which characterizes, in the absence of external magnetic field, the two degenerate minima $E(\pm k_{SO}) = -E_{SO}$ of the spectrum, where

$$E_{SO} = \frac{m^*\alpha^2}{2\hbar^2} = \frac{\hbar^2 k_{SO}^2}{2m^*} \tag{2.6}$$

is called the spin-orbit energy.

In the case $h_z = 0$, the spectrum (2.3) is symmetric $E_\pm(-k) = E_\pm(+k)$ and two regimes can be identified: (a) in the *Zeeman-dominated regime* ($\Delta_Z > 2E_{SO}$) both bands have a minimum at $k = 0$, which takes values $E_\pm^{\min} = \pm\Delta_Z$, respectively.
(b) in the *Rashba-dominated regime* ($\Delta_Z < 2E_{SO}$), the upper band still has a minimum $E_+^{\min} = +\Delta_Z$ at $k = 0$, while the lower band acquires two lower and degenerate minima $E_-^{\min} = -E_{SO} - \Delta_Z^2/4E_{SO}$ occurring at $k = \pm k^{min}$, with

$$k^{min} = k_{SO}\sqrt{1 - \Delta_Z^2/4E_{SO}^2} \quad . \tag{2.7}$$

When a component $h_z \neq 0$ parallel to the RSOC field is also present, the minimal gap $2\Delta_Z$ between the two bands occurs at $k = -h_z/\alpha$ and the spectrum is no longer symmetric $E_\pm(-k) \neq E_\pm(+k)$.

The eigenfunctions related to the spectrum (2.3) read

$$\psi_{k\pm}(x) = w_{k\pm} \exp[ikx]/\sqrt{\Omega} \quad , \tag{2.8}$$

with Ω denoting the system length. They describe plane waves with spinors

$$w_{k-} = \begin{pmatrix} \cos\frac{\theta_k}{2} \\ \\ \sin\frac{\theta_k}{2} \end{pmatrix} \quad w_{k+} = \begin{pmatrix} -\sin\frac{\theta_k}{2} \\ \\ \cos\frac{\theta_k}{2} \end{pmatrix} , \tag{2.9}$$

whose spin orientation $\mathbf{n}(k) \equiv (\sin\theta_k, 0, \cos\theta_k)$ lies on the x-z substrate plane and forms with the z-axis an angle $\theta_k \in [-\pi, \pi]$. The latter, defined through

$$\begin{cases} \cos\theta_k &= \dfrac{\alpha k + h_z}{\sqrt{(\alpha k + h_z)^2 + h_x^2}} \\ \\ \sin\theta_k &= \dfrac{h_x}{\sqrt{(\alpha k + h_z)^2 + h_x^2}} \end{cases} , \tag{2.10}$$

depends on the wavevector k, the magnetic field and the RSOC α. In particular, it is worth recalling that in the case of a magnetic field along the NW axis ($h_z = 0$) and in the deep Rashba-dominated regime ($\Delta_Z \ll 2E_{SO}$) the states with energy inside the magnetic gap mimic the helical edge states of the quantum spin Hall effect. Indeed their spin orientation, determined mainly by the RSOC, is opposite for right- and left-moving electrons, whose helicity is determined by the *sign* of the RSOC α. This is precisely the most suitable regime for the topological phase to be induced by an additional *s*-wave superconducting coupling [66, 65, 238, 239] and we will exploit this property in Ch.3 while studying the Dirac paradox.

The NW with a RSOC interface

When an interface separates two portions of a NW characterized by two different values α_L and α_R of RSOC [see Fig.2.1(b)], the momentum p_x does not commute with the Hamiltonian characterized by an inhomogeneous $\alpha(x)$-profile, and the spectrum cannot be labelled by a wavevector k. Before attacking the inhomogeneous problem in the next section, it is worth identifying the energy scales and the possible scenarios one can expect in the interface problem from a preliminary analysis of the bulks of the two regions across the RSOC interface. To begin with, the two bulk values α_L and α_R of the two NW regions

lead to two spin-orbit energies (2.6)

$$E_{SO,\nu} = \frac{m^*\alpha_\nu^2}{2\hbar^2} \qquad\qquad \nu = R/L \quad . \qquad (2.11)$$

Without loss of generality, we shall choose the RSOC with higher magnitude $|\alpha|$ on the right-hand side, and we can set it to a positive value, $\alpha_R > 0$, whereas the RSOC on the left-hand side is allowed to take any value in the range $-\alpha_R \leq \alpha_L \leq \alpha_R$[2]. Correspondingly, one has $E_{SO,L} \leq E_{SO,R}$. The fact that the magnetic field is uniform has important consequences, which are easily illustrated in the case $h_z = 0$: First, in the bulk of each region the gap between the bands is always given by $2\Delta_Z$, regardless of the regime (Rashba- or Zeeman-dominated) of each interface side. Secondly, the overall minimum of the two energy band bottoms is determined by the band bottom of the side with higher spin-orbit energy, i.e., the right-hand side, and is thus given by

$$E_{band}^{\min} = \begin{cases} -\Delta_Z & \text{if } \Delta_Z > 2E_{SO,R} \\[2ex] -E_{SO,R}\left(1 + \frac{\Delta_Z^2}{4E_{SO,R}^2}\right) & \text{if } \Delta_Z < 2E_{SO,R} \end{cases} \qquad (2.12)$$

With these notations, if the right-side is in the Zeeman-dominated regime, so is the left-hand side, whereas if the right-side is in the Rashba-dominated regime the left-hand side can be either in the Rashba- or in the Zeeman-dominated regime. There can thus be only three possible regime combinations: (i) $E_{SO,L} \leq E_{SO,R} \leq \Delta_Z/2$, where both sides are Zeeman-dominated; (ii) $\Delta_Z/2 \leq E_{SO,L} \leq E_{SO,R}$, where both sides are Rashba-dominated; (iii) $E_{SO,L} \leq \Delta_Z/2 \leq E_{SO,R}$, where the left-side is Zeeman-dominated while the right-side is Rashba-dominated. The bands of the latter case are illustrated as an example in Fig.2.1(c).

2.3   Interface bound state and its stability

In this section we focus on the inhomogeneous interface problem. By diagonalizing the inhomogeneous Hamiltonian, with methods to be described here below, we find that its spectrum always exhibits a continuum branch, whose bottom $E_{cont}^{\min}$ coincides with the minimal band energy obtained in Eq.(2.12) from the comparison of bare bulk spectra.

---

[2]The case where $\alpha_R < 0$ can easily be mapped into the one considered here, since the case with a $\alpha(x)$ profile can be mapped into the case $-\alpha(x)$ by space parity $(p_x \to -p_x)$, as is clear from the Hamiltonian (2.2).

However, for some parameter range (see below), the spectrum also displays an additional eigenvalue E_{bs}, lying *below* the continuum spectrum $E_{cont}^{\min}$. The related eigenfunction exhibits an evanescent behavior for $|x| \to \infty$. When such interface bound state exists, we define its positive 'binding energy' as

$$E_b = E_{cont}^{\min} - E_{bs} > 0 \quad . \tag{2.13}$$

Here below we now analyze the conditions for its existence.

2.3.1 The case of a sharp interface

Let us start by analyzing the existence of the bound state in the case of a sharp interface, where the smoothening length $\lambda_s \to 0$ vanishes and the profile can be assumed as

$$\alpha(x) = \alpha_L \theta(-x) + \alpha_R \theta(x) \tag{2.14}$$

with θ denoting the Heaviside function. In this case the eigenfunctions of the inhomogeneous problem can be obtained analytically by combining the eigenstates (2.8) of the homogeneous problem in each side and by matching them appropriately at the interface. In particular, since bound states are eigenstates with evanescent wavefunction for $|x| \to \infty$, they are obtained requiring that the wavevector k acquires an imaginary part. Details of such calculation can be found in Appendix A.1.

By keeping one side of the junction as a reference, e.g. the right-hand side where the bulk spin-orbit energy is maximal, the problem can be formulated in terms of dimensionless parameters, namely the RSOC ratio $\alpha_L/\alpha_R \in [-1, 1]$ and the energy ratios $E_b/E_{SO,R}$ and $\mathbf{h}/E_{SO,R}$ to the maximal spin-orbit energy $E_{SO,R}$. We shall focus here below on the case where the applied magnetic field is directed only along the nanowire axis x, $\mathbf{h} = h_x \mathbf{i}_x$, while the effects of a parallel magnetic field component h_z will be discussed later.

The results are presented in Fig.2.2. In particular, panel (a) displays the phase diagram of the existence of the interface bound state. For a sufficiently strong magnetic field, $\Delta_Z > 2E_{SO,R}$, i.e., when both NW sides are in the Zeeman-dominated regime, the bound state always exists, while for $\Delta_Z < 2E_{SO,R}$, where the NW right side is in the Rashba-dominated regime, the bound state may or may not exist, depending on the ratio α_L/α_R. In particular, for $\Delta_Z = 0$ (no external magnetic field), the bound state never exists, regardless of the ratio of the two RSOC values across the interface. This shows that this

interface bound state, although it has no topological origin, it is not an intrinsic interface state like the ones occurring at a customary semiconductor interface.
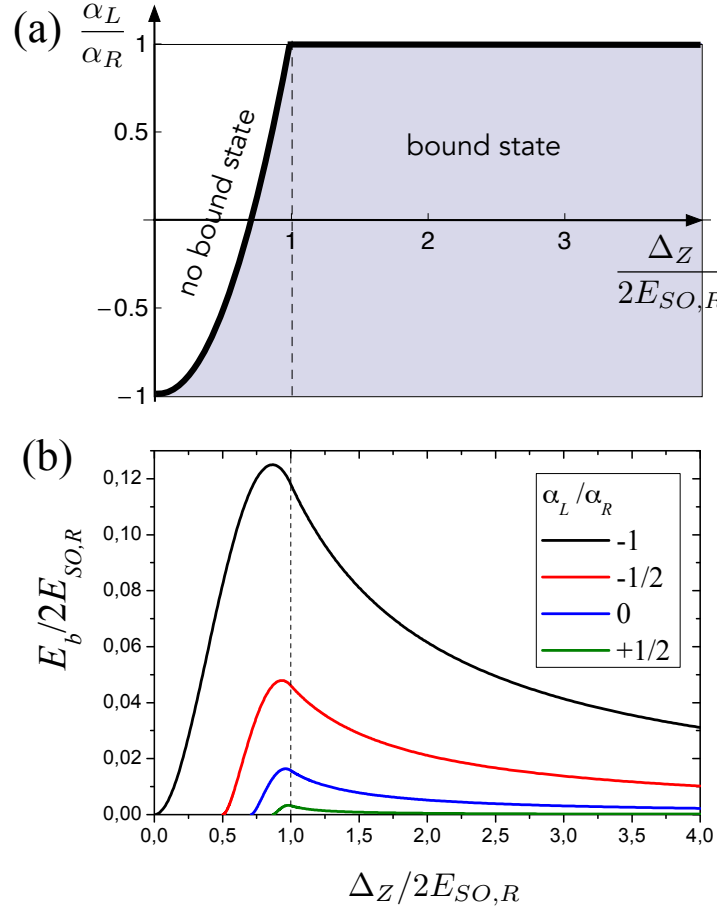
Fig. 2.2 The case of a sharp profile interface Eq.(2.14). (a) The phase diagram for the existence of the bound state is shown as a function of the magnetic gap energy (in units of twice the maximal spin-orbit energy $2E_{SO,R}$) and of the ratio between the two RSOC values across the interface. The thick black line identifies the transition curve, where the binding energy vanishes. The vertical thin dashed line indicates the crossover value from the Rashba-dominated to the Zeeman-dominated regime for the right-side of the interface. (b) The binding energy E_b of the bound state as a function of $\Delta_Z/2E_{SO,R}$ for four different values of the RSOC ratio across the interface.

The thick black line in Fig.2.3(a) denotes the transition curve for the existence of the bound state, and corresponds to the vanishing of the binding energy, $E_b = 0$. In particular, the parabolic curve for $\Delta_Z/2E_{SO,R} < 1$ is described by the equation

$$\frac{\Delta_Z^\star}{2E_{SO,R}} = \sqrt{\frac{1 + \alpha_L/\alpha_R}{2}} \quad , \tag{2.15}$$

while the upper horizontal line corresponds to the homogeneous NW in the Zeeman-dominated regime, where the bound state does not exist, as is obvious to expect. Then, Fig.2.2(b) shows, for four different values of the ratio α_L/α_R, the behavior of the binding energy E_b as a function of the ratio $\Delta_Z/2E_{SO,R}$. Several features are noteworthy.

First, in all cases the binding energy exhibits a non-monotonic behavior as a function of the magnetic gap energy, with a maximum $E_b^{\max}$ occurring for a magnetic gap energy slightly below the transition value $\Delta_Z = 2E_{SO,R}$ between the Rashba- and Zeeman-dominated regime of the right-hand side, highlighted by the vertical dashed line as a guide to the eye.

Secondly, the bound state energy strongly depends on the ratio α_L/α_R of the two RSOC values, and is typically much higher when the RSOC changes sign across the interface. In particular, the optimal condition for the existence of the bound state is $\alpha_L/\alpha_R = -1$, i.e., when the RSOC takes *equal and opposite* values of two sides: In this situation not only the bound state always exists, its binding energy is also higher than any other case. For these reasons, we shall henceforth term such case the 'optimal configuration'. In particular, it can be shown that, for weak applied field ($\Delta_Z \ll 2E_{SO,R}$) the binding energy of the optimal configuration behaves as $E_b \simeq \Delta_Z^2/4E_{SO,R}$ while for strong field ($\Delta_Z \gg 2E_{SO,R}$) one finds $E_b \simeq E_{SO,R}^2/2\Delta_Z$.

Third, for all other cases ($-1 < \alpha_L/\alpha_R < 1$) the bound state exists only if the magnetic gap energy overcomes a minimal threshold value, which precisely corresponds to the transition curve of Fig.2.2(a) described by Eq.(2.15). The threshold of the magnetic gap energy increases as the RSOC ratio α_L/α_R increases from the negative value -1 to the value $+1$, corresponding to the homogeneous case.

Furthermore, the following 'rule of thumb' can be inferred: when the band bottoms of the two interface sides are equal, the bound state certainly exists. Indeed a close inspection of Fig.2.2 shows that this certainly occurs in these two situations: (i) when $\Delta_Z/2E_{SO,R} > 1$, i.e., when both sides are in the Zeeman-dominated regime and their band bottoms are both equal to $-\Delta_Z$; (ii) when $\alpha_L = -\alpha_R$, i.e., when the two spin-orbit energies (2.11) are equal, both sides are in the same regime (Rashba- or Zeeman-dominated) and thus have the same band bottoms. In all other cases the existence of the bound state depends on the specific energy ratios.

Finally, even when the bound state exists, its binding energy can be quite small. For instance, the maximal binding energy in the case where $\alpha_L/\alpha_R = 1/2$ is about 25 times

smaller than the maximal value in the optimal case $\alpha_L/\alpha_R = -1$. Similarly, even in the regime $\Delta_Z/2E_{SO,R} > 1$ the binding energy decreases with increasing magnetic field.

2.3.2 Effects of a finite smoothening length

In any realistic system the crossover between two RSOC bulk values occurs over a finite smoothening length λ_s. To include such effect we now assume the following profile function

$$\alpha(x) = \frac{\alpha_R + \alpha_L}{2} + \frac{\alpha_R - \alpha_L}{2} \operatorname{Erf}\left(\frac{\sqrt{8}\,x}{\lambda_s}\right), \tag{2.16}$$

which varies from α_L to α_R up to 2% within the lengthscale λ_s. In Eq.(2.16) Erf denotes the error function. Although in the presence of such smoothened profile the model cannot be solved analytically, it can be approached by an exact numerical diagonalization of the Hamiltonian (2.2), whose details are summarized in App.A.2. Instead of expressing the results in terms of dimensionless parameters, we now choose to fix the parameters to realistic setup values. For definiteness, we consider the case of a InSb NW, with an effective mass $m^* = 0.015\,m_e$ and a maximal spin-orbit energy $E_{SO,R} = 0.25\,\text{meV}$. Furthermore, in order to appreciate the effects of the smoothening length, we focus on the case of the optimal configuration $\alpha_R/\alpha_L = -1$. The results, displayed in Fig.2.3(a), show the binding energy as a function of the magnetic gap energy Δ_Z for four different values of the smoothening length. As one can see, while for the ideal case $\lambda_s \to 0$ (sharp profile) the bound state always exists, for any finite smoothening length the bound state only appears above a threshold value for the Zeeman field. For sufficiently strong applied magnetic field (Zeeman-dominated regime) the bound state always exists. However, the binding energy exhibits an overall suppression for increasing λ_s. These effects can be understood be realizing that a crossover from $-\alpha_R$ to α_R in the RSOC profile occurring over a finite smoothening length can, to a first approximation, be considered as a stair-like sequence of smaller sharp α-steps. As the analysis carried out above on the sharp profile indicates (see Fig.2.2), in the case of a non-optimal jump $\alpha_L > -\alpha_R$, a threshold value for Δ_Z does exist and the binding energy is reduced. In summary, a finite smoothening length λ_s broadens the white portion of the sharp-profile phase diagram Fig.2.2(a) where the bound state does not exist, and suppresses the binding energy.
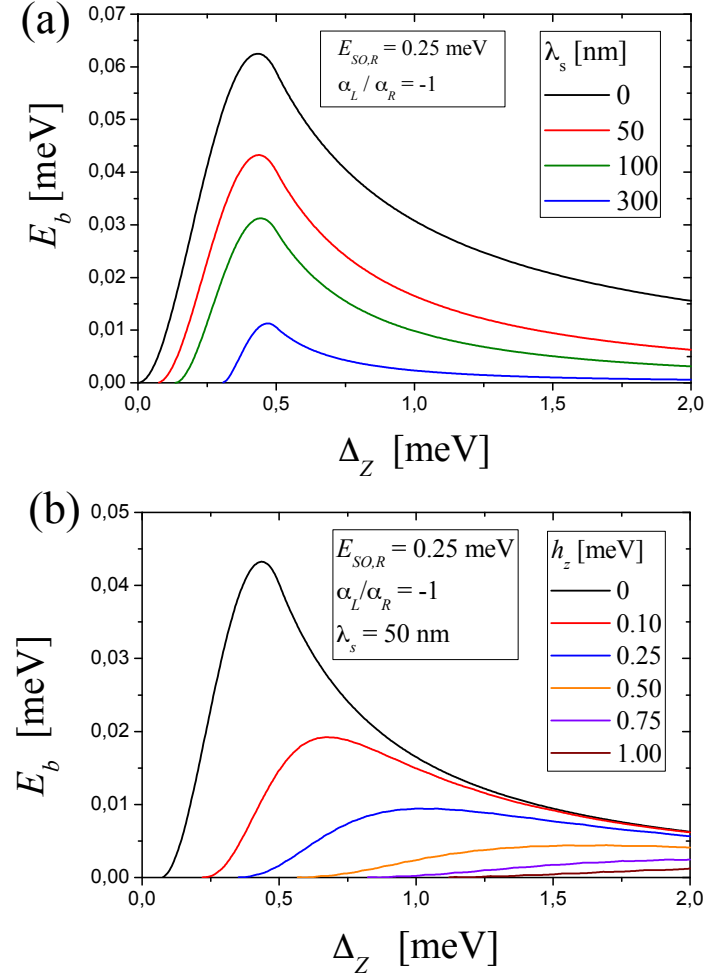
Fig. 2.3 The binding energy as a function of the magnetic gap energy, for an interface with $\alpha_L = -\alpha_R$, with $E_{SO,R} = E_{SO,L} = 0.25\,\text{meV}$. (a) The effects of a smoothening length. (b) Effects of a magnetic field component h_z parallel to the spin-orbit field on the binding energy, for a fixed smoothening length $\lambda_s = 50\,\text{nm}$.

2.3.3   Effects of a parallel field component

So far, we have analyzed cases where the magnetic field h_x is directed along the NW. Here we want to discuss the effect of a magnetic field component h_z parallel to the spin-orbit field. We first point out that, for $h_z \neq 0$ and $h_x = 0$, i.e., for a magnetic field directed purely along the spin-orbit field direction z, the eigenvalue problem for the Hamiltonian (2.2) completely decouples in the two spin-$\uparrow$ and spin-$\downarrow$ components, and it can be shown that the bound state does not exist (see App.A.1). The orthogonal field component h_x is thus a necessary, though not sufficient, condition for the bound state to exist. One can then

analyze how the parallel field component h_z modifies the existence of the bound state, for a fixed value of $h_x \neq 0$. To this purpose, we focus again on a InSb NW, with an optimal configuration $\alpha_R = -\alpha_L > 0$, and we take a realistic smoothening length $\lambda_s = 50\,\mathrm{nm}$. The result, displayed in Fig.2.3(b), shows that the presence of an additional parallel field component h_z modifies the dependence of the binding energy E_b as a function of the magnetic gap energy Δ_Z, especially by increasing the threshold value $\Delta_Z^\star$ at which the bound state starts to exist. Similarly to the case of the smoothening length, the binding energy values are quite reduced as compared to the case $h_z = 0$.

2.4   Charge and spin density spatial profiles

In the previous section we have discussed the existence and the robustness of the interface bound state, which is a spectral feature. Here we wish to analyze the spatial behavior of physical observables, namely the charge and spin densities, described by the operators

$$\hat{n}(x) = \mathrm{e}\,\hat{\Psi}^\dagger(x)\,\hat{\Psi}(x) \tag{2.17}$$

$$\hat{\mathbf{S}}(x) = \frac{\hbar}{2}\,\hat{\Psi}^\dagger(x)\,\boldsymbol{\sigma}\,\hat{\Psi}(x) \quad, \tag{2.18}$$

respectively, where e denotes the electron charge. The presence of the interface makes the NW an inhomogeneous system, and we aim to investigate the spatial profile of the equilibrium expectation values

$$\rho(x) \equiv \frac{1}{\mathrm{e}}\langle\hat{n}(x)\rangle_\circ \tag{2.19}$$

$$\mathbf{s}(x) \equiv \frac{2}{\hbar}\langle\hat{\mathbf{S}}(x)\rangle_\circ \tag{2.20}$$

with a particular focus on their behavior near the interface. Details about the computation of such expectation values can be found in App.A.2. Before presenting our results, a few general comments are in order.

Chemical potential and Temperature. The equilibrium distribution determining the expectation values (2.19) and (2.20) is characterized by a well defined value of chemical potential μ and temperature T. As pointed out above, the whole spectrum of the inhomogeneous Hamiltonian (2.2), which we obtain by an exact numerical diagonalization,

consists of a continuum spectrum, related to extended propagating states, and possibly (if present) a bound state, energetically lying below the continuum and corresponding to a state localized at the interface. At equilibrium, and ideally at zero temperature, all states (localized or extended) with energy up to the chemical potential μ are filled up, and contribute to determine the equilibrium expectation values $\rho(x)$ and $\mathbf{s}(x)$, while at finite temperature the Fermi function is smeared over a range $k_B T$ around the chemical potential. We shall choose for T and μ realistic values of low-temperature experimental setups involving NWs, namely $T = 250\,\text{mK}$ and $\mu = 0$, corresponding to the energy value in the middle of the magnetic gap [see Fig.2.1(c)]. This is the situation, for instance, where the Fermi energy states of a NW in the Rashba-dominated regime mimic the helical states of a quantum spin Hall system.

Orthogonal spin density. Concerning the spin density $\mathbf{s}(x)$ in Eq.(2.20), we shall specifically focus on s_y component, which we shall refer to as the *orthogonal spin density*, since it is orthogonal to the x-z plane identified by the applied magnetic field and the spin-orbit field. The interest in analyzing the profile of $s_y(x)$ stems from a comparison with the topological phase. Indeed it has been predicted [213, 214, 215] that the MQPs appearing at the ends of a proximitized NW in the topological phase, are precisely characterized by a non-vanishing expectation value s_y. However, we shall show here below that such orthogonal spin density already appears in the NW interface problem, where the NW is certainly in the topologically trivial phase, so that it cannot be considered as a signature of a MQP.

Full vs. bound state contribution. Interface bound states and orthogonal spin density s_y share two properties. First, both can only exist at an interface, i.e., in the presence of inhomogeneities. Indeed, in the bulk of a homogeneous NW, s_y vanishes since the spin orientation of each electron lies in the x-z plane [see Eqs.(2.9)-(2.10)]. Second, just like the bound state, s_y may only exist if both a magnetic field component h_x and the spin-orbit field are present. Indeed if $h_x = 0$ (or $\alpha = 0$) the electron spin is directed, along z (or x) for all states. In view of such common features, one is naively tempted to conclude that an orthogonal spin density is necessarily ascribed to the presence of the bound state. However, this is not the case. To this purpose, we shall illustrate below two types of spatial profiles. First, we shall show the actual equilibrium values $\rho(x)$ and $s_y(x)$ [see Eqs.(2.19) and (2.20)], which can be referred to as the 'full' density and orthogonal spin density profiles, as they result from contributions of all states, with the customary weight given by the Fermi function. In particular, since we focus on the low temperature regime, the latter

essentially amounts to the contribution of all states occupied up to the chemical potential μ. Then, we shall also provide the profiles $\rho_{bs}(x)$ and $s_{y,bs}(x)$ describing the contribution to $\rho(x)$ and $s_y(x)$ due to the localized bound state only [see App.A.2 for details].

This distinction enables us to show that an orthogonal spin density peak, besides being no evidence for a MQP, may also not originate from any bound state.
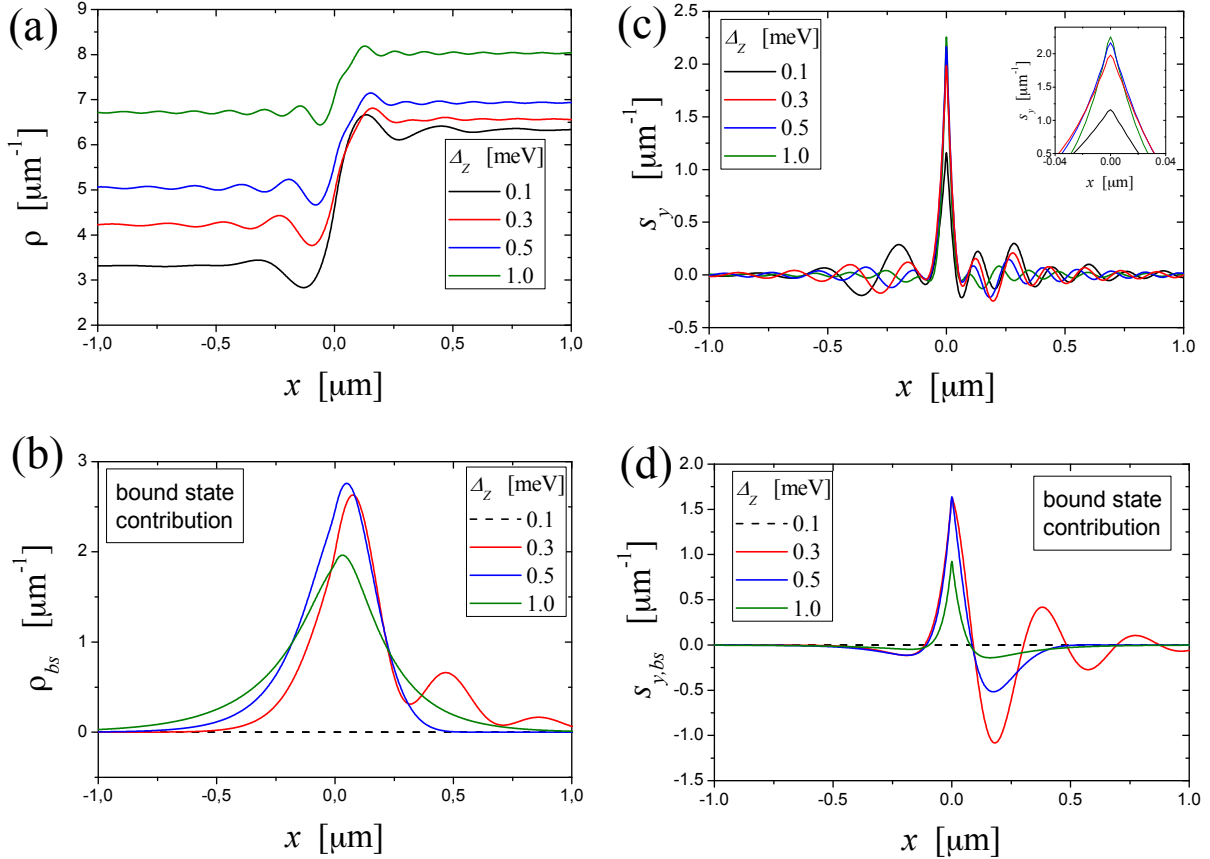

Fig. 2.4 Spatial profiles of charge density and orthogonal spin density for a sharp interface profile Eq.(2.14) with $\alpha_L/\alpha_R = -1/2$ and $E_{SO,R} = 0.25\,\mathrm{meV}$. The four different curves in each panel refer to four different values of the magnetic gap energy $\Delta_Z = (0.1, 0.3, 0.5, 1.0)\,\mathrm{meV}$. (a) The actual equilibrium density profile $\rho(x)$ [see Eq.(2.19)]. (b) The bound state contribution $\rho_{bs}(x)$ to the density $\rho(x)$. For $\Delta_Z = 0.1\,\mathrm{meV}$ the bound state does not exist and yields a vanishing contribution (black dashed curve). Panel (c) describes the full orthogonal spin density s_y Eq.(2.20) (with the inset magnifying the peaks) while panel (d) describes the related bound state contribution $s_{y,bs}$.

2.4.1 The case of a sharp profile with an orthogonal magnetic field

Let us start our analysis from the case of a sharp profile interface and a magnetic field applied along the NW axis. As an illustrative example, we consider an interface with $\alpha_L/\alpha_R = -1/2$, which implies $E_{SO,L} = E_{SO,R}/4$ [see Eq.(2.11)], and we choose a value of $E_{SO,R} = 0.25\,\text{meV}$ for the maximal spin-orbit energy.

Figure 2.4(a) shows the full equilibrium density Eq.(2.19), for four different values of the magnetic gap energy Δ_Z of the applied magnetic field h_x. Its spatial profile $\rho(x)$ exhibits a crossover at the interface $x = 0$ between two different bulk density values. The density increases towards the right-hand side, namely the region with higher spin-orbit energy. This indicates that a higher spin-orbit energy has a similar effect on the density as a lower gate voltage bias.

In Fig.2.4(b) we have singled out the contribution ρ_{bs} due to the interface bound state only. Differently from $\rho(x)$, the profile of $\rho_{bs}(x)$ is localized only around the interface and is dramatically sensitive to the value of Δ_Z. Indeed, as can be deduced from Eq.(2.15), the minimal threshold for the appearance of the bound state is, for the chosen parameters, $\Delta_Z^\star = E_{SO,R} = 0.25\,\text{meV}$. For values $\Delta_Z > \Delta_Z^\star$ [red, blue and green curves in Fig.2.4(b)], where the bound state exists, a comparison of the shape of the peak of ρ_{bs} with the profile of the full ρ [Fig.2.4(a)] would suggest that a small kink in ρ across the interface might be due to the presence of the bound state. However, the behavior of the full $\rho(x)$ across the interface [Fig.2.4(a)] is qualitatively very similar for all values of the magnetic gap energy Δ_Z, independently on whether the bound states exists or not. This sounds reasonable, since the electron density is a bulk equilibrium property receiving contributions from all states up to the chemical potential, and the bound state is just one of such contributions. The same reasoning holds for the s_x component of the spin density [see Eq.(2.20)], which is also a bulk equilibrium quantity, due to the applied magnetic field h_x.

Let us now turn to consider the spin density s_y. Differently from ρ and from s_x, the orthogonal spin density s_y is vanishing in the bulk of a homogeneous NW, as observed above. The profile of the full s_y, plotted in Fig.2.4(c), provides two important insights. First, a peak of the orthogonal spin density s_y does exist, even if the NW is in the topologically trivial phase, implying that it cannot be a unique signature of MQP. Second, the central peak at the interface is weakly sensitive to the values of the magnetic gap energy Δ_Z. This is in striking contrast to the behavior of the bound state contribution

$s_{y,bs}$, shown in Fig.2.4(d), which is again strongly dependent on the magnetic field. In particular, just like the density ρ_{bs}, for weak Zeeman field $s_{y,bs}$ vanishes since the bound state is absent (dashed curve), while for higher magnetic field its broadening depends on Δ_Z. These results show that a localized peak of orthogonal spin density s_y is not necessarily ascribed to the presence of a bound state, neither topological nor trivial.

Before concluding this subsection, a few further comments about Fig.2.4 are in order. We observe that, while the spatial profile of the bound state density ρ_{bs} [panel (b)] is smooth, the profile of $s_{y,bs}$ [panel (d)] exhibits a cusp at the interface. This difference originates from the boundary conditions induced by the sharp profile (2.14), which cause spin-diagonal observables like ρ and s_z to have continuous derivatives, while spin off-diagonal observables like s_x and s_y to exhibit a cusp at the interface (see App.A.1). Moreover, for $\Delta_Z = 0.3\,\mathrm{meV}$, i.e., slightly above the threshold $\Delta_Z^\star = 0.25\,\mathrm{meV}$, the profiles of the bound state contributions exhibit a slowly decaying oscillations on the right-hand side, since the bound state wavefunction is characterized by a complex wavevector k on such side. In contrast, for $\Delta_Z = 0.5\,\mathrm{meV}$ and $\Delta_Z = 1.0\,\mathrm{meV}$ the wavevector is purely imaginary, and the bound state density profile has an exponential decay without oscillations. Finally, the peak of the orthogonal spin density $s_{y,bs}$ has a narrower extension than the one of ρ_{bs}. This is due to the fact that, since on each interface side the bound state wavefunction is a linear combination of two elementary spinorial waves [see Eq.(2.8)], ρ_{bs} and $s_{y,bs}$ are determined by different combinations of w-spinor components of the wavefunctions, resulting also into different weights for the space-dependent profiles.

2.4.2 Effects of a smoothened profile and parallel magnetic field on the orthogonal spin density

In the previous subsection we have shown that the peak of the orthogonal spin density is far more robust than the interface bound state. In order to test how general such effect is, we now extend the previous analysis including the presence of a finite smoothening length in the RSOC profile and a magnetic field component h_z parallel to the spin-orbit field. For simplicity, we focus on the optimal configuration $\alpha_L/\alpha_R = -1$ and $E_{SO,R} = 0.25\,\mathrm{meV}$, with a smoothening length $\lambda_s = 50\,\mathrm{nm}$. These are the parameters also used in Fig.2.3(b), whence we observe that, keeping a fixed value of the magnetic gap energy Δ_Z, and varying the additional parallel field component h_z represents a natural physical knob to control the weight and the existence of the bound state.
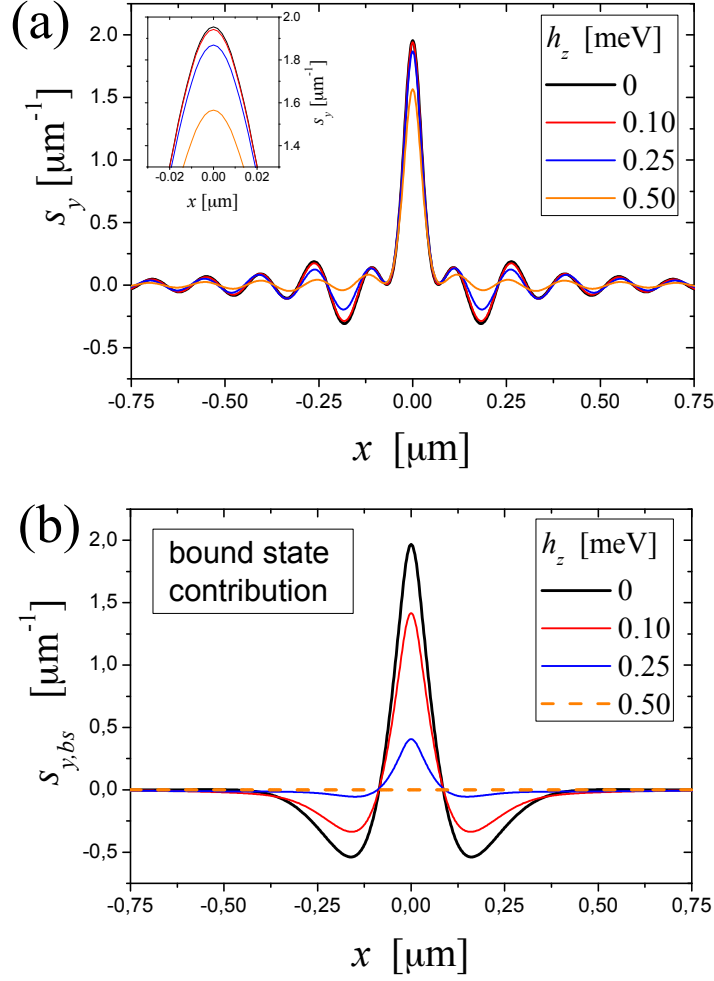
Fig. 2.5 Spatial profile of the orthogonal spin density for a NW interface with $\alpha_L/\alpha_R = -1$ and a smoothening length of $\lambda_s = 50\,\text{nm}$. The maximal spin-orbit energy is $E_{SO,R} = 0.25\,\text{meV}$, and the magnetic gap is $\Delta_Z = 0.50\,\text{meV}$. Different curves refer to different values of the magnetic field component h_z parallel to the spin-orbit field. (a) The actual s_y due to all states, with the inset magnifying the peaks. (b) The bound state contribution to s_y.

Figure 2.5 shows the spatial profile of the orthogonal spin density for $\Delta_Z = 0.50\,\text{meV}$ and for various values of h_z. In particular, panel (a) displays the full s_y, while panel (b) shows the bound state contribution $s_{y,bs}$. Two features are noteworthy. In the first instance, as compared to the cuspid peaks obtained at the interface in the case of the sharp profile [Fig.2.4(c)-(d)], the peaks of Fig.2.5 are rounded off by the finite smoothening length λ_s. Secondly, while the peak of the full s_y [Fig.2.5(a)] is very weakly affected by the parallel magnetic field component h_z, the bound state peak shown in Fig.2.5(b) rapidly decreases and eventually disappears when the parallel magnetic field component h_z is ramped up, yielding a vanishing contribution (dashed line). This is in agreement with

the binding energy behavior previously shown in Fig.2.3(b), where one can see that, at $\Delta_Z = 0.50\,\mathrm{meV}$, the bound state disappears for $h_z = 0.50\,\mathrm{meV}$. The comparison between panels (a) and (b) of Fig.2.5 clearly indicates that, when the bound state exists and has a relatively high binding energy, the peak of s_y is mainly due to it. However, when the binding energy decreases, the bound state contribution to the peak is replaced by the one of the excited states, so that the orthogonal spin density peak remains present. Indeed, we will show in Ch.3 that extended states with energies inside the magnetic gap might develop a localized orthogonal spin density at the interface between regions with different RSOC.

2.5   Equilibrium spin current

We have demonstrated that the peak of the orthogonal spin density localized at the interface does not necessarily stem from a localized bound state, and appears to be a quite general feature. Two natural questions then arise, namely i) what parameters characterizing the interface determine such peak? ii) can one explain its presence on some general principle? Here we wish to address these two questions.

2.5.1   General features of the orthogonal spin density

To answer the first question, we consider for definiteness the case of magnetic gap energy $\Delta_Z = 0.50\,\mathrm{meV}$ and a maximal spin-orbit energy $E_{SO,R} = 0.25\,\mathrm{meV}$. Two parameters characterize the interface, namely the ratio α_L/α_R of the two RSOC, and the smoothening length of the profile. In Fig.2.6(a) we show, for a fixed smoothening length $\lambda_s = 50\,\mathrm{nm}$, the orthogonal spin density profile for different values of the RSOC ratio α_L/α_R across the interface. As one can see, the height of the peak grows with the relative RSOC jump, in a roughly linear way.

In Fig.2.6(b), keeping now the ratio of the two RSOC bulk values to $\alpha_L/\alpha_R = -1$, we vary the smoothening length λ_s of the profile. The peak decreases and broadens with increasing λ_s. Importantly, one can verify by a numerical integration that the area underneath each $s_y(x)$ profile is to a very good approximation *independent* of the value of the smoothening length λ_s.
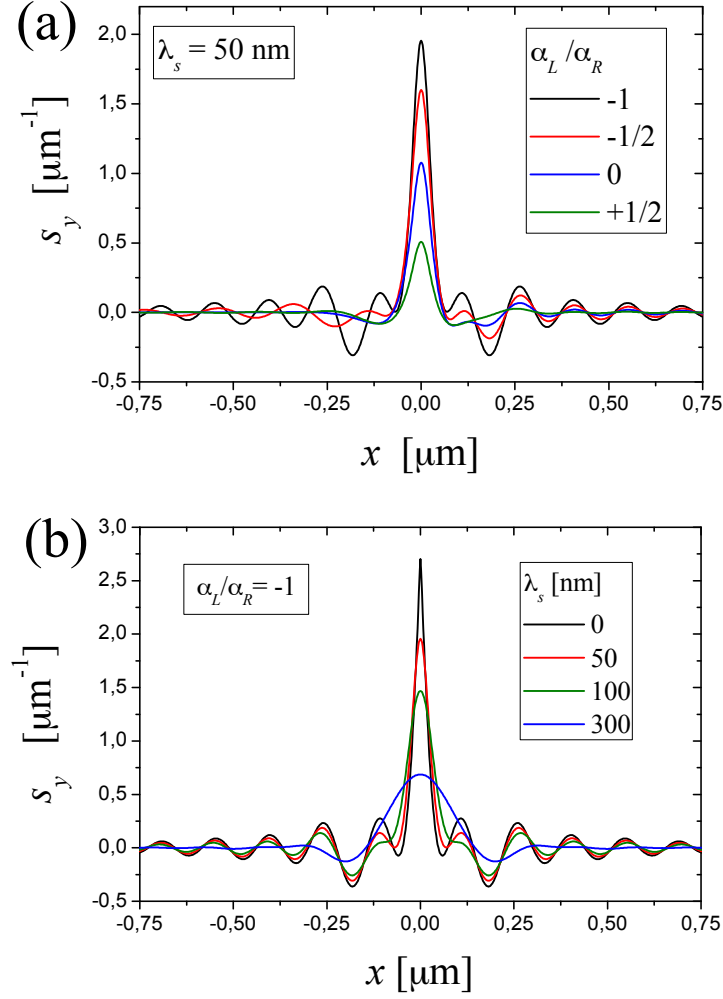
Fig. 2.6 Spatial profile of the orthogonal spin density for an interface with $E_{SO,R} = 0.25\,\mathrm{meV}$, and a magnetic gap energy $\Delta_Z = 0.50\,\mathrm{meV}$. (a) The effects of the ratio between the two values of RSOC, for a fixed smoothening length $\lambda_s = 50\,\mathrm{nm}$. (b) Effects of the smoothening length, for the configuration $\alpha_L/\alpha_R = -1$.

2.5.2   Origin of the orthogonal spin density

Keeping in mind the two features described in the previous subsection, let us now discuss the origin of the orthogonal spin density peak. As is well know, a magnetic moment exposed to a magnetic field experiences a magnetic torque[240]. So is the case for spin magnetic moments of electrons moving in a NW, where both the externally applied magnetic field **h**

and the effective spin-orbit field $\mathbf{h}^{SO}$ give rise to corresponding torques, defined as

$$\hat{\mathbf{T}}^h \equiv \hat{\Psi}^\dagger \left(\boldsymbol{\sigma} \times \mathbf{h}\right) \hat{\Psi} \quad , \tag{2.21}$$

$$\hat{\mathbf{T}}^{SO} \equiv \frac{1}{2} \left(\hat{\Psi}^\dagger (\boldsymbol{\sigma} \times \mathbf{h}^{SO})\hat{\Psi} + \text{H.c.}\right) \quad , \tag{2.22}$$

respectively, where

$$\mathbf{h}^{SO}(x,t) = \frac{\{\alpha(x), p_x\}}{2\hbar}(0,0,1) \tag{2.23}$$

is the spin-orbit field (see Appendix A.3 for details). Note that, by definition Eqs.(2.22)-(2.23), the spin-orbit torque $\hat{\mathbf{T}}^{SO} = (\hat{\mathrm{T}}^{SO}_x, \hat{\mathrm{T}}^{SO}_y, 0)$ has no component along the Rashba field direction z.

Importantly, the torques determine the spin-dynamics through the operator identity

$$\partial_t \hat{\mathbf{S}} + \partial_x \hat{\mathbf{J}}^s = \hat{\mathbf{T}}^h + \hat{\mathbf{T}}^{SO} \tag{2.24}$$

where $\hat{\mathbf{S}}$ is the spin density operator in Eq.(2.18), and

$$\begin{aligned}
\hat{\mathbf{J}}^s &= \frac{1}{2} \left(\hat{\Psi}^\dagger(x)\, \hat{\mathbf{S}}\, v\, \hat{\Psi}(x) + \text{H.c.}\right) \\
&= \frac{\hbar}{2} \left(-\frac{i\hbar}{2m^*} \left(\hat{\Psi}^\dagger(x)\, \boldsymbol{\sigma}\, \partial_x \hat{\Psi}(x) - \partial_x \hat{\Psi}^\dagger(x)\, \boldsymbol{\sigma}\, \hat{\Psi}(x)\right)\right. \\
&\quad \left. - \frac{\alpha(x)}{\hbar} \hat{\Psi}^\dagger(x)\, \frac{\{\boldsymbol{\sigma}, \sigma_z\}}{2}\, \hat{\Psi}(x)\right)
\end{aligned} \tag{2.25}$$

is the spin current density operator [240, 241]. Having denoted by

$$v = \frac{[x, H(x)]}{i\hbar} = \frac{p_x}{m^*} - \frac{\alpha(x)}{\hbar}\sigma_z \tag{2.26}$$

the velocity operator. Differently from the continuity equation for charge, in Eq.(2.24) the torques on the right-hand side play the role of sources and sinks of spin.

At equilibrium the expectation values of $\hat{\mathbf{S}}$ is time-independent, while the one of the magnetic torque is straightforwardly related to the equilibrium spin-density Eq.(2.20), through $\mathbf{T}^h = \langle \hat{\mathbf{T}}^h \rangle_\circ = \mathbf{s} \times \mathbf{h}$. Thus, taking the equilibrium expectation value of Eq.(2.24) one has

$$\partial_x \mathbf{J}^s = \mathbf{s}(x) \times \mathbf{h} + \mathbf{T}^{SO}(x) \tag{2.27}$$

where $\mathbf{T}^{SO} = \langle \hat{\mathbf{T}}^{SO} \rangle_\circ$. Let us focus on the most customary situation where the magnetic field is directed along the NW axis x ($\mathbf{h} = h_x \mathbf{i}_x$), i.e., orthogonal to the spin-orbit field. In this case, one can show that the spin-orbit torque $\mathbf{T}^{SO}(x)$ vanishes and that the spin current is oriented along z, so that Eq.(2.27) reduces to

$$\partial_x J_z^s = -h_x \, s_y(x) \quad . \tag{2.28}$$

We shall now argue that this equation, derived under quite general hypotheses, is the key to interpret the appearance of the orthogonal spin density at the interface, even when the bound state is absent.

Indeed, as has been demonstrated in Ref.[234], when uniform spin-orbit and magnetic fields are present in a NW, an equilibrium spin current J_z^s flows in its bulk. Such bulk spin current arises from the interplay between spin-orbit field and a magnetic field orthogonal to it, which induce non-trivial quantum correlation between spin and velocity, in close similarity to what happens in the helical states of a quantum spin Hall system. The bulk equilibrium spin current is odd in α and even in h_x. For example, for $\mu = 0$ and in the regime $\Delta_Z \gg E_{SO}$, one has $J_z^s = -\text{sgn}(\alpha)\sqrt{\Delta_Z E_{SO}}/3\pi$. Equilibrium spin currents have been predicted for other RSOC systems as well [241, 242, 243, 244, 245, 246, 247, 248, 249, 250, 240, 251, 252, 253, 254, 255] and, in fact, they can be regarded to as the diamagnetic color currents associated to the non-abelian spin-orbit gauge fields [256, 257]. However, its measurement in actual experiments has not been achieved thus far. In this respect, Eq.(2.28) suggests that, while the equilibrium spin current itself is perhaps elusive, its *variation* in the presence of inhomogeneities could be detected, as it is straightforwardly connected to the orthogonal spin density. Indeed, when two regions with different RSOC are connected, a kink $\partial_x J_z^s$ must arise at the interface to match the different spin current values in the two bulks. In view of Eq.(2.28), a peak in the orthogonal spin density s_y necessarily appears. This is the reason why the peak of s_y shown in Fig.2.6(a) is the more pronounced the higher the difference in the RSOC of the two regions. Furthermore, integrating both sides of Eq.(2.28), one can see that the integral of the s_y profile equals the difference between the two bulk spin currents, which is independent of the smoothening length. This is precisely what we found in Fig.2.6(b). Finally, this argument is quite general and is not based on the existence of a bound state at the interface. This explains why the peak shown in Fig.2.4(d) persists even when the bound state is absent, and shows that the naive interpretation of an orthogonal spin density localized peak in terms of a bound state is in general wrong.

2.6 The case of two interfaces

Thus far, we have considered the case of one single interface along the NW. Here we wish to discuss the case of two interfaces, modeling a NW inner region characterized by a RSOC parameter α_{in} sandwiched between two outer regions, where the RSOC shall be taken for simplicity equal to α_{out} in both. This model might describe an experimental setup where a gate partly covers the nanowire, thereby locally changing the SIA and the RSOC of the region underneath, similarly to what occurs in constrictions in quantum spin Hall systems[258, 259, 260]. Thus, the RSOC profile reads

$$\alpha(x) \;\; = \;\; \alpha_{out} + \frac{\alpha_{in} - \alpha_{out}}{2} \left[\text{Erf} \left(\frac{\sqrt{8}}{\lambda_s}(x + \frac{L}{2}) \right) - \text{Erf} \left(\frac{\sqrt{8}}{\lambda_s}(x - \frac{L}{2}) \right) \right] \;\; , \qquad (2.29)$$

and it is sketched in Fig.2.7(a), here L denotes the length of the inner NW region, supposed to be much bigger than the smoothening length λ_s, so that the notion of interfaces still makes sense. When the distance L is much larger than the typical variation lengthscale for observables in the single interface problem, the two interfaces act independently. However, when such two scales become comparable, noteworthy aspects emerge, which are illustrated in Fig.2.7.

First, if the interface bound states exist, they overlap across the distance L, causing a splitting of their degeneracy. The density profile of the resulting lowest eigenstate is mainly peaked at the interfaces, but is non vanishing also in the center of the inner region, as illustrated by the black curve in Fig.2.7(b).

Second, pronounced orthogonal spin density peaks appear at the interfaces, regardless of whether interface bound states exist or not. Remarkably, the signs of the peaks are *opposite* at the two interfaces, as shown in Fig.2.7(c). This is because the opposite jump in the RSOC across the two interfaces causes two opposite kinks in the equilibrium spin current, as observed in Sec.2.5.2. Thus, despite the NW is in the topologically trivial phase, the emerging scenario is identical to the one occurring in a NW in the topological phase, where the spin density of the MQPs is orthogonal to both the magnetic field and the RSOC field direction, and takes opposite signs at the two NW ends [213, 214, 215]. This explicitly demonstrates that such orthogonal spin polarization pinned at the NW ends can neither be taken as a hallmark of the topological phase, nor as an evidence of bound states. Note also that the orthogonal spin polarization peaks are typically narrower than the interface bound state and are thus more robust to finite length L effects too.
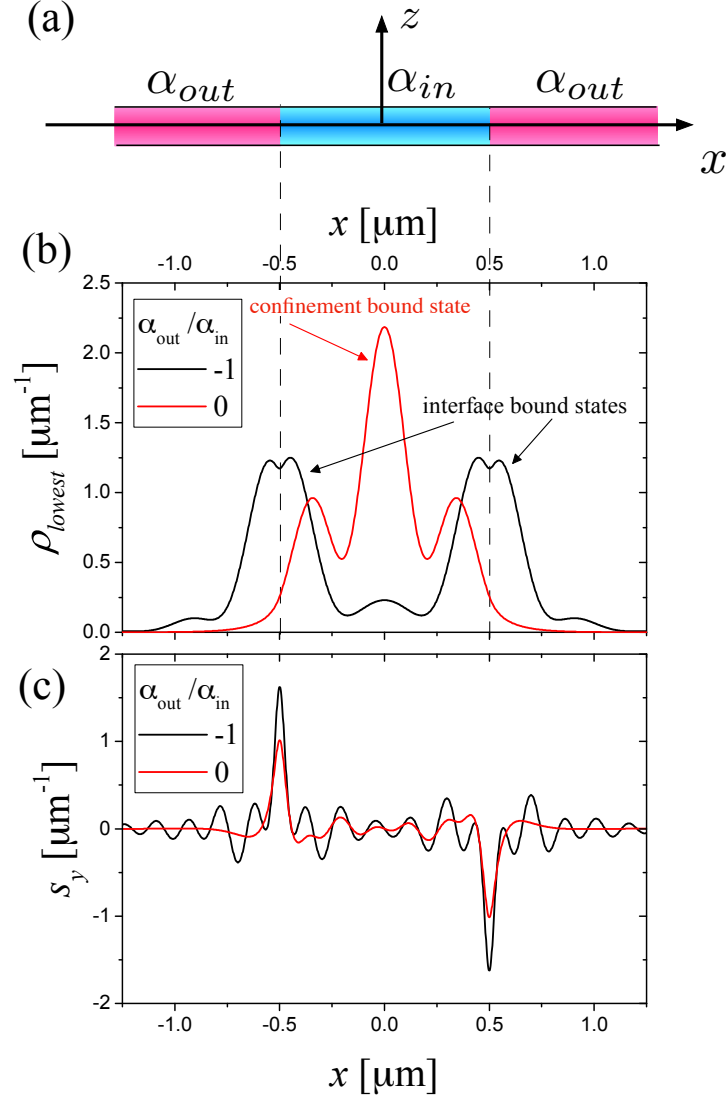
Fig. 2.7 (a) Sketch of a double interface problem, modeled by the RSOC profile (2.29). The parameters are $L = 1\,\mu$m, $\lambda_s = 50$ nm, the value $\alpha_{in} > 0$ in the inner region corresponds to $E_{SO,in} = 0.25$ meV, while the magnetic gap energy is $\Delta_Z = 0.25$ meV. (b) The density profile of the lowest electron state, for two values $\alpha_{out} = -\alpha_{in}$ (black curve) and $\alpha_{out} = 0$ (red curve), showing the difference between interface and Rashba dot bound states. (c) The total orthogonal spin density, for the same two values of α_{in}, shows two opposite peaks at the interfaces.

The third interesting feature of the double interface problem is that, even if the interface bound states are not present, another type of bound states, dubbed confinement bound states, may appear, as we shall now elaborate.

2.6.1   Confinement bound states

In order to illustrate the emergence of confinement bound states, it is sufficient to consider the case without magnetic field ($h_x = 0$). In this case, the Hamiltonian in Eq.(2.2) is diagonal in spin space and, by performing the spin-dependent gauge transformation

$$\hat{\Psi}(x) = e^{i\frac{m^*}{\hbar^2}\sigma_3 \int_0^x \alpha(x')dx'}\,\hat{\Psi}'(x) \quad , \tag{2.30}$$

it can be rewritten as

$$\hat{\mathcal{H}} = \int \hat{\Psi}'^\dagger(x)\left(\frac{p_x^2}{2m^*} + U_{SO}(x)\right)\hat{\Psi}'(x)\,dx \quad , \tag{2.31}$$

where the effective potential

$$U_{SO}(x) = -E_{SO}(x) = -\frac{m^*\alpha^2(x)}{2\hbar^2} \quad , \tag{2.32}$$

depending on the RSOC profile $\alpha(x)$, corresponds to (minus) the inhomogeneous Rashba spin-orbit energy. Notice that, due to the absence of magnetic field h_x, the problem becomes purely scalar when rewritten in terms of the new fields $\hat{\Psi}' = (\Psi'_\uparrow\,,\,\Psi'_\downarrow)^T$. In terms of the original fields $\hat{\Psi}(x) = (\hat{\Psi}_\uparrow(x)\,,\,\hat{\Psi}_\downarrow(x))^T$, the spin-$\uparrow$ and spin-$\downarrow$ components acquire opposite space-dependent phase factors, as shown by Eq.(2.30). As an example, for a uniform RSOC $\alpha(x) \equiv \alpha$, one has

$$\Psi_{\uparrow,\downarrow}(x) = e^{\pm i\,\mathrm{sgn}(\alpha)\,k_{SO}x}\,\Psi'(x) \tag{2.33}$$

which corresponds, in momentum space, to shifting horizontally the parabolic spectrum by a spin-orbit wavevector $k_{SO} = m^*|\alpha|/\hbar^2$, in opposite directions for spin $s = \uparrow, \downarrow$.
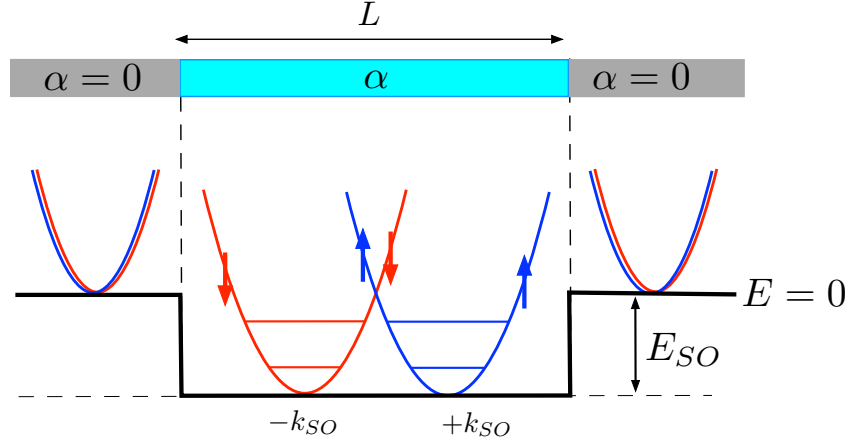
Fig. 2.8 Sketch of a nanowire coupled to a gate in the absence of magnetic field, and the related energy bands characterizing the bulks of the inner/outer regions. While the outer regions are characterized by a vanishing RSOC and by a spin-degenerate parabolic spectrum, the RSOC α present in the inside region lifts the spin degeneracy even without magnetic field. Furthermore, the energy bands are lowered by an amount corresponding to the spin-orbit energy $E_{SO} = m^*\alpha^2/2\hbar^2$, giving rise to the potential well described by Eq.(2.32) and depicted by the thick black line. The finite length of the central region yields the presence of confinement bound states, whose energy lie in the energy window between the band bottoms of the inner/outer portions of the nanowire.
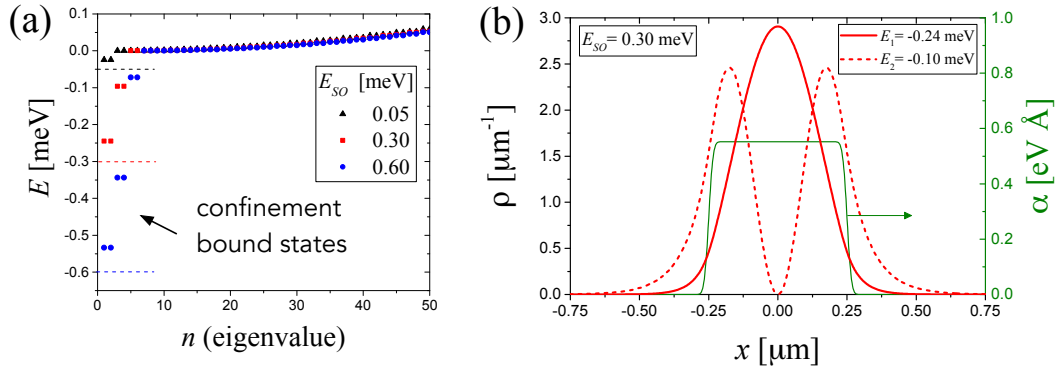

Fig. 2.9 Panel (a): The energy spectrum of a InSb nanowire+gate system, sketched in Fig.2.8 and described by the inhomogeneous RSOC Eq.(2.29), with an inside region $L = 500\,\mathrm{nm}$ and a smoothening length $\lambda_s = 50\,\mathrm{nm}$. The effective mass is $m^* = 0.015 m_e$. No magnetic field is applied ($\Delta_Z = 0$). Different colors and symbols refer to three different value of the spin-orbit energy of the inside region, $E_{SO} = 0.05\,\mathrm{meV}$ (black triangles), $E_{SO} = 0.30\,\mathrm{meV}$ (red squares), $E_{SO} = 0.60\,\mathrm{meV}$ (blue circles). Besides the continuum spectrum, discrete bound states appear, in spin-degenerate pairs, in the energy window between the bulk band bottom $E = 0$ of the outer regions and the bulk band bottom $-E_{SO}$ of the inside region (indicated by an horizontal dashed lines as a guide to the eye). Panel (b): for the case $E_{SO} = 0.30\,\mathrm{meV}$, the spatial profiles of the density $\rho(x)$ of the ground bound state (solid red curve) and the first excited bound state (dashed red curve) are shown. The thin green curve displays the inhomogeneous spatial profile $\alpha(x)$ in Eq.(2.29).

For suitable inhomogeneous $\alpha(x)$ profiles, a possibility opens up that the effective potential Eq.(2.32) represents a quantum well hosting confinement bound states [236, 237]. The simplest model describing this situation, sketched in Fig.2.8, is a square profile, $\alpha(x) = \alpha\,\theta(L/2 - |x|)$, with θ denoting the Heaviside function. This corresponds to setting $\alpha_{in} = \alpha$, $\alpha_{out} = 0$ and $\lambda_s = 0$ in Eq.(2.29). Then, Eq.(2.32) represents a square quantum well with a width L and a depth $-E_{SO}$, given by the spin-orbit energy $E_{SO} = m^*\alpha^2/2\hbar^2$ of the inside region of the nanowire. As is well known, at least one bound state is always present, and the number of bound states increases with the magnitude of the RSOC. Furthermore, if the length L is short enough, the energy separation between the bound states becomes appreciable (see Fig.2.8).

A more realistic model to describe the nanowire+gate system assumes a finite smoothening length λ_s. In Fig.2.9 we analyze this case for $L = 500$nm, a smoothening length $\lambda_s = 50$ nm and for three different values of the inside RSOC, corresponding to three different values of spin-orbit energy E_{SO}, in a InSb nanowire. Panel (a) displays the spectrum, which exhibits both a continuum branch, for energies above the band bottom $E = 0$ of the outer regions, and some additional discrete bound states, always appearing in spin-degenerate pairs, whose number increases with the magnitude of the RSOC. As expected, the bound states energies E_{bs} are located in the energy window $-E_{SO} \leq E_{bs} < 0$ between the bulk band bottom $-E_{SO}$ of the inside region (indicated by dashed horizontal lines as a guide to the eye) and the bulk band bottom $E = 0$ of the outside regions, as also sketched in Fig.2.8. Figure 2.9(b) shows, for the case $E_{SO} = 0.30$ meV, the spatial profile of the density $\rho(x)$ of the ground bound state (solid red curve) and the first excited bound state (dashed red curve), as well as the inhomogeneous spatial profile $\alpha(x)$ (thin green curve).

It is worth emphasizing that a prerequisite for the formation of confinement bound state is that the RSOC profile varies non-monotonically. In the case *e.g.* of one single interface separating two regions characterized by different RSOC values, where the profile $\alpha(x)$ varies *monotonically* from the value α_L on the left of the interface to the value α_R on the right, the effective potential in Eq.(2.32) never creates a quantum well. Indeed, if α_L and α_R have the same sign, U_{SO} also changes monotonically, whereas if α_L and α_R have opposite signs, so that the profile $\alpha(x)$ crosses zero, U_{SO} describes a *barrier* at the interface. In neither case a monotonic $\alpha(x)$ profile can give rise to bound states.

2.6.2   Magnetic control of the charge distribution

We shall now generalize the previous analysis to the situation $|\alpha_{in}| > |\alpha_{out}|$ and, in particular, we shall discuss how the spectrum and the equilibrium properties are modified when a magnetic field is applied.

Based on the material previously discussed in Sec.2.3.1 and Sec.2.6.1, let us first point out the scenario one can expect in this situation. On the one hand, when no magnetic field is present, the band bottom $-E_{SO,in}$ of the central region is lower than the outer band bottom $-E_{SO,out}$, and confinement bound states exist, while no interface bound state may be present. On the other hand, when a magnetic field is applied, the confinement bound states get modified by the magnetic field, while additional interface bound states appear at the two interfaces. The latter are energetically located below the lower bulk band bottom and are thus more favorable than confinement bound states. In fact, when the magnetic field is sufficiently strong, the band bottoms of the central and outer regions get aligned and the confinement bound states disappear completely, leaving only the interface bound states.

We also wish to point out that the inhomogeneous RSOC problem in the presence of an applied magnetic field is intrinsically more difficult than the field-free case. To illustrate that, we apply again the gauge transformation (2.30), and rewrite the Hamiltonian (2.2) as

$$\hat{\mathcal{H}} = \int \hat{\Psi}'^{\dagger}(x) \left(\frac{p_x^2}{2m^*} + U_{SO}(x) - h_x \left(\sigma_x \cos\theta_{SO}(x) + \sigma_y \sin\theta_{SO}(x) \right) \right) \hat{\Psi}'(x) \, dx \,, \quad (2.34)$$

where $\theta_{SO}(x) = 2m^* \int_0^x \alpha(x') dx'/\hbar^2$ is called the spin-orbit angle. In terms of the new fields $\hat{\Psi}'$ the RSOC has been re-absorbed into the previously discussed potential Eq.(2.32), whereas the original uniform magnetic field has transformed into an effective *inhomogeneous* magnetic field, whose consequences are more subtle.
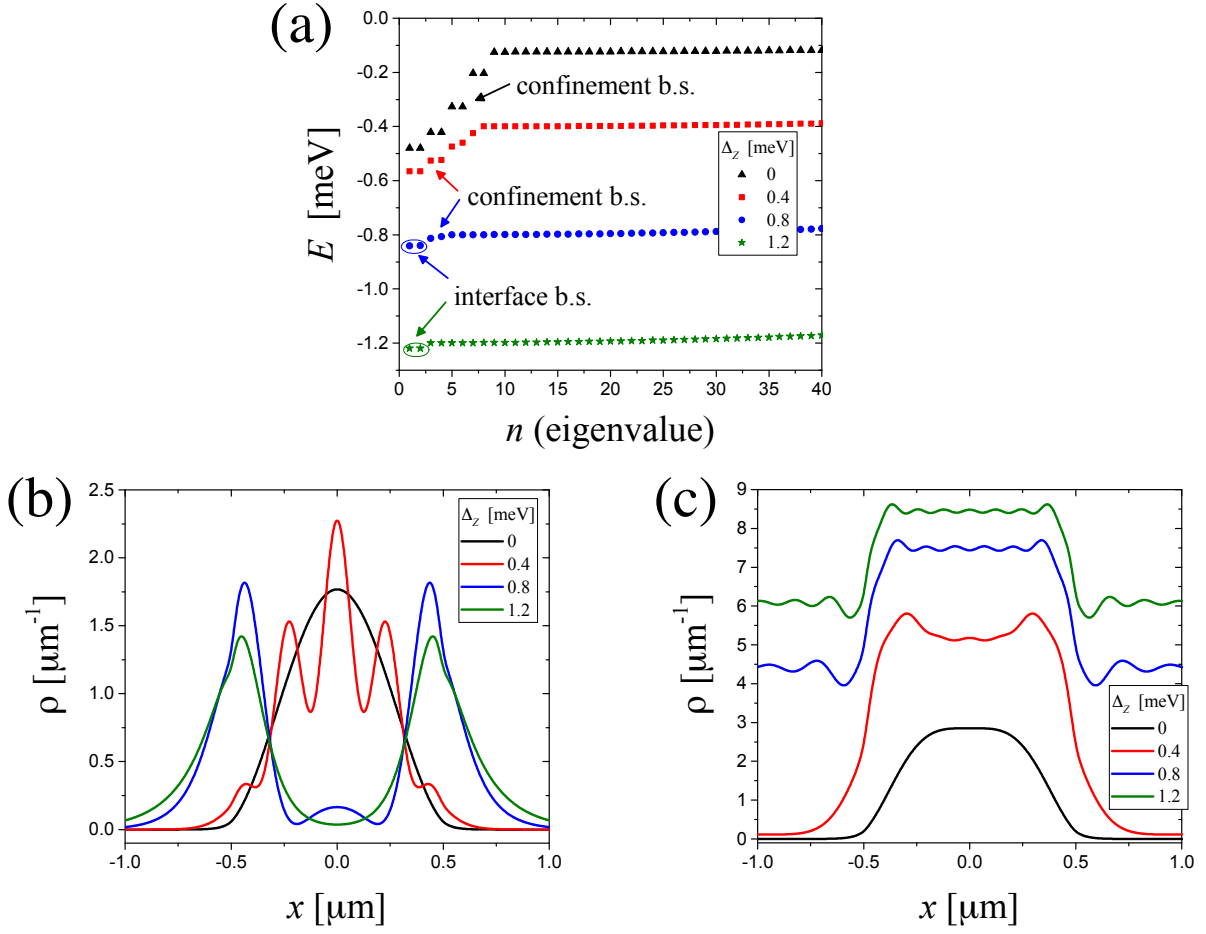
Fig. 2.10 A portion $L = 1\mu$m of a InSb nanowire takes a RSOC value α_{in} different from the value α_{out} characterizing the rest of the nanowire, *e.g.* due to the presence of a metallic gate covering it. The RSOC α_{in} corresponds to a spin-orbit energy $E_{SO,in} = 0.5$ meV for the central region, while $\alpha_{out} = -\alpha_{in}/2$, and $E_{SO,out} = 0.125$ meV. The smoothening length of the RSOC profile (2.29) is $\lambda_s = 50$ nm. The inhomogeneous nanowire is exposed to an external magnetic field along the nanowire axis. Panel (a): The spectrum of the inhomogeneous nanowire is plotted for four different values of the applied magnetic field: for vanishing or weak magnetic field (black triangles and red squares) only confinement bound states are present. For $\Delta_Z > \Delta_Z^\star \simeq 0.5$ meV, two additional interface bound states appear below the confinement bound states (blue circles), while for $\Delta_Z > 2E_{SO} = 1$ meV (green stars) the confinement bound states have disappeared and only the interface bound states survive. Panel (b): The density profile ρ_{lowest} of the lowest energy state, plotted for the same four values of applied magnetic field, shows a change in the nature of the electronic ground state from a confinement to interface bound states, determining a displacement of the electron charge from the center to the interfaces with the leads located at $x = \pm 0.5\,\mu$m. Panel (c): the profile of the total density ρ, involving all occupied states up to a chemical potential $\mu = -0.45$ meV is shown for the four different values of applied magnetic field.

We illustrate these effects in a InSb nanowire, where the central region has a bulk spin-orbit energy $E_{SO,in} = 0.5\,\text{meV}$, while the outer regions are characterized by $\alpha_{out} = -\alpha_{in}/2$, yielding $E_{SO,out} = 0.125\,\text{meV}$. Moreover, the length of the central region is $L = 1\,\mu\text{m}$ and the smoothening length across each interface is $\lambda_s = 50\,\text{nm}$. In Fig.2.10(b) the spectrum of the inhomogeneous nanowire is plotted for four different values of the applied magnetic gap energy $\Delta_Z = (0, 0.4, 0.8, 1.2)\,\text{meV}$. As one can see, for vanishing magnetic field $\Delta_Z = 0$ (black triangles), four doubly degenerate confinement bound states are present, within the energy window between the band bottoms $-E_{SO,out} = -0.125\,\text{meV}$ and $-E_{SO,in} = -0.50\,\text{meV}$ of the outer and central regions, respectively. When the magnetic field is increased (red squares), the energy window determined by such band bottom mismatch reduces, and so does the number of confinement bound states. Furthermore, if the magnetic gap energy overcomes a threshold value $\Delta_Z > \Delta_Z^\star \simeq 0.5\,\text{meV}$ (blue circles), two additional interface bound states appear. They are linear combinations of the two bound states appearing at the two interfaces and are almost degenerate, with a tiny energy splitting caused by a non vanishing overlap due to the finite length L of the central region. Note that in this situation confinement and interface bound states coexist, although the interface bound state are always energetically more favorable, as they lie below the band bottoms. However, for even stronger magnetic fields, $\Delta_Z \geq 2E_{SO} = 1\,\text{meV}$, the confinement bound states disappear and only the interface bound states survive (green stars).

In Fig.2.10(c) we have plotted the density profile ρ_{lowest} of the lowest energy state, for each of the four Δ_Z values. One can thus clearly see that, while for vanishing magnetic field (black curve) the energetically most favorable state is mainly located at the center of the confinement region, by increasing the magnetic field the interface bound state becomes more favorable (blue and green curves). By operating with the magnetic field one can thus displace the charge of the electronic ground state from the center of the gated nanowire region towards the interfaces located at $x = \pm 0.5\,\mu\text{m}$, yielding a stronger coupling with the outer regions. Finally, in Fig.2.10(d) we have plotted the full electron density, due to all states filled up to a chemical potential value $\mu = -0.45\,\text{meV}$, again for the four values of applied magnetic gap energy. While for $\Delta_Z = 0$ the charge is purely localized in the center of the nanowire, the application of a magnetic field leads the charge to be delocalized also in the outside regions. Notably, even for the green curve at $\Delta_Z = 1.2\,\text{meV}$, where both nanowire regions are in the Zeeman dominated regime ($\Delta_Z > 2E_{SO,in} > 2E_{SO,out}$) and their bulks have the same band bottom, the stronger spin-orbit coupling in the central region causes the density therein to exhibit a plateau higher than the density in the outer regions.

2.7 Possible setup realizations

Several experiments in topological systems are based on InSb[261, 198, 262, 224, 263, 200] or InAs [264, 222, 265, 225, 266, 72] NWs deposited on a substrate. In the case of InSb the effective mass and the g-factor are $m^* \simeq 0.015 m_e$ and $g \simeq 50$, respectively, while the value of the RSOC depends on the specific implementation and experimental conditions and can be widely tunable, ranging from $\alpha \sim 0.03\,\mathrm{eV\,\AA}$ to $\alpha \sim 1\,\mathrm{eV\,\AA}$ [222, 224, 68, 261, 198, 262]. The spin-orbit energy E_{SO} resulting from these values [see Eq.(2.6)] is a fraction of meV. The same order of magnitude is obtained for the magnetic gap energy Δ_Z in a magnetic field range of some hundreds of mT. These are the values adopted in our plots. Similarly, in the case of InAs nanowires $m^* \simeq 0.022\,m_e$, $g \simeq 20$ and the RSOC ranges from $\alpha \sim 0.05\,\mathrm{eV\,\AA}$ to $\alpha \sim 0.3\,\mathrm{eV\,\AA}$ [197, 264, 222, 265]. The temperature value of $250\,\mathrm{mK}$ used in our plots is state of the art with modern refrigeration techniques.

Interfaces between regions with different RSOC emerge quite naturally in typical NW setups, where a portion of the NW is covered by e.g. a superconductor or by a normal metal to induce proximity effect, to measure the current, or to locally vary the potential. The resulting SIA is inhomogeneous along the NW, and can be controlled e.g. by the application of different gate voltage values applied to top/bottom gates or to the substrate, similarly to the case of constrictions in quantum spin Hall systems [258, 259, 260]. In particular, covering one portion with the gate-all-around technique and by applying a sufficiently strong gate voltage, it is reasonable to achieve an inversion of the sign of the RSOC as compared to the uncovered NW portion, as has already been done in similar setups [267, 223, 268, 269].

Finally, the orthogonal spin polarization predicted here can be measured by spatially resolved detection of spin orientation. In particular, nanometer scale resolution can be reached with various methods such as magnetic resonance force microscopy [270],[271], spin-polarized scanning electron microscopy [272, 273], by using quantum dots as probes [274, 275], or also electrically by potentiometric measurements exploiting ferromagnetic detector contacts [276, 277].

2.8 Conclusions

In conclusions, in this Chapter we have considered a NW with an interface between two regions with different RSOC values, as sketched in Fig.2.1, when the proximity effect is turned off and the NW is in the topologically trivial phase.

In Sec.2.3 we have shown that at the interface bound states may appear, whose energy is located below the continuum spectrum minimum. Such bound states are neither topological (since proximity effect is absent), nor intrinsic interface bound states (since they only exist if an external magnetic field is applied along the NW axis). Analyzing first the case of a sharp interface RSOC profile Eq.(2.14), we have obtained the phase diagram determining the existence of the bound state [see Fig.2.2(a)], as well as the dependence of its binding energy on the magnetic gap energy [see Fig.2.2(b)]. While the bound state always exists if the RSOC takes equal and opposite values across the interface (optimal configuration), for all other situations it only exists if the magnetic field overcomes a minimal threshold value. Furthermore, even in the optimal configuration, it can be suppressed by either a finite smoothening length in the RSOC profile or a magnetic field component parallel to the spin-orbit field (see Fig.2.3).

In Sec.2.4 we have then investigated the spatial profile of the charge density ρ and the spin density, with a special focus on the spin density component s_y, orthogonal to both the applied magnetic field and the RSOC field direction, which is known to characterize the MQPs localized at the edges of a NW in the topological phase. By analyzing both the full equilibrium values ρ and s_y due to all occupied states, and the bound state contributions ρ_{bs} and $s_{y,bs}$, we have been able to gain two useful insights. First, the orthogonal spin density appears also in the topologically trivial phase as a quite general effect characterizing any interface between two different RSOC regions under a magnetic field. Second, for realistic and typical values of chemical potential and temperature, the orthogonal spin density peak is relatively robust to parameter changes, and persists even when the bound state is absent (see Figs.2.4 and 2.5). This means that also the propagating states of the continuum spectrum modify their spin texture around the interface to preserve the peak, so that a localized orthogonal spin-density cannot be considered a signature of a bound state.

Furthermore, in Sec.2.5, after analyzing the peak dependence on the single interface parameters (see Fig.2.6), we have also shown that such stable peaks may in fact have an impact on the detection of spin currents. Indeed a spin current flows in the bulk of a NW as a result of quantum correlations between spin and velocity induced by the interplay between magnetic and spin-orbit field, similarly to the case of quantum spin Hall helical states. Despite various proposals in the literature, the measurement of equilibrium spin currents has not been achieved yet. Our results suggest that, while the equilibrium spin current itself may be elusive, its variations can be detected through the orthogonal

spin density s_y, which is instead experimentally observable with spin-resolved detection techniques. Indeed the orthogonal spin density peak is precisely related to the kink of the spin current localized at the interface. This analysis has recently been confirmed also in Ref.[278].

Finally, in Sec.2.6 we have addressed the case of two interfaces [see Fig.2.7]. While for a large distance L between the interfaces the single-interface scenario is merely doubled, for a shorter L the interface bound states may overlap and additional confinement bound states may appear [see Figs.2.7-2.8-2.9]. In all cases, and independently of the presence of interface bound states, the spin density s_y, *orthogonal* to both the magnetic field and the Rashba spin-orbit field, exhibits relatively robust peaks taking *opposite signs* at the two interfaces [see Fig.2.7(c)]. Remarkably, these are the same features predicted for the spin density of the MQPs emerging at the ends of a NW in the topological phase, despite the NW considered here is in the topologically trivial phase. Our results thus show that such orthogonal spin polarization pinned at the NW ends can neither be taken as a hallmark of the topological phase, nor as an evidence of bound states. However, the interplay of magnetic and spin-orbit fields open the possibility to magnetically tune the property of the bound states in the system and to control the equilibrium charge density [see Fig.2.10].

With the provided description of possible implementations in realistic NW setups, the predicted effects seem to be at experimental reach.

Chapter 3

The Dirac paradox in $1 + 1$ dimensions

The content of this Chapter is based on the published paper [279]

3.1 Introduction

Conventional semiconductor heterostructures are typically described, within the envelope function and effective mass approximations, by a Schrödinger Hamiltonian with a space dependent effective electron mass varying along the growth direction and accounting for the different effective masses of the component materials.

In the last two decades, however, it has been realized that in various materials such as graphene, topological insulators and Weyl semimetals, the dynamics of the conduction electrons is well captured, in physically relevant regimes, by a (D+1)-dimensional *massless* Dirac electron model[280, 281, 282, 1, 2, 283, 284], where D denotes the spatial dimension, and "+1" the time dimension. These discoveries have thus spurred the interest in the investigation of Dirac heterojunctions. Each massless Dirac cone is characterized by a given helicity of the electron eigenstates, i.e. a sign encoding the locking between the propagation direction and the orientation of a "spin-like" degree of freedom, which can be a sublattice pseudospin, like in graphene, or the actual angular momentum in topological insulators. In particular, when a junction is formed between two Dirac materials with opposite helicity, a paradoxical situation emerges, as sketched in Fig.3.1. A right-moving electron (blue line on the left-hand side) impinging transversally towards a spin-inactive interface can neither

be transmitted nor be reflected, due to spin conservation. The Dirac paradox has been discussed in heterojunctions between two 3D Topological insulators, whose surface states are governed by a 2D massless Dirac Hamiltonian. In such a case the surface electrons turn out to "escape" the problem by leaking along the interface surface[285, 286, 287, 288]. However, in a truly 1D realization of a Dirac model such way out to an extra dimension does not exist and the Dirac paradox becomes even more interesting. The challenging question is whether a solution in 1D exists and, if so, whether it can be realized in some physical system.
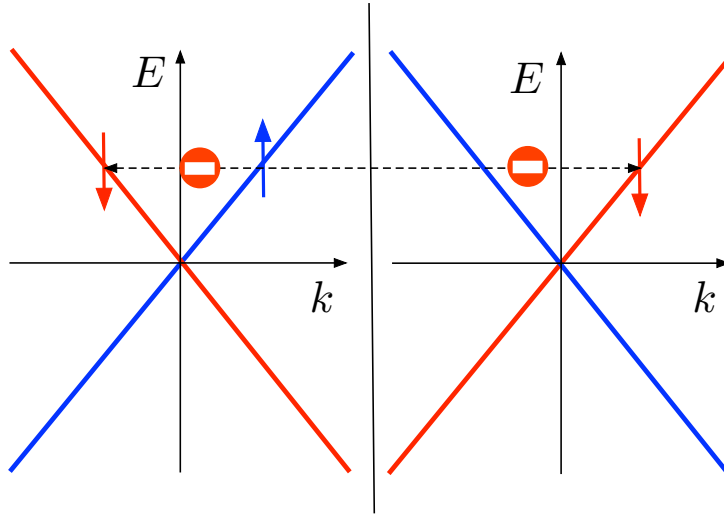
Fig. 3.1 Schematic representation of the Dirac paradox emerging at a heterojunction between two massless Dirac models with opposite helicity. Blue and red lines describe spin-↑ and spin-↓ states, respectively. On the left-hand side of the junction, right-moving electrons are characterized by spin-↑ and left-moving electrons by spin-↓, while the opposite occurs on the right-hand side. A spin-↑ electron impinging from the left onto the interface can seemingly neither be transmitted nor reflected, due to spin conservation.

In this Chapter we investigate the Dirac paradox in 1D and address these problems. First, we show that, if the helicity change across the interface is accounted for by an inhomogeneous velocity profile, the paradox has no solution, in the sense that the continuity equation forbids the existence of scattering states and only allows for eigenstates that involve electron injection from both sides of the junction, which carry a vanishing current. If, however, the interface directly introduces spin-rotation processes, the solution of the paradox is of course trivial and transmission is possible. We then investigate whether non-trivial solutions with proper scattering states and finite transmission exist without a spin-active interface. To this purpose, we propose an extended model involving both massless and massive Dirac modes. We show that, despite carrying no current for energies

within their gap, the massive modes play a crucial role in inhomogeneous problems like the Dirac paradox. In particular, as will be discussed in details, scattering states describing a transmission from a spin-↑ incoming massless mode to a spin-↓ outgoing massless mode do exist, due to the interface coupling between massless and massive modes. Moreover, the resulting transmission coefficient is finite and tuneable.

We then discuss the possible realization of such extended model. While massless Dirac helical states have been proven to exist at the edges of quantum spin Hall systems[21, 289, 290, 291, 292], this implementation is not optimal for the Dirac paradox in 1D. Indeed, since these states flow at the boundaries of a 2D quantum well, an heterojunction between two such wells with opposite edge helicity would exhibit a linear interface, whereto electrons could leak, like in the case of heterojunctions between two 3D Topological insulators mentioned above. However, as already mentioned in Ch.2, a truly 1D implementation of helical states has been realized with spin-orbit coupled nanowires (NWs) exposed to a magnetic field[293, 294, 295, 68, 196, 197, 198, 199, 73, 72, 200], in the regime of spin-orbit energy much larger than the Zeeman energy and for a chemical potential lying in the middle of the magnetic gap[296, 66, 65, 297, 238, 239].

So far, this remarkable discovery has been mostly exploited in the search for Majorana quasi-particles[66, 65, 68, 196, 197, 198, 199, 73, 72, 200, 57, 298, 299, 71] and we have explored connections with such quest in the previous Chapter. However, the possibility to experimentally control the Rashba spin-orbit coupling (RSOC), both in magnitude[222, 223, 224, 225, 226, 227, 228, 230, 229, 232, 233] and sign[267, 223, 268, 269, 231], fosters us to explore applications of the NWs also along different research directions. In particular, because in a NW the helicity of the massless modes is determined by the sign of the RSOC, a NW with two differently gated regions can represent a truly 1D implementation of the Dirac paradox configuration. Notably, in such an inhomogeneous setup, the massless helical modes are not sufficient to describe the low energy physics around the chemical potential, which turns out to be well captured by the massless+massive Dirac model we propose here, instead. The resulting conductance can be tuned electrically over a wide range of values.

This Chapter is organized as follows. In Sec.3.2 we analyze the Dirac paradox with two different models involving only massless modes. Then, in Sec.3.3 we introduce a model with both massless and massive Dirac modes and show how this can yield a finite transmission coefficient depending on three parameters. Furthermore, in Sec.3.4 we show that this model can be implemented in a suitably designed setup involving spin-orbit coupled NWs. Finally, in Sec.3.5 we discuss our results and draw our conclusions.

3.2 Massless Dirac heterojunctions

Let us thus consider a junction connecting two 1+1 dimensional massless Dirac models

$$\hat{\mathcal{H}}_{L/R} = v_{L/R} \int \hat{\Psi}^\dagger(x)\sigma_z p_x \,\hat{\Psi}(x)\, dx \qquad (3.1)$$

where $\hat{\mathcal{H}}_L$ and $\hat{\mathcal{H}}_R$ denote the Hamiltonians on the left and on the right side of the interface region, respectively, $\hat{\Psi} = (\hat{\Psi}_\uparrow, \hat{\Psi}_\downarrow)^T$ is the 2×1 electron spinor field operator, $p_x = -i\hbar\partial_x$ is the momentum operator, and σ_z is a Pauli matrix in spin space. Finally $v_{L/R}$ denotes the Fermi velocity. When v_R and v_L have opposite signs, the helicity changes across the interface and the Dirac paradox emerges. The answer to the paradox, if any, heavily depends on how the crossover from $\hat{\mathcal{H}}_L$ to $\hat{\mathcal{H}}_R$ occurs, as we shall discuss here below considering different models.

3.2.1 Model 1: velocity sign change

The most straightforward way to implement the crossover from $\hat{\mathcal{H}}_L$ to $\hat{\mathcal{H}}_R$ is to assume that the entire system is characterized by an inhomogeneous velocity $v(x)$, varying from v_L to v_R over a certain crossover length λ. Since the momentum operator p_x does not commute with an inhomogeneous velocity profile $v(x)$, a quite natural approach is to replace their product $p_x v$ by a half of their anticommutator, obtaining the following Hamiltonian

$$\hat{\mathcal{H}} = \int \hat{\Psi}^\dagger(x)\sigma_z \frac{\{v(x), p_x\}}{2} \,\hat{\Psi}(x)\, dx \quad . \qquad (3.2)$$

The current operator associated to Eq.(3.2) is

$$\hat{J}(x) = \mathrm{e}\, v(x)\hat{\Psi}^\dagger(x)\sigma_z\hat{\Psi}(x) \quad , \qquad (3.3)$$

with e denoting the electron charge, whereas the Heisenberg Equation dictated by Hamiltonian (3.2) reads

$$\partial_t \hat{\Psi} = -\sigma_z \left(v(x)\partial_x \hat{\Psi} + \frac{\partial_x v}{2}\hat{\Psi} \right) \quad . \qquad (3.4)$$

Looking for stationary solutions $\hat{\Psi}(x,t) = \hat{\Psi}_E(x)e^{-iEt/\hbar}$ and multiplying Eq.(3.4) by σ_z on the left, the equation reduces to

$$\partial_x \hat{\Psi} = v^{-1}(x) \left(-\frac{\partial_x v}{2}\sigma_0 + i\frac{E}{\hbar}\sigma_z \right) \hat{\Psi} \quad , \qquad (3.5)$$

whose formal solution is

$$\hat{\Psi}_E(x) = \exp\left[-\frac{1}{2}\int_{x_R}^x \frac{\partial_x v}{v(x')}dx'\right]\exp\left[iE\sigma_z\int_{x_R}^x \frac{dx'}{\hbar v(x')}\right]\hat{\Psi}_E(x_R) \quad , \tag{3.6}$$

where x_R is some arbitrary reference space point. One can now exploit $\partial_x \ln|v(x)| = \partial_x v/v(x)$, denote $k_E(x) = E/\hbar v(x)$ and write

$$\hat{\Psi}_E(x_R) = \frac{u}{\sqrt{2\pi\hbar|v(x_R)|}}\,\hat{a}_E \quad , \tag{3.7}$$

where u is a position-independent 2×1 spinor and $\hat{a}_E$ the related energy-E mode operator fulfilling $\{a_E, a_{E'}^\dagger\} = \delta(E - E')$. At each energy E there are thus two independent solutions, corresponding to two mutually orthogonal choices for the spinor u. Then, Eq.(3.6) takes the form

$$\hat{\Psi}_E(x) = \frac{1}{\sqrt{2\pi\hbar|v(x)|}}\,e^{i\sigma_z\int_{x_R}^x k_E(x')dx'}\,u\,\hat{a}_E \quad , \tag{3.8}$$

which straightforwardly implies that at any space point x, including possible discontinuity points of $v(x)$, the following boundary condition holds

$$\sqrt{|v(x^+)|}\hat{\Psi}_E(x^+) = \sqrt{|v(x^-)|}\hat{\Psi}_E(x^-) \tag{3.9}$$

where $x^\pm = x \pm \varepsilon$ with $\varepsilon \to 0$.

If $v(x)$ varies in magnitude from v_L to v_R while preserving a (say) positive sign, $v(x) = |v(x)|$, the Hamiltonian (3.2) can equivalently be rewritten as

$$\hat{\mathcal{H}} = \int \hat{\Psi}^\dagger(x)\sigma_z\sqrt{v(x)}\left[p_x\sqrt{v(x)}\right]\hat{\Psi}(x)\,dx \quad . \tag{3.10}$$

In this case, one finds that the transmission coefficient is always 1, regardless of the specific values of $v_L, v_R > 0$, as discussed in Ref.[300].

If, however, $v(x)$ vanishes at some point x_0, like in the Dirac paradox, the problem becomes more subtle. Indeed in such case the energy dependent phase factor involving $k_E(x)$ in the solution Eq.(3.8) is well defined only if $v(x)$ vanishes as $|v(x)| = O(|x - x_0|^\alpha)$ with $0 < \alpha < 1$. Moreover the solution diverges as $\sim 1/\sqrt{|v(x)|}$ for $x \to x_0$. Yet, in view of the condition (3.9), the current in Eq.(3.3) is finite. Denoting by $\hat{J}_E^\pm \doteq \hat{J}_E(x_0^\pm)$ the current operator for a stationary solution at energy E at the two sides of the point x_0 of vanishing velocity, one straightforwardly finds from Eq.(3.9) that $\hat{J}_E^+ = -\hat{J}_E^-$. For stationary solutions, however, the continuity equation requires the expectation value of

the current to be continuous and independent of the position. The only possibility is that no current flows through the system, $\langle \hat{J}_E(x) \rangle \equiv 0 \; \forall x$, implying that the spinor u appearing in Eq.(3.8) *must be* chosen to have vanishing spin along z, i.e. $u^\dagger \sigma_z u = 0$. Up to an overall dimensional coefficient, two independent choices are $u_+ = (1, e^{i\phi})^T/\sqrt{2}$ and $u_- = (e^{-i\phi}, -1)^T/\sqrt{2}$, where ϕ is an arbitrary phase.

As an illustrative example, consider for instance the spatially odd profile $v(x) = -v_F \,\text{sgn}(x) \tanh^\alpha(|x|/\lambda)$, which describes a velocity sign change from $v_L = +v_F$ to $v_R = -v_F$ across the interface located at $x_0 = 0$, occurring over a lengthscale λ and with an exponent $0 < \alpha < 1$. It is straightforward to prove that the solution (3.8) is spatially even. Explicitly, choosing e.g. $x_R = -4\lambda$ as a reference point and taking the phase $\phi = 0$ in the above spinors u, one finds $k_E(x) \simeq -E \,\text{sgn}(x)/\hbar v_F$ for $|x| \gg \lambda$. The two physically correct solutions of the Heisenberg Eq.(3.4) then read

$$\hat{\Psi}_\pm(x, t) = \int \frac{dE}{\sqrt{2\pi\hbar v_F}} \, \psi_{E\pm}(x) \, e^{-iEt/\hbar} \, \hat{a}_{E\pm} \quad , \tag{3.11}$$

where the wavefunctions $\psi_{E\pm}$ for $|x| \gg \lambda$ take the form

$$\psi_{E\pm}(x) = \frac{e^{-iE|x|/\hbar v_F}}{\sqrt{2}} \begin{pmatrix} 1 \\ 0 \end{pmatrix} \pm \frac{e^{+iE|x|/\hbar v_F}}{\sqrt{2}} \begin{pmatrix} 0 \\ 1 \end{pmatrix} \quad . \tag{3.12}$$

These solutions fulfill the continuity equation by carrying a vanishing current [see Eq.(3.3)]. Note that the spatially even wavefunctions in Eq.(3.12) involve incoming waves from *both* sides and cannot be scattering state solutions. Moreover, any attempt to construct scattering states by their linear combinations would fail and would also violate the continuity equation.

In summary, the answer to the Dirac paradox provided by model 1 is that, when v_L and v_R have opposite signs, it is impossible to construct scattering state solutions that respect the continuity equation. The transmission coefficient cannot be properly defined. Physically correct solutions must necessarily involve incoming waves from both sides and carry no current, regardless of the specific magnitudes of $|v_L|$ and $|v_R|$. We conclude this section by noticing that the model 1 only involves the σ_z-component of spin [see Eq.(3.2)], and the space-dependent $v(x)$ changes magnitude and sign of such component. In this respect, the model is purely scalar.

3.2.2   Model 2: spin-active interface

The second model to approach the Dirac paradox is described by the Hamiltonian

$$\hat{\mathcal{H}} = v_F \int \hat{\Psi}^\dagger(x) \left(e^{-i\theta(x)\sigma_x/2} p_x \sigma_z \, e^{+i\theta(x)\sigma_x/2} \right) \hat{\Psi}(x)\, dx \tag{3.13}$$

where the helicity changes sign through a counter-clockwise rotation of the σ_z spin around the x-axis by a space-dependent angle $\theta(x)$ varying from $\theta_L = 0$ to $\theta_R = \pi$, over a certain crossover length. Thus, differently from the purely scalar model (3.2), the model (3.13) exploits the full SU(2) spin structure and Hamiltonian terms at two different points do not commute in general. The current operator related to the Hamiltonian (3.13) is

$$\begin{aligned}
\hat{J}(x) &= \mathrm{e}v_F \hat{\Psi}^\dagger(x) \left(e^{-i\theta(x)\sigma_x/2} \sigma_z \, e^{+i\theta(x)\sigma_x/2} \right) \hat{\Psi}(x) = \\
&= \mathrm{e}v_F \hat{\Psi}^\dagger(x) \left[\sigma_z \cos\theta(x) - \sigma_y \sin\theta(x) \right] \hat{\Psi}(x) \ .
\end{aligned} \tag{3.14}$$

Integrating the Heisenberg equation for the field operator

$$\partial_x \left(e^{i\theta(x)\sigma_x/2} \hat{\Psi}(x) \right) = -\frac{\sigma_z}{v_F} e^{i\theta(x)\sigma_x/2} \partial_t \hat{\Psi}(x) \tag{3.15}$$

around any point x, including possible discontinuity points of $\theta(x)$, the following boundary condition is found

$$e^{i\theta(x^+)\sigma_x/2} \hat{\Psi}(x^+) = e^{i\theta(x^-)\sigma_x/2} \hat{\Psi}(x^-) \quad , \tag{3.16}$$

which in turn straightforwardly implies the continuity of the current operator (3.14). In particular, for a step-like model $\theta(x < 0) = 0$ and $\theta(x > 0) = \pi$ of an interface located at $x_0 = 0$, Eq.(3.16) reduces to

$$\begin{aligned}
\hat{\Psi}_\uparrow(0^+) &= i\hat{\Psi}_\downarrow(0^-) \\
\hat{\Psi}_\downarrow(0^+) &= i\hat{\Psi}_\uparrow(0^-)
\end{aligned} \tag{3.17}$$

and describes a spin-rotation process occurring at the interface. Differently from model 1, the Heisenberg equation (3.15) does admit scattering state solutions $\hat{\Psi}_{E,\pm}(x,t) = \exp[-iEt/\hbar]\psi_{E\pm}(x)\hat{a}_{E,\pm}/\sqrt{2\pi\hbar v_F}$, where $\hat{a}_{E,\pm}$ are the energy-E mode operators for scattering from the left(+) and from right(-), respectively, and $\psi_{E\pm}(x)$ are the related scattering

wavefunctions. For instance, the scattering state from left is given by

$$
\begin{aligned}
\psi_{E+}(x<0) &= \begin{pmatrix} 1 \\ 0 \end{pmatrix} e^{iEx/\hbar v_F} + r \begin{pmatrix} 0 \\ 1 \end{pmatrix} e^{-iEx/\hbar v_F} \\
\psi_{E+}(x>0) &= t \begin{pmatrix} 0 \\ 1 \end{pmatrix} e^{iEx/\hbar v_F}
\end{aligned}
\tag{3.18}
$$

and, when inserted in Eq.(3.17), straightforwardly implies $r = 0$ and $t = i$, leading to a perfect transmission $T = |t| = 1$.

In summary, model 2 trivially solves the Dirac paradox by simply introducing spin-rotation processes at the interface.

3.3 Dirac Heterojunctions with massless and massive modes

So far, we have considered heterojunctions that purely involve Dirac massless modes and we have obtained two opposite answers to the Dirac paradox, depending on how the helicity change across the interface is modelled. Model 1, based on an inhomogeneous scalar velocity profile, implies that physical solutions necessarily involve injections from both sides of the junction and predicts no current flowing through the system, whereas model 2 "circumvents" the paradox by introducing a spin-active interface. In this section we propose a model that, *without* introducing any direct spin-rotation processes at the interface, leads to a non-vanishing transmission.

Suppose that, along with the massless propagating Dirac fermions illustrated in Fig.3.1, the system is also characterized by massive Dirac fermions, as sketched by the green curves of Fig.3.2. Specifically, the model we consider is

$$
\begin{aligned}
\hat{\mathcal{H}} = {} & v_F \int \hat{\Psi}^\dagger(x) U^\dagger(x) \tau_z \sigma_z p_x \left(U(x)\, \hat{\Psi}(x) \right) dx + \\
& -\frac{\Delta}{2} \int \hat{\Psi}^\dagger(x)(\tau_0 - \tau_z)\sigma_x\, \hat{\Psi}(x)\, dx
\end{aligned}
\tag{3.19}
$$

where $\hat{\Psi} = (\hat{\xi}_\uparrow, \hat{\xi}_\downarrow, \hat{\eta}_\uparrow, \hat{\eta}_\downarrow)^T$, with $\hat{\xi}_\uparrow, \hat{\xi}_\downarrow$ and $\hat{\eta}_\uparrow, \hat{\eta}_\downarrow$ denoting the massless and massive fields, respectively. Here σ_0 and $\boldsymbol{\sigma} = (\sigma_x, \sigma_y, \sigma_z)$ denote the 2×2 identity matrix and Pauli matrices acting on the spin space, whereas τ_0 and $\boldsymbol{\tau} = (\tau_x, \tau_y, \tau_z)$ the corresponding

quantities acting on the massless-massive degree of freedom, which we shall label as pseudospin.
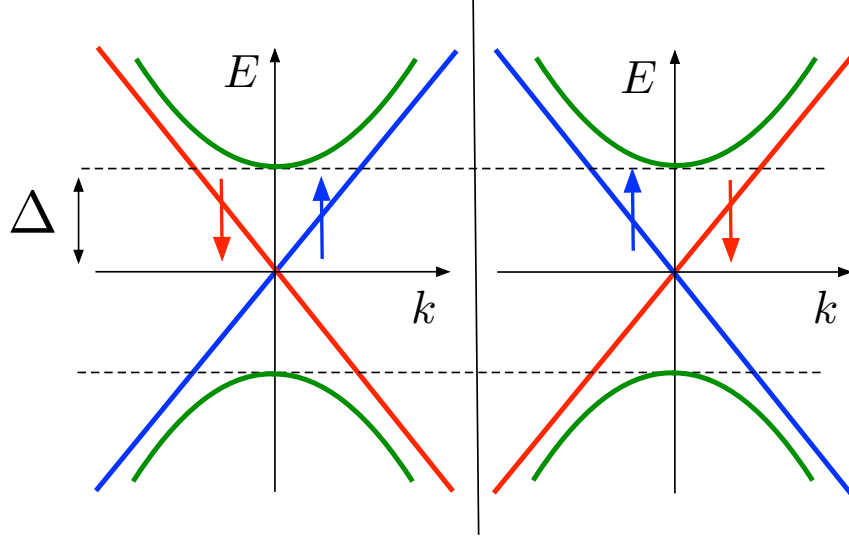

Fig. 3.2 The band spectrum of the massless+massive Dirac model with opposite helicity across an interface. While blue and red curves denote the spectrum of the massless modes, as in Fig.3.1, the green curves describe the spectrum of the massive modes, characterized by a gap 2Δ.

In the first term of Eq.(3.19) the 4×4 matrix $U(x)$ interpolates from U_L on the left of the interface to its value U_R on the right, where $U_{L/R}$ are required to fulfill the following properties

$$U_L^\dagger \tau_z \sigma_z U_L \ = \ +\tau_z \sigma_z \tag{3.20}$$

$$U_R^\dagger \tau_z \sigma_z U_R \ = \ -\tau_z \sigma_z \quad , \tag{3.21}$$

so that the $\hat{\xi}_\uparrow, \hat{\xi}_\downarrow$ modes have helicity $+1$ on the left of the interface and -1 on the right, just like in the Dirac paradox configuration of Fig.3.1, whereas the opposite occurs for the $\hat{\eta}_\uparrow, \hat{\eta}_\downarrow$ modes. The simplest example of a $U(x)$-matrix fulfilling the conditions (3.20)-(3.21) is $U(x) = \exp[i\theta(x)\tau_x \sigma_0/2]$, where $\theta(x)$ is a space-dependent angle describing a rotation in *pseudospin* space around τ_x from $\theta_L = 0$ to $\theta_R = \pi$ and causing the helicity flip, just like the spin-active model (3.13) introduces a rotation in spin space. As we shall see below, there exists in fact a much broader set of possible choices for $U(x)$ that turn out to describe interesting and realistic cases. The second term in Eq.(3.19) describes the mass term for $\hat{\eta}_\uparrow$ and $\hat{\eta}_\downarrow$, and we shall be interested in the energy window $|E| < \Delta$ inside their gap, where these massive modes carry no current.

In view of Eqs.(3.20)-(3.21), the current operator related to the Hamiltonian (3.19)

$$\hat{J}(x) = ev_F\hat{\Psi}^\dagger(x)U^\dagger(x)\tau_z\sigma_z\,U(x)\hat{\Psi}(x) \tag{3.22}$$

takes opposite expressions $\hat{J}_{L/R} = \pm ev_F\hat{\Psi}^\dagger(x)\tau_z\sigma_z\,\hat{\Psi}(x)$ at the two sides of the interface. However, the boundary condition

$$U(x^+)\hat{\Psi}(x^+) = U(x^-)\hat{\Psi}(x^-) \quad, \tag{3.23}$$

obtained from integration of the Heisenberg equation around any point x, guarantees that the current is in fact continuous for any $U(x)$. In particular, adopting again a step-like model $U(x) = U_L\,\mathrm{H}(-x) + U_R\,\mathrm{H}(x)$ for an interface located at $x_0 = 0$, with $\mathrm{H}(x)$ denoting the Heaviside function, the field $\hat{\Psi}$ fulfills the interface boundary condition

$$\hat{\Psi}(0^+) = \mathsf{M}\,\hat{\Psi}(0^-) \quad, \tag{3.24}$$

where

$$\mathsf{M} = U_R^{-1}U_L \tag{3.25}$$

is the transfer matrix, which must fulfill

$$\mathsf{M}^\dagger\tau_z\sigma_z\mathsf{M} = -\tau_z\sigma_z \qquad (\textit{Requirement \#1}) \tag{3.26}$$

as a straightforward consequence of Eqs.(3.20)-(3.21). Note that Eq.(3.24) implies that the field $\hat{\Psi}$ is discontinuous, as is customary for Dirac models in the presence of a $\delta(x)$-term, which in this case originates from $p_xU(x)$ term in the Hamiltonian (3.19).

Importantly, in order to avoid trivial solutions to the Dirac paradox like in model (3.13), we require that the model (3.19) does not directly introduce any spin-rotation process at the interface. This leads to impose another requirement on the transfer matrix Eq.(3.24), namely that M is diagonal in spin space, i.e.

$$\begin{array}{l}\mathsf{M}\ \text{must involve}\\ \text{only } \sigma_0 \text{ and } \sigma_z\end{array} \qquad (\textit{Requirement \#2}) \quad . \tag{3.27}$$

It can be shown (see Appendix B.1 for details) that the most general matrix fulfilling the requirements Eqs.(3.26)-(3.27) has the following form in the $\tau \otimes \sigma$ basis

$$
\mathsf{M} = \begin{pmatrix}
i\beta_\uparrow e^{i(\nu_\uparrow - \gamma_\uparrow)} & 0 & (1 - i\beta_\uparrow)e^{i(\nu_\uparrow + \chi_\uparrow)} & 0 \\
0 & i\beta_\downarrow e^{i(\nu_\downarrow - \gamma_\downarrow)} & 0 & (1 - i\beta_\downarrow)e^{i(\nu_\downarrow + \chi_\downarrow)} \\
(1 + i\beta_\uparrow)e^{i(\nu_\uparrow - \chi_\uparrow)} & 0 & -i\beta_\uparrow e^{i(\nu_\uparrow + \gamma_\uparrow)} & 0 \\
0 & (1 + i\beta_\downarrow)e^{i(\nu_\downarrow - \chi_\downarrow)} & 0 & -i\beta_\downarrow e^{i(\nu_\downarrow + \gamma_\downarrow)}
\end{pmatrix}
\tag{3.28}
$$

and depends on 8 parameters, namely 4 real parameters $\chi_\sigma, \gamma_\sigma, \beta_\sigma, \nu_\sigma$ for each spin sector $\sigma = \uparrow, \downarrow$. The vanishing entries in Eq.(3.28) encode the decoupling of the two spin sectors dictated by Eq.(3.27).

3.3.1 Scattering states

Let us now focus on $E = 0$, i.e. on the middle of the massive energy gap, and build up scattering state solutions on both sides of the junction, namely

$$
\hat{\Psi}(x < 0) = \tag{3.29}
$$

$$
= \hat{a}_{L\uparrow} \begin{pmatrix} 1 \\ 0 \\ 0 \\ 0 \end{pmatrix} e^{ik_0 x} + \hat{b}_{L\downarrow} \begin{pmatrix} 0 \\ 1 \\ 0 \\ 0 \end{pmatrix} e^{-ik_0 x} + \frac{\hat{c}_L}{\sqrt{2}} \begin{pmatrix} 0 \\ 0 \\ -i \\ 1 \end{pmatrix} e^{\kappa_0 x}
$$

and

$$
\hat{\Psi}(x > 0) = \tag{3.30}
$$

$$
= \hat{a}_{R\uparrow} \begin{pmatrix} 1 \\ 0 \\ 0 \\ 0 \end{pmatrix} e^{-ik_0 x} + \hat{b}_{R\downarrow} \begin{pmatrix} 0 \\ 1 \\ 0 \\ 0 \end{pmatrix} e^{ik_0 x} + \frac{\hat{c}_R}{\sqrt{2}} \begin{pmatrix} 0 \\ 0 \\ -i \\ 1 \end{pmatrix} e^{-\kappa_0 x}
$$

where $k_0 = 0$, $\kappa_0 = \Delta/\hbar v_F$. Here $\hat{a}_{L\uparrow}$ and $\hat{a}_{R\uparrow}$ are incoming operators describing a propagating mode impinging from the left(L) and from the right(R) of the interface, respectively, whereas $\hat{b}_{L\downarrow}$ and $\hat{b}_{R\downarrow}$ are outgoing operators for modes propagating to the left and to the right, respectively. Note that in the Dirac paradox configuration (see

Fig.3.2) incoming states and outgoing states have opposite spin, namely spin-↑ and spin-↓, respectively. Furthermore in Eqs.(3.29) and (3.30) $\hat{c}_L$ and $\hat{c}_R$ describe evanescent modes on the left- and on the right-hand side of the interface. Importantly, because they are massive, their spinors have two non vanishing components and their spin points along y [1]. Introducing Eqs.(3.29) and (3.30) into Eq.(3.24) and using Eq.(3.28), one can write

$$\begin{pmatrix} \hat{b}_{L\downarrow} \\ \hat{b}_{R\downarrow} \\ \hat{c}_L \\ \hat{c}_R \end{pmatrix} = \begin{pmatrix} \mathsf{S} \\ \tilde{\mathsf{S}} \end{pmatrix} \begin{pmatrix} \hat{a}_{L\uparrow} \\ \hat{a}_{R\uparrow} \end{pmatrix} \quad , \tag{3.31}$$

where S denotes the Scattering Matrix returning the outgoing propagating modes

$$\mathsf{S} = \frac{ie^{-i\Delta\chi}}{(1-i\beta_\uparrow)(1+i\beta_\downarrow)} \times \tag{3.32}$$

$$\begin{pmatrix} e^{i\Delta\nu} + e^{-i\Delta\gamma}\beta_\uparrow\beta_\downarrow & i(e^{i(\gamma_\downarrow-\nu_\uparrow)}\beta_\downarrow - e^{i(\gamma_\uparrow-\nu_\downarrow)}\beta_\uparrow) \\ i(e^{i(\nu_\uparrow-\gamma_\downarrow)}\beta_\downarrow - e^{i(\nu_\downarrow-\gamma_\uparrow)}\beta_\uparrow) & e^{-i\Delta\nu} + e^{i\Delta\gamma}\beta_\uparrow\beta_\downarrow \end{pmatrix}$$

with $\Delta\chi \doteq \chi_\uparrow - \chi_\downarrow$, $\Delta\nu \doteq \nu_\uparrow - \nu_\downarrow$ and $\Delta\gamma \doteq \gamma_\uparrow - \gamma_\downarrow$, whereas

$$\tilde{\mathsf{S}} = \frac{\sqrt{2}\, e^{-i\chi_\uparrow}}{1-i\beta_\uparrow} \begin{pmatrix} \beta_\uparrow e^{-i\gamma_\uparrow} & ie^{-i\nu_\uparrow} \\ ie^{+i\nu_\uparrow} & \beta_\uparrow e^{i\gamma_\uparrow} \end{pmatrix} \tag{3.33}$$

is the matrix yielding the evanescent modes.

In Eq.(3.31), setting $\hat{a}_{R\uparrow} \to 0$ yields a scattering state with injection from left, while a scattering state with injection from right is obtained for $\hat{a}_{L\uparrow} \to 0$. Thus, differently from model 1 in Eq.(3.2), the model in Eq.(3.19) does allow for scattering solutions. The transmission coefficient $T_0 = |t_0|^2$, obtained from the off-diagonal entries of the Scattering

---

[1]This observation concurs with the appearance of orthogonal spin density peaks at interfaces where no bound state is present, as shown in Ch.2. Indeed, as we will show in Sec.3.4 below, the present model captures the essential physics of the interface in a spin-orbit coupled nanowires with an inhomogeneous spin-orbit profile. We can thus conclude that the matching conditions for the extended helical modes of a nanowire with inhomogeneous spin-orbit coupling induce an orthogonal polarization at the interface, due to the evanescent modes localized at the interface.

Matrix (3.32), reads

$$T_0 = \frac{\beta_\uparrow^2 + \beta_\downarrow^2 - 2\beta_\uparrow\beta_\downarrow\cos\varphi}{(1 + \beta_\uparrow^2)(1 + \beta_\downarrow^2)} \quad , \tag{3.34}$$

and depends on the three parameters $\beta_\uparrow$, $\beta_\downarrow$ and $\varphi = \Delta\gamma + \Delta\nu$. To understand how the transmission between two propagating electronic states with oppositely oriented spins is possible, let us for instance set $\hat{a}_{R\uparrow} \to 0$ in Eq.(3.31), which corresponds to a scattering process where a spin-$\uparrow$ state incoming from the far left is transmitted into a spin-$\downarrow$ state outgoing to the far right. By inspecting the spin spatial profile of Eqs.(3.29)-(3.30), one observes that far away from the interface the total spin is mainly carried by the massless propagating states and is directed along the z-axis. However, near the interface, spin acquires also a component along y because of the presence of the massive states (third terms of Eqs.(3.29)-(3.30)). Indeed the conservation of $S_z^{tot} = \hbar\hat{\Psi}^\dagger\tau_0\sigma_z\hat{\Psi}/2$ is broken precisely by the mass in the Hamiltonian Eq.(3.19). Thus, when approaching the interface, the total spin *rotates* in the y-z plane, thereby allowing the transmission from a spin-$\uparrow$ to a spin-$\downarrow$ massless state. Note the essential difference with respect to model 2: There, the spin-rotation is induced *directly* on the massless modes by a spin-active interface [see Eq.(3.13)], whereas here the transfer matrix in Eqs.(3.24) and (3.28) is fully diagonal in spin [see Eq.(3.27)] and the spin rotation occurs *indirectly*, i.e. through the coupling between massless and massive modes localized at the interface.

To a more formal level, the process can be illustrated in terms of the Transfer Matrix as follows. Let us again consider for definiteness the scattering from left, i.e. $\hat{a}_{R\uparrow} \to 0$ in Eq.(3.31), and also set for simplicity all phases to zero ($\gamma_\sigma = \chi_\sigma = \nu_\sigma = 0$) in Eqs.(3.28), (3.32) and (3.33). We first focus on the case $\beta_\uparrow = 0$, where the scattering state resulting from Eqs.(3.31)-(3.32)-(3.33) is sketched on the left-hand side of Fig.3.3(a): The blue (red) wiggy line describes the incoming spin-$\uparrow$ state (outgoing spin-$\downarrow$ states), while an evanescent wave (green solid line) is present only for $x > 0$. Its role is elucidated on the right hand side of Fig.3.3(a), which is a graphical representation of Eq.(3.24) where the non-vanishing components of such a scattering state are connected across the interface by the transfer matrix entries (black lines). When the massless spin-$\uparrow$ state propagates towards the interface from the left, the transfer matrix Eq.(3.28) connects it through the entry $\mathsf{M}_{31} = 1$ to its massive evanescent partner with the same spin located across the interface, represented by a green dashed box, with the thick solid lines inside it denoting its two spin components. Because such a mode is massive, inside the gap it always exhibits *both* spin components [see third term in Eq.(3.30)]. Thus, its spin-$\downarrow$ component is also present and is connected through the transfer matrix entry $\mathsf{M}_{42} = 1 + i\beta_\downarrow$ to its spin-$\downarrow$

massless partner, which describes the reflected wave propagating to the left of the junction. Finally, the latter is also coupled, through the entry $\mathsf{M}_{22} = i\beta_\downarrow$, to the massless spin-$\downarrow$ state outgoing to the right of the junction. Thus, despite the interface connects only states with the same spin on the two sides, the presence of an evanescent massive mode exhibiting both spin components leads to an effective spin-flip transmission between massless modes.
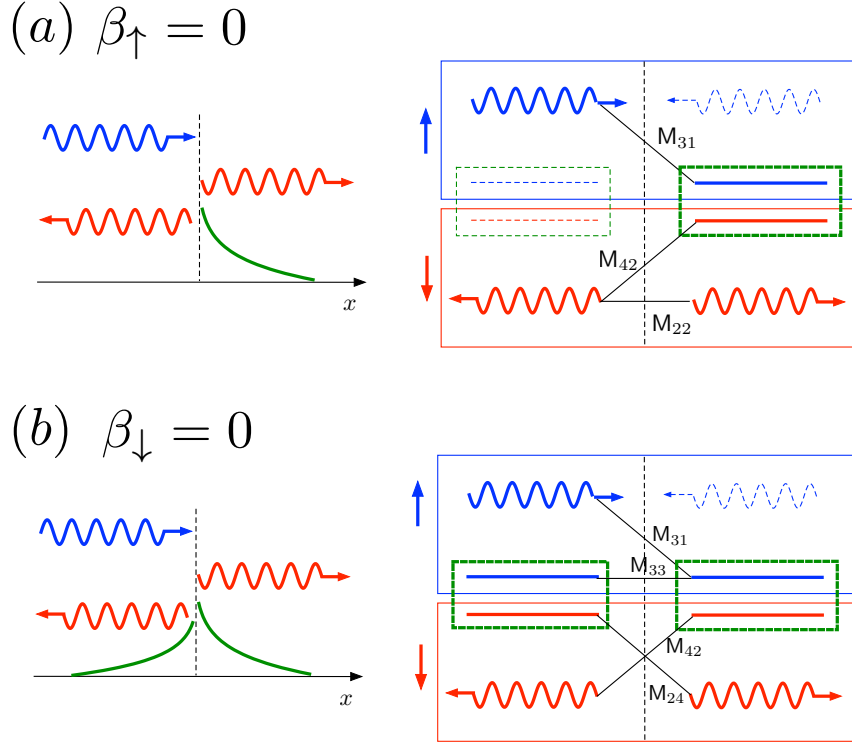

Fig. 3.3 For each panel, the left-hand side sketches the scattering state wavefunction in the case of injection from the left, resulting from Eqs.(3.31)-(3.32)-(3.33) for $\hat{a}_{R\uparrow} \to 0$. Blue and red wiggy lines describe spin-$\uparrow$ and spin-$\downarrow$ propagating massless states, respectively, whereas solid green lines describe the evanescent wave of the massive mode. The right-hand side of each panel is a graphical representation of Eq.(3.24), where black lines represent the transfer matrix entries connecting the non vanishing components of such scattering state. (a) The case with $\beta_\uparrow = 0$. The evanescent mode is present only on the right side of the interface. Here $\mathsf{M}_{31} = 1$, $M_{42} = 1 + i\beta_\downarrow$ and $\mathsf{M}_{22} = i\beta_\downarrow$. (b) The case with $\beta_\downarrow = 0$. In this case the evanescent modes are present on both sides of the junction. Here $\mathsf{M}_{31} = 1 + i\beta_\uparrow$, $M_{33} = -i\beta_\uparrow$ and $\mathsf{M}_{24} = \mathsf{M}_{42} = 1$. In all cases, despite the transfer matrix only connects states with the same spin, the presence of the evanescent modes of the massive field enables a spin-flip transmission between the propagating modes.

Let us now consider the case $\beta_\downarrow = 0$. In this case the scattering state resulting from the solution Eqs.(3.31)-(3.32)-(3.33) exhibits evanescent modes on both sides of the junction, as sketched in the left hand side of Fig.3.3(b). The scheme on the right hand side of Fig.3.3(b)

illustrates the related Eq.(3.24). While the entry M_{31} is modified to $\mathsf{M}_{31} = 1 + i\beta_\uparrow$, a connection $\mathsf{M}_{33} = -i\beta_\uparrow$ opens up across the junction between the two spin-$\uparrow$ components of the massive modes. In turn, their corresponding spin-$\downarrow$ components are connected through the entries $\mathsf{M}_{24} = \mathsf{M}_{42} = 1$ to the spin-$\downarrow$ massless modes across the junction, thereby inducing again spin-flipped reflection and transmission.

The general case, where both $\beta_\uparrow$ and $\beta_\downarrow$ are non vanishing, is a combination of the two elementary cases and yields the transmission coefficient (3.34). Note that in the limit where both $\beta_\uparrow \to 0$ and $\beta_\downarrow \to 0$, the transmission coefficient (3.34) vanishes. This can also be understood by realizing that in such limit the transfer matrix (3.28) reduces to $\mathsf{M} = \tau_x \sigma_0$, yielding the boundary conditions

$$
\begin{cases}
\hat{\xi}_\sigma(0^+) & = & \hat{\eta}_\sigma(0^-) \\
\hat{\eta}_\sigma(0^+) & = & \hat{\xi}_\sigma(0^-)
\end{cases}
\qquad \sigma = \uparrow, \downarrow \quad ,
\tag{3.35}
$$

so that e.g. a massless mode incoming from the left towards the interface is completely transformed into its massive evanescent mode partner across the interface (with the same spin), which carries no current.

In summary, although massive modes do not carry any current inside the gap, their presence is important in inhomogeneous problems because they may localize at the interfaces. In particular they are crucial in the Dirac paradox, for they provide an indirect coupling between the two spin channels that would be otherwise uncoupled by the interface transfer matrix. This leads to an effective spin-flip transmission of the massless propagating modes. Moreover, in contrast with the models 1 and 3 discussed in Sec.3.2, here the transmission coefficient is tunable from 0 to 1 through the 3 knobs $\beta_\uparrow, \beta_\downarrow$ and φ. This is one of the main results of this Chapter.

3.4   Spin-orbit coupled nanowires

In this section we shall show that the model presented in Sec.3.3 can be realized with spin-orbit coupled NWs, under suitable circumstances. First, we shall briefly recall how these systems, introduced in Sec.2.2, can host helical states described by Dirac massless fermions, as well as gapped Dirac states, when exposed to an external magnetic field. Then, focussing on energies inside the gap opened up by the magnetic field, we shall explicitly derive the effective low-energy model for these systems. Finally, we shall consider

an inhomogeneous spin-orbit coupling profile that, in suitable regimes, realizes the Dirac paradox configuration involving both massless and massive modes, just like in the model proposed above.

3.4.1 The NW Hamiltonian and its low energy limit

As described in Ch.2, we consider a ballistic single-channel semiconductor NW deposited on a substrate and we assume that a uniform magnetic field is applied parallel to the nanowire axis, denoted by x, while the substrate plane will be identified as x-z. We shall adopt the same model of Sec.2.2, whose main ingredients are summarized here below for convenience (see also Appendix B.2 for additional details). With respect to Sec.2.2, we only have to slightly adjust the notation for the electron field operator, in order to avoid confusion. We shall denote by $\hat{\Phi}(x) = (\hat{\Phi}_\uparrow(x)\,,\,\hat{\Phi}_\downarrow(x))^T$ the electron spinor field associated to the entire NW energy range, with $\uparrow, \downarrow$ corresponding to spin projections along z, whereas the symbol $\hat{\Psi}(x)$ will be used to denote the spinor field restricted to the low energy modes around the Fermi energy [see Eq.(3.42) below]. Hence the full NW Hamiltonian reads $\hat{\mathcal{H}}_{NW} = \int \hat{\Phi}^\dagger(x)\, H_{NW}(x)\, \hat{\Phi}(x)\, dx$, where [see Eq.(2.2)]

$$H_{NW}(x) = \frac{p_x^2}{2m^*}\sigma_0 - \frac{\alpha}{\hbar}p_x\sigma_z - h_x\sigma_x \qquad (3.36)$$

contains the kinetic term characterized by an effective mass m^*, the Rashba term with a RSOC α, and the Zeeman term describing the coupling $h_x = g\mu_B B_x/2$ with the external magnetic field $\mathbf{B} = (B_x, 0, 0)$, with μ_B denoting the Bohr magneton and g the NW Landé factor. The model is characterized by two energy scales, namely the spin-orbit energy $E_{SO} = m^*\alpha^2/2\hbar^2$ and the Zeeman energy $E_Z = |h_x|$. For definiteness, we shall henceforth assume $h_x > 0$ and identify $h_x = E_Z$. The spin-orbit wavevector [see Eq.(2.5)]

$$k_{SO} = \frac{\sqrt{2m^* E_{SO}}}{\hbar} = \frac{|\alpha|m^*}{\hbar^2} \quad, \qquad (3.37)$$

and the Zeeman wavevector

$$k_Z = \sqrt{2m^* E_Z}\,/\hbar \qquad (3.38)$$

are the wavevectors associated to such energies. Diagonalizing the model in momentum space, one obtains a spectrum characterized by two energy bands separated at $k = 0$ by a gap $2E_Z$ centered around the energy $E = 0$. Depending on the ratio of E_Z to E_{SO}, the qualitative behavior of these bands is different (see Sec.2.2.2).
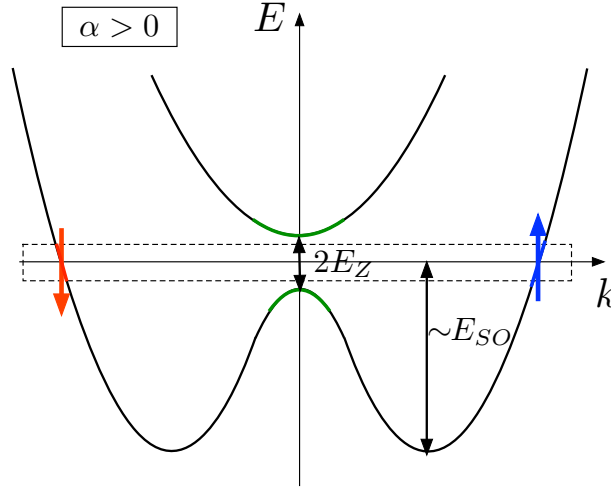
Fig. 3.4 In the deep Rashba-dominated regime ($2E_{SO} \gg E_Z$) and for energies $|E| \ll E_Z$, a NW exposed to an external magnetic field exhibits helical states near the Fermi points $\pm 2k_{SO}$. Their spin orientation is locked to the propagation direction and is determined by the sign of the RSOC α. The spin orientation is shown for the case $\alpha > 0$. The low energy massless and massive modes are highlighted with the same colors as in Fig.3.4.

In the following we shall focus on the deep Rashba-dominated regime ($E_Z \ll 2E_{SO}$), illustrated in Fig.3.4, and analyze the energy window inside the magnetic gap ($|E| \ll E_Z$), highlighted by the dashed box. As is well known, in this range the NW propagating eigenstates are helical[296, 66, 65, 297, 238, 239, 293, 294, 295]: Their dispersion relation is well described by a linear behavior near the Fermi points $k \simeq \pm 2k_{SO}$, while their spin orientation, mainly dictated by the Rashba term, is locked to the propagation direction. For $\alpha > 0$, right-moving electrons near the right Fermi point $k \simeq +2k_{SO}$ are characterized by spin-↑, while left-moving electrons near the left Fermi point $k \simeq -2k_{SO}$ have spin-↓ (see Fig.3.4). The opposite occurs if $\alpha < 0$. The dynamics of these low energy propagating modes, which we shall denote by $\hat{\xi}_\uparrow$, $\hat{\xi}_\downarrow$, is thus described by a massless Dirac Hamiltonian. Note that the presence of one single Dirac cone is not an artifact of the continuum model (3.36) and can be found also in a regularized lattice version of it (see Appendix B.3). Importantly, the helicity of the Dirac cone is determined by the *sign* of the RSOC α

$$s_\alpha = \text{sgn}(\alpha) \quad . \tag{3.39}$$

This suggests that a junction between two NW regions with opposite values of RSOC realizes the Dirac paradox configuration.

However, as highlighted by the green lines in Fig.3.4, the NW also exhibits low-energy gapped modes near $k = 0$, whose spin components shall be denoted as $\hat{\eta}_\uparrow$ and $\hat{\eta}_\downarrow$. Notably,

these modes turn out to behave as massive Dirac fermions with a mass term $\Delta = E_Z$. In problems involving homogeneous NWs these modes are dropped because they are not normalizable. However, as observed in Sec.3.3, in inhomogeneous problems such as the Dirac paradox configuration they describe evanescent waves that, despite carrying no current, ensure the wavefunction matching at the interface. For these reasons, the effective low energy theory capturing the physical properties of the Dirac paradox configuration realized with NWs is a Dirac model involving both massless and massive modes.

To derive such effective theory describing low energy excitations $|E| \ll E_Z \ll 2E_{SO}$, we assume that the ground state is the Fermi sea where all NW states below the midgap energy ($E < 0$) are occupied, and we perform an expansion near the points $k \simeq \pm 2k_{SO}$ and $k \simeq 0$. It is possible to show (details can be found in Appendix B.2), that the low energy excitations of the NW Hamiltonian are equivalent to low energy excitations of the massless+massive Dirac model

$$
\hat{\mathcal{H}}_{NW} = \sum_{q=-\infty}^{+\infty} (\hat{\xi}_{q\uparrow}^\dagger \; \hat{\xi}_{q\downarrow}^\dagger) \begin{pmatrix} \hbar s_\alpha v_{so} q & 0 \\ 0 & -\hbar s_\alpha v_{SO} q \end{pmatrix} \begin{pmatrix} \hat{\xi}_{q\uparrow} \\ \hat{\xi}_{q\downarrow} \end{pmatrix}
$$
$$
+ \sum_{q=-\infty}^{+\infty} (\hat{\eta}_{q\uparrow}^\dagger \; \hat{\eta}_{q\downarrow}^\dagger) \begin{pmatrix} -\hbar s_\alpha v_{so} q & -E_Z \\ -E_Z & \hbar s_\alpha v_{SO} q \end{pmatrix} \begin{pmatrix} \hat{\eta}_{q\uparrow} \\ \hat{\eta}_{q\downarrow} \end{pmatrix} \tag{3.40}
$$

where $v_{SO} = \hbar k_{SO}/m^*$. Introducing the low-energy fields ($\sigma = \uparrow, \downarrow$)

$$
\hat{\xi}_\sigma(x) = \frac{1}{\sqrt{\Omega}} \sum_q \hat{\xi}_{q,\sigma} e^{iqx} \quad , \quad \hat{\eta}_\sigma(x) = \frac{1}{\sqrt{\Omega}} \sum_q \hat{\eta}_{q,\sigma} e^{iqx} \tag{3.41}
$$

that physically describe excitations varying over lengthscales much longer than the spin-orbit length $l_{SO} = k_{SO}^{-1}$, the NW Hamiltonian can be expressed as

$$
\hat{\mathcal{H}}_{NW} = \int dx \hat{\Psi}^\dagger(x) \left(s_\alpha v_{SO} \tau_z \sigma_z p_x - \frac{E_Z}{2} (\tau_0 - \tau_z) \sigma_x \right) \hat{\Psi}(x) \tag{3.42}
$$

where $\hat{\Psi}(x) = (\hat{\xi}_\uparrow, \hat{\xi}_\downarrow, \hat{\eta}_\uparrow, \hat{\eta}_\downarrow)^T$ is a 4-component spinor field. One can now realize the connection between the NW Hamiltonian (3.42) and the model introduced in Sec.3.3 in Eq.(3.19). Indeed, identifying $v_{SO} \to v_F$ and $E_Z \to \Delta$, Eq.(3.42) describes one side of the junction model (3.19), where the sign s_α of the RSOC [see Eq.(3.39)] implements the condition Eq.(3.20) or (3.21) and determines which side of the junction is described.

Finally, the original field $\hat{\Phi}$ can be expressed in terms of the Dirac slowly varying modes $(\hat{\xi}, \hat{\eta})$ and the fast oscillating plane waves related to the midgap Dirac points, as follows

$$\begin{pmatrix} \hat{\Phi}_\uparrow(x) \\ \hat{\Phi}_\downarrow(x) \end{pmatrix} = \begin{pmatrix} e^{+2is_\alpha k_{SO}x} \, \hat{\xi}_\uparrow(x) + \hat{\eta}_\uparrow(x) \\ e^{-2is_\alpha k_{SO}x} \, \hat{\xi}_\downarrow(x) + \hat{\eta}_\downarrow(x) \end{pmatrix} \quad . \tag{3.43}$$

3.4.2   The case of inhomogeneous RSOC

Because the helicity of the NW low energy massless modes is determined by the sign of the RSOC, one can envisage a setup where two different NW portions are characterized by values of α with opposite signs, as illustrated in Fig.3.5. The overall system can thus be described by a *inhomogeneous* spin-orbit coupling $\alpha(x)$ and the Hamiltonian (3.36) is generalized to[236, 237, 301, 302, 303, 205, 234] (see Sec.2.2.1)

$$H(x) = \frac{p_x^2}{2m^*}\sigma_0 - \frac{\{\alpha(x), p_x\}}{2\hbar}\sigma_z \; - h_x\sigma_x \tag{3.44}$$

In particular, as an elementary building block, one can consider a step-like RSOC profile $\alpha(x) = \alpha_L \, \mathrm{H}(x_0 - x) + \alpha_R \, \mathrm{H}(x - x_0)$ describing an interface located at x_0 between two regions with RSOC equal to α_L and α_R. In such a configuration one can straightforwardly derive the following matching conditions (see Appendix A.1)

$$\begin{cases} \hat{\Phi}_\uparrow(x_0^-) = \hat{\Phi}_\uparrow(x_0^+) \\ \hat{\Phi}_\downarrow(x_0^-) = \hat{\Phi}_\downarrow(x_0^+) \\ \partial_x\hat{\Phi}_\uparrow(x_0^-) = \partial_x\hat{\Phi}_\uparrow(x_0^+) - i\frac{m^*}{\hbar^2}(\alpha_R - \alpha_L)\hat{\Phi}_\uparrow(x_0) \\ \partial_x\hat{\Phi}_\downarrow(x_0^-) = \partial_x\hat{\Phi}_\downarrow(x_0^+) + i\frac{m^*}{\hbar^2}(\alpha_R - \alpha_L)\hat{\Phi}_\downarrow(x_0) \, . \end{cases} \tag{3.45}$$

This provides all the ingredients for a concrete implementation of the Dirac paradox. In order to be more realistic, we shall consider a three-region configuration where the RSOC varies as

$$\alpha(x) = \begin{cases} +\alpha > 0 & \text{for} \quad x < -L/2 \quad \text{(region 1)} \\ 0 & \text{for} \quad |x| < L/2 \quad \text{(region 2)} \\ -\alpha < 0 & \text{for} \quad x > +L/2 \quad \text{(region 3)} \end{cases} \quad , \tag{3.46}$$

where the two outer regions 1 and 3 with opposite RSOC are both assumed in the deep Rashba-dominated regime ($2E_{SO} \gg E_Z$), and are separated by the central crossover region 2 with length L and with vanishing RSOC, i.e. in the Zeeman-dominated regime (see Fig.3.5).
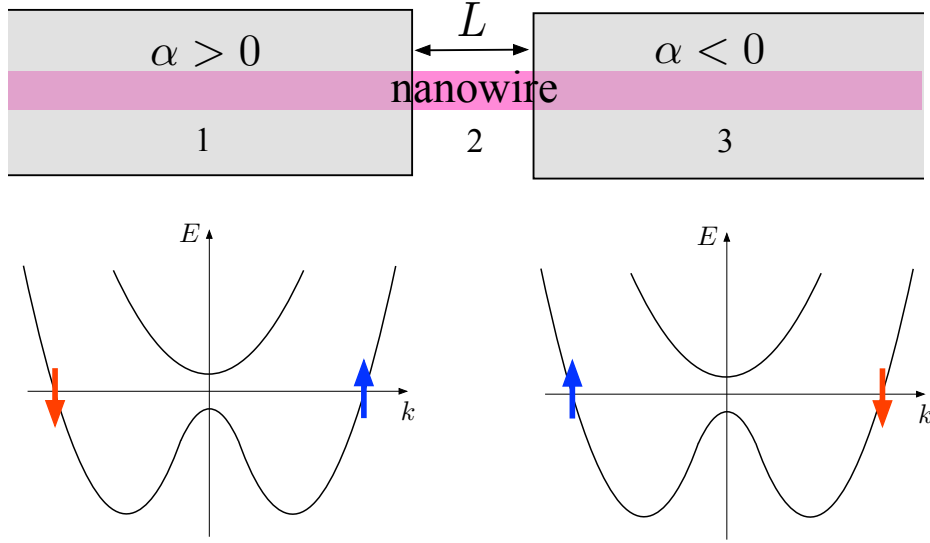
Fig. 3.5 By gating different portions of the NW with metallic electrodes an inhomogeneous RSOC like (3.46) can be realized. Inside the Zeeman gap, induced by an external magnetic field applied along the nanowire axis, the helical states in the two outer regions have opposite helicity and thus realize the Dirac paradox configuration.

Applying the general interface condition (3.45) to the two interfaces $x_1 = -L/2$ and $x_2 = +L/2$ of the piecewise constant profile (3.46), one can match the NW wavefunction in the three regions and obtain the solution for the NW scattering problem with standard techniques[304] (see Appendix B.4). Although the resulting transmission coefficient is numerically exact and available for arbitrary values of E, E_{SO} and E_Z, it is not quite amenable. However, in the energy window $|E| \ll E_Z \ll 2E_{SO}$ where the Dirac paradox emerges, an analytical expression can be gained from the effective low energy model. To this purpose, one can insert the expression (3.43) for the field $\hat{\Phi}$ in the outer Rashba-dominated regions into the interface condition (3.45) and obtain the low energy boundary conditions at the left interface $x_1 = -L/2$

$$\begin{cases} e^{-ik_{SO}L}\hat{\xi}_\uparrow(x_1^-) + \hat{\eta}_\uparrow(x_1^-) = \hat{\Phi}_\uparrow(x_1^+) \\ e^{+ik_{SO}L}\hat{\xi}_\downarrow(x_1^-) + \hat{\eta}_\downarrow(x_1^-) = \hat{\Phi}_\downarrow(x_1^+) \\ +ik_{SO}\left[e^{-ik_{SO}L}\hat{\xi}_\uparrow(x_1^-) - \hat{\eta}_\uparrow(x_1^-)\right] = \partial_x\hat{\Phi}_\uparrow(x_1^+) \\ -ik_{SO}\left[e^{+ik_{SO}L}\hat{\xi}_\downarrow(x_1^-) - \hat{\eta}_\downarrow(x_1^-)\right] = \partial_x\hat{\Phi}_\downarrow(x_1^+) \end{cases} \qquad (3.47)$$

and at the right interface $x_2 = +L/2$

$$
\begin{cases}
\hat{\Phi}_\uparrow(x_2^-) = e^{-ik_{SO}L}\hat{\xi}_\uparrow(x_2^+) + \hat{\eta}_\uparrow(x_2^+) \\
\hat{\Phi}_\downarrow(x_2^-) = e^{+ik_{SO}L}\hat{\xi}_\downarrow(x_2^+) + \hat{\eta}_\downarrow(x_2^+) \\
\partial_x\hat{\Phi}_\uparrow(x_2^-) = -ik_{SO}\left[e^{-ik_{SO}L}\hat{\xi}_\uparrow(x_2^+) - \hat{\eta}_\uparrow(x_2^+)\right] \\
\partial_x\hat{\Phi}_\downarrow(x_2^-) = +ik_{SO}\left[e^{+ik_{SO}L}\hat{\xi}_\downarrow(x_2^+) - \hat{\eta}_\downarrow(x_2^+)\right]
\end{cases}
\quad,
\tag{3.48}
$$

where, consistently with the low energy limit, we have neglected the derivatives $\partial_x\hat{\xi}$ and $\partial_x\hat{\eta}$ of the slowly varying fields with respect to the term proportional to k_{SO}, since they are characterized by wavevectors $|q| \ll k_{SO}$.

In the central region 2, where only the Zeeman coupling is present, the field $\hat{\Phi}$ can be expressed as a linear combination of propagating and evanescent waves that are eigenfunctions of σ_x, so that for $|x| < L/2$

$$
\begin{aligned}
\hat{\Phi}(x) &= \frac{\hat{h}_E}{\sqrt{2}}\begin{pmatrix} 1 \\ 1 \end{pmatrix}e^{ik_{2,E}x} + \frac{\hat{g}_E}{\sqrt{2}}\begin{pmatrix} 1 \\ 1 \end{pmatrix}e^{-ik_{2,E}x} \\
&+ \frac{\hat{d}_E}{\sqrt{2}}\begin{pmatrix} 1 \\ -1 \end{pmatrix}e^{\kappa_{2,E}x} + \frac{\hat{f}_E}{\sqrt{2}}\begin{pmatrix} 1 \\ -1 \end{pmatrix}e^{-\kappa_{2,E}x}
\end{aligned}
\tag{3.49}
$$

where $\hat{h}_E, \hat{g}_E, \hat{d}_E$ and $\hat{f}_E$ are mode operators, whereas $k_{2,E} = k_Z\sqrt{1 + E/E_Z}$, $\kappa_{2,E} = k_Z\sqrt{1 - E/E_Z}$ and k_Z is given in Eq.(3.38). Inserting Eq.(3.49) into Eqs.(3.47)-(3.48), one can obtain the link between the fields in the outer Rashba-dominated regions

$$
\begin{pmatrix}
\hat{\xi}_\uparrow(L/2) \\
\hat{\xi}_\downarrow(L/2) \\
\hat{\eta}_\uparrow(L/2) \\
\hat{\eta}_\downarrow(L/2)
\end{pmatrix} = \mathsf{M}_E
\begin{pmatrix}
\hat{\xi}_\uparrow(-L/2) \\
\hat{\xi}_\downarrow(-L/2) \\
\hat{\eta}_\uparrow(-L/2) \\
\hat{\eta}_\downarrow(-L/2)
\end{pmatrix}
\tag{3.50}
$$

where the transfer matrix M_E depends on the energy E and on the size L of the central region through two dimensionless parameters k_ZL and $k_{SO}L$. Details about the derivation of M_E can be found in the Appendix B.4. As an illustrative example, here we shall focus on the midgap value ($E = 0$), which in fact well represents the entire low energy range $|E| \ll E_Z$. Moreover, since in the deep Rashba-dominated regime $k_ZL \ll k_{SO}L$, one can keep $k_{SO}L$ finite and consider k_ZL as a small parameter, performing an expansion of $\mathsf{M}_{E=0}$

in its powers. Neglecting orders $O((k_Z L)^4)$ one obtains

$$\mathsf{M}_0 \simeq \begin{pmatrix} ik_{SO}L/2 & A & (1 - ik_{SO}L/2)e^{ik_{SO}L} & B \\ A^* & -ik_{SO}L/2 & B^* & (1 + ik_{SO}L/2)e^{-ik_{SO}L} \\ (1 + ik_{SO}L/2)e^{-ik_{SO}L} & -B & -ik_{SO}L/2 & A^* e^{2iLk_{SO}} \\ -B^* & (1 - ik_{SO}L/2)e^{ik_{SO}L} & Ae^{-2ik_{SO}L} & ik_{SO}L/2 \end{pmatrix} \tag{3.51}$$

where

$$A = i\frac{-6 + k_{SO}L(k_{SO}L + 6i)}{12k_{SO}L}e^{2iLk_{SO}}(k_Z L)^2 \tag{3.52}$$

$$B = -i\frac{(k_{SO}L)^2 + 6}{12k_{SO}L}e^{ik_{SO}L}(k_Z L)^2 \quad . \tag{3.53}$$

The 8 entries of the transfer matrix (3.51) containing A and B couple spin-$\uparrow$ to spin-$\downarrow$ components. Notably, such terms are of the order $O((k_Z L)^2)$ and in the regime $k_Z L \ll 1$ can be neglected with respect to the other terms, which are $O(1)$ with respect to the variable $k_Z L$. Then, the transfer matrix reduces to

$$\mathsf{M}_0 \simeq \begin{pmatrix} i\frac{k_{SO}L}{2} & 0 & (1 - i\frac{k_{SO}L}{2})e^{ik_{SO}L} & 0 \\ 0 & -i\frac{k_{SO}L}{2} & 0 & (1 + i\frac{k_{SO}L}{2})e^{-ik_{SO}L} \\ (1 + i\frac{k_{SO}L}{2})e^{-ik_{SO}L} & 0 & -i\frac{k_{SO}L}{2} & 0 \\ 0 & (1 - i\frac{k_{SO}L}{2})e^{ik_{SO}L} & 0 & i\frac{k_{SO}L}{2} \end{pmatrix} . \tag{3.54}$$

The expression (3.54) has precisely the form Eq.(3.28) of the transfer matrix of the massless+massive Dirac model described in Sec.3.3, when setting $\beta_\uparrow = -\beta_\downarrow = k_{SO}L/2$, $\chi_\uparrow = -\chi_\downarrow = k_{SO}L$ and $\gamma_\uparrow = \gamma_\downarrow = \nu_\uparrow = \nu_\downarrow = 0$. Thus, in the regime $k_Z L \ll 1$, where the central region is much shorter than the Zeeman wavelength $l_Z = k_Z^{-1}$ characterizing the wavefunction (3.49) at $E = 0$, the transfer matrix is diagonal in spin and becomes independent of the Zeeman energy E_Z. Yet, M_0 couples massless to massive modes and still depends on $k_{SO}L$. This parameter, which represents the ratio of the crossover region L to the spin-orbit length $l_{SO} = k_{SO}^{-1}$, may be finite because of the deep Rashba-dominated regime $k_Z \ll k_{SO}$.

In turn, the transmission coefficient related to Eq.(3.54) can be obtained from the general formula Eq.(3.34),

$$T_0 = \frac{(k_{SO}L)^2}{(1 + (k_{SO}L/2)^2)^2} \quad , \tag{3.55}$$
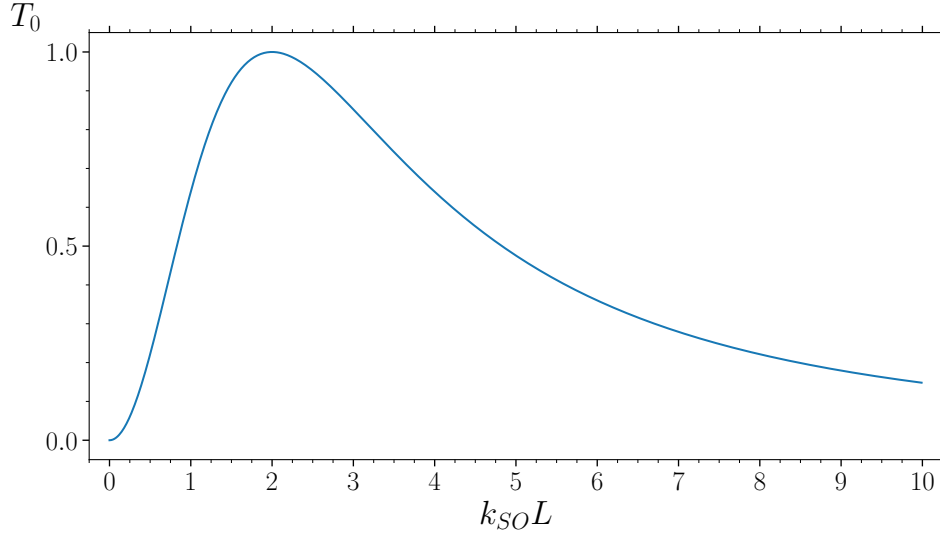
Fig. 3.6 The transmission coefficient (3.55), plotted as a function of $k_{SO}L$, covers the entire range $T_0 \in [0,1]$.

and varies over the entire range $T_0 \in [0,1]$ as a function of $k_{SO}L$, as shown in Fig.3.6. In particular, while for small values $k_{SO}L \ll 1$ the transmission is low, $T_0 \sim (k_{SO}L)^2$, for finite values of $k_{SO}L$ we observe from Fig.3.6 that T_0 increases, and a perfect transmission $T_0 = 1$ is obtained for $k_{SO}L = 2$. Then, for large values of $k_{SO}L$ the transmission decreases again as $T_0 \sim 16/(k_{SO}L)^2$. The ratio of the spin-orbit length $l_{SO} = k_{SO}^{-1}$ to the distance L is thus the parameter controlling the value of T_0.

3.4.3   Transmission coefficient in the case of InSb

For definiteness, we consider here an implementation with a ballistic InSb NW with effective electron mass $m^* = 0.015 m_e$. Two different portions of the NW are supposed to be gated by differently biased metals inducing opposite RSOC values, as previously sketched in Fig.3.5, and are separated by a crossover region $L = 100$nm where the RSOC is negligible. In Fig.3.7(a) the solid curves display the midgap transmission coefficient $T_0 = T_{E=0}$ as a function of the spin-orbit energy E_{SO}, for different values of the Zeeman energy E_Z, obtained from the numerically exact solution of the model (3.44) with the profile (3.46) (see Appendix B.4 for technical details). Moreover the dashed curve describes the analytical result (3.55) obtained from the low-energy limit in the Rashba-dominated regime of the outer regions, i.e. the massless+massive Dirac model. As one can see, for

$E_{SO} \to 0$, the exact transmission coefficient tends to 1, regardless of the value of E_Z, since all three regions become equal in such a limit.
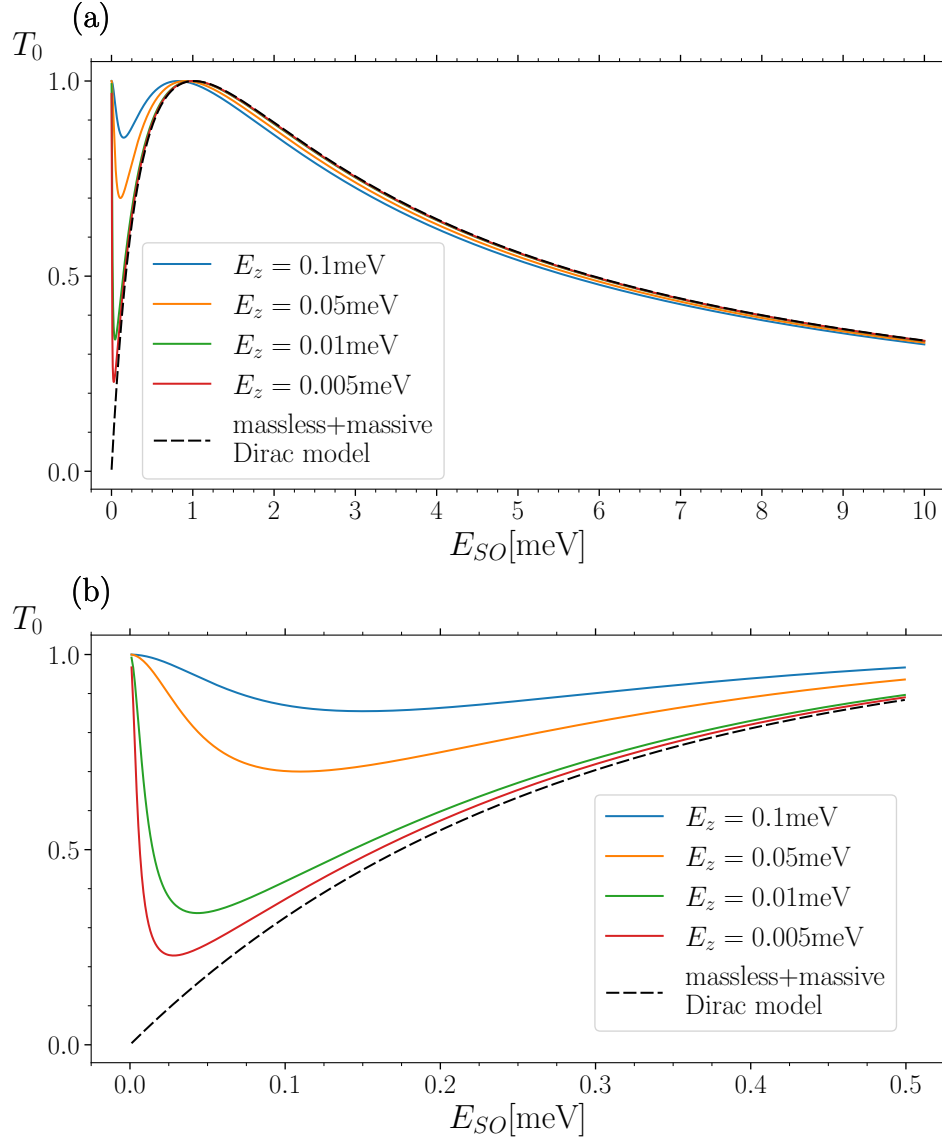
Fig. 3.7 The Dirac paradox configuration realized with a InSb NW setup where two outer gated regions are characterized by opposite RSOC and the central region has a width $L = 100\,\mathrm{nm}$ (see Fig.3.5). The midgap transmission coefficient ($E = 0$), obtained from the numerically exact solution of the model (3.44) with the profile (3.46), is plotted as a function of the spin orbit energy, for different values of the external magnetic field E_Z (solid curves). When the Rashba-dominated regime ($2E_{SO} \gg E_Z$) is reached, the various solid curves all tend to the dashed curve describing the result Eq.(3.55), obtained in the low energy limit from the effective massless+massive Dirac model. Panel (b) is a zoom of panel (a) in the regime of spin-orbit values that are realistic with present gating techniques.

However, for each Zeeman energy value, when E_{SO} is sufficiently large to enter the deep Rashba-dominated regime ($2E_{SO} \gg E_Z$), all solid curves are well reproduced by the low-energy limit Eq.(3.55) (dashed curve), which is independent of E_Z. This is thus the regime where the NW gap states are helical and the setup realizes the Dirac paradox. Despite the absence of a spin-active interface, the transmission coefficient is non-vanishing because the propagating massless modes are coupled to the evanescent massive modes. In Fig.3.7(b) the same quantities as in panel (a) are shown, with a zoom in the range of spin-orbit energy values up to $E_{SO} = 0.5$meV, which is the realistic range presently reachable. Correspondingly, the range of Zeeman energy values E_Z ensuring a deep Rashba dominated regime for the external gated regions is $E_Z < 0.1$meV. This implies that the linear conductance G_0, straightforwardly connected to the transmission coefficient through the relation $G_0 = (e^2/h)T_{E=0}$, is tunable from low to high values with varying the spin-orbit energy, which can electrically be done through the gate voltage.

3.5   Conclusions

In this Chapter we have analyzed the Dirac paradox, illustrated in Fig.3.1, where an electron impinging towards an interface can seemingly neither be transmitted nor reflected. In particular, we have focussed on the interesting case of one spatial dimension. Indeed, differently from higher dimensional realizations such as heterojunctions between two 3D Topological Insulators where electrons can leak along the interface surface, in 1D electrons do not have a "way out" to escape the paradox. We have first analyzed models that purely involve massless modes. The first model Eq.(3.2), where the helicity change across the interface is accounted for by a spatially inhomogeneous velocity, leads to conclude that the paradox has no actual solution, namely it is not possible to build up a scattering state solution. Indeed physical solutions must necessarily involve electron injection from both sides and are characterized by a vanishing current. In contrast, the second model Eq.(3.13), where the helicity change occurs through a rotation of the spin across the interface, provides a trivial solution to the paradox, for it directly introduces a spin-active interface, which leads to a perfect transmission.

Then, we have proposed a model, Eq.(3.19), involving both massless and massive Dirac modes [see Fig.3.2] and we have shown that it leads to a non-trivial solution of the Dirac paradox, even for a spin-inactive interface. This is possible because of the massive modes that, despite carrying no current for energies inside their gap, always exhibit both spin components. Thus, a massless-massive coupling at the interface indirectly enable an

incoming massless electron impinging with spin-↑ to get transmitted as a massless electron with spin-↓ (see Fig.3.3). Properly defined scattering state solutions thus exist, and the transmission coefficient depends in general on three parameters [see Eq.(3.34)].

Moreover, in Sec.3.4, we have shown that such model can be implemented in spin-orbit coupled NWs exposed to an external magnetic field, whose midgap states are characterized by massless modes near the Fermi points $k \sim \pm 2k_{SO}$ and massive modes near $k \sim 0$ [see Fig.3.4]. The massless modes are helical in the deep Rashba-dominated regime $(2E_{SO} \gg E_Z)$ and their helicity is determined by the sign of the RSOC. Because the latter can be tuned by state-of-the-art gating techniques, a NW with two regions characterized by opposite RSOC values, as shown in Fig.3.5, is a suitable candidate to realize the Dirac paradox configuration in one spatial dimension. We have shown that the low energy limit of such inhomogeneous NW model is precisely a particular case of the proposed model (3.19). The resulting transmission coefficient Eq.(3.55) varies over the full range $T_0 \in [0, 1]$ (see Fig.3.6) as a function of the parameter $k_{SO}L$, where L is the distance between the two differently gated regions and k_{SO} is the spin-orbit wavevector that is directly controlled by the RSOC [see Eq.(3.37)]. Focussing on the specific case of an inhomogeneous InSb NW, we have determined from model (3.44) the exact transmission coefficient, which in general depends both on the spin-orbit and the Zeeman energies [solid curves of Fig.3.7]. Whenever the Rashba-dominated regime is reached, the setup realizes the Dirac paradox configuration. Then, the transmission coefficient is well captured by the low energy limit result (3.55) (dashed curve of Fig.3.7) obtained from the proposed massless+massive Dirac model and only depends on the spin-orbit energy E_{SO}. Because E_{SO} can be controlled via the gate bias coupled to the NW, the transmission coefficient and the linear conductance are electrically tuneable.

Chapter 4

Negative Absorption Induced by a Local Quench

The content of this Chapter is based on the published paper [305]

4.1 Introduction

The concept of quantum quench [87, 79, 80, 81] has found an extraordinary impact in both technological applications and fundamental physics. Not only does it represent a basic operational tool for quantum state manipulations, it also enables one to tailor material properties [306] and quantum phases [307]. In the present Chapter we exploit the quench protocol as a tool to address the questions: "*Does an isolated many-body quantum system thermalize after an initial perturbation? Can it reach a non-thermal (eventually meta-stable) steady state? if so, what are the properties of the steady state?*" These questions have intrigued scientists ever since the foundations of quantum mechanics[106] and have found renewed interests in recent years, in part due to the technological advances in realizing experimental platforms with a high level of isolation and coherence, such as trapped ultra-cold atoms [94], as well as ultra-fast pump and probe set-ups, which can investigate the out of equilibrium behaviour of the system before thermalization eventually is reached [96]. The answers to these non trivial problems mainly depend on two aspects. First, the type of quench: While early studies considered quenches of spatially homogeneous parameters [308, 309, 310, 311, 312, 313, 314, 315, 316, 317], recent works have focused on *inhomogeneous* quenches such as extensive disorder potentials [318, 319], e.g., in view of many-body localization [320, 321], and spatially localized perturbations [322, 323, 324, 325,

326, 327, 328, 329, 330, 331, 332], which can for instance generate persistent oscillations in physical observables thus preventing the reaching of a steady state [319, 318, 330]. The second important ingredient in the problem is the type of system. In particular, in the case of integrable post-quench Hamiltonian [119], the dynamics is restricted by a complete set $\{\hat{I}_\alpha\}$ of local constants of motions commuting with the post-quench Hamiltonian [118]. This implies that, if an out of equilibrium steady state is reached, it can be described by a Generalized Gibbs Ensemble (GGE) density matrix [333, 308, 334, 123, 120, 335, 336, 337, 338]

$$\hat{\rho}_{GGE} = \frac{\exp(-\sum_\alpha \lambda_\alpha \hat{I}_\alpha)}{\mathrm{Tr}\left[\exp(-\sum_\alpha \lambda_\alpha \hat{I}_\alpha)\right]}\,, \tag{4.1}$$

where the Lagrange multipliers $\{\lambda_\alpha\}$ are determined by the pre-quench state and uniquely characterize the GGE.

On the theoretical side, there is a growing consensus that the GGE hypothesis works both for homogeneous [333, 308, 334, 123, 120, 335, 336, 337, 338] and inhomogeneous [319, 318, 339, 340, 341] quenches. However, only a few experimental GGE signatures have been observed so far, mostly limited to trapped one-dimensional Bose gases [128]. As far as Fermi systems are concerned, the proposals for GGE detection are based on homogeneous quenches of the interaction strength [342, 343] and have not found experimental evidence yet. Different schemes are thus needed.

A particularly illuminating case where sound results concerning GGE are known is when the post-quench Hamiltonian $\hat{\mathcal{H}}$ is a quadratic form in the creation and annihilation operators, i.e., a one-body operator [319, 318, 344, 345, 346]. In such a case, the latter can always be brought into a diagonal form $\hat{\mathcal{H}} = \sum_\alpha \varepsilon_\alpha \hat{\gamma}_\alpha^\dagger \hat{\gamma}_\alpha$ through a change of basis to suitable creation/annihilation operators $\hat{\gamma}_\alpha^\dagger$, $\hat{\gamma}_\alpha$ of single particle states α and the complete set of constants of motion $\{\hat{I}_\alpha\}$ are identified as the number operators $\hat{n}_\alpha \equiv \hat{\gamma}_\alpha^\dagger \hat{\gamma}_\alpha$[1].

The analysis of these systems provides useful insights on fundamental questions. In particular, the way quantum dynamics is described by a GGE heavily depends on the type of inhomogeneities that are possibly quenched in the system. On the one hand, quenching an extensively dense disorder prevents the system from reaching a strict stationarity, and only long time *time-averages* of one-body observables equal the GGE statistical average over Equation (4.1) [319, 318]. On the other hand, recent results have shown that, if the localized states of $\hat{\mathcal{H}}$ are sufficiently spatially separated, i.e., if disorder is rare and weak

---

[1]If the $\hat{n}_\alpha$ themselves are not local, as is customary in the case of homogeneous quenches, it is always possible to construct local conserved quantities out of them, following the lines of Ref.[345] (see e.g. Eqs.(18)-(19) therein).

enough, the expectation values of local observables tend *in time* to the ones prescribed by the GGE density matrix [345].

Importantly, in the case of post-quench one-body Hamiltonians, one can also *quantify* the deviation of GGE from thermal equilibrium. This can be done through the single-particle reduced density matrix stemming from $\hat{\rho}_{GGE}$, which is explicitly given by $\hat{\rho}_D = \sum_\alpha |\alpha\rangle\langle\alpha| f_\alpha$ and is thus called the "diagonal ensemble" in the α-basis. Here $f_\alpha \equiv \langle\hat{n}_\alpha\rangle_\circ = \mathrm{Tr}[\hat{n}_\alpha\hat{\rho}_\circ]$ represent the occupancies of the post-quench constants of motion over the pre-quench state $\hat{\rho}_\circ$. They are in one-to-one correspondence with the $\{\lambda_\alpha\}$, which are fixed through the relation $\langle\hat{n}_\alpha\rangle_{GGE} = \langle\hat{n}_\alpha\rangle_\circ$. In particular, for fermionic systems, this implies $f_\alpha = (1 + \exp[\lambda_\alpha])^{-1}$. Thus, while the equilibrium state at temperature T and chemical potential μ corresponds to the Fermi distribution $f_\alpha^{eq} = f^{eq}(\varepsilon_\alpha) = \{1 + \exp[(\varepsilon_\alpha - \mu)/k_B T]\}^{-1}$, or equivalently to $\lambda_\alpha^{eq} = (\varepsilon_\alpha - \mu)/k_B T$, the out of equilibrium state is characterized by the actual set $\{f_\alpha\}$, or equivalently by the set $\{\lambda_\alpha\}$, and is thus quantified in terms of "how many" occupancies f_α deviate from f_α^{eq} and by "how much".

In this Chapter we focus on quadratic Fermi systems and address the following question: what is the most elementary deviation from equilibrium that can produce observable effects? We shall show that quenching a *spatially localized potential* can lead, under suitable circumstances, to an out of equilibrium state that (i) reaches stationarity and (ii) is described by a GGE distribution where only one parameter λ_α deviates from equilibrium, corresponding to an only partially occupied bound state lying *below* a continuum of fully occupied extended states. Furthermore, we show that such condition yields a negative absorption spectrum, also known in optoelectronics as the optical gain, thereby paving the way to observe signatures of GGE through optical measurements.

The Chapter is organized as follows. After presenting the model in Section 4.2, we first focus on the case of a sudden quench of a rectangular quantum well to provide the proof of concept of the effect. In particular, in Section 4.3, we determine the post-quench out of equilibrium distribution, while in Section 4.4 we evaluate the related absorption spectrum, displaying the quench-induced negative absorption peak. Then, in Section 4.5, we generalize these results by including realistic effects, namely a finite switching time and a smooth quantum well potential profile. Finally, in Section 4.6, we draw our conclusions.

4.2 Model and Post-Quench Occupancies for a Sudden Quench

In order to illustrate the effect, we consider as a pre-quench system a homogeneous one-dimensional gas of free spinless electrons, described by the Hamiltonian $\hat{\mathcal{H}}^{\mathrm{pre}} = -\hbar^2 \int dx \, \hat{\Psi}^\dagger(x) \, \partial_x^2 \hat{\Psi}(x)/2m$, with $\hat{\Psi}$ denoting the electron field operator. The system is initially at equilibrium with a reservoir, at a temperature T and a chemical potential μ. This entails that the Fourier mode operators $\hat{c}(k)$ diagonalizing the Hamiltonian, $\hat{\mathcal{H}}^{\mathrm{pre}} = \int dk \, \varepsilon(k)\hat{c}^\dagger(k)\hat{c}(k)$, are characterized by

$$\langle \hat{c}^\dagger(k)\hat{c}(k')\rangle_\circ = \delta(k-k')f^{eq}(\varepsilon(k)) \quad , \tag{4.2}$$

where $\varepsilon(k) = \hbar^2 k^2/2m$ is the pre-quench spectrum. Then, the system is disconnected from the reservoir and, at the time $t = 0$, a localized attractive potential $V(x) < 0$ is switched on near the origin $x = 0$, so that the post-quench Hamiltonian is $\hat{\mathcal{H}}^{\mathrm{post}} = \hat{\mathcal{H}}^{\mathrm{pre}} + \int dx \hat{\Psi}^\dagger(x)V(x)\hat{\Psi}(x)$. For the moment, we shall focus on the case of a sudden quench, while the effects of a finite switching time will be considered in Section 4.5. Notably, while $\hat{\mathcal{H}}^{\mathrm{pre}}$ has a purely continuous spectrum, $\hat{\mathcal{H}}^{\mathrm{post}}$ also displays a discrete set of bound states, spatially localized around the origin, and with energies $\varepsilon_n < 0$ ($n = 0, 1, 2 \ldots$) lying below the continuum branch $\varepsilon > 0$.

The post-quench dynamics of this isolated system is intriguing in view of two opposite expectations. On the one hand, because the quenched potential is local, the energy change experienced by the entire system is vanishingly small in the thermodynamic limit, suggesting that even the post-quench distribution should remain a thermal one, just like the pre-quench state. In particular, if the initial state is the pre-quench ground state, one might expect the system to fall into the post-quench ground state, with all the bound states fully occupied. On the other hand, the Anderson orthogonality catastrophe [347, 348] ensures that, precisely in the thermodynamic limit, the many-body ground states of the pre- and post-quench Hamiltonians are orthogonal, suggesting a different post-quench distribution. In order to characterize the out of equilibrium dynamics, we first bring the post-quench Hamiltonian, quadratic in the fermionic fields $\hat{\Psi}$ and $\hat{\Psi}^\dagger$, to its diagonal form $\hat{\mathcal{H}}^{\mathrm{post}} = \fint_\alpha \varepsilon_\alpha \hat{\gamma}_\alpha^\dagger \hat{\gamma}_\alpha$ through a unitary transformation. Here the symbol $\fint$ is a compact notation indicating a summation over the discrete spectrum branch and an integral over the continuous spectrum branch. This implies, as observed above, that the out of equilibrium dynamics of the system is governed by a GGE, which is characterized by the set of post-quench occupancies f_α of the constants of motion.
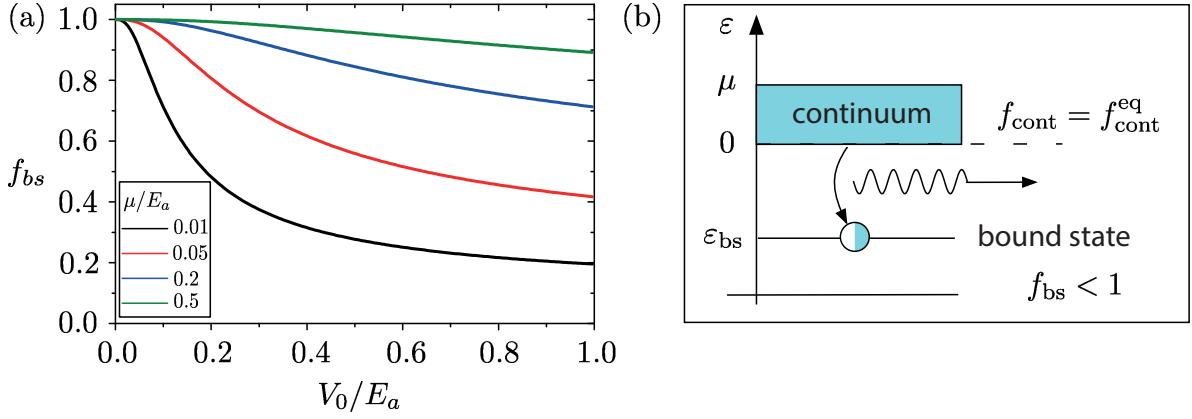
Fig. 4.1 (**a**) The occupancy of the bound state $\varepsilon_{\text{bs}} < 0$ induced by the quench as a function of the quantum well (QW) parameters V_0/E_a, at pre-quench temperature equal to zero, and for four different values of the pre-quench chemical potential μ. (**b**) Sketch of the occupancy of the post-quench states: While the states of continuum ($\varepsilon > 0$) are fully occupied up to μ, just like in the pre-quench state, the quench induced bound state gets only partially occupied, realizing the population-inversion regime (optical gain) leading to a stimulated emission of radiation (see Section 4.4).

However, because the post-quench spectrum contains both a discrete and a continuum branch, care must be taken in identifying the occupancies f_α, which in this case are determined from the diagonal ensemble density matrix through the relation $(\hat{\rho}_D)_{\alpha'\alpha} \equiv \langle \hat{\gamma}_\alpha^\dagger \hat{\gamma}_{\alpha'} \rangle_{GGE} = d_{\alpha\alpha'} f_\alpha$, where $d_{\alpha\alpha'} \equiv \delta_{\alpha\alpha'}$ for $\alpha, \alpha' \in$ discrete spectrum, while $d_{\alpha\alpha'} \equiv \delta(\alpha - \alpha')$ for $\alpha, \alpha' \in$ continuum spectrum and $d_{\alpha\alpha'} = 0$ otherwise [2]. In turn, the $\hat{\rho}_D$ entries can be computed by exploiting the transformation $\hat{\gamma}_\alpha = \int dk \, U(\alpha, k) \, \hat{c}(k)$ linking the post- to the pre-quench operators, where $U(\alpha, k) = \int dx \, \psi_\alpha^*(x) \varphi_k(x)$ is the overlap integral between the post-quench eigenfunctions ψ_α and the pre-quench eigenfunctions φ_k. By recalling the expectation values (4.2) of the pre-quench operators, it is straightforward to show that

$$(\hat{\rho}_D)_{\alpha\alpha} = \int dk \, |U(\alpha, k)|^2 \, f^{eq}(\varepsilon(k)) \quad , \tag{4.3}$$

whence the post-quench occupancies f_α are obtained through the above prescription.

---

[2] The operators fulfill $\{\hat{\gamma}_\alpha, \hat{\gamma}_{\alpha'}^\dagger\} = d_{\alpha,\alpha'}$ at equal-time.

4.3 The Case of a Quantum Well

For definiteness, we shall evaluate the post-quench occupancies for the case of a rectangular quantum well (QW) potential $V(x) = -V_0\,\theta(a/2 - |x|)$, characterized by a potential depth V_0 and a width a around the origin. Here, θ denotes the Heaviside function. In this case, space parity is conserved across the quench, the post-quench eigenfunctions ψ_α are well known, just like the pre-quench free-particle eigenfunctions φ_k, and the occupancies Equation (4.3) can be evaluated for all the post-quench states.

As far as the continuous spectrum is concerned, it is worth recalling that the presence of the QW does modify the continuum states with respect to the free-particle waves, especially at small energies ($0 < \varepsilon < V_0$). Nevertheless, a lengthy but straightforward calculation (see Appendix C for details), shows that in the thermodynamic limit, the post-quench occupancy of the continuum is $f_\alpha = f^{eq}(\varepsilon_\alpha)$, i.e., it coincides with the equilibrium Fermi function of the pre-quench state, with the same temperature and chemical potential, regardless of the values a and V_0 of the QW parameters. This is the hallmark of the locality of the quench. In particular, at zero temperature all continuum states are fully occupied up to the chemical potential μ.

The situation is different for the bound states. As is well known, the number of bound states in a rectangular QW depends on the ratio between the well potential depth V_0 and the kinetic energy $E_a = \pi^2\hbar^2/2ma^2$ associated to the confinement in the well width a. The smallest deviation from equilibrium is when one single discrete level, lying below the continuous spectrum of occupied states, is not fully occupied. Moreover, the existence of only one bound state ensures that the system reaches a stationary state after the quench [345]. Focusing then on the regime $V_0 < E_a$, where the QW hosts only one bound state, one can exploit the well known expression for the bound state of a rectangular QW and evaluate its occupancy $f_{\text{bs}} = (\hat{\rho}_D)_{\text{bs,bs}}$ numerically from Equation (4.3). The result is shown in Figure 4.1(a), where f_{bs} is plotted as a function of the ratio V_0/E_a, at zero temperature, for four values of chemical potential μ. While for an extremely shallow and thin well ($V_0/E_a \ll 1$) one has $f_{\text{bs}} \simeq 1$, i.e., the value one would obtain if the post-quench system were at equilibrium, for $V_0/E_a \lesssim 1$ the occupancy decreases. Notably, such a reduction is, the more pronounced the lower μ is, which can be understood from the following arguments. Since the pre-quench eigenfunctions φ_k are essentially plane waves, the $U(\text{bs}, k)$ coefficient is the Fourier transform of the bound state wavefunction ψ_{bs} and becomes negligible for $k \gg 1/\ell$, where $\ell \gtrsim a$ is the length scale over which ψ_{bs} is localized. The chemical potential μ of the pre-quench state appearing in the Fermi

function, cuts the integral in Equation (4.3) at the Fermi wavevector $k_F = \sqrt{2m\mu}/\hbar$. Thus, while for $k_F \gg 1/\ell$ the occupancy is $f_{\rm bs} = \int dk\, |U({\rm bs}, k)|^2 f^{eq}(\varepsilon(k)) \simeq \int dk\, |U({\rm bs}, k)|^2 = 1$ (unitarity of the U transformation), for small chemical potential, such that $k_F \ll 1/\ell$, the integral is cut before yielding the occupancy 1.

The resulting occupancy of the post-quench spectrum is sketched in Figure 4.1(b) at zero temperature: While the continuum states $\varepsilon > 0$ are characterized by the very same Fermi function as the equilibrium pre-quench state and are thus fully occupied up to the chemical potential μ for any QW parameter, the bound state $\varepsilon_{\rm bs} < 0$ is only partially occupied, despite being energetically more favorable than the continuum. This peculiar out of equilibrium effect thus realizes the most elementary GGE deviation from equilibrium: only the bound state $\lambda_{\rm bs} = \ln[(1 - f_{\rm bs})/f_{\rm bs}]$ deviates from the equilibrium value. In particular, this is quite different from the case of a homogeneous quench, where typically an extensive number of post-quench occupancies deviate from equilibrium [336].

Note that, because of particle conservation, the partial occupation of the quench-induced bound state corresponds to an infinitesimally small depletion (by at most one electron) of the continuum spectrum. In the thermodynamic limit, no directly seizable effect thus occurs in the continuum states. In contrast, the emergence of an only partially occupied bound state, energetically separated from the fully occupied continuum above, has a remarkable consequence: It realizes the condition of population-inversion, well known in optoelectronics. While at equilibrium a radiation impinging onto an electron system yields the absorption of an energy quantum causing a transition from energetically lower and more populated levels to upper and less populated levels, the out of equilibrium population obtained here leads to a release of energy, causing a stimulated emission or, a "negative" absorption. This opens up the possibility to observe this GGE signature through optical measurement, as we shall describe in the next section.

4.4 Absorption Spectrum

For an electron system coupled to an electromagnetic radiation of frequency ω, the non-linear absorption spectrum $A(\omega)$ is given, within the conventional perturbation-theory based on a Fermi's golden rule treatment of the light-matter interaction [349], by

$$A(\omega) = \frac{2\pi e^2}{c\,\epsilon_0\, n_\Re \mathcal{V} m_e^2 \omega} \sum_{\alpha} \sum_{\alpha'} |\langle \alpha'|p|\alpha \rangle|^2 \, \delta\left(\varepsilon_{\alpha'} - \varepsilon_\alpha - \hbar\omega\right) (f_\alpha - f_{\alpha'}), \qquad (4.4)$$

where $p = -i\hbar\partial_x$ is the momentum operator, $n_\Re$ denotes the real part of the refraction index, c the speed of light, ϵ_0 the vacuum dielectric constant, m_e the bare electron mass and $\mathcal{V}$ the volume. Equation (4.4) describes all transitions from initial states α to final states α' compatible with the transition energy $\hbar\omega$, and its non-linear nature is determined by the factor $f_\alpha - f_{\alpha'}$. While at equilibrium, the final state α' is necessarily less populated than α ($f_\alpha > f_{\alpha'}$), causing an actual absorption, $A(\omega) > 0$, in the population-inversion regime induced by the quench, one has $f_{\alpha'} > f_\alpha$ for $\alpha = $ bs and α' in the occupied continuous spectrum, opening up the possibility of a *negative* absorption coefficient, $A(\omega) < 0$, i.e., to the emission of an electromagnetic radiation stimulated by the quench. This is known in optoelectronics as the optical gain effect [350]. However, unlike the more conventional inter-band transitions, the effect described here can be considered as "intraband", as it originates from a quench on one single pre-quench band. We also point out that the semiclassical treatment underlying Equation (4.4) is valid for time scales longer than the decoherence time scale, where the density matrix exhibits damped out off-diagonal entries and reduces to the time independent GGE diagonal ensemble. Indeed, as we shall argue in Section 4.5, there exists a finite relaxation time τ_{rel}, after which all local observables are effectively described by such diagonal ensemble. Thus, within the specified time window, the semiclassical treatment captures the gist of the population-inversion effect.

4.4.1 Implementation

As can be deduced from Figure 4.1(a), the optimal regime to obtain a population-inversion is in principle $\mu \ll V_0 \lesssim E_a$. However, a too small chemical potential reduces screening effects and makes electron–electron interaction effects relevant. A still quite acceptable regime is $\mu \lesssim V_0 \lesssim E_a$, which can be achieved, e.g., with an InSb nanowire (NW), characterized by a small effective mass $m = 0.015 m_e$, and a realistic QW realized by a finger gate deposited on a NW portion with size $a = 150$ nm and biased by a gate voltage $V_0 < 0$. This yields $E_a \simeq 1.12$ meV and, by taking a realistic value $\mu = 0.2$ meV, one still has an energy window for the QW depth V_0. Furthermore, due to the large g-factor of InSb NWs ($g \sim 50$) [294] the application of a magnetic field of a few Teslas is sufficient to widely spin-split the NW bands, thereby avoiding double occupancy of the bound state, ruling out the related electron–electron interaction effects inside the quantum well.

Since Equation (4.4) cannot be computed analytically, we have performed a numerically exact evaluation on a finite system, whose total length $L = 16\,\mu m$ is two orders of magnitude bigger than the QW width a, at a realistic pre-quench temperature of $T = 250$ mK. Furthermore, the unavoidable presence of inelastic processes broadening the
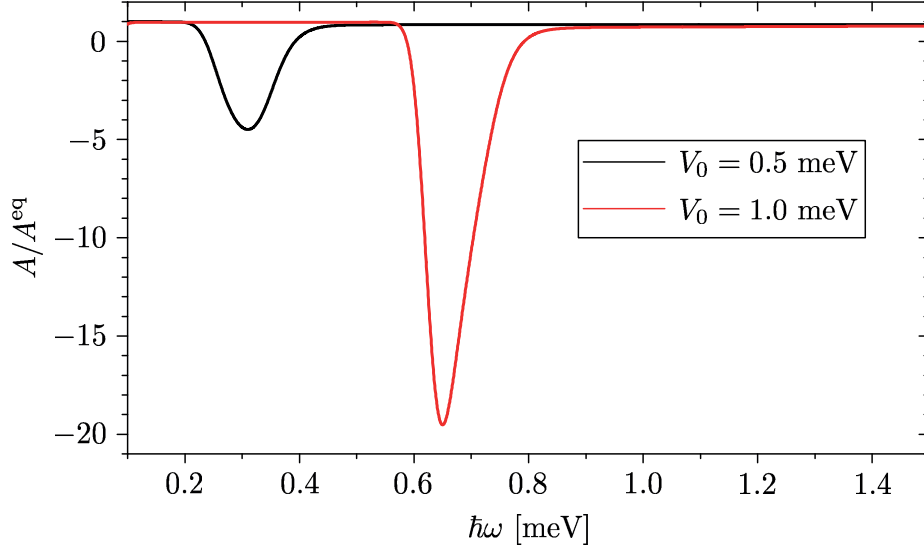
Fig. 4.2 The ratio R between the out of equilibrium absorption spectrum $A(\omega)$ induced by the quench and the equilibrium absorption spectrum $A^{eq}(\omega)$ of the post-quench system, for an InSb nanowire (NW) with a QW width $a = 150\,\mathrm{nm}$ ($E_a \simeq 1.12\,\mathrm{meV}$) and depth $V_0 = 0.5\,\mathrm{meV}$ (black curve) and $V_0 = 1.0\,\mathrm{meV}$ (red curve). The pre-quench temperature and chemical potential are $T = 250\mathrm{mK}$ and $\mu = 0.2\,\mathrm{meV}$, respectively. While at low frequencies the quench does not induce any deviation from equilibrium ($R \to 1$), a significant negative peak appears at $\hbar\omega^* = |\varepsilon_{\mathrm{bs}}|$ corresponding to the energy separation between the continuum and the bound state.

otherwise sharp energy levels has been taken into account by replacing the ideal Dirac δ-function appearing in Equation (4.4) with a broadened function of Gaussian shape $\delta(\varepsilon) \to \delta_b(\varepsilon) = \exp[-\varepsilon^2/2\varepsilon_{\mathrm{b}}^2]/\sqrt{2\pi}\varepsilon_{\mathrm{b}}$, where the value of broadening energy has been taken as $\varepsilon_{\mathrm{b}} = 20\,\mu\mathrm{eV}$. This roughly corresponds to $k_B T$, i.e., the typical broadening related to electron–acoustic phonon energy exchange. The result is illustrated in Figure 4.2, where we have plotted the ratio $R(\hbar\omega) \equiv A(\omega)/A^{eq}(\omega)$ between the out of equilibrium absorption spectrum induced by the quench and the equilibrium case corresponding to the situation where the post-quench system is at equilibrium, for two different values of QW depth V_0.

At low frequencies one has $R(\hbar\omega) \simeq 1$, indicating that the spectrum of the quench-induced absorption coefficient is just like the equilibrium one. In this regime the intraband absorption processes are caused by continuum→continuum transitions from energetically lower and almost fully occupied states $0 < \varepsilon < \mu$ to energetically higher and almost empty states $\varepsilon' > \mu$. It is worth pointing out that such transitions occur because of the presence of the QW, which makes the dipole matrix entries $\langle \alpha'|\hat{p}|\alpha\rangle$ non vanishing for $\alpha \neq \alpha'$.

The most interesting effect, however, arises as the frequency approaches the value $\omega^* \equiv |\varepsilon_{\mathrm{bs}}|/\hbar$, where transitions can occur from the fully occupied lowest continuum

states to the only partially occupied bound state lying underneath. This is how the population-inversion regime causes a negative absorption, i.e., the stimulated emission of an electromagnetic radiation. The hallmark of this optical gain effect is the negative peak located around $\hbar\omega^*$. Note that, just like the value of such resonance frequency, also the depth R^* of the negative peak is controlled by the value of the potential depth V_0, and its magnitude can be significantly higher than 1, so that the negative absorption is much stronger than the equilibrium positive absorption contribution. For higher frequencies, the ratio $R(\omega)$ becomes positive again. This corresponds to an actual absorption, arising from transitions to the energetically higher and almost empty continuum states from both the bound state and the energetically lower and occupied continuum states.

4.5   Finite Switching Time and Smooth Potential

So far, we have considered the ideal situation of a sudden quench in a quantum well with a sharp rectangular profile. In realistic implementations, however, the quench is applied over a finite switching time τ_{sw} and the potential profile of the well is smooth. In this section we thus generalize the results of the previous Sections by taking these aspects into account. This enables us to demonstrate that the predicted effect relies neither on the instantaneous switching of the potential nor on the details of the potential profile, but rather on its property of being local, attractive and hosting a single bound state. Moreover, by simulating the complete time dependent dynamics of the quench, we are able to provide an explicit example of convergence to stationarity of a post-quench local observable, and to show that its stationary profile is accurately described by the GGE density matrix.

To this purpose, we now consider a time-dependent Hamiltonian $\hat{\mathcal{H}}(t) = \hat{\mathcal{H}}^{\mathrm{pre}} + g_{sw}(t)\int dx\hat{\Psi}^\dagger(x)V(x)\hat{\Psi}(x)$, where $g_{sw}(t) = \{1 + \mathrm{Erf}[\sqrt{8}\,(t-\tau_{sw})/\tau_{sw}]\}/2$ is a switching function ranging from 0 to 1, up to 2%, within a time scale τ_{sw}. Moreover the potential profile $V(x) = -V_0/2\{\mathrm{Erf}[\sqrt{8}\,(x+a/2)/\lambda] - \mathrm{Erf}[\sqrt{8}\,(x-a/2)/\lambda]\}$ corresponds to a QW with depth V_0, width a and edges smoothened over a length λ. The overall quench dynamics is thus governed by an inhomogeneous and time-dependent Hamiltonian that cannot be treated analytically. By solving numerically the Liouville–von Neumann equation $i\hbar\partial_t\hat{\rho} = [\mathcal{H}, \hat{\rho}]$ for the single-particle density matrix $\hat{\rho}$, the related diagonal density matrix $\hat{\rho}_D$, associated to the time independent post-quench eigenbasis, is extracted [3]. Differently

---

[3]The post-quench Hamiltonian is defined as the time-independent Hamiltonian once the localized potential is completely switched on, i.e. $\hat{\mathcal{H}}^{\mathrm{post}} = \hat{\mathcal{H}}(t\to\infty) = \hat{\mathcal{H}}^{\mathrm{pre}} + \int dx\hat{\Psi}^\dagger(x)V(x)\hat{\Psi}(x)$. In practice, due to the form of the ramp function $g_{sw}(t)$, one has $\hat{\mathcal{H}}(t\gtrsim 2\tau_{sw}) \simeq \hat{\mathcal{H}}^{\mathrm{post}}$.
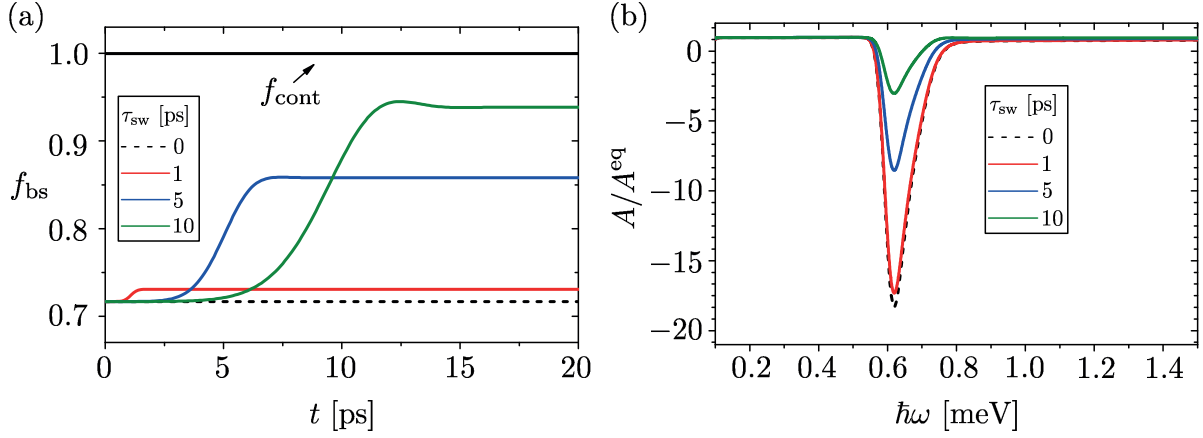
Fig. 4.3 (**a**) The time evolution of the occupancy of the bound state, and of the low lying delocalized states, is plotted for different values of the switching time τ_{sw}. While the occupancy of the delocalized states remains constant and indistinguishable from 1 independently on the switching time, the occupancy of the bound state grows from the initial value during the switching time, and reaches a stationary value lower than 1 after the switching is complete. The dashed curve describes the sudden quench case, for comparison. (**b**) The ratio R between the out of equilibrium absorption spectrum $A(\omega)$ induced by the quench and the equilibrium absorption spectrum $A^{eq}(\omega)$ of the post-quench system is shown, at different values of the switching time τ_{sw}. Although the finite switching time reduces the depth of the negative peak with respect to the sudden quench case (dotted curve), its magnitude remains significantly higher than the values of the equilibrium spectrum $A^{eq}(\omega)$. In all panels, the computations are performed for an InSb NW with a pre-quench thermal state corresponding to $\mu = 0.2$ meV and $T = 250$ mK and a post-quench Hamiltonian with a QW potential of width $a = 150$ nm, depth $V_0 = 1.0$ meV and a profile smoothening length $\lambda = 20$ nm. The energy broadening $\varepsilon_b = 20\,\mu$eV has been taken.

from the case of a sudden quench, $\hat{\rho}_D$ exhibits a non trivial evolution during the ramp and it becomes constant only after the switching is complete. From $\hat{\rho}_D(t)$ one can then directly observe the time evolution of the occupancies of the post-quench energy levels.

Taking again as a reference physical system an InSb nanowire of $L = 16\,\mu m$ and starting from a thermal pre-quench state with $\mu = 0.2$ meV and $T = 250$ mK, the occupancies of the post-quench bound state and of the post-quench low lying delocalized states (i.e., states with energies $0 < \varepsilon \ll \mu$) are plotted in Figure 4.3(a) for different values of the switching time τ_{sw}. The QW parameters are $a = 150$ nm (width), $V_0 = 1.0$ meV (depth) and $\lambda = 20$ nm (smoothening length). Several features are noteworthy. The occupancy of the low lying delocalized states is always indistinguishable from 1, independently of the switching time τ_{sw}, as one can see from the thick black horizontal line of Figure 4.3(a). In fact, one can verify that the overall distribution of the post-quench delocalized states does not appreciably differ from a thermal one, consistently with the analytical result found

for the sudden quench of the rectangular QW in the thermodynamic limit. In contrast, the dynamical behavior of the bound state occupancy does depend on the finite switching time, as shown by the colored solid curves. In particular, while at $t = 0$ it always coincides with the occupancy found in a sudden quench (dashed line), it grows during the ramp and then saturates to a higher value once the switching is complete. Note that the longer the switching time τ_{sw}, the higher is the final occupancy of the bound state, consistently with the picture that an infinitely slow dynamical evolution favors the system relaxation to a lower energy state with the lowest available level being fully occupied. However, for finite but realistic switching time values (see colored curves in Figure 4.3(a)), the occupancy of the bound state is still lower than 1 by an appreciable fraction, confirming the above described picture of a partially occupied bound state lying underneath a continuum of fully occupied delocalized states.

The robustness of the resulting population inversion effect is supported by the analysis of the absorption spectrum. Specifically, the 'post-quench' absorption spectrum, i.e., the value of Equation (4.4) evaluated at time $t \gg \tau_{sw}$ and normalized to the equilibrium absorption spectrum, is shown in Figure 4.3(b) for various switching time values. By increasing τ_{sw}, the shape of the negative peak is roughly unaltered, whereas its depth R^* is reduced. The value $R^* \simeq -18$ obtained for an ideally instantaneous quench (dashed curve in Figure 4.3(b)) reduces to $R^* \simeq -17$ (red curve), $R^* \simeq -8$ (blue curve) and $R^* \simeq -3$ (green curve) for τ_{sw} values of 1, 5 and 10 ps, respectively. Yet, the value $|R^*| > 1$ indicates that the out of equilibrium contribution of the negative peak is still larger than the positive equilibrium one. This clearly visible negative peak is thus a stable signature of the predicted out of equilibrium GGE distribution.

Having addressed the robustness of this GGE distribution, we conclude this section by explicitly showing that the unitary dynamics following the quench effectively generates a stationary state whose local properties are well captured by the GGE density matrix. In doing so, we thus provide not only an explicit numerical confirmation of the analytical results found for sudden quenches [344, 345], but also their generalization to the more realistic cases with finite switching times. In particular, we have focused on the spatial profile of the charge density. Note that its time evolution is characterized by three time scales: the switching τ_{sw}, the recurrence τ_{rec} and the relaxation time τ_{rel}. The first one depends on the chosen quench protocol and determines the time after which $\hat{\rho}_D(t)$ becomes stationary. The second one, associated to the recurrences emerging in any finite size system, scales with the system size and thus tends to infinity in the thermodynamic limit. Finally τ_{rel} is the time after which the expectation values of any local observable should

be reproduced by the stationary $\hat{\rho}_D(t \gg \tau_{sw})$, up to the chosen accuracy. For sudden quenches it is known that, under suitable hypotheses, a sufficiently large system size always enables one to find a relaxation time $\tau_{rel} < \tau_{rec}$, thus identifying a finite time window in which the state becomes effectively stationary and is accurately described by the GGE density matrix [344, 345].
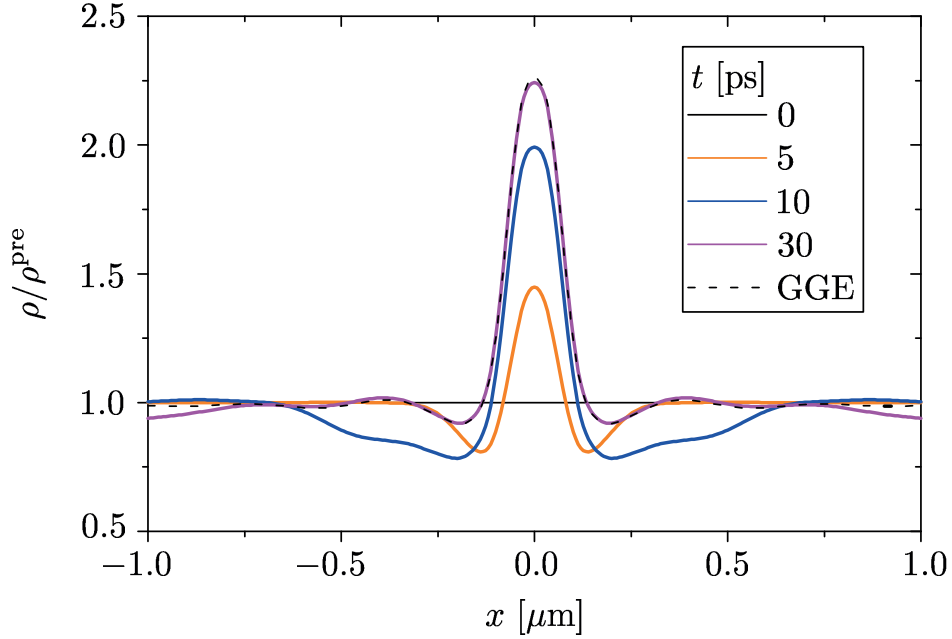
Fig. 4.4 Different snapshots of the post-quench charge density profile, normalized to the pre-quench spatially uniform profile, are shown for an InSb NW with the same parameters as in Figure 4.3, for a switching time $\tau_{sw} = 5\,\text{ps}$ of the QW potential. The charge density profile relaxes to the stationary distribution predicted by the Generalized Gibbs Ensemble (GGE) within a finite time $\tau_{rel} \simeq 30\,\text{ps} > \tau_{sw}$. It remains in this out of equilibrium distribution until the recurrence time related to finite size of the system.

Here we test this prediction in our model for a finite switching time. The charge density profile, renormalized to the pre-quench spatially uniform distribution, is reported in Figure 4.4 for a finite switching time $\tau_{sw} = 5\,\text{ps}$, at various snapshots. During the switching of the potential $(0 < t < 2\tau_{sw})$ the charge density profile starts to deviate from the pre-quench uniform profile. After the switching has been completed $(t > 2\tau_{sw})$, it gradually relaxes in a finite time to the stationary profile predicted by $\hat{\rho}_D(t \gg \tau_{sw})$. In particular, within a spatial region of 2 μm including the QW, the convergence to the GGE occurs within $\simeq$30 ps (magenta curve in Figure 4.4). The convergence to the GGE result thus holds for a finite switching time as well, with the necessary further restriction $\tau_{sw} < \tau_{rel} < \tau_{rec}$. We thus conclude that, in the prescribed time window $\tau_{rel} < t < \tau_{rec}$,

the state of the system is effectively stationary and indistinguishable from a GGE density matrix. We emphasize that, since the *local* quenched potential is set to induce one single bound state, the convergence to the GGE-prescribed profile occurs *in time*, not just upon time-average as in the case of an extensively distributed disorder potential [318, 319]. Furthermore, such out of equilibrium GGE distribution corresponds to a very peculiar population-inversion regime, which leads to a unique fingerprint in the absorption spectrum of the system.

4.6 Conclusions

We have shown that, by quenching a suitable local attractive potential in an isolated one-dimensional free electron gas, the out of equilibrium dynamics is determined by a GGE describing the elementary deviation from equilibrium, where only one Lagrange multiplier λ_{bs} deviates from its equilibrium value. The proof of concept of this prediction has been provided in Sections 4.3 and 4.4, where we have considered the case of a sudden quench in a rectangular QW. This case can be analytically evaluated and the resulting post-quench GGE distribution has been computed exactly. We have found that the occupancy of the continuum states is unaltered by the quench and is still described by an equilibrium Fermi function, so that all such states are occupied up to the chemical potential at zero temperature. In striking contrast, the bound state generated by the quench is only partially occupied, despite being energetically more favorable than the continuum (see Figure 4.1). Such population-inversion regime has been shown to cause a negative peak in the absorption spectrum, realizing an optical gain (see Figure 4.2). The implementation in InSb NWs has also been discussed.

Then, in Section 4.5, we have considered the more realistic case of a QW potential that is switched on in a finite switching time and that exhibits a smooth profile. This analysis, which has been carried out numerically, confirms the robustness of the predicted effect. Indeed, as shown in Fig. 4.3(a), the population of the bound state saturates, after a transient time, to a value that is lower than 1 and that depends on the switching time. The negative absorption thus persists, as shown in Fig. 4.3(b). Furthermore, we have also proven in Figure 4.4 that, since the *locally* quenched potential is set to induce one single bound state, the spatial profile of the electron density tends to the profile prescribed by the out of equilibrium GGE *in time*, not just upon time average like in the cases of extensively distributed quenched potentials. In conclusion, these results based on a local quench protocol could pave the way to observe via optical measurements signatures of

GGE in fermionic systems, which have been elusive so far within proposals based on homogeneous quenches.

Chapter 5

Real-space effects of a quench in the Su–Schrieffer–Heeger model

The content of this Chapter is based on the published paper [351]

5.1   Introduction

After a decade characterized by a remarkable effort to find signatures of topological edge states in various materials, presently one of the most fascinating challenges in Physics is the possibility to manipulate these states and to possibly encode information therein [352, 353, 354]. To this purpose, the implementation with cold atoms in optical lattices[355, 356, 357, 358, 165, 359, 360, 361, 362, 363, 364, 365, 366, 367, 368, 369, 370, 371] offers a twofold advantage, namely a pretty reliable system isolation from the environmental decoherence, and an extremely precise control of the system Hamiltonian. In particular, it is possible to realize quantum quenches of the Hamiltonian parameters [87, 79, 80, 81], both over the entire system and on a spatially localized portion. These experimental advances thus also bring up new interesting questions about topological systems. Consider, for instance, a topological insulator characterized by some symmetry and suppose that, by a quantum quench preserving such symmetry, the system is dynamically brought from the trivial to the topological phase, passing through a gap closing. Can one observe the topological states *dynamically* appear in real-space at its edges? Conversely, how do they evolve and possibly disappear when the quench is towards the trivial phase? In this Chapter we aim to answer these questions, focussing on a prototypical case, namely the

Su-Schrieffer-Heeger (SSH) model[372, 373].

The SSH model describes spinless fermions in a bipartite one-dimensional lattice through the following tight-binding Hamiltonian

$$\hat{\mathcal{H}}_{SSH} = v \sum_j \left(\hat{c}^\dagger_{j,A} \hat{c}_{j,B} + \hat{c}^\dagger_{j,B} \hat{c}_{j,A} \right) + w \sum_j \left(\hat{c}^\dagger_{j,B} \hat{c}_{j+1,A} + \hat{c}^\dagger_{j+1,A} \hat{c}_{j,B} \right) \quad , \qquad (5.1)$$

where $\hat{c}^\dagger_{j,s}$ and $\hat{c}_{j,s}$ denote the fermionic creation/annihilation operators for electrons localized at atom $s = A, B$ within the j-th cell of the lattice, whereas v and w indicate the intra- and inter-cell tunneling amplitudes, respectively. The model, first introduced in the description of opto-electronic properties of polyacetylene[372, 373, 374], is considered as a paradigmatic example of one-dimensional topological insulators [375, 376]. Indeed at half filling (one electron per unit cell) the SSH model describes a band insulator characterized by a band gap $2\varepsilon_g$ with $\varepsilon_g = ||v| - |w||$ and by a sublattice symmetry called chiral symmetry, which identifies for $|v| < |w|$ and for $|v| > |w|$ two topologically different phases that cannot be connected to each other without closing the gap. In the topologically non-trivial phase, a SSH chain exhibits at its edges localized states that are protected by the chiral symmetry. Recently, soliton states and topological indices of the SSH model have been experimentally observed in implementations with cold atoms[377, 378]. Moreover, the effects of time-dependent perturbations to the SSH hopping amplitudes have been analyzed in the context of topologically protected quantum gates [379] and Floquet nonequilibrium states generated by periodic drives [380, 381, 382, 383].

Consider now a SSH chain-lattice, initially in the ground state of the topologically trivial phase ($|v| > |w|$), at half filling, and perform a quench of the hopping amplitudes to the topological phase ($|v| < |w|$). If the quench remains within the chiral symmetry class, the gap closes at some time and, by inspecting the dynamical evolution of the occupancy at each chain site, one would expect localized topological states to gradually emerge at the chain edges. Here we show that this is not the case: the site occupancy remains exactly equal to the one of the trivial pre-quench state at any time and any site, including at the chain edges, regardless of the quench protocol (fast or slow) and even in the presence of chiral disorder. As we shall demonstrate, the reason boils down to the charge conjugation or time-reversal symmetries of the pre-quench state and of the quenching Hamiltonian. In an open chain, these additional symmetries are typically present and completely mask any effect of the quench in real-space, including the appearance of the topological states.

Effects of a quench can be observed in real-space occupancies only when such symmetries are broken, which can be done in two ways: i) remaining within the topological insulator framework, i.e. preserving the chiral symmetry and the half-filling condition[1]; ii) by "brute force", i.e. by breaking the chiral symmetry and/or by moving away from an insulating state.

We shall first explore the first option and propose two ways to observe the dynamical effects of the quench in real-space. The quench protocols are based on a local quench, where a ring lattice is cut into a chain or, viceversa, two edges of a chain are bridged to form a ring. In both cases the presence of a magnetic flux threading the ring is crucial to induce a real-space dynamical response to the quench, which is different depending on whether the involved chain is in the trivial or in the topological phase.

Then, we shall explore the second option and analyze the effects of quenches beyond the framework of topological insulator, i.e. by breaking the chiral symmetry and by considering filling values different from $1/2$, where the SSH model describes a metallic state. We find that the optimal way to observe the dynamical appearance of the edge states characterizing the topological insulator is to have a slightly metallic system. Then, the dynamical appearance of these states is robust even in the limit of short quench time and in the presence of chiral breaking disorder.

The Chapter is organized as follows. In Sec.5.2, after briefly summarizing the aspects of the SSH model that are needed to illustrate our results, including its symmetries, we shall describe the method we used to compute the dynamical evolution. In Sec.5.3 we present a general theorem ensuring that the site occupancy remains locked to $1/2$ when charge conjugation symmetry is present. In particular, this explains the case of a quenched half-filled SSH chain. Then, in Sec.5.4 we show how to violate the hypotheses of the theorem and observe real-space effects of the quench without breaking the chiral symmetry. Finally, after analyzing the effects of chiral breaking terms and of a filling different from $1/2$ in Sec.5.5, we discuss our results and draw our conclusions in Sec.5.6.

---

[1]In fact, this corresponds to a dynamical breaking of chiral symmetry, see Sec.1.2.3

5.2   Model, symmetries and method

5.2.1   Generalized SSH model and symmetries

In this Chapter we consider a generalized SSH model

$$\hat{\mathcal{H}}_{SSH,\chi} = \sum_j \left(v_j \hat{c}_{j,A}^\dagger \hat{c}_{j,B} + v_j^* \hat{c}_{j,B}^\dagger \hat{c}_{j,A} \right) + \sum_j \left(w_j \hat{c}_{j,B}^\dagger \hat{c}_{j+1,A} + w_j^* \hat{c}_{j+1,A}^\dagger \hat{c}_{j,B} \right) \qquad (5.2)$$

extending the SSH Hamiltonian (5.1) to the case where the tunneling amplitudes $\{v_j, w_j\}$ are possibly complex and site-dependent. Here $j = 1, 2 \ldots, M$, where M is the number of cells in the lattice. Furthermore, because symmetries play an important role in the dynamical effects that we aim to discuss, it is worth briefly recalling the behavior of the Hamiltonian (5.2) under three transformations that are local on the lattice site operators. The first one is *charge-conjugation* $\mathcal{C}$, a linear and unitary transformation mapping the lattice site creation/annihilation operators as follows

$$\begin{cases} \mathcal{C} \hat{c}_{j,A} \mathcal{C}^{-1} &= \hat{c}_{j,A}^\dagger \\ \mathcal{C} \hat{c}_{j,B} \mathcal{C}^{-1} &= -\hat{c}_{j,B}^\dagger \end{cases} , \qquad (5.3)$$

and fulfilling $\mathcal{C}^{-1} = \mathcal{C}^\dagger = \mathcal{C}$. The second one is the *chiral transformation* $\mathcal{S}$. Despite acting on the lattice site operators in the same way as $\mathcal{C}$

$$\begin{cases} \mathcal{S} \hat{c}_{j,A} \mathcal{S}^{-1} &= \hat{c}_{j,A}^\dagger \\ \mathcal{S} \hat{c}_{j,B} \mathcal{S}^{-1} &= -\hat{c}_{j,B}^\dagger \end{cases} , \qquad (5.4)$$

it is by definition anti-linear ($\mathcal{S} i \mathcal{S} = -i$) and anti-unitary $\langle \mathcal{S}\Psi_1 | \mathcal{S}\Psi_2 \rangle = \langle \Psi_1 | \Psi_2 \rangle^*$. Finally, the *time-reversal* transformation, which leaves lattice site operators unaltered

$$\begin{cases} \mathcal{T} \hat{c}_{j,A} \mathcal{T}^{-1} &= \hat{c}_{j,A} \\ \mathcal{T} \hat{c}_{j,B} \mathcal{T}^{-1} &= \hat{c}_{j,B} \end{cases} \qquad (5.5)$$

but is also anti-linear and anti-unitary, with $\mathcal{T}^2 = \mathbb{I}$, as is the case for spinless fermions. In fact, only two of these transformations are independent because the chiral symmetry $\mathcal{S}$ can be obtained as the product $\mathcal{S} = \mathcal{T}\mathcal{C}$.

The Hamiltonian (5.2) exhibits the chiral symmetry (5.4)

$$\mathcal{S} \hat{\mathcal{H}}_{SSH,\chi} \mathcal{S}^{-1} = \hat{\mathcal{H}}_{SSH,\chi} \quad \Leftrightarrow \quad \left[\hat{\mathcal{H}}_{SSH,\chi} , \mathcal{S} \right] = 0 \quad , \qquad (5.6)$$

and the subscript χ stands in fact for 'chiral'. In chiral-symmetric models like $\hat{\mathcal{H}}_{SSH,\chi}$, $\mathcal{T}$ and $\mathcal{C}$ are intimately related. Indeed, because $\mathcal{C} = \mathcal{T}\mathcal{S}$, time-reversal and charge conjugation transformations are either both preserved or both broken. In particular, for $\{v_j, w_j\} \in \mathbb{R}$, the Hamiltonian (5.2) also commutes with time-reversal $\mathcal{T}$ and charge conjugation $\mathcal{C}$. However, when $v_j = |v_j|e^{i\phi_j^v}$ and $w_j = |w_j|e^{i\phi_j^w}$ have non-vanishing complex phases, the preservation of $\mathcal{T}$ and $\mathcal{C}$ heavily depends on the geometric boundary conditions. In particular, in a chain, i.e. a lattice with open boundary conditions (OBCs), $\mathcal{T}$ and $\mathcal{C}$ are always preserved, since such complex phases can be eliminated through a canonical transformation onto the lattice operators $c_{j,A} \to \tilde{c}_{j,A} = e^{i\alpha_j}c_{j,A}$ and $c_{j,B} \to \tilde{c}_{j,B} = e^{i(\alpha_j + \phi_j^v)}c_{j,B}$, where $\alpha_1 = 0$ and $\alpha_j = \sum_{i=1}^{j-1}(\phi_i^v + \phi_i^w)$ for $j = 2, \ldots M$, recasting the Hamiltonian into the case of real and positive tunneling amplitudes[375]. In contrast, in a ring-shaped lattice, the periodic boundary conditions (PBCs) prevent the elimination of the phases of v_j and w_j. Physically, this can be understood in terms of the Peierls substitution[384, 385], where the complex phases of the tunneling amplitudes describe the integral of a vector potential from one lattice site to next one. While in a chain the vector potential can always be gauged out, in a ring this is not possible, for its circulation yields the magnetic flux Φ threading the ring, and one has $\sum_{j=1}^{M}(\phi_j^v + \phi_j^w) = 2\pi\Phi/\Phi_0 \neq 0$, where $\Phi_0 = h/e$ is the flux quantum. Thus, in the SSH ring with a flux $\Phi \neq p\Phi_0/2$ (with $p \in \mathbb{Z}$), $\mathcal{T}$ and $\mathcal{C}$ are broken.

To perform our time-dependent analysis, we represent the second-quantized Hamiltonian (5.2) in the real-space basis as follows

$$\hat{\mathcal{H}}_{SSH,\chi} = \sum_{j_1,j_2=1}^{M} \sum_{s_1,s_2=A,B} \hat{c}_{j_1,s_1}^{\dagger} H_{j_1 s_1, j_2 s_2} \, \hat{c}_{j_2,s_2} \quad , \tag{5.7}$$

where

$$H = \begin{pmatrix} 0 & v_1 & & & & & w_M^* \\ v_1^* & 0 & w_1 & & & & \\ & w_1^* & 0 & v_2 & & & \\ & & v_2^* & 0 & w_2 & & \\ & & & w_2^* & \ddots & & \\ & & & & \ddots & & \\ & & & & & \ddots & w_{M-1} \\ & & & & w_{M-1}^* & 0 & v_M \\ w_M & & & & & v_M^* & 0 \end{pmatrix} \tag{5.8}$$

is the related first-quantized Hamiltonian matrix, whose entries $H_{j_1 s_1, j_2 s_2}$ are labelled by the cell j and the site $s = A, B = +/-$ within the cell. In terms of the first quantized Hamiltonian (5.8), symmetries are expressed in a different way as compared to the second quantized Hamiltonian (5.2). Explicitly, the chiral symmetry (5.6) implies

$$S\, H\, S^{-1} = -H \quad \Leftrightarrow \quad \{H, S\} = 0 \tag{5.9}$$

where $S = \oplus_{j=1}^{M} (\sigma_z)_j$ is the first-quantized version of the chiral transformation $\mathcal{S}$ defined in Eq.(5.4), and is unitary. From Eq.(5.9) one straightforwardly deduces that, for any realization of the parameters $\{v_j\,,\,w_j\}$, the single-particle spectrum is symmetric around $\varepsilon = 0$. Indeed if ψ is a single-particle wavefunction with eigenvalue ε, i.e. $H\psi = \varepsilon\,\psi$, the wavefunction $S\psi$, obtained from ψ by changing the sign at the B-sites, is also an eigenfunction of H with eigenvalue $-\varepsilon$. The set of eigenfunctions of Eq.(5.8) can thus be chosen as $\{\psi_\alpha\}$ (positive eigenvalues $\varepsilon_\alpha > 0$) and $\{S\psi_\alpha\}$ (negative eigenvalues $-\varepsilon_\alpha < 0$), where $\alpha = 1, \ldots M$ is the quantum number running over the positive spectrum. The corresponding operators

$$\begin{cases} \gamma_{\alpha,+} = \sum_{j=1}^{M} \sum_{s=A/B=\pm} (\psi_\alpha^*)_{j,s}\, \hat{c}_{j,s} \\ \gamma_{\alpha,-} = \sum_{j=1}^{M} \sum_{s=A/B=\pm} (\psi_\alpha^*)_{j,s}\, (-1)^s\, \hat{c}_{j,s} \end{cases} \tag{5.10}$$

diagonalize the Hamiltonian (5.2)

$$\hat{\mathcal{H}}_{SSH,\chi} = \sum_\alpha \varepsilon_\alpha \left(\gamma_{\alpha,+}^\dagger \gamma_{\alpha,+} - \gamma_{\alpha,-}^\dagger \gamma_{\alpha,-} \right) \tag{5.11}$$

and fulfill the relations

$$\mathcal{S}\gamma_{\alpha,\pm}\mathcal{S}^{-1} = \gamma_{\alpha,\mp}^\dagger \tag{5.12}$$

While the chiral symmetry (5.9) always holds for Eq.(5.8), time-reversal and charge-conjugation symmetries hold if the Hamiltonian H fulfills further properties. Specifically the former symmetry holds if H is real

$$T\, H\, T^{-1} = H^* = H \tag{5.13}$$

where $T = K$ denotes the complex conjugation and is anti-unitary, whereas the latter symmetry holds if

$$C\, H\, C^{-1} = S\, H^*\, S^{-1} = -H \tag{5.14}$$

where $C = ST$ is the first-quantized version of $\mathcal{C}$ [see Eq.(5.3)] and is anti-unitary[2].

Note that the hopping amplitude w_M appearing in the lower-left and upper-right corners of Eq.(5.8) is vanishing for a chain. In such a case, an argument similar to the one used above for the second quantized Hamiltonian, leads to conclude that Eqs.(5.13) and (5.14) always hold, as can be checked by merely redefining the real-space basis by local phase factors.

We conclude this subsection by recalling that, for *homogeneous* hopping amplitudes ($v_j \equiv v$ and $w_j \equiv w$) the model (5.2) can be exactly solved both in a ring (PBCs) and in a chain (OBCs). In particular, in the ring geometry and in the thermodynamic limit one can identify two different topological classes[375], and by analyzing the chain one can see that one phase is topologically non-trivial, hosting two discrete levels in the spectrum near $\varepsilon = 0$, which correspond to states localized at the edges. For the sake of completeness, a short summary of these aspects in given in the Appendix D.

5.2.2 Quenches, density matrix approach and observables

In the following, we shall investigate the dynamical effects of a quench in the parameters $\{v_j, w_j\}$ of the Hamiltonian (5.2). Specifically, the system is prepared in an initial state $\boldsymbol{\rho}^{\mathrm{pre}}$, typically the ground state or the thermal equilibrium state of a pre-quench Hamiltonian $\hat{\mathcal{H}}^{\mathrm{pre}} = \hat{\mathcal{H}}_{SSH,\chi}(t < t_0)$. Then, at $t = t_0$ the system is disconnected from the environment and the dynamics is unitarily governed by the Hamiltonian $\hat{\mathcal{H}}_{SSH,\chi}(t)$, which varies until a time t_f from $\hat{\mathcal{H}}^{\mathrm{pre}}$ to a post-quench Hamiltonian $\hat{\mathcal{H}}^{\mathrm{post}} = \hat{\mathcal{H}}_{SSH,\chi}(t > t_f)$. The quench protocol specifies the way the parameters $\{v_j(t), w_j(t)\}$ in Eq.(5.2) are varied during the quench time $\tau_q = t_f - t_0$.

Although in our analysis we shall mainly focus on short quench time limit ($\tau_q \to 0$), we shall keep the parameter time dependence arbitrary because, as we shall see, some results are independent of the specific quench protocol. Moreover, we shall deal with both global and local quenches. A global quench involves a change in a significant number (scaling like the number M of cells) of hopping amplitudes along the chain. This occurs, for instance, when all the hopping amplitudes of a homogeneous chain ($v_j \equiv v$ and $w_j \equiv w$) are brought from the trivial to the topological phase. In contrast, a local quench only involves a limited number of hopping amplitudes. For instance, the cutting of a ring into a chain is described by quenching to zero the hopping amplitude of one single bond. Note

---

[2]Further details about the symmetry constraints in a translation invariant Hamiltonian are reported in Appendix D.1.

that, because of Eq.(5.6), the chiral symmetry is preserved at any time, so that the quench occurs within the chiral symmetry class. Yet, the result of a quench depends not only on the quenching Hamiltonian, but also on the pre-quench state and its symmetries, as we shall see. Furthermore, in Sec.5.5, we shall also analyze the quench in chiral symmetry broken cases.

We shall be interested in one-body observables $\hat{\mathcal{A}} = \sum_{j_1 s_1, j_2 s_2} \hat{c}_{j_1, s_1}^\dagger A_{j_1 s_1, j_2 s_2} \hat{c}_{j_2, s_2}$, whose expectation values are straightforwardly evaluated in terms of the single-particle density matrix $\rho_{j_1 s_1, j_2 s_2}(t) = \text{Tr}\{c_{j_2, s_2}^\dagger \hat{c}_{j_1 s_1} \hat{\boldsymbol{\rho}}(t)\}$, where $\hat{\boldsymbol{\rho}}(t)$ denotes the dynamical evolution of the full system density matrix and Tr the trace over the Fock space. Due to the quadratic structure of Eq.(5.7), the Liouville-von Neumann equation for $\hat{\boldsymbol{\rho}}$ straightforwardly implies the dynamical equation for ρ, which reads

$$i\hbar \frac{d\rho}{dt} = [H(t), \rho] \quad . \tag{5.15}$$

We numerically solve Eq.(5.15) with the initial condition $\rho(t_0) = \rho^{\text{pre}}$ corresponding to the single-particle density matrix of the pre-quench state, typically the ground state of the pre-quench Hamiltonian. Then, the expectation values of an observable $\hat{\mathcal{A}}$ are obtained as

$$\langle \hat{\mathcal{A}} \rangle(t) = \text{tr}\{A\,\rho(t)\} \tag{5.16}$$

where "tr" denotes the trace over the single-particle Hilbert space. In particular, we shall henceforth focus on the site occupancy, evaluated as

$$N_{j,s}(t) = \langle \hat{n}_{j,s} \rangle(t) = \rho_{js,js}(t) \quad , \tag{5.17}$$

and on the cell polarization

$$P_j(t) = \langle \hat{n}_{j,A} \rangle(t) - \langle \hat{n}_{j,B} \rangle(t) \quad , \tag{5.18}$$

obtained as $P_j = \rho_{jA,jA} - \rho_{jB,jB}$. The total number of electrons $N_e = \sum_{j,s} N_{j,s}$ is simply given by $N_e = \text{tr}\rho$ and is constant as a consequence of Eq.(5.15). In Sec.5.5 we shall also discuss the non-equilibrium energy distribution in the post-quench eigenbasis $\{\lambda\}$, where $\hat{\mathcal{H}}^{\text{post}} = \sum_\lambda \varepsilon_\lambda \hat{n}_\lambda$ is diagonal. The energy distribution is obtained as

$$\langle \hat{n}_\lambda \rangle(t) = \sum_{j_1, j_2 = 1}^{M} \sum_{s_1, s_2 = A, B} U_{\lambda, j_2 s_2} U_{\lambda, j_1 s_1}^* \, \rho_{j_2 s_2, j_1 s_1}(t) \tag{5.19}$$

where $U_{\lambda,js} = \langle \lambda | js \rangle$ is the unitary matrix determining the single-particle change of basis from the real-space basis to the post quench eigenbasis.

5.3 Quenches in half-filled SSH models: The locking of site occupancy

We start by considering a chain of the customary SSH model Eq.(5.1) with homogeneous hopping amplitudes, which can be assumed to be positive ($v, w > 0$). Let the pre-quench state be the half-filled ground state of the chain in the trivial phase, so that there is one electron per cell ($N_e = M$), i.e. half an electron per site on average, and

$$w^{\mathrm{pre}} < v^{\mathrm{pre}} \quad , \tag{5.20}$$

where $w^{\mathrm{pre}} \equiv w(t < 0)$ and $v^{\mathrm{pre}} \equiv v(t < 0)$. No edge state is present. At $t = 0$ we start to quench the Hamiltonian parameters towards the topological phase, as sketched in Fig.5.1. This means that, within a quench time τ_q, the values of the hopping amplitudes are brought to

$$w^{\mathrm{post}} > v^{\mathrm{post}} \quad , \tag{5.21}$$

where $w^{\mathrm{post}} \equiv w(t > \tau_q)$ and $v^{\mathrm{post}} \equiv v(t > \tau_q)$.
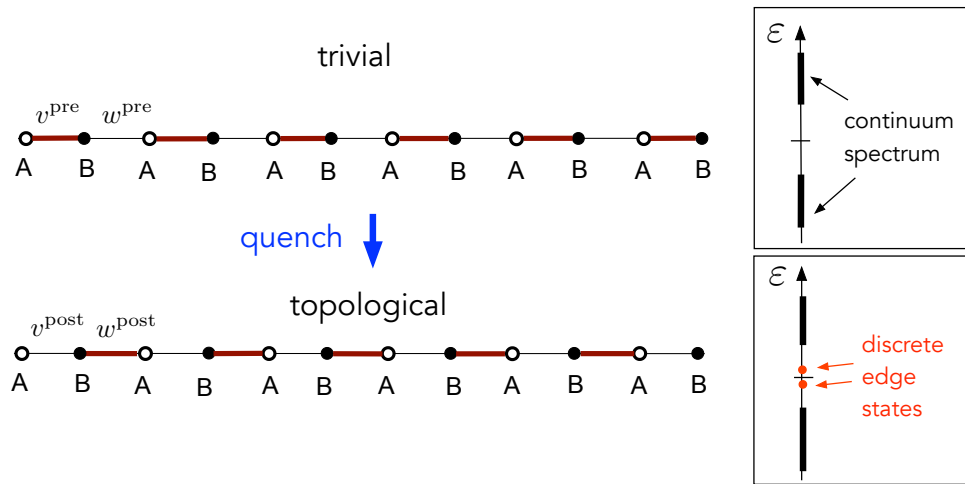
Fig. 5.1 A global quench is applied to a half-filled SSH chain from the trivial to the topological phase. The insets on the right-hand side sketch the spectra of the two phases: while the trivial phase only exhibits a continuum spectrum, the topological phase also hosts two discrete states.

At first, one would expect the discrete states characterizing the chain spectrum in the topological phase to gradually appear in real-space, causing an occupancy increase localized at the two edges. However, this is not the case: we find that the site occupancy is locked at $1/2$ *at any time* and *at any site*, including the chain edges

$$N_{j,s}(t) = 1/2 \qquad \forall t \quad \forall j, s \tag{5.22}$$

just like in the trivial pre-quench phase. Notably, such a locking of the real-space occupancy occurs for any quench duration τ_q, regardless of the specific way one changes the hopping amplitudes from $(v^{\mathrm{pre}}, w^{\mathrm{pre}})$ to $(v^{\mathrm{post}}, w^{\mathrm{post}})$. Furthermore, it also holds in the presence of chiral disorder and/or if the pre-quench state is a thermal state at finite temperature. Indeed the result (5.22) is a consequence of a general theorem that we shall prove here below. Before doing that, it is worth emphasizing that the quench does affect the system, though. For instance, the energy distribution of the post-quench Hamiltonian strongly differs from the pre-quench equilibrium distribution and exhibits a striking band population inversion, as has been proven in Ref.[336] for a SSH ring exposed to a sudden quench.

5.3.1   General theorem about site occupancy

The following general result can be proven: (i) If the pre-quench state ($t = t_0$) is invariant under charge-conjugation

$$\mathcal{C}\hat{\boldsymbol{\rho}}^{\mathrm{pre}}\mathcal{C}^{-1} = \hat{\boldsymbol{\rho}}^{\mathrm{pre}} \tag{5.23}$$

and (ii) if the time-dependent Hamiltonian $\hat{\mathcal{H}}(t)$ characterizing the quench ($t > t_0$) commutes with charge-conjugation transformation

$$\left[\hat{\mathcal{H}}_{SSH,\chi}(t > t_0), \, \mathcal{C}\right] = 0 \quad , \tag{5.24}$$

then Eq.(5.22) holds. The proof starts by recalling that the pre-quench state $\hat{\boldsymbol{\rho}}^{\mathrm{pre}}$ evolves as $\hat{\boldsymbol{\rho}}(t) = \mathcal{U}(t)\hat{\boldsymbol{\rho}}^{\mathrm{pre}}\mathcal{U}^\dagger(t)$, where the evolution operator is

$$\mathcal{U}(t) = \overleftarrow{\mathrm{T}}\left[\exp\left(-\frac{i}{\hbar}\int_{t_0}^t \hat{\mathcal{H}}(t')dt'\right)\right] \qquad \forall t > t_0 \tag{5.25}$$

and $\overleftarrow{\mathrm{T}}$ denotes the time-ordering. Moreover, the property (5.24) and the linearity of $\mathcal{C}$ imply that

$$[\mathcal{C}, \mathcal{U}(t)] = 0 \qquad \forall t > t_0 \tag{5.26}$$

By using Eqs.(5.23) and (5.26) the time evolution of the site occupancy $N_{j,s} = \langle \hat{n}_{j,s} \rangle$ is then computed as

$$
\begin{aligned}
N_{j,s}(t) &= \text{Tr}\left\{ \hat{\boldsymbol{\rho}}(t)\, \hat{n}_{j,s} \right\} = \\
&= \text{Tr}\left\{ \mathcal{U}(t)\hat{\boldsymbol{\rho}}^{\text{pre}}\mathcal{U}^\dagger(t)\, \hat{n}_{j,s} \right\} = \\
&= \text{Tr}\left\{ \mathcal{U}(t)\, \mathcal{C}\, \hat{\boldsymbol{\rho}}^{\text{pre}}\mathcal{C}^{-1}\mathcal{U}^\dagger(t)\, \hat{n}_{j,s} \right\} = \\
&= \text{Tr}\left\{ \mathcal{C}\mathcal{U}(t)\hat{\boldsymbol{\rho}}^{\text{pre}}\mathcal{U}^\dagger(t)\, \mathcal{C}^{-1}\hat{n}_{j,s} \right\} = \\
&= \text{Tr}\left\{ \mathcal{U}(t)\hat{\boldsymbol{\rho}}^{\text{pre}}\mathcal{U}^\dagger(t)\, \mathcal{C}\hat{n}_{j,s}\mathcal{C}^{-1} \right\} = \\
&= \text{Tr}\left\{ \hat{\boldsymbol{\rho}}(t)\,(1 - \hat{n}_{j,s}) \right\} = \\
&= 1 - N_{j,s}(t)
\end{aligned}
\tag{5.27}
$$

where we have used $\mathcal{C} = \mathcal{C}^{-1}$ and $\mathcal{C}\hat{n}_{j,s}\mathcal{C}^{-1} = 1 - \hat{n}_{j,s}$. The result Eq.(5.22) follows from Eq.(5.27), and shows that the site occupancy remains locked to its trivial phase value $1/2$. We also observe that, by a very similar argument, the hypotheses of the theorem also imply that the off-diagonal single-particle density matrix entries are always either real or purely imaginary, at any time. Specifically $\rho_{iA,jB}(t) = \langle c_{jB}^\dagger c_{iA} \rangle$ is real $\forall i, j$, while $\rho_{is,js}(t) = \langle c_{js}^\dagger c_{is} \rangle$ is purely imaginary $\forall i \neq j$ and $s = A, B$.

5.3.2 Global quench in a SSH chain

We shall now show that a quench of the half-filled SSH chain satisfies the hypotheses Eqs.(5.23) and (5.24) of the above theorem, whence one straightforwardly deduces the locking of the site occupancy, Eq.(5.22). Indeed Eq.(5.24) is satisfied by $\hat{\mathcal{H}}_{SSH,\chi}(t)$ because, as observed in Sec.5.2.1, in a chain with OBCs the SSH model Eq.(5.2) preserves both charge-conjugation $\mathcal{C}$ and time-reversal symmetry $\mathcal{T}$. Furthermore, if the pre-quench state is the thermal equilibrium state at half-filling ($\mu = 0$) of the pre-quench SSH Hamiltonian $\hat{\mathcal{H}}^{\text{pre}}$

$$
\hat{\boldsymbol{\rho}}^{\text{pre}} = \frac{e^{-\beta\hat{\mathcal{H}}^{\text{pre}}}}{\text{Tr}[e^{-\beta\hat{\mathcal{H}}^{\text{pre}}}]}
\tag{5.28}
$$

where $\beta = 1/k_B T$ is the inverse temperature, the symmetry $[\hat{\mathcal{H}}^{\text{pre}}, \mathcal{C}] = 0$ straightforwardly implies Eq.(5.23). In particular, this is true for the half-filled ground state $\hat{\boldsymbol{\rho}}^{\text{pre}} = |\text{H.F.}\rangle\langle\text{H.F.}|$, where $|\text{H.F.}\rangle$ is constructed by occupying all the negative energy states of $\hat{\mathcal{H}}^{\text{pre}}$ $|\text{H.F.}\rangle = \prod_{\alpha=1}^{M} \gamma_{\alpha,-}^\dagger |0\rangle$ and is non-degenerate.

This explains why in a half-filled SSH chain the quench does not lead to any change of the site occupancy, which remains uniform and constant regardless of i) the specific quench time and protocol, ii) the presence of chiral disorder in the tunneling amplitudes $\{v_j, w_j\}$, and iii) finite temperature of the pre-quench thermal state. In particular, in a chain it is impossible to observe the appearance of the topological states or any other difference between the trivial and the topological phase in real-space occupancies. In Sec.5.4 we shall propose a different setup where real-space effects of a quench can be observed. However, we wish to first provide a more physical justification for the result Eq.(5.22).

The case of infinitely slow quench: Comparison between the trivial and topological half-filled ground states.

Because the result Eq.(5.22) is valid for any quench protocol, it holds in particular for an infinitely slow quench ($\tau_q \to \infty$), where the pre-quench ground state evolves into the post-quench ground state. In this particular limit, the result Eq.(5.22) can thus be understood by comparing the site occupancy profile of the trivial and topological half-filled ground states. In the trivial phase, where the spectrum is purely continuum, the uniform pattern $N_{j,s}^{\mathrm{pre}} \equiv 1/2$ is expected from the contribution of the bulk states extending over the entire chain. In the topological phase, where the additional discrete levels $\pm\varepsilon^{\mathrm{edge}}$ near $\varepsilon = 0$ are present, the site occupancy profile results from two types of contributions. The red curve in Fig.5.2(a) shows the discrete state contribution localized at the chain edges [see Eq.(D.6)], while the thin black curve displays, as an illustrative example, the contribution of one bulk state, whose wavefunction extends over the entire chain [see Eq.(D.5)]. Notably, the blue curve, describing the contribution of *all* the occupied bulk states of the chain, features two dips at the edges, which are perfectly complementary to the edge state contribution: The bulk states "feel" the presence of the edge states and make room for them by slightly modifying their behavior near the boundaries with respect to the trivial phase. This can be considered as a real-space imaging of the bulk-boundary correspondence[3]. The thick black curve is the sum of the two contributions and uniformly takes the value $N_{j,s}^{\mathrm{post}} \equiv 1/2$. Thus the half-filled ground state of the chain in the topological phase does not show any different feature in real-space occupancy with respect to the trivial phase, despite the presence of the edge states in the spectrum.

---

[3]It is also worth recalling that a similar phenomenon was observed in Ch.2, where bulk modes collectively compensate for the absence of interface bound states in the orthogonal spin density profile (see Fig.2.4).

(a) clean case
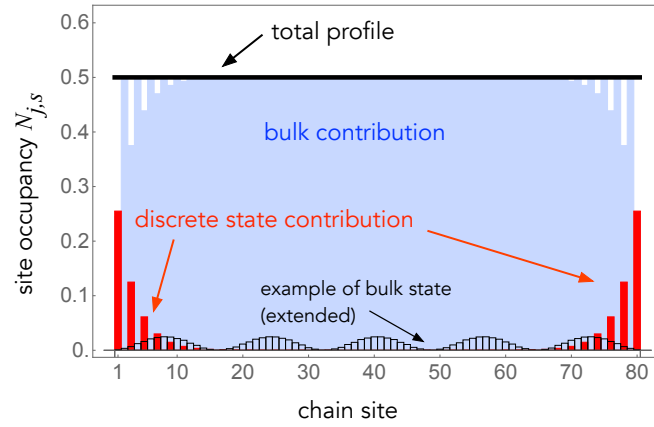
(b) chiral disorder
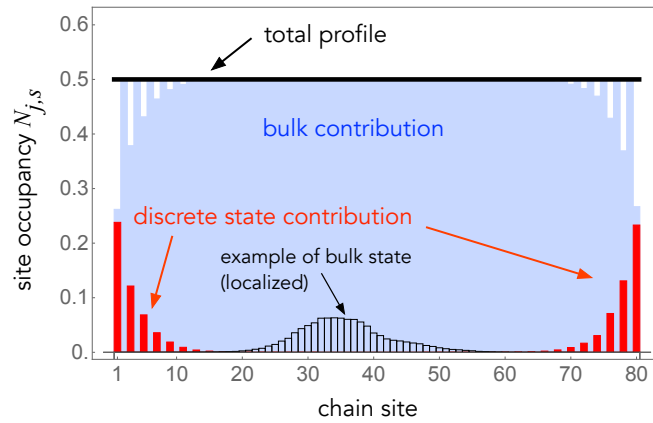
Fig. 5.2 The site occupancy profile of the half-filled SSH chain ($N = 80$ sites, i.e. $M = 40$ cells) in the topological phase (thick black curve), the discrete level contribution (edge states, in red) and the contribution of all the occupied states in the continuum spectrum (bulk states, blue). (a) in the clean case, where the tunneling amplitudes are homogeneous ($v_j \equiv v$, $w_j \equiv w$, with $v = 0.7w$), all bulk states are extended, and the thin black curve shows an example of a bulk state; (b) in the chiral-disordered case, where the tunneling amplitudes v_j, w_j are random variables with average values fulfilling $v = 0.7w$ and with disorder strength $d = 0.1$, the bulk states are also localized, and one example is shown by the thin black curve. In both cases the edge and bulk states contributions are perfectly complementary, so that the total site occupancy profile is flat and equal to $1/2$ everywhere.

Such a lack of difference seems at first to contradict the argument that is customarily invoked to illustrate the emergence of the edge states in the topological phase, based on the dimerized limit of the chain: When the extremal links of the chain are very weak, $v/w \to 0$, the outmost chain sites host a localized electron. However, this can only hold when the number N_e of electrons in the chain is $M + 1$. At half filling, $N_e = M$, only one

electron can be accommodated in the two edge sites and, in fact, each of them hosts "half an electron". Indeed the red curve of Fig.5.2, peaked at *both* chain edges, describes the contribution of only *one* discrete state, namely the one at energy $-\varepsilon^{\mathrm{edge}}$, which is occupied in the half-filled ground state.

We also emphasize that such uniform site occupancy profile is not merely due to the accidental spatial parity[4] of the homogeneous SSH model (5.1). The very chiral symmetry forbids disorder to localize the two discrete states on opposite sides of the chain: The two wavefunctions $\psi_{\pm}^{\mathrm{edge}}$ with opposite energies $\pm\varepsilon^{\mathrm{edge}}$ are mapped into each other by a mere sign change in the B-sites through the chiral transformation S [see Sec.5.2.1], so that their square moduli have to coincide, even in the presence of chiral disorder. This is illustrated in Fig.5.2(b), which refers to a disordered SSH model realized by taking $w_j = w(1 + \xi_j\,d)$ and $v_j = v(1 + \eta_j\,d)$ in Eq.(5.2), where $\{\xi_j, \eta_j\}$ are sets of random variables uniformly distributed in $[-1/2, 1/2]$, $v > 0$ and $w > 0$ are the average tunneling amplitudes, and $d < |v - w|/\max(v, w)$ is the disorder strength. For $v < w$ the spectrum of the disordered SSH chain still consists of a continuum branch and of two additional discrete levels. The red curve describes the only occupied discrete level and again is localized on both edges. In fact, disorder has a stronger impact on the bulk states, which get localized too, as shown by the thin black curve in Fig.5.2(b), in agreement with Anderson localization[131, 386]. However, their total contribution to the site occupancy profile [blue curve in Fig.5.2(b)] is still uniformly flat in the bulk and exhibits two dips by the edges, just like in the clean case of Fig.5.2(a). Again, at half filling, the sum of bulk and edge state contributions yields a perfectly uniform occupancy profile $N_{j,s} \equiv 1/2$ [black thick line in Fig.5.2(b)].
It is also straightforward to understand why such uniform profile is unaltered by finite temperatures: Despite the energy separation between the two discrete levels is tiny, the partial occupancy of the level at energy $+\varepsilon^{\mathrm{edge}}$ induced by thermal excitations is perfectly balanced by the corresponding depletion of the level at energy $-\varepsilon^{\mathrm{edge}}$.

5.4 Breaking charge conjugation in chiral symmetric models: A local quench

In order to observe some effects of the quench in the real-space occupancy, and possibly the appearance of the topological edge states, a necessary condition is that at least one of the two crucial hypotheses of the theorem, Eq.(5.23) and Eq.(5.24), is violated. Here below

---

[4]Specifically, Eq.(5.1) commutes with $\mathcal{P}$, defined through $\mathcal{P}c_{j,A}\mathcal{P}^{-1} = c_{M-j+1,B}$ and $\mathcal{P}c_{j,B}\mathcal{P}^{-1} = c_{M-j+1,A}$.

we show how this is possible while still *preserving the chiral symmetry* and while operating at *half-filling*, i.e under the conditions where the SSH model is rigorously characterized as a topological insulator.

5.4.1 Ring-to-chain quench

The first option is to violate the hypothesis of charge-conjugation invariance of the pre-quench state, Eq.(5.23). This can be achieved by choosing as $\hat{\boldsymbol{\rho}}^{\mathrm{pre}}$ a thermal equilibrium state of the homogeneous half-filled SSH model, like in Eq.(5.28), where $\hat{\mathcal{H}}^{\mathrm{pre}}$ is Eq.(5.2) defined on a ring-shaped lattice threaded by a magnetic flux Φ. In this case both $\hat{\mathcal{H}}^{\mathrm{pre}}$ and $\hat{\boldsymbol{\rho}}^{\mathrm{pre}}$ break time-reversal symmetry $\mathcal{T}$ and hence charge conjugation $\mathcal{C}$ symmetry, so that the condition Eq.(5.23) is violated. Note that, nevertheless, the pre-quench site occupancy still equals exactly $1/2$. Indeed, since $\hat{\mathcal{H}}^{\mathrm{pre}}$ commutes with the chiral symmetry $\mathcal{S}$, the relation

$$
\begin{aligned}
N_{j,s}^{\mathrm{pre}} &= \mathrm{Tr}\left[\hat{\boldsymbol{\rho}}^{\mathrm{pre}}\hat{n}_{j,s}\right] = \frac{\mathrm{Tr}\left[\mathcal{S}e^{-\beta\hat{\mathcal{H}}^{\mathrm{pre}}}\mathcal{S}^{-1}\mathcal{S}\hat{n}_{j,s}\mathcal{S}^{-1}\right]}{\mathrm{Tr}\left[e^{-\beta\hat{\mathcal{H}}^{\mathrm{pre}}}\right]} = \\
&= \frac{\mathrm{Tr}\left[e^{-\beta\hat{\mathcal{H}}^{\mathrm{pre}}}(1-\hat{n}_{j,s})\right]}{\mathrm{Tr}\left[e^{-\beta\hat{\mathcal{H}}^{\mathrm{pre}}}\right]} = 1 - N_{j,s}^{\mathrm{pre}}
\end{aligned}
\tag{5.29}
$$

implies that $N_{j,s}^{\mathrm{pre}} = 1/2 \ \forall j,s$. For definiteness, we take for $\hat{\boldsymbol{\rho}}^{\mathrm{pre}}$ the ground state of the SSH ring.

Then, after isolating the system from the environment, at $t=0$ we perform a *local* quench, i.e. we bring one single ring bond, e.g. w_M, from $w_M^{\mathrm{pre}} = w$ to $w_M^{\mathrm{post}} = 0$, leaving all the other bonds v and w unaltered. As a consequence, the ring gets cut into a chain, as illustrated in Fig.5.3(a). The post-quench Hamiltonian, being defined on a chain lattice, preserves $\mathcal{T}$ and $\mathcal{C}$ and the second hypothesis Eq.(5.24) of the theorem is satisfied. Depending on whether the cut bond is weak ($|w_M^{\mathrm{pre}}| < |v|$) or strong ($|w_M^{\mathrm{pre}}| > |v|$), the post quench chain is in the trivial or in the topological phase, respectively. For simplicity we shall consider the limit of an instantaneous quench. Still, two timescales characterize the post-quench evolution, namely

$$
\tau_g = \frac{\hbar}{||v|-|w||} \quad ,
\tag{5.30}
$$

which is the timescale related to the inverse half-gap, and

$$\tau_L = \frac{\hbar M}{\min(|v|, |w|)} \quad , \tag{5.31}$$

corresponding to the typical time an electron wavepacket takes to travel the system length $L = Ma$ (see Appendix D).

The space-time evolution of the site occupancy induced by the quench is depicted in Fig.5.3 for a ring of $N = 80$ sites ($M = 40$ cells), initially threaded by a magnetic flux $\Phi = \Phi_0/5$, where the w-bond between sites 1 and 80 is cut by the local quench. In the plot, the red (blue) color characterizes a positive (negative) fluctuation $N_{j,s} - 1/2$ from the pre-quench occupancy $1/2$ (white color), and time is expressed in units of τ_g. Panels (b) and (c) refer to the cases of quench from the ring to the trivial and to the topological chain, respectively. After the bond is cut ($t > 0$), we observe in both cases that the site occupancy remains roughly equal to $1/2$ everywhere until a time $\tau_L/2$, which corresponds to the timescale needed by the quench-induced electron waves propagating in opposite directions to meet again and interfere in the middle of the chain, i.e. at the opposite site of the cut bond.

After such time, the two panels feature qualitatively different behaviors. Indeed for a quench to the trivial chain [see Fig.5.3(b)], the fluctuations $N_{j,s} - 1/2$ from the pre-quench occupancy are more pronounced near the center of the chain and occur at times $t \simeq \tau_L(m + 1/2)$ corresponding to half-integer values of the typical time related to the chain length, Eq.(5.31). In contrast, for a quench to the topological chain [Fig.5.3(c)], the largest occupancy fluctuations are observed at the chain edges and dynamically appear for the first time at $t \simeq \tau_L$, and then again at odd integer multiples $(2m + 1)\tau_L$. Note that, at each appearance, the fluctuations take opposite signs at the two boundaries, since the total charge is conserved.

We emphasize that the pre-quench flux Φ is crucial in determining the magnitude of fluctuations from the occupancy value $1/2$, for both quenches to the trivial and to the topological chain. For the quench to the trivial chain this is clearly illustrated in panel (d), which displays the bulk polarization $P_{20} = N_{20,A} - N_{20,B}$, i.e. the polarization of the central cell $j = 20$, for the time range highlighted by the dashed box of panel (b), for various values of the flux Φ through the pre-quench ring. Similarly, for the case of quench to the topological chain, panel (e) shows the edge polarization $P_1 = N_{1,A} - N_{1,B}$, i.e. the polarization of the cell $j = 1$ in the time frame highlighted in panel (c). When

Φ is vanishing or equal to $\Phi = p\Phi_0/2$, with $p \in \mathbb{Z}$, the site occupancy remains locked to $N_{j,s} \equiv 1/2$ at any time.
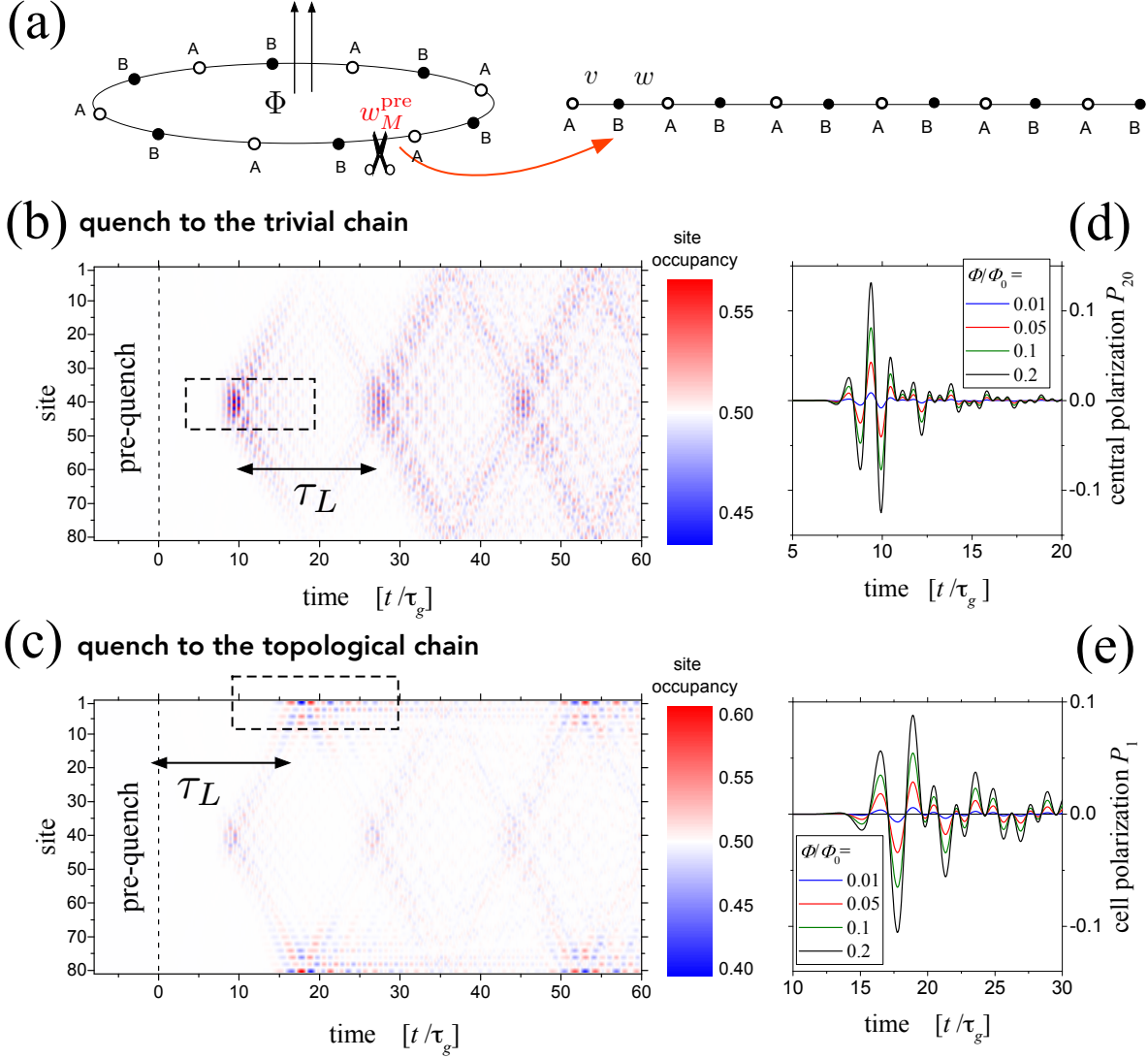
Fig. 5.3 (a) Sketch of a local quench: By cutting a bond w of an SSH ring threaded by a flux Φ, a SSH chain is obtained. Here we used a ring with $N = 80$ sites (i.e. $M = 40$ cells). (b) space-time evolution of the site occupancy $N_{j,s}$ for the case $\Phi = \Phi_0/5$ and $w = 0.7\,|v|$: the cut bond w is weak, so that the post-quench SSH chain is in the trivial phase; (c) space-time evolution of the site occupancy $N_{j,s}$ for the case $\Phi = \Phi_0/5$ and $|v| = 0.7\,|w|$: the cut bond w is strong, so that the post-quench chain is in the topological phase; (d) the central polarization $P_{20} = N_{20A} - N_{20B}$ is plotted in the time frame highlighted in panel (b) by the dashed box, for various values of the pre-quench ring flux Φ; (e) the edge polarization $P_1 = N_{1A} - N_{1B}$ is plotted in the time frame highlighted in panel (c) by the dashed box, for various values of Φ.

Furthermore, for a given flux Φ, the magnitude of the fluctuations also depends on the gap $2\varepsilon_g$ through the ratio $r = \varepsilon_g/\max(|w|, |v|)$. In particular, when $r \to 1$, the model tends to the dimerized limit where the flux plays no role and the fluctuations from occupancy $1/2$ vanish everywhere. In general, both for quenches to the trivial and to the topological phase, a decrease in the value of r implies an increase in the fluctuation magnitude. For instance, for $N = 80$ and $\Phi = \Phi_0/5$, when r is decreased from $r = 0.5$ down to $r = 0.1$, the fluctuation magnitude at the edge sites of the topological chain increases from 14% to 30% of the pre-quench site occupancy value $1/2$. However, when $r \to 0$ the model tends to the gapless metallic tight-binding model, and a difference between topological and trivial phase emerges. Indeed if such limit is taken from the trivial phase ($|v| > |w|$) the magnitude of fluctuations located near the center of the chain [see Fig.5.3(b)] tends to a finite value and survive even in the metallic case. In contrast, when the gap is decreased from the topological phase side ($|v| < |w|$), the magnitude of the fluctuations located at the chain edges [see Fig.5.3(c)] eventually drops to zero for $r < 10^{-2}$ and the effect is completely suppressed in the metallic case $r = 0$, in agreement with the fact that edge states disappear in such a case.
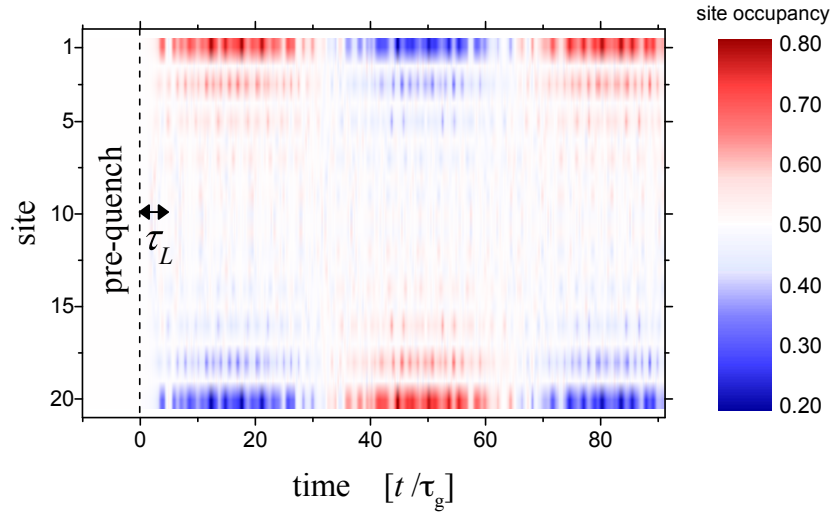
Fig. 5.4 Quench from a ring with flux to a chain in the topological phase: The space-time evolution of the site occupancy $N_{j,s}$ in the case of a small site number ($N = 20$, i.e. $M = 10$ cells). For comparison with a longer chain, the parameters $|v| = 0.7\,|w|$ and $\Phi = \Phi_0/5$ are the same as in Fig.5.3(c).

To conclude this subsection, we analyze how the site occupancy fluctuations induced by the quench depend on the chain length $L = Ma$. The cases analyzed so far in Fig.5.3 correspond to the regime $\tau_L \gg \tau_g$ of a long chain. In this regime the magnitude of site

occupancy fluctuations does not significantly change with the number $N = 2M$ of sites, while the occurrence timescale τ_L does of course depend on M [see Eq.(5.31)]. For fixed values of v and w, when the number of lattice sites is reduced one reaches the regime $\tau_L \sim \tau_g$, where the typical energy separation Δ between the bulk states becomes comparable with the gap $2\varepsilon_g$, so that the very notion of bulk gap becomes somewhat questionable. Yet, two discrete energy levels $\pm\varepsilon^{\text{edge}}$ near $\varepsilon = 0$ are still present in the topological phase. In Fig.5.4 we have plotted the space-time evolution of the site occupancy for a short lattice with $N = 20$ sites (i.e. $M = 10$ cells), when the ring with flux is cut into a chain in the topological phase, keeping all the other parameters unchanged with respect to the case of Fig.5.3(c). The comparison shows two interesting effects of the reduced system size on the dynamics. First, the magnitude of the fluctuations at the edges is bigger in the shorter chain [Fig.5.4] than in the longer chain [Fig.5.3(c)], highlighting the dynamical alternation of excess and depletion of occupancy at the two edges. Second, along with the short timescale τ_L determining the roughly periodic occurrence described above, we observe a second longer period that further modulates the fluctuation magnitude. Such a timescale is associated to the small energy splitting $2\varepsilon^{\text{edge}}$ between the two discrete edge states. Indeed such energy separation increases when reducing the system size and, despite being much smaller than the gap, it becomes visible through this time-dependent modulation.

The local quench cutting the ring thus leads to qualitatively different behaviors in real-space, depending on whether the post-quench chain is in the trivial or in the topological phase. In particular, in the quench to a topological chain the fluctuations of site occupancy are localized at the edges, and alternate in time from excess to depletion. A time-resolved measurement is thus needed to observe such real-space signatures, while a time-average would vanish, just like in any site of the bulk. This is typical of a half-filled system. In Sec.5.5 we shall discuss the case of different filling values.

5.4.2 Chain-to-ring quench

The second possibility to tackle the theorem of Sec.5.3.1 is to break the hypothesis Eq.(5.24). We keep the first hypothesis Eq.(5.23) by choosing as a pre-quench state the ground state of a homogeneous half-filled SSH chain. Then, one can perform a local quench binding the first and last site of the chain, i.e. bringing the tunneling amplitude w_M from $w_M^{\text{pre}} = 0$ to $w_M^{\text{post}} = w$, thereby enclosing the chain into a ring, as illustrated in Fig.5.5(a). If the ring is threaded by a magnetic flux, the quenching Hamiltonian breaks $\mathcal{T}$ and hence $\mathcal{C}$

symmetries, and the condition Eq.(5.24) is violated, opening up the possibility to observe real-space signatures of the quench.
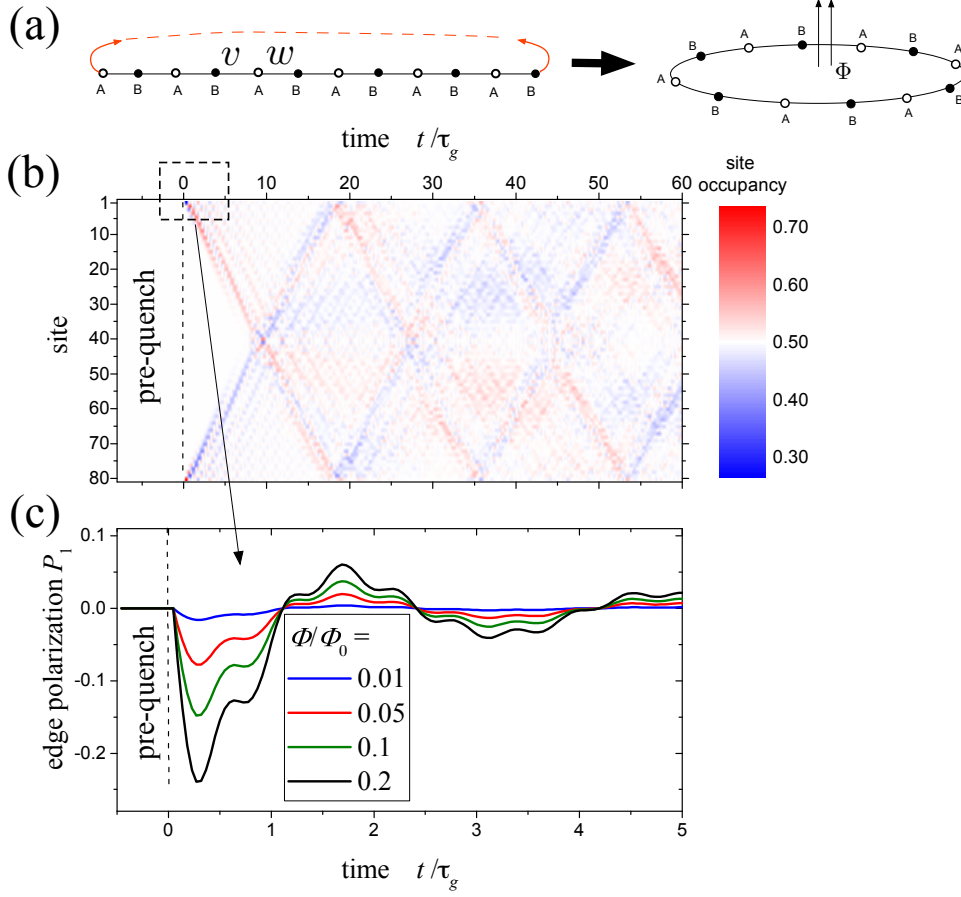
Fig. 5.5 (a) By binding the extremal sites of a SSH chain in the topological phase, the chain is brought into a SSH ring threaded by a flux. Here we have taken $N = 80$ sites (i.e. $M = 40$ cells) and $v = 0.7\,|w|$; (b) space-time evolution of the site occupancy $N_{j,s}$ along the ring, for a flux $\Phi = \Phi_0/5$; (c) time evolution of the edge polarization $P_1 = N_{1A} - N_{1B}$ of the first cell ($j = 1$), for various values of the flux Φ.

Figure 5.5(b) displays the space-time evolution of the site occupancy when the pre-quench state is the ground state of a 80-sites half-filled SSH chain in the topological phase ($|v| < |w|$) and the post-quench ring is threaded by a flux $\Phi = \Phi_0/5$. Note that, although the initial chain is in the topological phase, before the quench ($t < 0$) the site occupancy is locked to $1/2$ everywhere, in agreement with the theorem proven above, and no signature of the edge state emerges in real-space. However, after the quench ($t > 0$), two occupancy fluctuations $N_{j,s} - 1/2$ of opposite signs depart from the bridged link and propagate along the ring in opposite directions, determined by the sign of the flux Φ. When the SSH chain is initially in the trivial phase, such an effect is absent, the occupancy evolution is quite

similar to the case of a ring-to-trivial chain quench already shown in Fig.5.3(b) and is not reported here. The evolution of the edge polarization at the cell $j = 1$ is shown in Fig.5.5(c) in the early time range highlighted by the dashed circle of panel (b), for various flux values. Again the presence of the flux is crucial to observe real-space signatures of the quench.

5.5 Quenches in chiral-symmetry broken models and effects of band filling

In the previous section we have shown how to violate the conditions Eqs.(5.23) and (5.24), while preserving the chiral symmetry $\mathcal{S}$ in the half-filled SSH model. Here we want to explore the dynamical effect of quenches when the chiral symmetry is broken and the filling is not necessarily equal to $1/2$, i.e. beyond the framework where the model can be classified as a topological insulator. As a matter of fact, in a realistic electron model on a bipartite lattice, the chiral symmetry is fragile. A difference δ_j between the on-site energies of A and B sites is likely to exist, leading to an additional Hamiltonian term

$$\hat{\mathcal{H}}_{\chi b} = \sum_j \delta_j(\hat{n}_{j,A} - \hat{n}_{j,B}) \quad , \tag{5.32}$$

which breaks the chiral symmetry because $\mathcal{S}\hat{\mathcal{H}}_{\chi b}\mathcal{S}^{-1} = -\hat{\mathcal{H}}_{\chi b}$[5]. On the one hand, in the absence of chiral symmetry the very topological classification is not well defined since, for instance, one could go from the range $|v| > |w|$ to the range $|v| < |w|$ without closing the gap. A priori, there is no guarantee that the topological states exist at all. On the other hand, numerical analysis shows that, if the values of the δ_j are small compared to the band gap $2\varepsilon_g$, edge states still persist. Specifically, we shall consider a Hamiltonian

$$\hat{\mathcal{H}} = \hat{\mathcal{H}}_{SSH,\chi} + \hat{\mathcal{H}}_{\chi b} \quad , \tag{5.33}$$

where the first term, Eq.(5.2), contains a *chiral disorder* $w_j = w(1+\xi_j d)$ and $v_j = v(1+\eta_j d)$, while the second term, Eq.(5.32), contains a *chiral-breaking disorder* $\delta_j = \zeta_j \max(v,w)d$. Here we have assumed $v, w > 0$ and $\{\xi_j, \eta_j, \zeta_j\}$ denote real random variables uniformly distributed in $[-1/2, +1/2]$ with a disorder strength $d < |v - w|/\max(v, w)$. Note that, although for each disorder realization the chiral symmetry is broken by Eq.(5.33), the

---

[5]The first-quantized version of Eq.(5.32) is $H_{\chi b} = \oplus_{j=1}^M \delta_j(\sigma_z)_j$ and fulfills $SH_{\chi b}S^{-1} = +H_{\chi b}$, causing the breaking of Eq.(5.9).

disorder-averaged Hamiltonian Eq.(5.33) still preserves the chiral symmetry, so that the trivial and topological phases can still be defined in the sense of the average values v and w. While Ref.[387] analyzed the Hamiltonian Eq.(5.33) in the case of local quenches performed over a long quench time ($\tau_q \gg \tau_g$) and at half filling, here we shall focus on the complementary situation of a global quench in the short quench time limit ($\tau_q \ll \tau_g$) and consider also filling values different from a half, which turns out to be important for the effects in real-space.

Let us thus go back to the original problem illustrated in Fig.5.1, and analyze a global quench from the trivial to the topological chain, where now the Hamiltonian Eq.(5.33) includes the chiral-breaking term Eq.(5.32).
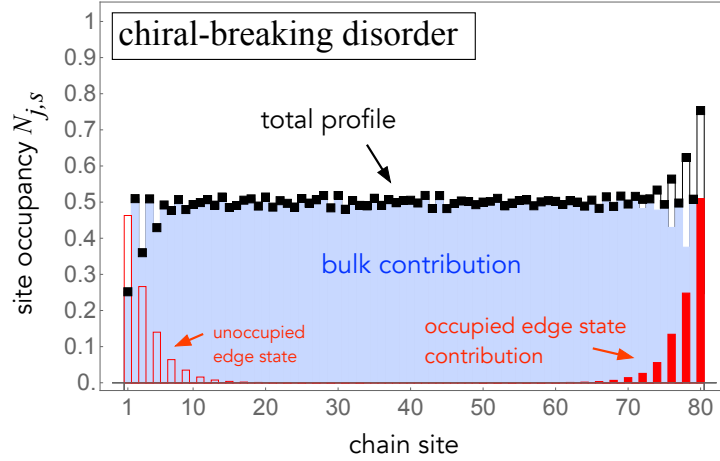
Fig. 5.6 The site occupancy profile of the half-filled chain of model (5.33) in the topological phase. The parameters are the same as in Fig.5.2, with the addition of the chiral-breaking disorder term. Its effect is to localize the two edge state wavefunctions on opposite edges (thick and thin red curves), differently from the case with purely chiral disorder [see Fig.5.2(b)]. The contribution of all occupied bulk states is described by the blue curve. The total site occupancy profile, depicted by the thick solid black curve, exhibits a peak at one edge and a depletion at the other edge.

5.5.1   The case of half-filling

At first, one might even expect that $\hat{\mathcal{H}}_{\chi b}$ may favor the appearance of the edge states already at half-filling. Indeed without such term Eq.(5.32) the site occupancy would always remain strictly locked to 1/2, due to the theorem proven in Sec.5.3.1. In contrast, because the term (5.32) also breaks the charge conjugation symmetry, $\mathcal{C}\hat{\mathcal{H}}_{\chi b}\mathcal{C}^{-1} = -\hat{\mathcal{H}}_{\chi b}$, the hypotheses of the theorem are violated, opening up the possibility to observe fluctuations of the site occupancy, possibly at the edges. This expectation seems to be confirmed

when analyzing how the edge state wavefunctions are modified by the term $\hat{\mathcal{H}}_{\chi b}$. While in the purely chiral SSH model $\hat{\mathcal{H}}_{SSH,\chi}$ each wavefunction is localized on *both* edges even in the presence of *chiral disorder* $\{v_j, w_j\}$ [see Fig.5.2], the addition of the chiral-breaking disorder $\hat{\mathcal{H}}_{\chi b}$ localizes each discrete state of the Hamiltonian (5.33) only on *one single* edge of the chain, as shown by the red curves of Fig.5.6. This is the hallmark of the break-up of the topological protection. Depending on the specific disorder realization, one of the two edge wavefunctions is energetically slightly more favoured than the other, so that the ground state of the half-filled topological chain with chiral-breaking disorder exhibits a site occupancy with an enhancement at one edge, a depletion on the other edge and a value roughly equal to $1/2$ in the bulk [see black curve of Fig.5.6]. In principle, such real-space signature of the edge state should appear by performing an infinitely slow quench from the trivial to the topological chain, where the pre-quench trivial ground state should evolve into the post-quench topological ground state. However, if the chiral-breaking disorder term is weak, the energy separation between the two localized states is very small. In practice, at half filling, any finite temperature in the pre-quench state leads the post-quench state to exhibit only *half-occupancy* of *both* discrete states, quite similarly to what happens in the chiral SSH model $\hat{\mathcal{H}}_{\chi b}$.

The same effect occurs when the duration of the quench is short, as shown in Fig.5.7(a), which illustrates the space-time evolution of the site occupancy of a 80-sites chain that is suddenly quenched from the ground state of the trivial phase ($w^{\mathrm{pre}} = 0.7 v^{\mathrm{pre}}$) to the topological phase ($w^{\mathrm{post}} = v^{\mathrm{pre}}$ and $v^{\mathrm{post}} = w^{\mathrm{pre}}$), for given pre-quench and post-quench realizations of chiral and chiral-breaking disorder with strength $d = 0.1$. Due to the chiral-breaking term Eq.(5.32), static deviations from the site occupancy $1/2$ are present even before the quench, while after the quench these deviations fluctuate in time as well. In Fig.5.7(b), the corresponding edge polarization $P_1 = N_{1,A} - N_{1,B}$ (black curve) is compared to the polarization at the central chain cell $P_{20} = N_{20,A} - N_{20,B}$ (red curve). As one can see, fluctuations do have larger amplitudes at the chain edges than in the chain bulk. However, at each edge, the site occupancy experiences an alternation of depletion and excess [blue and red colors in panel (a)], just like for the quenches preserving the chiral symmetry discussed above [see e.g. Fig.5.3(b) or Fig.5.4]. This quantitatively shows that the chiral-breaking term does not really improve the observability of real-space effects of the quench. In particular, the time-average of the fluctuations at the edge and in the bulk is essentially the same, as highlighted by the arrows in Fig.5.7(b).

In energy-space, however, the effects of the quench are seizable. Indeed the energy distribution of the post-quench Hamiltonian displayed in Fig.5.7(c) strongly differs from

the pre-quench equilibrium one, depicted in red for comparison. In particular, as far as the continuum spectrum is concerned (black symbols), the non-equilibrium distribution that we obtain for the disordered chain-to-chain quench is quite similar to the result obtained for a quench in the clean bulk SSH model analyzed in Ref.[336], and describes the population inversion effect found upon quenching from one phase to the other. This effect can open up the possibility that, when the SSH model is coupled to a radiation[388], a stimulated emission occurs due to transitions from the (almost filled) continuum states near the bottom of the conduction band to the (almost depleted) states near the top of the valence band, with a radiation frequency corresponding to the band gap. Apart from the presence of disorder, the major difference from the ring case arises from the presence of the topological edge states in the post-quench spectrum of the chain, highlighted by the blue symbols. Note that their occupancy is roughly 1/2. On the one hand, this is precisely what disguises these states in the real-space occupancy at the chain edges, as argued above [see Fig.5.7(a)]. On the other hand, differently from a purely bulk SSH system, in a chain quenched to the topological phase the presence of half-occupied discrete levels near $\varepsilon = 0$ causes an additional emission process, characterized by a frequency corresponding to a half of the gap, similar to the phenomenon of a quenched quantum well potential, described in Ch.4 .

5.5.2   Away from half-filling

The results obtained above at half filling ($N_e = M$), where the model (5.33) describes a band insulator, indicate that a quench from a trivial to the topological phase of a chain does lead to the appearance of site occupancy fluctuations that are larger at the chain edges than in the bulk. However, the alternation of depletion and excess yields a vanishing result upon time-average, both at the edges and in the bulk. In the short quench time limit this holds for any temperature of the pre-quench state. We now analyze the effects of a quench in a non half-filled chain, where the number N_e of electrons differs from the number M of lattice cells. Note that in such a case the pre-quench ground state is *metallic*, with an excess of electrons (holes) in the conduction (valence) band for $N_e > M$ ($N_e < M$). At finite temperature this is described by

$$\hat{\boldsymbol{\rho}}^{\mathrm{pre}} = \frac{e^{-\beta(\hat{\mathcal{H}}^{\mathrm{pre}} - \mu \hat{N}_e)}}{\mathrm{Tr}[e^{-\beta(\hat{\mathcal{H}}^{\mathrm{pre}} - \mu \hat{N}_e)}]} \quad , \tag{5.34}$$

where $\hat{N}_e = \sum_{j,s} \hat{n}_{j,s}$ is the total electron number operator and μ the chemical potential. While in the insulator $\mu = 0$, the metallic state is described by $\mu \neq 0$. Moreover, because $\hat{N}_e$ transforms under charge conjugation as $\mathcal{C}\hat{N}_e\mathcal{C}^{-1} = 2M - \hat{N}_e$ the condition (5.23) of the theorem proven in Sec.5.3.1 is violated, opening up the way to observe effects of the quench in real-space.

In principle, if one takes the standard disorder-free SSH model Eq.(5.1), the ideal situation to observe the appearance of the topological edge states is a Gedankenexperiment where the pre-quench state is the ground state of the trivial SSH chain ($v^{\mathrm{pre}} > w^{\mathrm{pre}}$) with exactly $N_e = M + 1$ electrons, with the extra electron lying in the conduction band. By performing an infinitely slow quench ($\tau_q \to \infty$) to the topological chain ($w^{\mathrm{post}} > v^{\mathrm{post}}$), the ground state evolves to the post-quench ground state of the topological chain [see Fig.5.1], where now *both* discrete levels will be occupied, instead of only one like in the half-filled case. The extra electronic level, delocalized on both edges, causes the gradual appearance of peaks localized at the chain edges in the site occupancy profile, over a value of $N_{j,s} = 1/2$ in the bulk of the chain. In practice, however, such ideal conditions are not necessarily easy to realize and/or useful. First, chiral-breaking disorder Eq.(5.32) is typically present as well. Second, in view of technological applications, one typically wants these operations to be performed sufficiently fast. For a finite and possibly short quench time τ_q the post-quench state may differ from the slow-quench scenario. Third, in a metallic system the filling would deviate from $1/2$ not just by one single electron. A finite fraction of the (say) conduction band is occupied and, even in the adiabatic quench limit, these extra conduction states may mask the localized peaks due to the edge states. This is certainly the case, for instance, when the filling approaches 1. The question is thus whether the edge states dynamically appear in real-space when these aspects are taken into account.

For definiteness, we shall analyze the case $N_e > M$, where before the quench a small fraction of the conduction band of the trivial phase is occupied, e.g. $1/10$ of the conduction bandwidth from its band bottom. For the values $w^{\mathrm{pre}} = 0.7 v^{\mathrm{pre}}$ this corresponds to setting the chemical potential to $\mu = 0.44\, v^{\mathrm{pre}}$. Then, we consider a quench to the topological phase of the chain ($w^{\mathrm{post/pre}} = v^{\mathrm{pre/post}}$), in the short quench time limit ($\tau_q \to 0$). The resulting time evolution of the site occupancy is shown in Fig.5.7(d). As one can see, while in the pre-quench state the edge states are absent, after the quench they start to become visible and stable. This can be seen explicitly in Fig.5.7(e), where the polarization of the edge cell (black curve) and of the central chain cell (red curve) are compared.

$N_e{=}M$ (insulating)

$N_e{>}M$ (metallic)
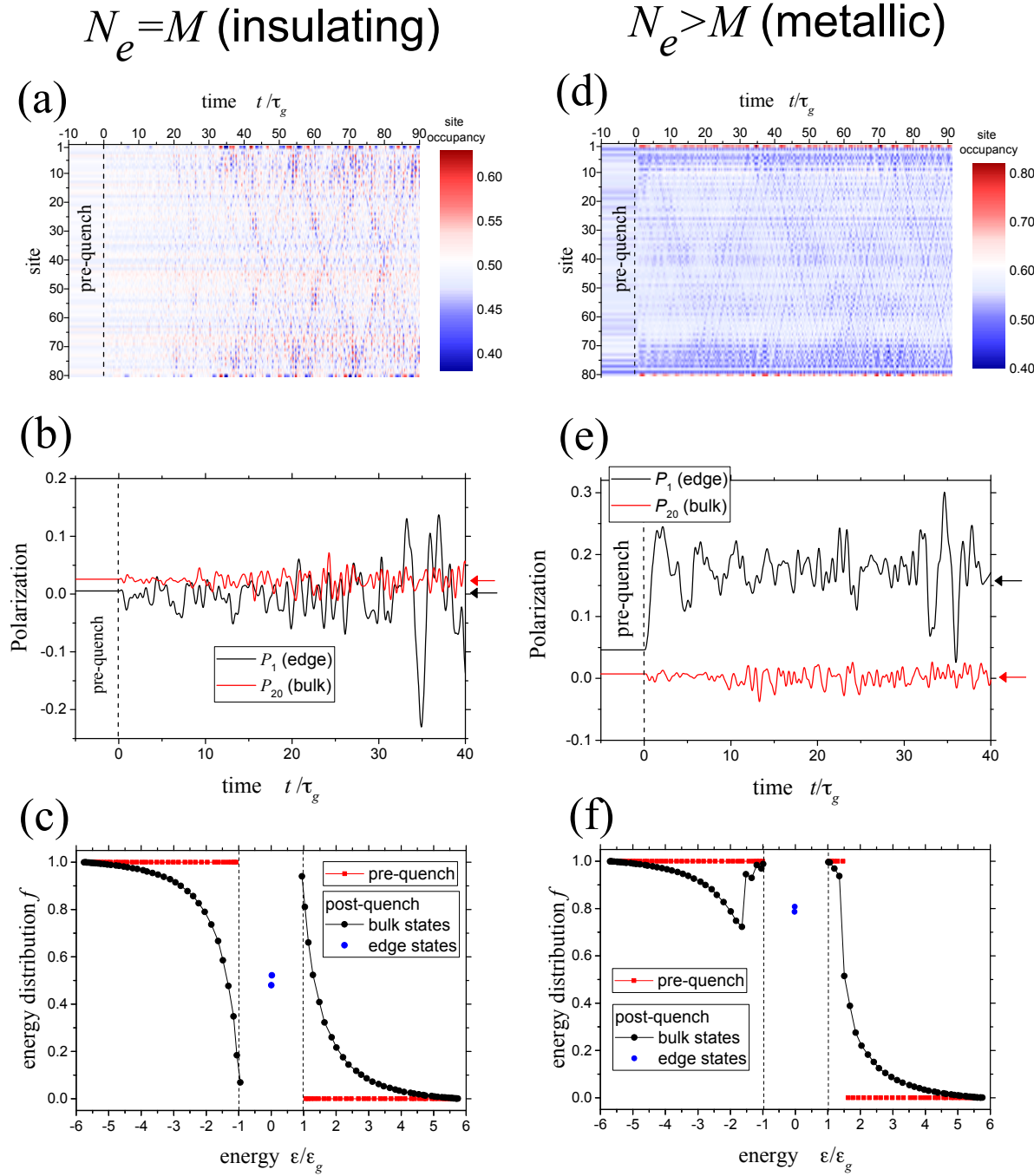
Fig. 5.7 Effects of an instantaneous quench in a 80-sites chain ($M = 40$ cells) from the trivial phase ($w^{\mathrm{pre}} = 0.7v^{\mathrm{pre}}$) to the topological phase ($w^{\mathrm{post}} = v^{\mathrm{pre}}$ and $v^{\mathrm{post}} = w^{\mathrm{pre}}$), for a given realization of both chiral and chiral-breaking disorder with strength $d = 0.1$. Panels (a)-(b)-(c) refer to the case $N_e = M$ ($\mu = 0$, half filling, insulating pre-quench state), while panels (d)-(e)-(f) to the case $N_e > M$ ($\mu = 0.44\,v^{\mathrm{pre}}$, metallic pre-quench state). Panels (a) and (d) describe the space-time evolution of the site occupancy. Panels (b) and (e) display the polarizations P_1 and P_{20} of the edge cell ($j = 1$) and the central cell ($j = 20$). Panels (c) and (f) show the nonequilibrium distribution of the post-quench Hamiltonian (black and blue circles for bulk and edge states, respectively). For comparison, the pre-quench equilibrium distribution is shown in red squares.

Differently from the half-filling case [panel(b)], the edge occupancy oscillates around an average value that is finite and thus differs from the small one obtained in the bulk of the chain, as highlighted by the arrows. Finally Fig.5.7(f) shows the corresponding nonequilibrium post-quench energy distribution. Note that the occupancy of the discrete states near $\varepsilon = 0$ significantly differs from $1/2$. On the one hand, this is the reason for their appearance in real-space at the chain edges. On the other hand, this reduces the occupancy difference from the (almost filled) states near the bottom of the conduction band, thereby reducing the spontaneous emission effect as compared to the half-filling case shown panel (c).

5.6   Discussion and conclusion

In this Chapter we have analyzed how a quantum quench applied to the SSH model (5.2) impacts on observables that are local in real-space, namely the site occupancy and the cell polarization.

In Sec.5.3 we have proven a general theorem ensuring that, when the pre-quench state and the quenching Hamiltonian fulfill the charge conjugation symmetry $\mathcal{C}$, the occupancy of each lattice site remains firmly locked to the value $1/2$, at any time. These symmetries are always satisfied in the customary case of a half-filled SSH chain. Indeed, because $\mathcal{C} = \mathcal{S}\mathcal{T}$ and the chiral symmetry $\mathcal{S}$ is preserved by the SSH model, the breaking of $\mathcal{C}$ requires also the breaking of time-reversal symmetry $\mathcal{T}$, which is not possible for spinless electrons in a chain lattice with OBCs. As a consequence of the proven theorem, a quench from the trivial to the topological phase performed on a SSH chain has no effect whatsoever on the site occupancies. In particular, no signature of the topological edge states appears locally in real-space, independently of the quench protocol, of the temperature of the pre-quench thermal state and also of the presence of chiral disorder. This is strikingly different from what is known to happen in k-space. Indeed when a quench between two topologically different phases is performed, a dynamical quantum phase transition[312] is known to arise, and the momentum distribution exhibits a band population inversion related to a dynamical topological invariant[389, 336, 390]. Our result thus implies that these out of equilibrium phenomena can be detected in real space only through *non-local* quantities, such as correlation functions.

The effects of the quench can become visible in observables that are local in real space only when charge conjugation symmetry is broken. This can be done either remaining

within the framework of the topological insulator characterization, i.e. by preserving the chiral symmetry $\mathcal{S}$ and the half-filling condition, or going out of such framework. The first case requires suitably engineered setups. In particular, in Sec.5.4 we have shown that a *local* quench cutting a SSH ring threaded by a flux into a SSH chain (or viceversa), violates the hypotheses of the above theorem while still remaining in the topological insulator framework. Real-space effects of the quench then become observable and quite distinct dynamical features appear in the two phases. In particular, when the pre-quench ring is cut into a trivial chain the site occupancy fluctuations appear near the center of the chain, while when the ring is cut into a topological chain these fluctuations appear at the chain edges after a time τ_L [see Fig.5.3], and then repeat with a dynamical alternation of excess and depletion at each edge. Such effect at the edges appears even more clearly in a lattice with smaller number of sites [see Fig.5.4]. Conversely, when the local quench bridges a chain to form a ring with flux, the site occupancy fluctuations propagate towards the chain center if the pre-quench chain is in the topological phase[see Fig.5.5], whereas such effect is absent if the chain is in the trivial phase. In all such dynamical effects the presence of the flux Φ threading the ring is crucial. For vanishing flux or for $\Phi = p\Phi_0/2$, where time-reversal and charge conjugation hold, the site occupancy remains locked to the pre-quench value $1/2$.

In Sec.5.5 we have explored the effects of the quench beyond the framework of the topological insulator. By adding a disordered on-site potential term Eq.(5.32) both the chiral and the charge conjugation symmetries get broken. Although for a disorder realization the topological classification is in principle not well defined and the existence of the edge states is not guaranteed, the disorder-averaged Hamiltonian (5.33) still preserves $\mathcal{S}$, and the topological phases can still be considered to hold for weak enough disorder. We have thus analyzed the effects of a quench from a trivial to a topological chain. Our results show that, although the chiral-breaking disorder localizes each edge state wavefunction on one edge only [see Fig.5.6], in practice such term does not lead to any improvement in terms of their observability in real-space as compared to the purely chiral SSH model. In particular, for a half-filled system, while the edge occupancy exhibits much larger fluctuations than the bulk, its time average is roughly equal to the bulk one [see Fig.5.7(b)]. Thus, real-space effects of the quench do exist, but time-resolved measurements are needed to probe the quench-induced appearance of the edge states. In contrast, for filling values different from $1/2$, where the model is slightly metallic, the edge site occupancy fluctuates around a value that is different from the bulk. In this case the dynamical signature of the topological states survive both time-average and the presence of chiral-breaking disorder, and persist even in the short quench time limit [see Fig.5.7(d)-(e)].

In conclusion our analysis points out that, when a topological insulator is driven out of equilibrium by a quantum quench, the presence of additional symmetries (such as charge conjugation or time-reversal) in the quenching Hamiltonian and in the pre-quench state can completely mask the impact of the quench in real-space occupancies, even in customary cases where the energy distributions are typically strongly affected. Only when such additional symmetries are suitably broken, like in the setups and protocols proposed here in Secs. 5.4 and 5.5, real-space effects do emerge in local observables, and exhibit distinct dynamical behavior in the topological and trivial phases. The huge advances in realizing topological models with cold atoms in optical lattices, which nowadays also enable one to effectively implement a Peierls substitution in tunneling amplitudes[391, 392, 393], represent a promising perspective to test the predicted quench effects.

Chapter 6

Nonlinear current and dynamical quantum phase transitions induced by a flux quench

The content of this Chapter is based on the published paper [394]

6.1 Introduction

Many important features of a quantum mechanical system can be gained from the Linear Response Theory (LRT), where the out of equilibrium response of the system to a weak perturbation is encoded in a correlation function evaluated at its equilibrium state[395, 396]. In particular, LRT is used to establish whether a fermionic system is a conductor or an insulator. Operatively this can be done through the following Gedankenexperiment: We first imagine to switch off all sources of extrinsic scattering phenomena, e.g. with a bath or with disorder. Then, we apply a weak uniform electric pulse $E(t) = \mathcal{E}\delta(t)$ and observe the long time behavior of the current in the thermodynamic limit. If a finite persistent current eventually flows, the system is a conductor, otherwise it is an insulator. Explicitly, the LRT current is expressed as $J(t) = (2\pi)^{-1}\mathcal{E}\int d\omega\, \sigma(\omega)e^{-i\omega t}$, and its stationary value $J(+\infty) = D\mathcal{E}$ is determined by the Drude weight D, i.e. the coefficient appearing in the low frequency singular term of the conductivity[397] $\sigma(\omega) = \sigma_{\text{reg}}(\omega) + iD/(\omega + i0^+)$ and characterizing the possibility of a system to sustain ballistic transport. The evaluation of the Drude weight[398] has allowed to identify interaction-induced insulating states in exactly solvable fermionic models, either by a direct investigation, like e.g. in the Hubbard

model[399, 400, 401] , or indirectly through spin models that can be mapped into fermionic ones through the Jordan-Wigner transformation[402, 403, 404, 405, 124, 406]. Moreover, the linear response of systems that are in a stationary out-of-equilibrium state has been investigated [407].

Remarkably, the high control and tunability of cold atom systems in optical lattices[408, 88], together with the ability to realize artificial gauge fields[409, 410], intriguingly suggest that the above Gedankenexperiment could actually be realized in a quantum quench protocol[87, 79, 80, 81]. Consider an isolated fermionic system on a one dimensional (1D) ring, initially prepared in the ground state of a given Hamiltonian $\hat{\mathcal{H}}_i$. Then, suppose that the unitary dynamics is governed by a different final Hamiltonian $\hat{\mathcal{H}}_f$, obtained from the previous one by a sudden change in a magnetic flux piercing the ring. Such sudden variation precisely generates the uniform electric pulse mentioned above.

These experimental advances have also spurred the interest in the dynamics *beyond* LRT, i.e. when the stationary state properties of the system are no longer sufficient to describe its dynamical response. In particular, the dynamics resulting from a flux quench has been analyzed in the case of a single-band model of spinless fermions with a homogeneous nearest neighbour hopping and interaction[411]. Although quantitative discrepancies from the LRT prediction have been numerically found in the gapless phase, the overall qualitative picture relating the existence of a persistent current to a non vanishing Drude weight seems quite robust.

Here we would like instead to highlight qualitative differences from LRT predictions emerging after a flux quench in a model of spinless fermions hopping in a *dimerized* ring lattice. Specifically, we shall focus on the Su-Schrieffer-Heeger(SSH) model[372, 373], recently realized in optical lattices[165, 377, 378]. As already discussed in the previous Chapter, such model is gapped even without interactions and, at half filling, describes a two-band (topological) insulator[375, 376]. By quenching the initial flux to zero and by analyzing the resulting dynamics, we find two main results. First, while LRT predicts a vanishing Drude weight and a vanishing current[397], the flux quench does lead to a persistent current flowing along the ring, which is thus a signature of non-linear effects. Second, if the initial flux exceeds a critical value (dependent on the dimerization strength) dynamical quantum phase transitions (DQPTs)[312] occur. Notably, while a quench performed across the two different topological phases of the SSH model is known to give rise to DQPTs[389], the DQPTs we find occur even if the quench is performed within the same topological phase.

We emphasize that the effects predicted here are intrinsically ascribed to the dimerization and arise even without interaction, in sharp contrast with the customary single-band tight-binding model with homogeneous hopping, where interaction is needed to observe any non trivial dynamical effect of the flux-quench[411]. Here, dimerization provides an intrinsically spinorial nature to the Hamiltonian and to its eigenstates, implying that the current operator is not a constant of motion even without interaction. Furthermore, in the single band model the eigenstates of the Hamiltonian are uniquely determined by their (quasi)-momenta and do not depend on the flux, while in the dimerized case the eigenstates exhibit a non-trivial dependence on the flux. Finally, it is the spinorial nature, which is thus absent in the single-band tight-binding model, that leads to the DQPTs.

This Chapter is organized as follows. In Sec.6.2 we present the model and describe the flux quench dynamics of a two-band model. In Sec.6.3 we derive the expression of the persistent current and show that, while in the limit of vanishing dimerization the LRT captures the metallic behavior, in the presence of dimerization the persistent current flows despite the LRT predicts a vanishing Drude weight and an insulating behavior. In Sec.6.4 we then analyze the DQPTs induced by the dimerization. Finally, in Sec.6.5 we discuss our results and draw our conclusions.

6.2 Model and state evolution

6.2.1 The SSH model

As mentioned in the Introduction, in this Chapter we take as a reference system the Su-Schrieffer-Heeger (SSH) model[372, 373] in a 1D ring geometry pierced by a magnetic flux. Since the model was already described in Ch.5 and App.D, here below we briefly recall a few aspects that are needed to our analysis. The SSH Hamiltonian in real space can be written as [see Eq.(5.1)]

$$\hat{\mathcal{H}}[\phi] = v \sum_{j=1}^{M} \left(e^{i\phi} \hat{c}_{jA}^{\dagger} \hat{c}_{jB} + r e^{i\phi} \hat{c}_{jB}^{\dagger} \hat{c}_{j+1A} + \text{H. c.} \right), \tag{6.1}$$

where M denotes the number of cells, containing two sites A and B each, v is a real positive hopping amplitude, $r \geq 0$ is the dimerization parameter, and $\hat{c}_{j\alpha}^{\dagger}$ creates a spinless fermion in the site $\alpha = A, B$ of the j-th cell. Denoting by Φ the total magnetic flux threading the ring, we adopt the gauge where the phase related to its vector potential[384, 385], denoted by ϕ in Eq.(6.1), is uniform along the ring links, so that $2M\phi = 2\pi(\Phi/\Phi_0)$,

where $\Phi_0 = h/e$ is the elementary flux quantum. We are interested in the thermodynamic limit $M \to +\infty$ with a finite flux per unit cell Φ/M.

In Eq.(6.1) we assume periodic boundary conditions (PBCs), so that the k wavevectors are quantized (also in the presence of flux) as $ka = 2\pi\, n/M$, where $n \in \{-\lfloor M/2 \rfloor, \dots, \lfloor (M-1)/2 \rfloor\}$ and a denotes the size of the unit cell. The SSH Hamiltonian is thus rewritten in momentum space as

$$\hat{\mathcal{H}}[\phi] = \sum_{ka=-\pi}^{\pi} (\hat{c}_{kA}^\dagger, \hat{c}_{kB}^\dagger)\, \mathbf{d}(k,\phi) \cdot \boldsymbol{\sigma} \begin{pmatrix} \hat{c}_{kA} \\ \hat{c}_{kB} \end{pmatrix} \tag{6.2}$$

where

$$\mathbf{d}(k,\phi) = v(\cos\phi + r\cos(ka+\phi), -\sin\phi + r\sin(ka+\phi), 0) \tag{6.3}$$

and $\boldsymbol{\sigma} = (\sigma_x, \sigma_y, \sigma_z)$ are Pauli matrices acting on the sublattice degree of freedom. The spectrum of single particle eigenvalues consists of two symmetric energy bands $\varepsilon_\pm(k,\phi) = \pm v\epsilon(k,\phi)$, where

$$\epsilon(k,\phi) = \sqrt{1 + r^2 + 2r\cos(ka+2\phi)} \quad . \tag{6.4}$$
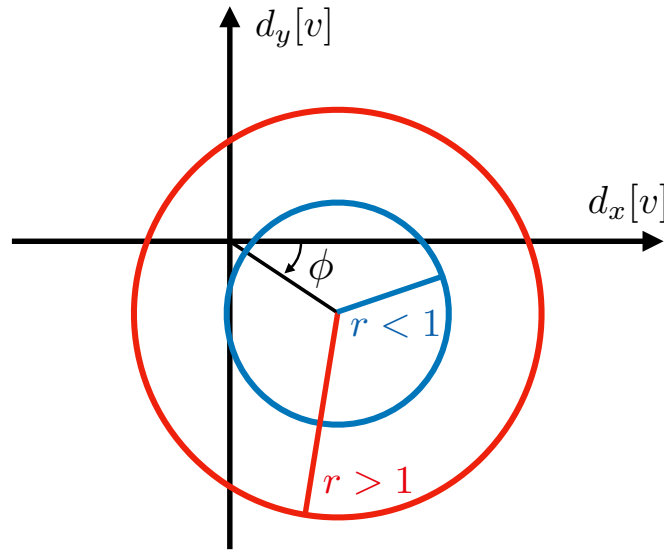
Fig. 6.1 The closed loops traced by the $\mathbf{d}(k,\phi)$ vector Eq.(6.3) as a function of k, for a given value of ϕ and for two different dimerization ratios, namely $r < 1$ in red and $r > 1$ in blue. The blue circle, corresponding to the topological phase $r > 1$, winds once around the origin, while the red circle, associated to the topologically trivial phase $r < 1$, has a vanishing winding.

The two topologically distinct phases [375] are identified by $r \lessgtr 1$, with $r = 1$ identifying the non-dimerized gapless case, see Fig.6.1. The density matrices of the single

particle eigenstates, in the $\{|kA\rangle, |kB\rangle\}$ basis, are given by

$$\rho_\pm(k, \phi) = \frac{1}{2}\left(\sigma_0 \pm \hat{\mathbf{d}}(k, \phi) \cdot \boldsymbol{\sigma}\right) \tag{6.5}$$

where σ_0 is the 2×2 identity matrix, and $\hat{\mathbf{d}}(k, \phi) = \mathbf{d}(k, \phi)/|\mathbf{d}(k, \phi)|$ is a unit vector.

Notably, in the presence of a magnetic flux ($\phi \neq 0$), the energy spectrum (6.4) depends on the wavevector k and on the flux phase ϕ only though the combination $ka + 2\phi$, whereas the Hamiltonian (6.2) and its eigenstates (6.5) depend on *both* these quantities separately. This is due to the dimerization. Indeed, in the limit $r \to 1$ of vanishing dimerization, in the Hamiltonian (6.2) one has $\mathbf{d}(k, \phi) \cdot \boldsymbol{\sigma} = 2v \cos(ka/2 + \phi)(\sigma_x \cos(ka/2) + \sigma_y \sin(ka/2))$, and the dependence on the flux phase reduces to a mere multiplicative factor. In this case the single particle eigenstates become independent of ϕ.

6.2.2   State evolution upon a flux quench

Let us suppose that the system is initially prepared in the insulating ground state of the half filled SSH model with an initial flux phase value ϕ_i, corresponding to a completely filled lower band $\varepsilon_-(k, \phi_i)$. The k-th component of the single particle density matrix at $t = 0$ can thus be written in the $\{|kA\rangle, |kB\rangle\}$ basis as $\rho_i(k) = \left[\sigma_0 - \hat{\mathbf{d}}_i(k) \cdot \boldsymbol{\sigma}\right]/2$, where $\hat{\mathbf{d}}_i(k) = \hat{\mathbf{d}}(k, \phi_i)$. Then, the magnetic flux is suddenly switched off and the initial state evolves according to the final Hamiltonian $\hat{\mathcal{H}}_f$ characterized in Eq.(6.2) by $\hat{\mathbf{d}}_f(k) = \hat{\mathbf{d}}(k, \phi = 0)$.

Since the k modes do not couple in the quench process, the Liouville-Von Neumann equation can be easily integrated and the k-th component of the one-body density matrix is uniquely identified, in the $\{|kA\rangle, |kB\rangle\}$ basis, by the time evolving Bloch vector $\hat{\mathbf{d}}(k, t)$ through

$$\rho(k, t) = \frac{1}{2}\left[\sigma_0 - \hat{\mathbf{d}}(k, t) \cdot \boldsymbol{\sigma}\right] \quad . \tag{6.6}$$

Specifically, the Bloch vector precesses around the final direction $\hat{\mathbf{d}}_f(k)$ and can be expressed as the sum of three orthogonal contributions[390]

$$\hat{\mathbf{d}}(k, t) = \mathbf{d}_\parallel(k) + \mathbf{d}_\perp(k) \cos\left[\frac{2\epsilon(k, 0)vt}{\hbar}\right] + \mathbf{d}_\times(k) \sin\left[\frac{2\epsilon(k, 0)vt}{\hbar}\right] \tag{6.7}$$

whose explicit expression can be deduced from the general state evolution in a two-band model (see Appendix E.1) and read

$$\mathbf{d}_\parallel(k) \;\;=\;\; d_\parallel(k, \phi_i)\hat{\mathbf{d}}_f(k) \tag{6.8}$$

$$\mathbf{d}_\perp(k) \;\;=\;\; d_\perp(k, \phi_i)\mathbf{R}_z[\hat{\mathbf{d}}_f(k)] \tag{6.9}$$

$$\mathbf{d}_\times(k) \;\;=\;\; d_\perp(k, \phi_i)(-\mathbf{e}_z) \quad . \tag{6.10}$$

Here

$$\mathbf{R}_z = \begin{pmatrix} 0 & 1 & 0 \\ -1 & 0 & 0 \\ 0 & 0 & 1 \end{pmatrix} \tag{6.11}$$

is a matrix describing a rotation by $-\pi/2$ around the z-axis identified by the unit vector $\mathbf{e}_z$ and orthogonal to the $\mathbf{d}_i$-$\mathbf{d}_f$ plane, while

$$d_\parallel(k, \phi_i) \;\;=\;\; \frac{(1+r^2)\cos\phi_i + 2r\cos(ka+\phi_i)}{\epsilon(k, \phi_i)\epsilon(k, 0)} \tag{6.12}$$

$$d_\perp(k, \phi_i) \;\;=\;\; \frac{(1-r^2)\sin\phi_i}{\epsilon(k, \phi_i)\epsilon(k, 0)} \quad . \tag{6.13}$$

As a last remark we notice that, in the limit $r \to 1$ of vanishing dimerization, the dynamics in Eq.(6.7) becomes trivial, since $d_\perp(k, \phi_i) = 0$ and $d_\parallel(k, \phi) = \mathrm{sign}[\cos(ka/2+\phi_i)\cos(ka/2)]$. Indeed without dimerization the initial state is an eigenstate of $\hat{\mathcal{H}}_f$ and its density matrix does not evolve with time.

6.3 Current

Let us now investigate the dynamical behavior of the particle current generated by the quench. We first note that, because the system is bipartite, there actually exist two types of currents, namely inter-cell and to intra-cell current operators. Their explicit expression straightforwardly stems from the continuity equation related to the post-quench

Hamiltonian $\hat{\mathcal{H}}_f$ (see Appendix E.2) and reads

$$\hat{J}_j^{inter} = \frac{rv}{\hbar} \left[i\hat{c}_{jB}^\dagger \hat{c}_{j+1A} - i\hat{c}_{j+1A}^\dagger \hat{c}_{jB} \right] \tag{6.14}$$

$$\hat{J}_j^{intra} = \frac{v}{\hbar} \left[i\hat{c}_{jA}^\dagger \hat{c}_{jB} - i\hat{c}_{jB}^\dagger \hat{c}_{jA} \right] \quad . \tag{6.15}$$

Note that, since $\hat{\mathcal{H}}_f$ has a vanishing flux, these operators do not depend on the flux explicitly. Due to the translational invariance of both the initial state and the final Hamiltonian, the expectation values of Eqs.(6.14)-(6.15) are actually independent on the specific cell label j. It is thus worth introducing the space-averaged operators $\hat{J}^l \equiv M^{-1} \sum_{j=1}^M \hat{J}_j^l$ (with $l = inter/intra$), obtaining

$$\hat{J}^l = \frac{1}{M} \sum_{ka=-\pi}^{\pi} (\hat{c}_{kA}^\dagger, \hat{c}_{kB}^\dagger) \, \mathcal{J}_k^l \begin{pmatrix} \hat{c}_{kA} \\ \hat{c}_{kB} \end{pmatrix} \tag{6.16}$$

where

$$\mathcal{J}_k^{inter} = \frac{rv}{\hbar} \left(-\sin(ka)\sigma_x + \cos(ka)\sigma_y \right) \tag{6.17}$$

$$\mathcal{J}_k^{intra} = -\frac{v}{\hbar}\sigma_y \quad . \tag{6.18}$$

Their expectation values $J^l(t) \equiv \langle \hat{J}^l \rangle(t) = M^{-1} \sum_k \text{tr}[\mathcal{J}_k^l \rho(k,t)]$ for $t > 0$ can be written as

$$J^l(t) = J_{dc} + J_{ac}^l(t) \qquad l = inter/intra \tag{6.19}$$

where the first term J_{dc} describes a steady state contribution and is thus the same for inter/intra contributions, while the second term describes the time-dependent fluctuations around it and is different in the two contributions. Explicitly, the *ac*-terms read

$$J_{ac}^{inter}(t) = \frac{rv}{\hbar} \frac{1}{M} \sum_{ka=-\pi}^{\pi} d_\perp(k,\phi_i) \frac{r + \cos(ka)}{\epsilon(k,0)} \cos\left[\frac{2\epsilon(k,0)vt}{\hbar} \right] \tag{6.20}$$

and

$$J_{ac}^{intra}(t) = -\frac{v}{\hbar} \frac{1}{M} \sum_{ka=-\pi}^{\pi} d_\perp(k,\phi_i) \frac{1 + r\cos(ka)}{\epsilon(k,0)} \cos\left[\frac{2\epsilon(k,0)vt}{\hbar} \right] \tag{6.21}$$

whereas the *dc*-current is

$$J_{dc} = \frac{rv}{\hbar} \frac{1}{M} \sum_{ka=-\pi}^{\pi} d_\parallel(k,\phi_i) \frac{\sin(ka)}{\epsilon(k,0)} \tag{6.22}$$

with $d_\parallel(ka, \phi_i)$ and $d_\perp(ka, \phi_i)$ given by Eqs.(6.12)-(6.13). Figure 6.2 displays the time evolution of $J^{intra}(t)$ and $J^{inter}(t)$ in the thermodynamic limit $M^{-1} \sum_k \to (2\pi)^{-1} \int d(ka)$. As one can see, the two currents are in general different and exhibit long living fluctuations, described by the *ac*-terms in Eq.(6.19). However, these fluctuations eventually vanish and both currents converge to the same steady state contribution J_{dc}, highlighted by the green line.
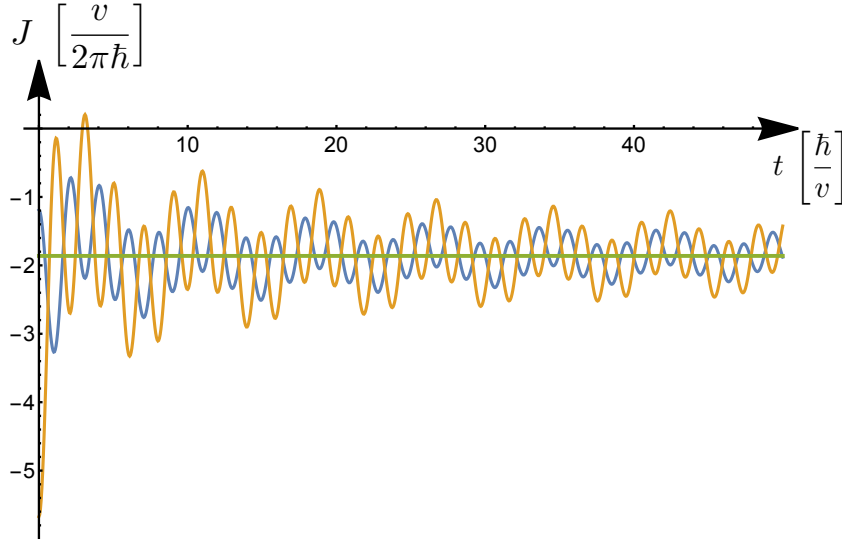
Fig. 6.2 The inter-cell current J^{inter} (blue curve) and the intra-cell current J^{intra} (yellow curve) resulting from a sudden flux quench in the SSH model are plotted as a function of time. At long-time, they both tend to the same stationary contribution J_{dc} (green curve). The time evolution is computed in the thermodynamic limit for $r = 0.6$ and $\phi_i = \pi/2$.

A few comments are in order about such persistent current J_{dc}. First, J_{dc} is essentially different from the current flowing at equilibrium in a mesoscopic ring threaded by a flux, since it is non-vanishing also in the thermodynamic limit, where it acquires the form

$$J_{dc} = \frac{v}{2\pi\hbar} \int_{-\pi}^{\pi} d(ka) \frac{r \sin(ka)}{\epsilon(k,0)} \frac{(1+r^2)\cos\phi_i + 2r\cos(ka+\phi_i)}{\epsilon(k,\phi_i)\epsilon(k,0)} \quad (6.23)$$

Second, J_{dc} cannot be captured by the LRT, which would predict a vanishing persistent current due to a vanishing Drude weight (see Appendix E.3). This can also be seen by inspecting Eq.(6.23) in the limit of weak initial flux $\phi_i \ll 1$, which corresponds to the limit of weak applied electric pulse. Indeed one obtains

$$J_{dc} \approx -\frac{v \, r^2}{\pi\hbar}(1-r^2)^2 \left[\int_{-\pi}^{\pi} d(ka) \frac{\sin^2(ka)}{\epsilon^7(k,0)} \right] \phi_i^3 \quad (6.24)$$

which highlights the non-linear (cubic) response of the insulating SSH ring.

It is now worth comparing the above results with the one of the non-dimerized limit $r \to 1$, where one obtains for the post-quench currents $(t > 0)$

$$J^{inter}(t) = J^{intra}(t) = -\frac{2v}{\pi\hbar}\sin\phi_i \quad . \tag{6.25}$$

Differently from the result obtained for the dimerized case (see Fig.6.2), the current (6.25) is time-independent after the quench[1] and, for a weak field $\phi_i \ll 1$, it exhibits a linear dependence on ϕ_i. One thus recovers the well known finite Drude weight[2] $D = -(e^2/\hbar)\mathtt{v}_F/\pi$, where $\mathtt{v}_F$ is the Fermi velocity, of a non interacting half filled metallic band, as predicted by LRT[412].

The role of dimerization is emphasized in Fig.6.3, where the persistent current (6.23) is depicted as a function of the initial flux, for various values of dimerization r. While at small flux values $\phi_i \ll 1$ the current J_{dc} of the dimerized case $r \neq 1$ is suppressed as compared to the metallic case $r = 1$ (green curve), for finite flux values the two cases exhibit comparable currents.

The origin of the persistent current term J_{dc} can be understood in terms of the out of equilibrium occupancies $n_{f,\pm}$ of the post-quench bands $\varepsilon_{\pm}(k, 0)$ induced by the flux quench. These can be computed, for each k, by projecting the initial state on the post-quench eigenmodes, obtaining time-independent expressions

$$
\begin{aligned}
n_{f,\pm}(k,\phi_i) &= \mathrm{tr}\left\{\rho_i(k)\left(\sigma_0 \pm \hat{\mathbf{d}}_f(k)\cdot\boldsymbol{\sigma}\right)/2\right\} \\
&= \frac{1}{2}(1 \mp \hat{\mathbf{d}}_i(k)\cdot\hat{\mathbf{d}}_f(k)) \\
&= \frac{1}{2} \mp \frac{(1+r^2)\cos\phi_i + 2r\cos(ka+\phi_i)}{2\epsilon(k,\phi_i)\epsilon(k,0)}
\end{aligned} \tag{6.26}
$$

which are plotted as a function of ka/π in Fig.6.4. By comparing Eq.(6.26) with Eq.(6.23), the persistent current can be rewritten as

$$J_{dc} = \frac{1}{2\pi a}\int_{-\pi}^{\pi} d(ka)\,\Delta n_f(k,\phi_i)\,\frac{1}{\hbar}\partial_k\varepsilon_-(ka) \tag{6.27}$$

---

[1]The non-dimerized limit acquires a time dependent current only in the presence of interactions, see Ref.[411].

[2]The expression for D is obtained by re-expressing the phase ϕ_i in terms of the the initial magnetic flux $\Phi_i = \mathcal{E}_i L$ (see Eq.(E.12) in Appendix E.3). Moreover an additional factor e has to be included to obtain the charge current from the particle current J in Eq.(6.25).
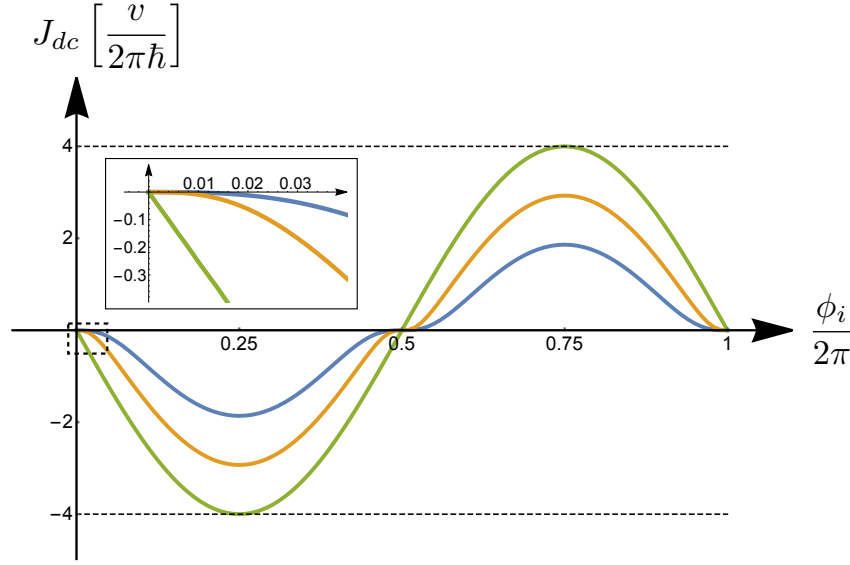
Fig. 6.3 The persistent current J_{dc} induced in the SSH model by quenching the flux to zero is plotted as a function of the initial flux ϕ_i. The blue, yellow and green curves are obtained for different dimerization strengths, namely $r = (0.6, 0.8, 1)$ respectively. For each value of $r \neq 1$ the current does not exhibit a linear term in ϕ_i for $\phi_i \ll 1$. The inset magnifies the behaviour at small fluxes to highlight the difference between linear and non linear response.

where $\frac{1}{\hbar} \partial_k \varepsilon_\pm(k) = \pm \frac{va}{\hbar} \frac{r \sin(ka)}{\epsilon(ka)}$ are the post quench group velocities, and

$$\Delta n_f(k, \phi_i) = n_{f,-}(k, \phi_i) - n_{f,+}(k, \phi_i) = \hat{\mathbf{d}}_i(k) \cdot \hat{\mathbf{d}}_f(k) \tag{6.28}$$

denotes the occupancy difference. Since in Eq.(6.27) the group velocities are odd functions in k, the origin of the non-vanishing persistent current J_{dc} boils down to the lack of even parity in k of the post quench occupancy distributions (6.26) and of their difference Δn_f. Such lack of symmetry, clearly seen in Fig.6.4, arises from the fact that the flux quench impacts on the *phase* of tunneling amplitudes, whereas quenches in the magnitude of the tunneling amplitudes lead to out of equilibrium occupancy distributions that preserve their even parity in k and cannot induce a net current [336].

We conclude this section by two comments. First, when moving away from half filling, the system becomes metallic even in the presence of dimerization. In this case one can show that the system develops a finite Drude weight and that the linear response theory well captures the quench-induced current for small initial fluxes. Nonetheless, there exist some qualitative differences with respect to the non-dimerized metallic case. Indeed, because of dimerization, the current also has a finite *ac*-contribution and, for small filling, it does not increase monotonically in $\phi_i \in [0, \pi/2]$, developing a local minimum for $\phi_i = \pi/2$ instead of
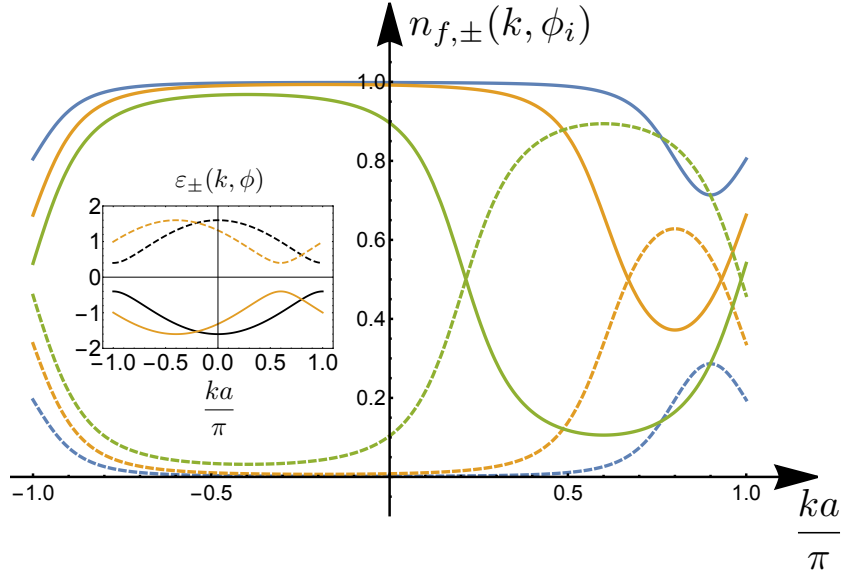
Fig. 6.4 Occupancies of the post-quench bands for different values of the initial flux ϕ_i and a fixed dimerization strength $r = 0.6$. Dashed lines correspond to the upper band, while solid lines correspond to the lower one. The blue, yellow and green colors correspond to $\phi_i = (0.1, 0.2, 0.4)\pi$, respectively. The distributions are not symmetric in $k \leftrightarrow -k$ for any value of the initial flux. As ϕ_i is increased, the upper band becomes more occupied and the lower band gets more depleted. Inset: bands $\varepsilon_\pm(k, \phi)$ of a SSH model pierced by a magnetic flux: Solid and dashed lines describe the lower and the upper bands, respectively. The bands are depicted for $v = 1$, a fixed dimerization strength $r = 0.6$ and for two different values of the flux, namely $\phi = 0.2\pi$ (yellow lines) and $\phi = 0$ (black lines).

a maximum. The second comment is concerned with the flux switching protocol. Here, in analogy to what was done in Ref.[411], we have considered the switching off of the initial flux, so that the latter only appears in the initial state. In the reversed protocol, where the flux is switched on, one obtains a current with opposite sign, as expected, provided that one consistently includes the flux phases related to the vector potential both in the post-quench Hamiltonian and in the current operators (6.14)-(6.15).

6.4 Dynamical Quantum Phase Transitions

Let us now analyze the properties of the Loschmidt amplitude $\mathcal{G}(t) = \langle \psi_0 | e^{-i\hat{\mathcal{H}}_f t/\hbar} | \psi_0 \rangle$, where $|\psi_0\rangle$ is the many-body initial state, while $\hat{\mathcal{H}}_f$ is the final Hamiltonian that governs the time evolution of the system after the quench. With applications in studies on quantum chaos and dephasing [413, 414, 415], the Loschmidt amplitude has a tight relation to the statistics of the work performed through the quench [416, 312, 417, 418]. Equivalently,

it can also be regarded as the generating function of the energy probability distribution encoded in the post quench diagonal ensemble, since $\mathcal{G}(t) = \int dE P(E) e^{-iEt/\hbar}$ and the post-quench diagonal ensemble is described by $P(E) = \sum_n |\langle n|\psi_0\rangle|^2 \delta(E - E_n)$, where E_n and $|n\rangle$ are the many-body eigenvalues and eigenstates of the final Hamiltonian respectively. Moreover, it has been suggested[312] that the Loschmidt amplitude can be interpreted as a dynamical partition function whose zeros, in analogy with the equilibrium case, are identified with DQPTs. The initial belief of a connection between DQPTs and quenches across different equilibrium phase transitions has been proved to be not rigorous [419, 420, 421, 422, 423, 424], and the impact of DQPTs on local observables has been found only in specific cases[312, 425, 426, 427, 428]. Nevertheless, the existence of zeros of $\mathcal{G}(t)$ can be interpreted as a clear signature of quench-induced population inversion[312, 429] and are necessary for the formation of a non trivial dynamical topological order parameter in the time-momentum domain [430, 431]
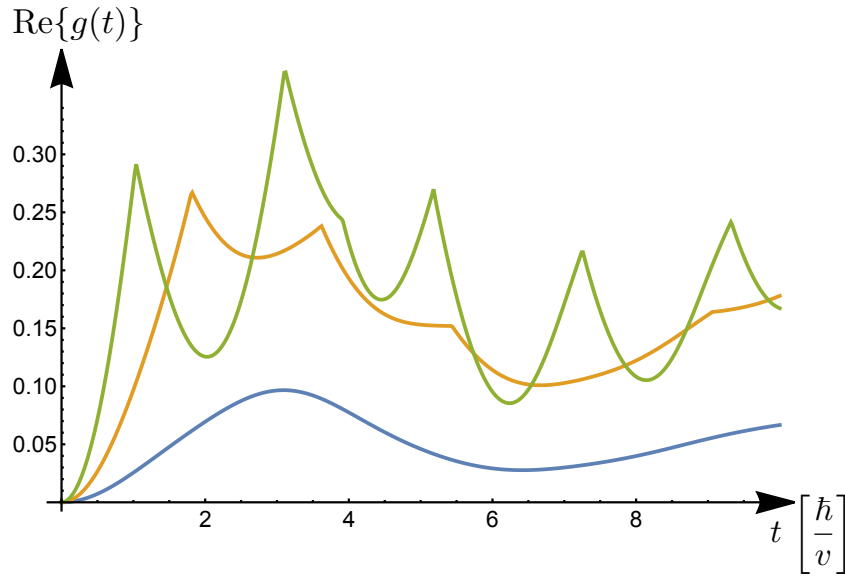
Fig. 6.5 Time evolution of the real part of the dynamical free energy density $g(t)$, for different values of the initial flux ϕ_i at a fixed dimerization strength $r = 0.6$. The blue curve corresponds to an initial flux $\phi_i = 0.1\pi$ lying outside the range identified by Eq.(6.32) and is smooth. The yellow and green curves correspond to flux values that fulfill Eq.(6.32) ($\phi_i = (0.2, 0.4)\pi$, respectively) and exhibit DQPT singularities.

For the present flux quench the Loschmidt amplitude explicitly reads[389]

$$\mathcal{G}(t) = \prod_{-\pi \leq ka \leq \pi} \left[\cos\left(\frac{\epsilon(k,0)vt}{\hbar} \right) + i \left[\hat{\mathbf{d}}_i(k) \cdot \hat{\mathbf{d}}_f(k) \right] \sin\left(\frac{\epsilon(k,0)vt}{\hbar} \right) \right] \quad (6.29)$$

whence the dynamical free energy density $g(t) = -M^{-1}\log[\mathcal{G}(t)]$ in the thermodynamic limit is straightforwardly given by

$$g(t) = -\frac{1}{2\pi}\int_{-\pi}^{\pi} d(ka)\log\left[\cos\left(\frac{\epsilon(k,0)vt}{\hbar}\right) + i[\hat{\mathbf{d}}_i(k)\cdot\hat{\mathbf{d}}_f(k)]\sin\left(\frac{\epsilon(k,0)vt}{\hbar}\right)\right] . \quad (6.30)$$

The argument of the logarithm in Eq.(6.30) may vanish at some critical times if and only if

$$\hat{\mathbf{d}}_i(k)\cdot\hat{\mathbf{d}}_f(k) = 0 \quad . \quad (6.31)$$

Using Eqs.(6.28) and (6.26) in the regime $r \neq 1$, this condition can be satisfied by some $ka \in [-\pi, \pi]$ if and only if

$$|\cos\phi_i| \leq \frac{2r}{1+r^2} \quad . \quad (6.32)$$

In conclusion, for each value of the dimerization strength $r \neq 1$, there exists a range of initial flux values, Eq.(6.32), such that singularities in the dynamical free energy density appear, as shown in Fig.6.5. Recalling Eq.(6.28), we observe that DQPTs appear if and only if the post-quench band occupancies cross at some k, i.e. if there exists a subregion of the Brillouin zone, where the post-quench upper band is more populated then the lower one (band population inversion). This is the case for the yellow and green curves in Figs.6.4 and 6.5. Notably, while a quench across the critical point $r = 1$ is sufficient to induce a DQPT[389], it is not a necessary condition and *accidental* DQPTs can also appear[419, 423]. This is the case here, where the DQPTs show up even if the quench is performed within the same topological phase.

Before concluding this section, a remark is in order about the specific case $r = 1$, which deserves some care. At first, by looking at the limit $r \to 1$ of Eq.(6.32), one could naively expect that DQPTs exist for any value of the initial flux. However, this is not the case since the scalar product $\hat{\mathbf{d}}_i(k)\cdot\hat{\mathbf{d}}_f(k)$ reduces to a pure sign and the argument of the logarithm in Eq.(6.30) can never vanish. Indeed for $r = 1$ the initial state is an (excited) eigenstate of the final Hamiltonian, its dynamics is trivial and $\mathcal{G}(t)$ reduces to a pure oscillating phase[417]. Hence the Loschmidt amplitude can never vanish and the dynamical free energy density is analytic for $t > 0$. Moreover, for $r = 1$ a description in terms of a two band structure is redundant and a proper band population inversion can not be defined without ambiguities.

6.5 Discussion and Conclusions

Our results have been obtained in the case of a sudden flux quench. Here we would like to briefly discuss the effects of a finite switch-off time τ_{sw}. By implementing a time-dependent flux phase $\phi(t) = \phi_i(1 - \text{Erf}(\sqrt{8}t/\tau_{sw}))$ and by numerically integrating the Liouville von-Neumann equation for the density matrix, one can show that the persistent current J_{dc} depends on the ratio τ_{sw}/τ_g, where $\tau_g = \hbar/(2v|1-r|)$ is the timescale associated to the energy gap of the SSH model. In particular, while for $\tau_{sw} \ll \tau_g$ the persistent current J_{dc} is robust, when $\tau_{sw} \simeq \tau_g$ it reduces with respect to the sudden quench value (e.g. to roughly 1/5 for the parameters of Fig.6.2) and it vanishes in the limit $\tau_{sw} \gg \tau_g$ of an adiabatic switch-off. In such limit, a vanishing stationary current is consistent with the recent generalization of LRT to higher order response, which predicts that in a band insulator the response to an adiabatic electric field vanishes to all orders in the field strength[432, 433, 434].

It is worth pointing out the essential difference between the quench induced dynamics in an insulating and in a metallic state. For a metallic state, where the response to a weak electric pulse is linear, the persistent current that eventually flows is independent of the quench protocol and is thus fully encoded in the Drude weight. In striking contrast, when a weak field is applied to an insulating state (like the half-filled SSH model), the response is *non-linear* and does depend on the quench protocol. Thus, while the vanishing higher order generalized Drude weights[432, 433] only capture the behavior of the system in the adiabatic switching limit, for a sufficiently fast switching a persistent current does flow even in an insulator.

In conclusion, in this Chapter we have analyzed the response of a half filled SSH ring to a sudden flux quench, or equivalently, to a sudden pulse of electric field. We have shown that the intrinsically spinorial nature of the problem, due to the dimerization of the hopping amplitudes, induces a non trivial current dynamics even without interactions. In particular, a time-dependent current flows along the ring and eventually reaches a stationary value, despite the insulating nature of the initial state (see Fig.6.2). Such persistent current J_{dc}, which depends cubically on a weak initial flux ϕ_i in the presence of dimerization [see Eq.(6.24) and Fig.6.3], is a clear hallmark of a non-linear dynamics and it is ascribed to the peculiar non-equilibrium occupancy induced by the quench (see Fig.6.4). For suitable dimerization and flux values, a post quench population inversion occurs, which in turn implies the occurrence of DQPTs (see Fig.6.5). Notably, the DQPTs

are present even without closing the gap, i.e. when the quench is performed within the same topological phase.

Chapter 7

Topology in the space-time scaling limit of quantum quench dynamics

The content of this Chapter is based on the preprint [435]

7.1 Introduction

While initially topology has mostly been used to unravel ground state properties of low temperature systems [6, 10, 16, 18, 21, 436], recent advances in experimentally controlling the quantum dynamics of atomic many-body states [437, 179] have triggered the study of topological features far from equilibrium. In particular, within the paradigmatic quantum quench protocol[79], new dynamical topological invariants, which are predicted to characterize the change in topology of the quenched Hamiltonian[389, 430, 438, 439, 390] have been observed[431, 440], and the dynamical robustness of topological features has been addressed, both theoretically[176, 177, 441, 186, 178, 187, 188, 189] and experimentally[190]. Since topological phases may be defined as equivalence classes under local unitary transformations [175], bulk topological properties of a quantum state cannot dynamically change during coherent time evolution generated by a local Hamiltonian[175, 176, 177, 178, 390, 179]. Notwithstanding these fundamental constraints, symmetry protected topological invariants can be fragile, if the underlying symmetries are dynamically broken [188, 189, 190]. In addition, topological invariants are typically defined in the thermodynamic limit (TL), while all experiments deal with finite systems. Hence, the conventional topological characterization is meaningful only for time scales such that $t \ll L/v^f$, where L measures system size, and v^f is a characteristic band velocity of the post quench Hamiltonian
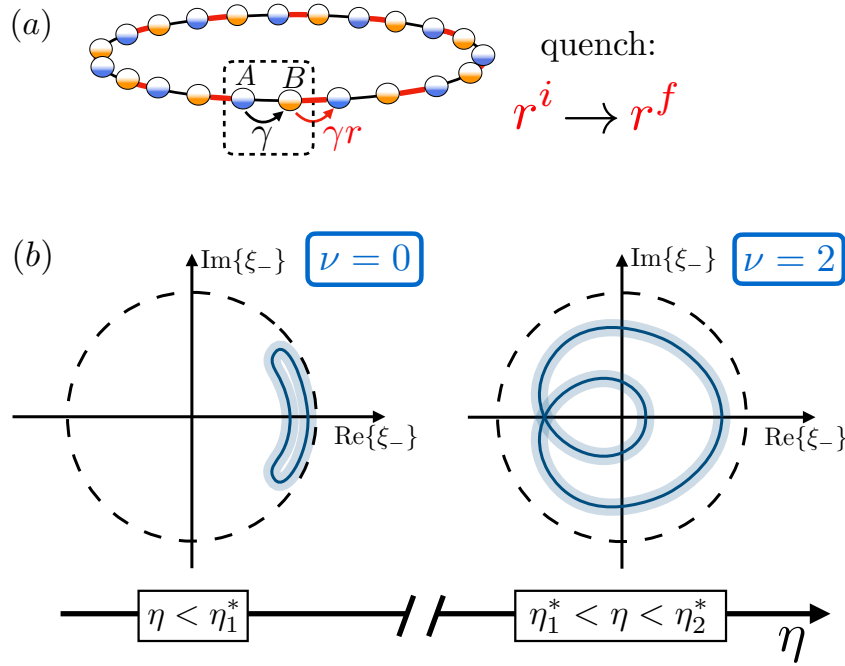
Fig. 7.1 (a) Illustration of a Rice-Mele lattice model on a ring [see Eq. (7.6)], subject to a quench by a sudden variation of the intercell hopping amplitude $\gamma r^i \to \gamma r^f$. (b) Schematic representation of the closed loops formed in the complex plane by the Bloch state overlap ξ_- [see Eq. (7.1)] as a function of quasi-momentum k. Non-trivial loops (right panel) may form in the STSL regime at at critical values η_m^* [see Eq. (7.3)] of the ratio $\eta = 2\pi t/L$. Solid lines represent the 0-th order contribution $\xi_-^{(0)}(k, \eta)$ [see Eq. (7.2)], shallow halos visualize the sub-leading contribution $2\pi\xi_-^{(1)}(k, \eta)/L$. When $\eta < \eta_1^*$ (left panel) the winding number ν vanishes, while for $\eta_1^* < \eta < \eta_2^*$ (right panel) $\nu = 2$. The dashed line depicts the unit circle as a guide to the eye.

[179]. At later times, since an extensively long unitary time evolution is no longer a local transformation, standard topological properties are expected to become ill defined [179] and previous works have thus mostly focused on the $t \ll L/v^f$ regime.

Here, investigating the space-time scaling limit (STSL) of quantum quench dynamics, where both time and system size tend to infinity while their ratio $\eta = 2\pi t/L$ is kept constant, we show how a novel dynamical topological invariant ν naturally arises. To understand its physical implications, we analyze the effect of a constant magnetic flux Φ threading a one dimensional (1D) system with periodic boundary conditions (PBC). Remarkably, while Φ, as a global property, remains invisible in the quench dynamics for sub-extensive times, in the STSL the Berry phase [442, 443, 375] is found to dynamically acquire a staircase behavior (see Fig. 7.2), whose plateau values are topologically quantized as $2\pi\nu\Phi/\Phi_0$, where $\Phi_0 = h/e$ is the flux quantum. Since the limits $t \to +\infty$ and $L \to +\infty$ do not commute, these properties are unique to the STSL regime and cannot be obtained by

applying the long time limit to formulae derived in the standard TL. Yet, we demonstrate that clear signatures of our predictions can be observed in finite systems of moderate size that are within reach of present day quantum simulators.

This Chapter is organized as follows. In Sec.7.2 we present the model and describe the definition of the Berry phase in the STSL of a quenched two-band model. In Sec.7.3 we introduce the dynamical winding number ν and discuss its interplay with a constant magnetic flux. In Sec.7.4 we illustrate the previous results focusing on the Rice-Mele model. In Sec.7.5 we discuss how the standard notion of Wannier functions, as well as the standard relation between current and Berry phase, are modified in the STSL. Finally, in Sec.7.6 we draw our conclusions and briefly outline possible experimental platforms for observing the predicted phenomena.

7.2   Model

We consider a sudden quench in a system of non-interacting spinless fermions hopping in a 1D bipartite lattice with PBC, and we assume the Hamiltonian to be traceless. We measure lengths in units of the lattice spacing a, so that the length of the system L coincides with the number of cells. Thanks to translation invariance we can write the initial/final realizations in reciprocal space as $\hat{\mathcal{H}}^{i/f} = \sum_k \hat{c}^\dagger(k)[\mathbf{d}^{i/f}(k) \cdot \boldsymbol{\sigma}]\hat{c}(k)$. Here $k \in 2\pi n/L$ is a dimensionless quasi-momentum, where $n \in \{-\lfloor L/2 \rfloor, \ldots, \lfloor (L-1)/2 \rfloor\}$, while $\boldsymbol{\sigma}$ is the three dimensional vector of Pauli matrices and $\hat{c}^\dagger(k) = (\hat{c}_A^\dagger(k), \hat{c}_B^\dagger(k))$ is a spinor of fermionic operators, which create spinless fermions with quasi-momentum k in sublattice A/B. All the information about the specific Hamiltonian realizations is thus encoded in the k-dependent three dimensional vectors $\mathbf{d}^{i/f}(k)$. In particular, the initial/final spectra are given by $\epsilon_\pm^{i/f}(k) = \pm|\mathbf{d}^{i/f}(k)|$. Moreover, the time evolved many-body state can be easily reconstructed out of the single particle time dependent Bloch spinors $|u_\pm(k,t)\rangle = e^{-i[\mathbf{d}^f(k)\cdot\boldsymbol{\sigma}]t/\hbar}|u_\pm^i(k)\rangle$, where $|u_\pm^i(k)\rangle$ are the Bloch single particle eigenstates of $\hat{\mathcal{H}}^i$.

We assume $\hat{\mathcal{H}}^i$ to have a finite band gap, initialize the system in its half filled insulating ground state, and follow the time evolution of the Berry phase in its discretized formulation, appropriate for finite system sizes $\varphi_B(t,L) = \sum_k \arg \xi_-(k,t,L)$ [444], where

$$\xi_-(k,t,L) = \langle u_-(k+\delta k,t)|u_-(k,t)\rangle \tag{7.1}$$

and $\delta k = 2\pi/L$. As in the standard continuous formulation, the discrete Berry phase is gauge invariant under $|u_-(k,t)\rangle \rightarrow |u_-^\lambda(k,t)\rangle = e^{i\lambda(k)}|u_-(k,t)\rangle$ and takes quantized values, equal to either 0 or π, when charge conjugation symmetry is present[3, 375] (see App.F for details). Moreover, in the usual TL, i.e. $L \rightarrow +\infty$ while $t \in \mathbb{R}$, it is straightforward to recognize that $\xi_-(k,t,L) = 1 + iA_B(k,t)\delta k + O(L^{-2})$, where $A_B(k,t) = \langle u_-(k,t)|i\partial_k|u_-(k,t)\rangle$ is the time dependent Berry connection, and the standard result $\varphi_B(t) = \int_{-\pi}^{\pi} dk\, A_B(k,t)$ is recovered [375].

However, in the STSL, when $t, L \rightarrow +\infty$ with fixed $\eta = \delta k\, t = 2\pi t/L \in \mathbb{R}$, the function $\xi_-(k,t,L)$ may develop a non-trivial dependence on k and η already to zeroth order in the $1/L$ expansion. Indeed one can write $\xi_-(k,t,L) = \xi_-^{(0)}(k,\eta) + \xi_-^{(1)}(k,\eta,t)\delta k + O(L^{-2})$ where (see App.F.3 for details)

$$\xi_-^{(0)}(k,\eta) = \cos[v^f(k)\eta] - i\,\mathcal{C}(k)\sin[v^f(k)\eta] \quad . \tag{7.2}$$

Here $\mathcal{C}(k) = \hat{\mathbf{d}}^i(k) \cdot \hat{\mathbf{d}}^f(k)$ is the cosine of the k-dependent angle between the initial and final unit vectors, while $v^f(k) = \partial_k \epsilon_+^f(k)/\hbar$ is the post quench band velocity. Then it is straightforward to derive $|\xi_-^{(0)}(k,\eta)| = \sqrt{1 - \{\mathcal{S}(k)\sin[v^f(k)\eta]\}^2}$, where $\mathcal{S}^2(k) = 1 - \mathcal{C}^2(k)$, and we notice that, if $\mathcal{C}(k) = 0$ is satisfied by some k^*, Eq.(7.2) vanishes at equally spaced critical ratios

$$\eta_m^* = \left(\frac{\pi}{2} + (m-1)\pi\right)\frac{1}{v^f(k^*)}, \quad m \in \mathbf{N}_+ \quad . \tag{7.3}$$

Before proceeding, some comments are in order. In the limit $\eta \rightarrow 0$ one has $\xi_-^{(0)}(k,\eta) \rightarrow 1 + O(L^{-1})$ and the standard TL result is recovered. Moreover, at finite η, Eq.(7.2) is reminiscent of the k-dependent contribution to the Loschmidt amplitude, appearing in the context of the dynamical quantum phase transitions (DQPT)[312, 389, 430], discussed in the previous Chapter (see Sec.6.4). Similarly, the condition $\mathcal{C}(k^*) = 0$ leading to a vanishing $\xi_-^{(0)}$ in Eq.(7.2) is formally equivalent to the requirement for observing DQPT[389] [see Eq.(6.31)]. However, we emphasize that, while the k dependent contribution to the Loshmidt amplitude stems from the overlap between the initial and the time evolved Bloch spinor at the same k, the quantity studied here, Eq.(7.1), is the overlap between Bloch spinors that are *both* time evolved and that are computed at *different* quasi-momenta, namely k and $k + \delta k$. It is precisely such a tiny deviation that yields to Eq.(7.2) at $t \sim L/v^f$. Thus, while DQPT occur at *finite* times in a TL system, Eq.(7.2) vanishes at *extensive* critical times $t_m^* = \eta_m^* L/2\pi$, with η_m^* given by Eq.(7.3).

7.3   Winding number in the STSL

We now start to investigate the topological features unique to the STSL regime, i.e. relying on a finite value of η even for arbitrarily large systems. Far away from its critical values, by treating η as a parameter, we can define $\alpha^{(0)}(k;\eta) = \arg \xi^{(0)}_-(k,\eta)$. The function $k \mapsto \alpha^{(0)}(k;\eta)$ from a circle to a circle naturally leads to the definition of a dynamical winding number $\nu(\eta) \in \mathbb{Z}$ through $\alpha^{(0)}(k;\eta) = \tilde{\alpha}^{(0)}(k;\eta) + k\,\nu(\eta)$, where $\tilde{\alpha}^{(0)}(k;\eta)$ is a $\mathbb{R}$-valued smooth periodic function. Remarkably, by contrast to the conventional equilibrium framework [3], this dynamical winding number does not require any symmetry to be properly defined. We can then write the Berry phase in the STSL regime as $\varphi_B(\eta) = \varphi_B^{(0)}(\eta) + \varphi_B^{(1)}(\eta)$, where

$$\varphi_B^{(0)}(\eta) = \frac{L}{2\pi} \int_{-\pi}^{\pi} dk \left[\tilde{\alpha}^{(0)}(k;\eta) + k\,\nu(\eta) \right] \quad , \tag{7.4}$$

while $\varphi_B^{(1)}(\eta)$ is analogous to the usual integral of the Berry connection (see App.F.3 for details). Thus, let us focus on the consequences of the new contribution stemming from a non-trivial $\xi^{(0)}_-$. A priori, $\varphi_B^{(0)}(\eta)$ is of order L and, given that the Berry phase is defined mod 2π, the zeroth order would produce a Berry phase that wildly fluctuates with time. Nonetheless, if $\mathbf{d}^i(k)$ and $\mathbf{d}^f(k)$ have the same parity under $k \leftrightarrow -k$, then $\alpha^{(0)}(k;\eta)$ becomes an odd function of k and the integral in Eq.(7.4) vanishes identically. This condition physically corresponds to a quench that does not generate any stationary current , as discussed in the previous Chapter [see Eq.(6.27)]. However, if we now assume that a finite and constant magnetic flux Φ is present throughout the entire quench dynamics, the quasi-momenta get shifted according to $k \to k + \phi$, where $\phi = \frac{2\pi}{L}\frac{\Phi}{\Phi_0}$. This shift does not affect the integral of the odd periodic part $\tilde{\alpha}^{(0)}(k;\eta)$, which remains vanishing. However, although ϕ is infinitesimal for large L, the shift yields a finite contribution proportional to $\nu(\eta)$, thanks to the factor L in Eq.(7.4). We thus end up with

$$\varphi_B^{(0)}(\eta;\Phi) = 2\pi\nu(\eta)\Phi/\Phi_0 + O(L^{-1}) \quad . \tag{7.5}$$

We can therefore conclude that, in the STSL, the Berry phase develops a non-trivial zeroth order contribution which induces a quantized response to an applied magnetic flux and the quantization is encoded in the dynamical topological invariant $\nu(\eta)$. Note that, since the winding number $\nu(\eta)$ can change only at the critical ratios η_m^* in Eq.(7.3), the topological invariant is stable for *extensive* time windows $\Delta t = L/2v^f(k^*)$. This means that the system undergoes a new kind of dynamical topological phase transition, where

a well defined topological invariant suddenly changes at the extensive critical times t_m^*. Moreover, since the quantized response does not depend on system size, it is remarkable to notice that even a fraction of the elementary flux quantum may yield a detectable signature in the coherent dynamics of a macroscopic quantum system.

7.4 Implementation in the Rice-Mele model

After the above general derivations, we now choose a specific setup to illustrate our results. We consider a sudden quench of the hopping amplitudes in the Rice-Mele model[445], which is defined by

$$\mathbf{d}(k) = \gamma(1 + r\cos k, r\sin k, u) \tag{7.6}$$

and depicted in Fig.7.1(a). Here γ is the reference energy scale, r is the ratio between intercell and intracell hopping, and u is the ratio between the staggered potential on A and B sublattice. We choose a quench such that $\mathcal{C}(k)$ vanishes for some k^*, namely we quench from $r^i = 0.5$ to $r^f = 2$ while keeping $u = -0.1$ constant. It is then straightforward to show that $\nu(\eta)$, which has to be zero for $\eta = 0$, increases by two at each critical ratio η_m^*. Such increase by two units can be easily understood if one recognizes that the condition $\mathcal{C}(k) = 0$ is satisfied by two quasi-momenta $\{k_1^*, k_2^*\}$ which, because of symmetry, are related by $k_1^* = -k_2^*$ and are thus associated to the same critical ratios η_m^*. Concurrently, the closed loop traced by $\xi_-^{(0)}(k, \eta)$ in the complex plane as a function of k touches the origin twice at the critical ratios and the winding increases by two. Far away from η_m^* the winding of $\xi_-^{(0)}(k, \eta)$ is instead a robust topological invariant. Moreover, it coincides with the winding of the whole overlap function Eq.(7.1), since the first order contribution $\xi_-^{(1)}(k, \eta)\delta k$ is suppressed by a factor L^{-1} and it cannot destroy the robustness of the invariant. A comparison between the loops traced by $\xi_-(k, \eta)$ for $\eta < \eta_1^*$ and $\eta_1^* < \eta < \eta_2^*$ is schematically depicted in Fig.7.1(b), where the solid lines denote the finite contribution given by $\xi_-^{(0)}(k, \eta)$, while the shallow halos around them account for the L^{-1} contribution carried by $\xi_-^{(1)}(k, \eta)\delta k$.

We can now fully appreciate the interplay between a finite dynamical winding number and a constant magnetic flux. In Fig.7.2, we plot the difference in Berry phases, with and without flux, $\Delta\varphi_B(\eta) = \varphi_B(\eta; \Phi \neq 0) - \varphi_B(\eta; \Phi = 0)$, for the above specified quench in a finite Rice-Mele lattice. We compute the same quantity for different system sizes while keeping the non-zero value of the magnetic flux always equal to $\Phi = 0.1\Phi_0$. Increasing L at constant η, hence going towards the STSL regime, a staircase profile becomes more and
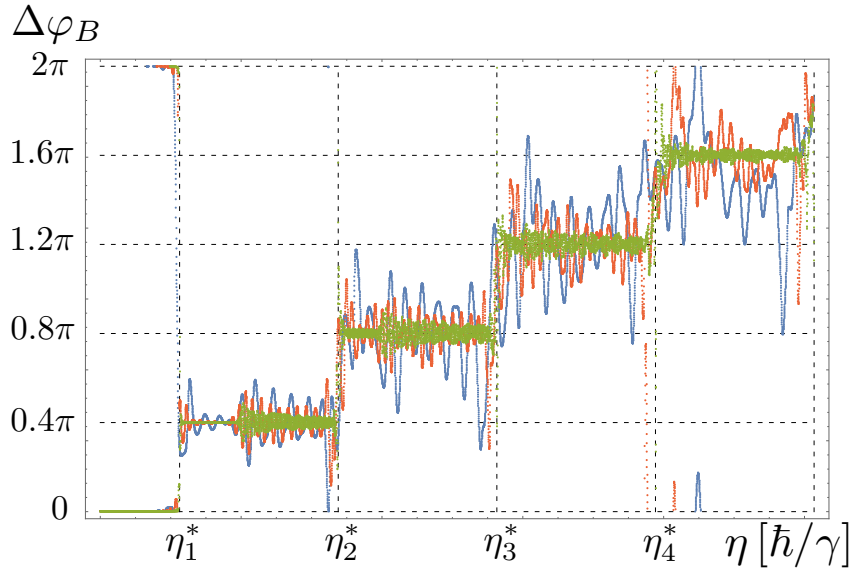
Fig. 7.2 The difference $\Delta\varphi_B$ between the Berry phase with and without flux is plotted as a function of $\eta = 2\pi t/L$ in the STSL regime, after quantum quenches in finite Rice-Mele lattices with PBC [see Eq. (7.6)]. In all quenches, the energy scale γ is fixed to a constant value throughout the entire protocol, together with the ratio of the staggered potential $u = 0.1$. The ratio r of the staggered hopping amplitudes is instead quenched from $r^i = 0.5$ to $r^f = 2$ while the magnetic flux, when present, is constant and equal to $\Phi/\Phi_0 = 0.1$. System sizes are $L = 40$ (blue), $L = 80$ (red), and $L = 400$ (green). The plateaus at 0.4π ($\nu = 2$), 0.8π ($\nu = 4$), 1.2π ($\nu = 6$), and 1.6π ($\nu = 8$) are clearly visible already for $L = 40$, they do not depend on system size and abruptly change at critical ratios η_m^*. The fluctuations are instead system size dependent and are suppressed with increasing L.

more pronounced. The critical ratios at which the jumps occur are given by Eq.(7.3) while the heights of the different plateaus are encoded in Eq.(7.5). The reason is straightforward: The contribution to the Berry phase given by $\Delta\varphi_B^{(1)}(\eta)$ amounts to bounded fluctuations with zero average, which are produced by the slight mismatch between k and $k+\phi$ and are suppressed in the STSL. The contribution carried by $\Delta\varphi_B^{(0)}(\eta)$ instead corresponds to rigid shifts of $4\pi\Phi/\Phi_0$ each time a critical ratio is reached, independent of system size. In the proper STSL a sharp staircase profile is thus recovered.

7.5 Berry phase, Wannier functions and particle current in the STSL

We would like to elaborate on the differences between the TL and the STSL in terms of the Berry phase, the Wannier wavefunctions, and the particle current density. In the standard TL ($\eta \to 0$), the many-body insulating state can be built out of a Slater determinant of exponentially localized Wannier functions[446]. Because a vector potential can be always gauged away for such wavefunctions[447], a constant magnetic flux cannot lead to observable signatures. At the same time, the time derivative of the Berry phase is linked, even out of equilibrium, to the particle current density[188]. In contrast, in the STSL regime, the localization length of the Wannier functions becomes comparable to system size, with a twofold implication. On the one hand, the magnetic flux can no longer be gauged away and can lead to observable signatures, such as the staircase profile depicted in Fig.7.2. On the other hand, the jumps of the Berry phase at the critical ratios η_m^* are not associated to a physical current. Instead one can show that (see App.F.4 for details)

$$
\begin{aligned}
\frac{d}{d\eta}\varphi_B^{(0)}(\eta) &= \frac{L}{2\pi}\int_{-\pi}^{\pi}dk\,\langle u_-^i(k)|\mathcal{J}_{DC}^f(k)|u_-^i(k)\rangle \\
&+ \frac{L}{2\pi}\int_{-\pi}^{\pi}dk\,\mathrm{Re}\left\{\frac{\chi_-^{(0)}(k,\eta)}{\xi_-^{(0)}(k,\eta)}\langle u_+^i(k)|\mathcal{J}_{DC}^f(k)|u_-^i(k)\rangle\right\}
\end{aligned}
\tag{7.7}
$$

where $\mathcal{J}_{dc}^f(k) = v^f(k)\,\hat{\mathbf{d}}^f(k)\cdot\boldsymbol{\sigma}$ is the component of the particle current operator that commutes with the post quench Hamiltonian and describes a DC current, while $\chi_-^{(0)}(k,\eta) = \langle u_-(k+\delta k,t)|u_+(k,t)\rangle + O(L^{-1})$. In the interesting case in which the Berry phase develops a staircase profile, the first integral, which is the expectation value of the DC current and it is the only contribution appearing in the long time limit of a TL system, is vanishing due to symmetry. The jumps are instead produced by the additional contribution in the second

line of Eq.(7.7), which is absent in the standard TL. Such integral does not correspond to the expectation value of a particle current and it rather involves the inter-band elements of the DC current operator.

7.6   Conclusions

In summary, we have shown that intriguing topological features arise in the STSL regime after a quantum quench, when both time and system size are sent to infinity while keeping their ratio finite. In particular, we have rigorously defined a novel dynamical winding number $\nu(\eta)$, which characterizes the many-body state of a 1D two-band model in the STSL regime, see Fig.7.1(b). Notably, its definition does not rely on any specific symmetry, at variance with the customary equilibrium setting. We have shown that the interplay of a non trivial winding and a constant magnetic flux yields a staircase behavior in the time dependent Berry phase, see Fig.7.2, where the different plateaus are quantized in units of $2\pi\nu(\eta)\Phi/\Phi_0$ and the jumps between them occur at well defined critical times given by Eq.(7.3). It is also worth mentioning that this phenomenon can be observed with state of the art experimental techniques. The long coherence time of ultracold atoms in optical lattices[94], which is also important for adiabatic state preparation [448, 449, 450, 451, 452], may also allow to approach the STSL regime experimentally in finite systems. Moreover, given the possibility to generate artificial gauge fields[410] and reconstruct the time dependent Berry phase through quantum state tomography techniques[431, 440, 190], we expect experiments with ultracold atoms, similar to the one described in Ref.[190], to enable observing the onset of a staircase profile as depicted in Fig.7.2. An alternative implementation could be based on quantum walks in photonic platforms where the present quench dynamics can be simulated and the time-dependent Berry phases can be measured [453, 454]. These results provide a starting point for investigating further topological properties unique to the STSL regime, including the study of higher dimensions with richer geometry of Bloch bands, and probing the robustness of the dynamical winding number ν to the breaking of translation invariance and its generalization in the presence of many-body interactions.

Chapter 8

Conclusive remarks

In conclusion, in this Thesis we have investigated several topological and out of equilibrium properties of one dimensional fermionic systems. We shall here summarize the main results and outline some possible future research directions.

In Ch.2 we showed that Majorana-like spin density peaks may emerge in topologically trivial nanowires at the interface between regions with different spin-orbit interactions. Moreover, two different kinds of topologically trivial bound states may emerge in these inhomogeneous platforms. On the one hand, this observation sets an additional obstacle to the experimental detection of Majorana zero modes, ruling out a supposedly unique fingerprint of these exotic quasi-particles. On the other hand it provides a possible handle to experimentally study equilibrium spin currents and suggests new avenues to manipulate charge and spin equilibrium densities by means of the interplay between gate potentials and magnetic fields.

Along these same lines, we discussed in Ch.3 how a Dirac paradox configuration could be realized in suitably gated nanowires. The paradoxical situation emerges when studying an interface between two helical liquids with opposite helicity. A particle impinging from one side of the interface can, apparently, neither be transmitted nor reflected. Interestingly, given the experimental vectorial control on the spin-orbit interaction [231], one can envisage to exploit a Dirac paradox configuration to realize a spin field-effect transistor [455]. Indeed, while helical states cannot be reflected by scalar potentials of by a change in their velocity, a sign reversal of the spin-orbit interaction in a inner portion of the nanowire, controlled by the appropriate gate potential, could potentially suppress the transmission coefficient of this ballistic channel. Further investigations, in view of spintronic applications [456], could thus be carried on along this direction.

As a last application of semiconducting nanowires, we proposed in Ch.4 a protocol to experimentally detect a Generalized Gibbs ensemble (GGE) distribution. By suddenly switching on a local attractive potential, the conducting electrons of a ballistic nanowire are set out of equilibrium, however local observables quickly relax towards the values predicted by a GGE distribution. Such out of equilibrium state, which entails a partially empty bound state lying energetically below a continuum of fully occupied states, can be detected through a characteristic negative peak in the absorption spectrum. Although similar in spirit to pump-probe experiments, this proposal provides a concrete approach to observe a GGE state in a fermionic system, a result still never accomplished. Moreover it neither relies on challenging ultrafast optical experiments nor on highly sophisticated matter wave interferometry with ultracold atoms.

In the subsequent Chapters we focused on the effects of a quench on (topological) lattice models. In Ch.5 we discussed local and global quenches in the Su-Schrieffer-Heeger (SSH) model. We proved that a global quench in a SSH chain does not lead to any detectable signature in real space local observables, due to charge conjugation symmetry. Instead, a local quench to/from a chirally symmetric SSH ring with complex hopping amplitudes, by explicitly breaking time reversal and charge conjugation, reveals the difference between a trivial and a topological chain in terms of site occupancy fluctuations. Furthermore, the dynamical appearance of edge modes in real space is found to be stable when chiral symmetry is explicitly broken too, e.g. by moving away from the half filling condition. As a possible extension of the present work, one might want to analyze the local quench produced by cutting a one dimensional boundary in a translationally invariant Haldane model, i.e. going form a toroidal to a cylindrical geometry. If the model realizes the quantum anomalous Hall phase, two counter propagating chiral currents might dynamically build-up along the two opposite edges of the cylinder, simply as a consequence of the cut.

In Ch.6 we studied how a flux quench can induce a finite stationary current in an insulating system, clarifying a key difference between linear and non-linear responses. While linear response probes the equilibrium properties of a system and does not depend on how fast the flux is switched off, rather only on the flux variation, non linear responses strongly depend on the time scales of the process involved. Therefore, the qualitative behaviour of a metallic system, that does not possess any intrinsic time scale, is always well captured by the linear theory. On the contrary, the behaviour of an insulating system strongly depends on the details of the flux variation. Furthermore, the multiple band structure of an insulator induces a non trivial current dynamics even without interactions. Additionally, a flux quench might generate a band population inversion that leads to

dynamical quantum phase transitions. It is an open question, though, whether the finite stationary current found for the SSH model survives in the presence of particle interactions. On the one hand, a system with both dimerization and interactions is not integrable and one expects it to thermalize. On the other hand, the existence of a single particle gap might reduce the impact of umklapp processes and prevent a fast thermalization.

Finally, in Ch.7, we introduced the space-time scaling limit (STSL) for a quenched system, namely the limit in which time and system size are sent to infinity at a constant ratio. We argued that the STSL cannot be captured by taking the long time limit in a thermodynamic system and we showed that a dynamical topological invariant naturally arises in this out of equilibrium setting, without the need for any symmetry. Interestingly, the time dependent Berry phase is deeply connected to the dynamical topological invariant and realizes, in the STSL, a dynamical analog of the integer quantum Hall conductance. While the latter develops a staircase behaviour as a function of the chemical potential, the former, in the presence of a constant magnetic flux, develops a similar behaviour as a function of time. Further investigations of the STSL might involve higher dimensional models, as well as the robustness of the topological invariant to disorder or interactions. Moreover, given their tight connections to the Berry phase, other quantities, such as Wannier wavefunctions and the quantum geometry tensor, deserve a deeper understanding.

List of publications and preprints

- L. Rossi, F. Dolcini, and F. Rossi, *Majorana-like localized spin density without bound states in topologically trivial spin-orbit coupled nanowires*, Phys. Rev. B **101**, 195421 (2020)

- L. Rossi, F. Dolcini, and F. Rossi, *Confinement versus interface bound states in spin-orbit coupled nanowires*, Eur. Phys. J. Plus **135**, 597 (2020)

- L. Rossi, F. Dolcini, F. Cavaliere, N. T. Ziani, M. Sassetti, and F. Rossi, *Signature of Generalized Gibbs Ensemble deviation from Equilibrium: Negative absorption induced by a local quench*, Entropy **23**(2), 220 (2021)

- L. Gogin, L. Rossi, F. Rossi, and F. Dolcini, *The Dirac paradox in 1+1 dimensions and its realization with spin-orbit coupled nanowires*, New J. Phys. **24**, 053045 (2022)

- L. Rossi, F. Rossi, and F. Dolcini, *Real-space effects of a quench in the Su-Schrieffer-Heeger model and elusive dynamical appearance of the topological edge states*, New J. Phys. **24**, 013011 (2022)

- L. Rossi, and F. Dolcini, *Non-linear current and dynamical quantum phase transitions in the flux-quenched Su- Schrieffer-Heeger model*, Phys. Rev. B **106**, 045410 (2022)

- L. Rossi, J. C. Budich, and F. Dolcini, *Topology in the space-time scaling limit of quantum dynamics*, arXiv:2301.07752

Appendix A

A.1 Calculation for sharp profile interface

In this Appendix we provide details about the calculation for a sharp profile interface (2.14), in the case where the applied magnetic field is orthogonal to the spin-orbit field ($h_z = 0$). In such situation the eigenvalue equation stemming from the Hamiltonian (2.2) at energy E reads

$$
\begin{pmatrix} -\frac{\hbar^2}{2m^*}\partial_x^2 + i\alpha(x)\partial_x + i\frac{\alpha_R - \alpha_L}{2}\delta(x) - h_z & -h_x \\ -h_x & -\frac{\hbar^2}{2m^*}\partial_x^2 - i\alpha(x)\partial_x - i\frac{\alpha_R - \alpha_L}{2}\delta(x) + h_z \end{pmatrix} \begin{pmatrix} \psi_\uparrow^{(E)}(x) \\ \psi_\downarrow^{(E)}(x) \end{pmatrix} =
$$

$$
= E \begin{pmatrix} \psi_\uparrow^{(E)}(x) \\ \psi_\downarrow^{(E)}(x) \end{pmatrix} \tag{A.1}
$$

equipped with the boundary conditions at the interface

$$
\begin{cases} \psi_\uparrow(0^-) = \psi_\uparrow(0^+) \\ \psi_\downarrow(0^-) = \psi_\downarrow(0^+) \\ \partial_x\psi_\uparrow(0^-) = \partial_x\psi_\uparrow(0^+) - i\frac{m^*}{\hbar^2}(\alpha_R - \alpha_L)\psi_\uparrow(0) \\ \partial_x\psi_\downarrow(0^-) = \partial_x\psi_\downarrow(0^+) + i\frac{m^*}{\hbar^2}(\alpha_R - \alpha_L)\psi_\downarrow(0) \end{cases} \tag{A.2}
$$

A few remarks about the boundary conditions (A.2) are in order. First, the discontinuity in the derivative of the wavefunction involves an imaginary unit too, making such boundary conditions intrinsically different from the ones of the well known problem of a particle in a scalar δ-potential. Second, as a consequence of such imaginary unit, it can straightforwardly be shown that, despite the derivative $\partial_x\psi_s$ is discontinuous ($s = \uparrow, \downarrow$), the derivative $\partial_x\rho_s$ of the quantity $\rho_s(x) \equiv \psi_s^*(x)\psi_s(x)$ is *continuous* at the interface $x = 0$. For this

reason, both the density $\rho(x) = \rho_\uparrow + \rho_\downarrow$ [see Eq.(2.19)] and the spin density component $s_z = \rho_\uparrow - \rho_\downarrow$ [see Eq.(2.20)] do not exhibit any cusp in their spatial profile. In contrast, off-diagonal spin density components s_x and s_y, which cannot be expressed in terms of the ρ_s's, do exhibit a cusp due to the discontinuity of the derivative implied by the boundary conditions (A.2). This difference becomes apparent by comparing e.g. panels (b) and (d) in Fig.2.4.

Let us now proceed with the calculation of the energy spectrum. As observed above, we have assumed $\alpha_R > 0$ and $|\alpha_L| \leq |\alpha_R|$ without loss of generality. As a consequence $E_{SO,R}$ is the higher spin-orbit energy, $E_{SO,R} \geq E_{SO,L}$ [see Eq.(2.11)]. By denoting the ratio between the two RSOC values

$$r \equiv \frac{\alpha_L}{\alpha_R} \quad \in [-1, 1] \tag{A.3}$$

one has $E_{SO,L} = r^2 E_{SO,R}$. One can introduce the momentum space Hamiltonian $H_k^\nu = \varepsilon_k^0 - \alpha_\nu k \sigma_z - h_x \sigma_x - h_z \sigma_z$ describing the homogeneous bulk of each side $\nu = R/L$ of the interface, and match the related eigenfunctions with the boundary conditions (A.2).

The energy spectrum characterizing the NW on the right-hand side and on the left-hand side of the interface can be suitably rewritten as

$$E_\pm^R(K) = \frac{K^2}{4E_{SO,R}} \pm \sqrt{\Delta_Z^2 + (K + h_z)^2} \tag{A.4}$$

$$E_\pm^L(K) = \frac{(rK)^2}{4E_{SO,L}} \pm \sqrt{\Delta_Z^2 + (rK + h_z)^2} \tag{A.5}$$

respectively, where $K = \alpha_R k$ has the dimension of an energy, while Δ_Z is the magnetic gap energy Eq.(2.4).

The eigenstates of the momentum Hamiltonian in each side can be written, for arbitrary complex wavevector K, in the following explicit form

$$\text{for } x > 0 \quad \begin{cases} w_-(K) &= \frac{1}{\sqrt{\Delta_Z^2 + |z(K)|^2}} \begin{pmatrix} z(K) \\ \Delta_Z \end{pmatrix} \\[4mm] w_+(K) &= \frac{1}{\sqrt{\Delta_Z^2 + |z(K)|^2}} \begin{pmatrix} -\Delta_Z \\ z(K) \end{pmatrix} \end{cases} \tag{A.6}$$

$$\text{for } x < 0 \quad \begin{cases} w_-(rK) &= \frac{1}{\sqrt{\Delta_Z^2 + |z(rK)|^2}} \begin{pmatrix} z(rK) \\ \Delta_Z \end{pmatrix} \\[4mm] w_+(rK) &= \frac{1}{\sqrt{\Delta_Z^2 + |z(rK)|^2}} \begin{pmatrix} -\Delta_Z \\ z(rK) \end{pmatrix} \end{cases} \tag{A.7}$$

where $z(K) = \sqrt{\Delta_Z^2 + (K + h_z)^2} + (K + h_z)$.

In order to determine the energy E_{bs} of the bound state, the crucial point is to correctly re-express Eqs.(A.6)-(A.7) as a function of the energy E, and then to impose the boundary conditions (A.2). To this purpose, the first step is to invert the dispersion relation in each side $\nu = R/L$. This can be done analytically in two specific cases, namely for $h_z = 0$ or for $h_x = 0$. Here below we shall discuss these two situations, while the general case $h_x, h_z \neq 0$ will be approached numerically as described in App.A.2.

A.1.1 The case $h_z = 0$

In this case the dispersion relation can be inverted yielding four possible K-values

$$K^\nu_{\epsilon, \epsilon'}(E) = \epsilon \sqrt{4E_{SO,R} \left[E + 2E_{SO,\nu} + \epsilon' \sqrt{\Delta_Z^2 + 4E_{SO,\nu}^2 + 4E_{SO,\nu}E} \right]} \tag{A.8}$$

where $\epsilon, \epsilon' = \pm 1$. Note that $K \in \mathbb{C}$, and we have adopted the convention $\sqrt{z} = \sqrt{|z|}e^{i\frac{\phi}{2}}$ for the square root of a complex number $z = |z|e^{i\phi}$ with $\phi \in (-\pi, \pi]$.

One then inserts the four possible values (A.8) of $K^\nu_{\epsilon, \epsilon'}$ into the two eigenvectors Eqs.(A.6)-(A.7). In doing that, some caution must be taken, since for a given energy E and

each side of the interface a seeming redundancy of eigenstates appears. However, only half of the possible eigenstates actually fulfill the equation $H_k\left[K(E)\right]w[K(E)] = E\,w[K(E)]$, as it should be. Their explicit expressions depend on the regime of the involved energy scales E, Δ_Z and $E_{SO,\nu}$, Focusing e.g. on the right hand side of the interface, one can identify three regimes where, for a given energy E lower than the overall minimum of the bulk bands, the corresponding 4 correct eigenspinors are given in Table Eq.(A.9).

Regime 2 differs from regime 3 because in the former wave vectors turn out to be strictly imaginary, while in the latter they exhibit a real part as well. The expression for the eigenspinors on the left hand side, together with their corresponding domain, can be directly obtained from the ones in Table (A.9) by simply replacing $E_{SO,R} \to E_{SO,L}$ and $K^R_{\pm\pm}(E) \to r\,K^L_{\pm\pm}(E)$.

regime		eigenvectors	
1) $\quad \Delta_Z > 4E_{SO,R}$ and $\quad -\dfrac{\Delta_Z^2 + 4E_{SO,R}^2}{4E_{SO,R}} < E < -\Delta_Z$		$w_- \begin{bmatrix} K^R_{\epsilon,+}(E) \\ K^R_{\epsilon,+}(E) \end{bmatrix}$	$\epsilon = \pm 1$
2) $\quad \Delta_Z > 2E_{SO,R}$ and $\quad -\dfrac{\Delta_Z^2 + 4E_{SO,R}^2}{4E_{SO,R}} < E < \min\left[-\dfrac{\Delta_Z^2}{4E_{SO,R}}, -\Delta_Z\right]$		$w_- \left[K^R_{\epsilon,\epsilon'}(E)\right]$	$\epsilon, \epsilon' = \pm 1$
3) $\quad \Delta_Z < 4E_{SO,R}$ and $\quad E < -\dfrac{\Delta_Z^2 + 4E_{SO,R}^2}{4E_{SO,R}}$		$w_- \left[K^R_{\epsilon,\epsilon'}(E)\right]$	$\epsilon, \epsilon' = \pm 1$

$$\text{(A.9)}$$

Once the four eigenspinors w and momenta K are identified, the wavefunction ψ is constructed as a linear superposition of each spinor w multiplied by the related phase factor e^{iKx/α_R}. In doing that, the requirement that ψ does not diverge at $x \to \pm\infty$ reduces the four terms to two in each side. Let thus $w_j^\nu(E)$ and $K_j^\nu(E)$ with $j = 1, 2$ denote such two eigenspinors and momenta related to non-divergent wavefunctions in the region $\nu = R/L$ at energy E in a given regime. Then, the eigenfunction $\psi^{(E)}(x)$ can be written as a linear superposition

$$\psi^{(E)}(x) = \begin{cases} \sum_{j=1}^2 l_j w_j^R(E)\, e^{i\frac{K_j^R(E)}{\alpha_R}x} & x > 0 \\[2mm] \sum_{j=1}^2 r_j w_j^L(E)\, e^{i\frac{K_j^L(E)}{\alpha_R}x} & x < 0 \end{cases}. \qquad \text{(A.10)}$$

Thus, the boundary condition Eq.(A.2) leads to a system of 4 linear equations in 4 unknowns l_1, l_2 r_1 and r_2. Imposing the solvability of the system one obtains an equation for the energy E whose solutions, if they exist, correspond to the energy E_b of the bound state

for given values of Δ_Z, $E_{SO,R}$ and r. The binding energy (2.13) is then straightforwardly obtained.

A.1.2   The case $h_x = 0$

In this case the eigenvalue problem (A.1) decouples into two separate problems for the spin-↑ and spin-↓ components of the wave function, and the magnetic gap energy $\Delta_Z = |h_x|$ vanishes. Accordingly, the eigenvectors (A.6) acquire the simple form

$$w_-(K)|_{\Delta_Z=0} = \begin{pmatrix} 1 \\ 0 \end{pmatrix} \, , \, w_+(K)|_{\Delta_Z=0} = \begin{pmatrix} 0 \\ 1 \end{pmatrix} \tag{A.11}$$

both for $x > 0$ and $x < 0$, while the eigenvalues have a quadratic dependence on K,

$$\begin{cases} E_\uparrow^R(K) = \frac{K^2}{4E_{SO,R}} - (K + h_z) & x > 0 \\ E_\uparrow^L(K) = \frac{(rK)^2}{4E_{SO,L}} - (rK + h_z) & x < 0 \\ E_\downarrow^R(K) = \frac{K^2}{4E_{SO,R}} + (K + h_z) & x > 0 \\ E_\downarrow^L(K) = \frac{(rK)^2}{4E_{SO,L}} + (rK + h_z) & x < 0 \quad . \end{cases} \tag{A.12}$$

Without loss of generality, we can focus on the spin-↑ component of the wave function. The dispersion relation can be easily inverted

$$\begin{cases} K_\pm^R(E) = 2E_{SO,R} \pm \sqrt{(2E_{SO,R})^2 + 4E_{SO,R}(h_z + E)} \\ K_\pm^L(E) = 2rE_{SO,R} \pm \sqrt{(2rE_{SO,R})^2 + 4E_{SO,R}(h_z + E)} \end{cases} \tag{A.13}$$

In order for $K_\pm^\nu(E)$ to exhibit an imaginary part, one has to consider energies in the range $E < -h_z - E_{SO,\nu}$ and the most general eigenfunction of energy E can thus be written as

$$\psi^{(E)}(x) = \begin{cases} a\, e^{i\frac{K_+^R(E)}{\alpha_R}x} + b\, e^{i\frac{K_-^R(E)}{\alpha_R}x} & x > 0 \\ c\, e^{i\frac{K_+^L(E)}{\alpha_R}x} + d\, e^{i\frac{K_-^L(E)}{\alpha_R}x} & x < 0 \end{cases} \tag{A.14}$$

where a, b, c, d are complex coefficients to be determined. The regularity at $x \to \pm\infty$ and the continuity in $x = 0$ reduce the wavefunction to the form

$$\psi^{(E)}(x) = \begin{cases} a\, e^{\frac{iK_+^R(E)x}{\alpha_R}} & x > 0 \\ a\, e^{\frac{iK_-^L(E)x}{\alpha_R}} & x < 0 \end{cases} \tag{A.15}$$

while the matching condition (A.2) on the first derivative in $x = 0$ implies

$$K_-^L(E) = K_+^R(E) - 2E_{SO,R}(1 - r) \tag{A.16}$$

whose only possible solution is:

$$\begin{cases} r^2 = 1 \\ E = -h_z - E_{SO,R} \end{cases} \tag{A.17}$$

However, this corresponds to the lowest energy eigenfunction of the continuum, demonstrating that no bound state exists in such case.

A.2 Diagonalization strategy in the presence of a smoothening length

Here we describe how to numerically approach the problem in the presence of the RSOC profile (2.16) characterized by a finite smoothening length λ_s, and when both perpendicular and parallel magnetic field components $h_x, h_z \neq 0$ are present. To this end, we impose periodic boundary conditions onto the NW, and express the electron spinor field in terms of discretized Fourier components $k = 2\pi n/\Omega$, namely

$$\hat{\Psi}(x) = \sum_k \frac{e^{ikx}}{\sqrt{\Omega}} \begin{pmatrix} \hat{c}_{k\uparrow} \\ \hat{c}_{k\downarrow} \end{pmatrix} \quad , \tag{A.18}$$

where Ω is the (large) NW periodicity length and $\hat{c}_{k,s}$ denotes the Fourier mode operators for spin $s = \uparrow, \downarrow$. The Hamiltonian (2.1) is thus rewritten in terms of the discretized k-basis introduced in Eq. (A.18) as

$$\hat{\mathcal{H}} = \sum_{k_1,k_2} \sum_{s_1,s_2=\uparrow,\downarrow} \hat{c}_{k_1,s_1}^\dagger H_{k_1,s_1;k_2 s_2} \hat{c}_{k_2,s_2} \quad , \tag{A.19}$$

where

$$H_{k_1 s_1; k_2 s_2} = \left[\left(\varepsilon_{k_1}^0 \sigma_0 - \mathbf{h} \cdot \boldsymbol{\sigma} \right) \delta_{k_1, k_2} - \alpha_{k_1 - k_2} \frac{k_1 + k_2}{2} \sigma_z \right]_{s_1, s_2} \quad , \quad (A.20)$$

where α_q is the (discretized) Fourier transform of the RSOC profile $\alpha(x)$. Specifically, taking for α_q the following expression

$$\alpha_q = \begin{cases} \frac{\alpha_L + \alpha_R}{2} & \text{for} \quad q = 0 \\ e^{-\frac{q^2 \lambda_s^2}{32}} \dfrac{\alpha_L \left(e^{\frac{iq\Omega}{2}} - 1 \right) - \alpha_R \left(e^{-\frac{iq\Omega}{2}} - 1 \right)}{iq\Omega} & \text{otherwise} \end{cases} \quad . \quad (A.21)$$

one obtains the (periodic version) of the prototypical profile Eq.(2.16) as Fourier series $\alpha(x) = \sum_q \alpha_q e^{iqx}$.

Then, we have performed an exact numerical diagonalization of the Hamiltonian matrix Eq.(A.20), thereby obtaining diagonalizing operators $\hat{d}_\xi$ defined through $\hat{c}_a = \sum_\xi U_{a,\xi} \hat{d}_\xi$, where $a = (k, s)$ is a compact quantum number notation for the original basis, and U is the matrix of the eigenvectors of Eq.(A.20). Denoting by E_ξ the eigenvalues, the NW Hamiltonian can be rewritten as

$$\hat{\mathcal{H}} = \sum_\xi E_\xi \, \hat{d}_\xi^\dagger \hat{d}_\xi \quad (A.22)$$

Finally, to compute the equilibrium expectation values $\langle \ldots \rangle_\circ$ of the operators (2.17), (2.18), one can re-express the electron field operator $\Psi_s(x)$ with spin component $s = \uparrow, \downarrow$ in terms of the diagonalizing operators $\hat{d}_\xi$'s,

$$\hat{\Psi}_s(x) = \frac{1}{\sqrt{\Omega}} \sum_{k,\xi} e^{ikx} U_{ks,\xi} \, \hat{d}_\xi \quad (A.23)$$

and to exploit $\langle \hat{d}_\xi^\dagger \hat{d}_{\xi'} \rangle_\circ = \delta_{\xi\xi'} f^\circ(E_\xi)$, with $f^\circ(E) = \{ 1 + \exp\left[(E - \mu)/k_B T \right] \}^{-1}$ denoting the Fermi distribution function. For instance, the density Eq.(2.19) is obtained as $\rho(x) = \sum_\xi \rho_\xi(x)$, where

$$\rho_\xi(x) = \frac{1}{\Omega} \sum_{s=\uparrow,\downarrow} \sum_{k_1, k_2} e^{-i(k_1 - k_2)x} \, U_{k_1 s, \xi}^* U_{k_2 s, \xi} \, f^\circ(E_\xi) \quad (A.24)$$

is the contribution arising from the ξ-th eigenstate. In this way, the contribution of each eigenstate (in particular the bound state) can be singled out.

A.3 Calculation of the spin continuity equation

In this Appendix we derive the equation of motion for the spin density operator $\hat{\mathbf{S}}(x) = \hat{\Psi}^\dagger(x)\left[\frac{\hbar}{2}\boldsymbol{\sigma}\right]\hat{\Psi}(x)$. Starting from the Heisenberg equation of motion for the electron field operator $\hat{\Psi}(x,t)$

$$\partial_t \hat{\Psi} = \frac{1}{i\hbar}\left[-\frac{\hbar^2}{2m^*}\partial_x^2\hat{\Psi} - \frac{\sigma_z}{2\hbar}\{\alpha(x), p_x\}\hat{\Psi} - \mathbf{h}\cdot\boldsymbol{\sigma}\,\hat{\Psi}\right] \quad, \tag{A.25}$$

together with the one of its adjoint $\hat{\Psi}^\dagger(x,t)$, the time evolution of the spin density operator reads

$$
\begin{aligned}
\partial_t \hat{\mathbf{S}} = & \frac{\hbar}{2}\Bigg\{-\frac{i\hbar}{2m^*}\left[\left(\partial_x^2\hat{\Psi}^\dagger\right)\boldsymbol{\sigma}\,\hat{\Psi} - \hat{\Psi}^\dagger\boldsymbol{\sigma}\left(\partial_x^2\hat{\Psi}\right)\right] + \frac{i}{2\hbar^2}\hat{\Psi}^\dagger\boldsymbol{\sigma}\,\sigma_z\left[\{\alpha(x),\,p_x\}\hat{\Psi}\right] \\
& +\frac{i}{2\hbar^2}\left[\{\alpha(x),\,p_x\}\hat{\Psi}\right]^\dagger\sigma_z\,\boldsymbol{\sigma}\,\hat{\Psi} + \frac{i}{\hbar}\hat{\Psi}^\dagger[\boldsymbol{\sigma},\mathbf{h}\cdot\boldsymbol{\sigma}]\,\hat{\Psi}\Bigg\} \quad.
\end{aligned}
\tag{A.26}
$$

Exploiting the relations $\boldsymbol{\sigma}\sigma_z = (\{\boldsymbol{\sigma},\sigma_z\} + [\boldsymbol{\sigma},\sigma_z])/2$ and $\sigma_z\boldsymbol{\sigma} = (\{\boldsymbol{\sigma},\sigma_z\} - [\boldsymbol{\sigma},\sigma_z])/2$ we can write

$$
\begin{aligned}
\partial_t \hat{\mathbf{S}} = & \frac{\hbar}{2}\Bigg\{\frac{i\hbar}{2m^*}\partial_x\left[\hat{\Psi}^\dagger\boldsymbol{\sigma}\left(\partial_x\hat{\Psi}\right) - \left(\partial_x\hat{\Psi}^\dagger\right)\boldsymbol{\sigma}\,\hat{\Psi}\right] + \frac{i}{\hbar}\hat{\Psi}^\dagger[\boldsymbol{\sigma},\mathbf{h}\cdot\boldsymbol{\sigma}]\,\hat{\Psi} \\
& +\frac{i}{2\hbar^2}\hat{\Psi}^\dagger\frac{\{\boldsymbol{\sigma},\sigma_z\}}{2}\left[\{\alpha(x),\,p_x\}\hat{\Psi}\right] + \text{H.c.} \\
& +\frac{i}{2\hbar^2}\hat{\Psi}^\dagger\frac{[\boldsymbol{\sigma},\sigma_z]}{2}\left[\{\alpha(x),\,p_x\}\hat{\Psi}\right] + \text{H.c.}\Bigg\} \quad.
\end{aligned}
\tag{A.27}
$$

Then it is straightforward to prove that

$$\frac{i}{2\hbar^2}\hat{\Psi}^\dagger\frac{\{\boldsymbol{\sigma},\sigma_z\}}{2}\left[\{\alpha(x),\,p_x\}\hat{\Psi}\right] + \text{H.c.} = \partial_x\left[\frac{\alpha(x)}{\hbar}\hat{\Psi}^\dagger\frac{\{\boldsymbol{\sigma},\sigma_z\}}{2}\hat{\Psi}\right] \tag{A.28}$$

while

$$\frac{i}{2\hbar^2}\hat{\Psi}^\dagger\frac{[\boldsymbol{\sigma},\sigma_z]}{2}\left[\{\alpha(x),\,p_x\}\hat{\Psi}\right] + \text{H.c.} = \frac{i}{\hbar}\hat{\Psi}^\dagger\frac{[\boldsymbol{\sigma},\boldsymbol{\sigma}\cdot\mathbf{h}^{SO}]}{2}\hat{\Psi} + \text{H.c.} \tag{A.29}$$

where $\mathbf{h}^{SO} = \{\alpha(x), p_x\}/2\hbar(0,\,0,\,1)$ is the spin-orbit field operator (see Eq.(2.23)). Thus, by recalling the definition of the spin current operator Eq.(2.25) and the one of the

magnetic and spin-orbit torques Eqs.(2.21)-(2.22), the spin continuity equation Eq.(2.24) is recovered.

Appendix B

B.1 Derivation of the transfer matrix Eq.(3.28)

In this Appendix we provide details about the derivation of the transfer matrix (3.28), i.e. the most general 4×4 matrix fulfilling the requirements (3.26) and (3.27). We first observe that the former requirement (3.26) straightforwardly stems from Eq.(3.21) and the property $(U_R^\dagger)^{-1} = (U_R^{-1})^\dagger$, which imply that U_R^{-1} fulfills Eq.(3.21) as well. When taking into account Eq.(3.20) and the definition (3.25), the condition Eq.(3.26) follows. Second, we observe that the requirement (3.27) can equivalently be formulated by requiring that M must only involve the combinations $\sigma_\uparrow = (\sigma_0 + \sigma_z)/2$ and $\sigma_\downarrow = (\sigma_0 - \sigma_z)/2$, i.e. M must have the form

$$\mathsf{M} = \mathsf{M}_\uparrow \sigma_\uparrow + \mathsf{M}_\downarrow \sigma_\downarrow \quad , \tag{B.1}$$

where $\mathsf{M}_{\uparrow,\downarrow}$ are 2×2 matrices acting on the massless-massive pseudospin space and fulfilling

$$\mathsf{M}_\sigma^\dagger \tau_z \mathsf{M}_\sigma = -\tau_z \qquad \sigma = \uparrow, \downarrow \tag{B.2}$$

as a consequence of Eq.(3.26) and of the properties $\sigma_{\uparrow,\downarrow}^2 = \sigma_{\uparrow,\downarrow}$ and $\sigma_\uparrow \sigma_\downarrow = [\sigma_\uparrow, \sigma_z] = [\sigma_\downarrow, \sigma_z] = 0$. For each spin sector $\sigma = \uparrow, \downarrow$, the requirement Eq.(B.2) imposed on a generic 2×2 complex matrix

$$\mathsf{M}_\sigma = \begin{pmatrix} a_\sigma & b_\sigma \\ c_\sigma & d_\sigma \end{pmatrix} \tag{B.3}$$

implies that $|c_\sigma|^2 - |a_\sigma|^2 = 1$, $|b_\sigma|^2 - |d_\sigma|^2 = 1$ and $a_\sigma^* b_\sigma = c_\sigma^* d_\sigma$. These conditions straightforwardly imply the following expression

$$\mathsf{M}_\sigma = e^{i\nu_\sigma} \begin{pmatrix} i\beta_\sigma e^{-i\gamma_\sigma} & (1 - i\beta_\sigma)\, e^{i\chi_\sigma} \\ (1 + i\beta_\sigma)\, e^{-i\chi_\sigma} & -i\beta_\sigma e^{i\gamma_\sigma} \end{pmatrix} \quad , \tag{B.4}$$

which also fulfills the properties $M_\sigma^{-1}(\beta_\sigma, \chi_\sigma, \nu_\sigma, \gamma_\sigma) = M_\sigma(\beta_\sigma, \chi_\sigma, -\nu_\sigma, -\gamma_\sigma)$ and $\det(M_\sigma) = -\exp[2i\nu_\sigma]$. Inserting the two independent matrices $M_\uparrow$ and $M_\downarrow$ given in Eq.(B.4) into Eq.(B.1), the transfer matrix M in the $\tau \otimes \sigma$ basis takes the form given in Eq.(3.28).

Finally, an explicit expression can be given for U_L and U_R as well. The requirement (3.20) can always be fulfilled by choosing for U_L the form

$$U_L = \tau_0 \sigma_0 \quad . \tag{B.5}$$

Then, the expression for $U_R = M^{-1}$ following from Eq.(3.25) can straightforwardly be obtained from Eq.(3.28) by exploiting the property $M^{-1}(\boldsymbol{\beta}, \boldsymbol{\chi}, \boldsymbol{\nu}, \boldsymbol{\gamma}) = M(\boldsymbol{\beta}, \boldsymbol{\chi}, -\boldsymbol{\nu}, -\boldsymbol{\gamma})$, where each bold symbols denotes the pair of related parameters, e.g. $\boldsymbol{\beta} = (\beta_\uparrow, \beta_\downarrow)$.

B.2 Details about the NW Hamiltonian and its low energy limit

The Hamiltonian for a NW with RSOC was already described in Sec.2.2. However, for the sake of completeness, we provide here some details that are relevant to Sec.3.4.1. Denoting by Ω the total NW length and re-expressing the field in terms of its Fourier modes $\hat{C}_k = (\hat{c}_{k\uparrow}, \ \hat{c}_{k\downarrow})^T$

$$\begin{pmatrix} \hat{\Phi}_\uparrow(x) \\ \hat{\Phi}_\downarrow(x) \end{pmatrix} = \frac{1}{\sqrt{\Omega}} \sum_k e^{ikx} \begin{pmatrix} \hat{c}_{k\uparrow} \\ \hat{c}_{k\downarrow} \end{pmatrix} \quad , \tag{B.6}$$

the NW Hamiltonian $\hat{\mathcal{H}}_{NW}$ is compactly rewritten in terms of a 2×2 matrix $H_{NW}(k)$, i.e. $\hat{\mathcal{H}}_{NW} = \sum_k \hat{C}_k^\dagger H_{NW}(k)\hat{C}_k$. In turn, this also highlights the energy scales involved in the problem. In particular, the first two terms acquire the form

$$\hat{\mathcal{H}}_{kin} + \hat{\mathcal{H}}_R = \sum_k \hat{C}_k^\dagger \left(\frac{\hbar^2}{2m^*}(k\sigma_0 - s_\alpha k_{SO}\sigma_z)^2 - E_{SO}\sigma_0 \right) \hat{C}_k \tag{B.7}$$

and describe two parabolic spin bands that are lowered by the spin-orbit energy [see Eq.(2.6)] and horizontally shifted by the spin-orbit wavevector Eq.(3.37) with the sign Eq.(3.39) of the RSOC determining whether the shift is positive or negative in k-axis.

Assuming $h_x > 0$ for definiteness, the Zeeman term is rewritten as

$$H_Z = -E_Z \sum_k \hat{C}_k^\dagger \sigma_x \hat{C}_k \quad , \tag{B.8}$$

where E_Z is the Zeeman energy (see eq. 2.4). Summing up Eqs.(B.7) and (B.8) the diagonalization of the resulting $H_{NW}(k)$ is straightforward. Denoting $\varepsilon_k^0 = \hbar^2 k^2 / 2m^*$, the spectrum consists of two energy bands [see Eq.(2.3)]

$$E_\pm(k) = \varepsilon_k^0 \pm \sqrt{E_Z^2 + \alpha^2 k^2} \quad , \tag{B.9}$$

separated at $k = 0$ by a gap $2E_Z$ centered around the midgap energy $E = 0$. The eigenfunctions related to the spectrum (B.9) are $\psi_{k,\pm}(x) = w_{k,\pm} \exp[ikx]/\sqrt{\Omega}$. They describe plane waves with spinors [see Eq.(2.9)]

$$w_{k,-} = \begin{pmatrix} \cos \frac{\theta_k}{2} \\ \\ \sin \frac{\theta_k}{2} \end{pmatrix} \quad w_{k,+} = \begin{pmatrix} -\sin \frac{\theta_k}{2} \\ \\ \cos \frac{\theta_k}{2} \end{pmatrix} , \tag{B.10}$$

whose spin orientation $\mathbf{n}(k) \equiv (\sin \theta_k, 0, \cos \theta_k)$ lies on the xz-plane and depends on the wavevector k, forming with the z-axis an angle $\theta_k \in [0, \pi]$ defined through

$$\begin{cases} \cos \theta_k & = & \dfrac{\alpha k}{\sqrt{E_Z^2 + \alpha^2 k^2}} \\ \\ \sin \theta_k & = & \dfrac{E_Z}{\sqrt{E_Z^2 + \alpha^2 k^2}} \end{cases} \quad . \tag{B.11}$$

Furthermore, for energies $|E| < E_Z$, the model also exhibits evanescent wave solutions $\tilde{\psi}_{\kappa,\pm}(x) = \tilde{w}_{\kappa,\pm} \exp[\kappa x]/\sqrt{\Omega}$. They describe plane waves with spinors

$$\tilde{w}_{\kappa,\pm} = \frac{1}{\sqrt{2}} \begin{pmatrix} \mp \exp\left[\pm i \arctan\left(\alpha\kappa/\sqrt{E_Z^2 - (\alpha\kappa)^2}\right)\right] \\ \\ 1 \end{pmatrix} \tag{B.12}$$

with energy $E_\pm = -\varepsilon_\kappa^0 \pm \sqrt{E_Z^2 - (\alpha\kappa)^2}$. While these solutions are not normalizable in a homogeneous NW, they must be taken into account in the inhomogeneous RSOC problem.

Let us now focus on the regime ($|E| \ll E_Z \ll 2E_{SO}$) and derive an effective low energy NW Hamiltonian.

Expansion near $k = \pm 2k_{SO}$. In the deep Rashba-dominated regime ($E_Z \ll 2E_{SO}$), one finds that, up to $O\big((E_Z/2E_{SO})^2\big)$,

$$
\begin{cases}
E_-(k) \approx 0 \Leftrightarrow k \approx \pm 2k_{SO} \\
\cos\theta_{k=\pm 2k_{SO}} \approx \pm s_\alpha
\end{cases}
, \tag{B.13}
$$

so that the spinors (B.10) of the lower band propagating modes near $k \sim \pm 2k_{SO}$ reduce to eigenstates of σ_z, $(1,0)^T$ or $(0,1)^T$, depending on the sign s_α of the RSOC [see Eq.(3.39)]. To extract the low energy Hamiltonian governing their dynamics, let us consider, for instance, $\alpha > 0$ like in Fig.3.4, and focus e.g. on the vicinity of the right Fermi point $+2k_{SO}$. Setting $k = 2k_{SO} + q$ and performing an expansion of Eqs.(B.7) and (B.8) for $|q| \ll k_{SO}$, one obtains

$$
\begin{aligned}
\hat{\mathcal{H}}_{NW}\Big|_{k \simeq +2k_{SO}} &\simeq \sum_{|q| \ll k_{SO}} \hat{C}^\dagger_{2k_{SO}+q} \begin{pmatrix} \hbar v_{SO}q & -E_Z \\ -E_Z & 8E_{SO} \end{pmatrix} \hat{C}_{2k_{SO}+q} \\
&\simeq \sum_{|q| \ll k_{SO}} \hbar v_{SO}q \, \hat{c}^\dagger_{2k_{SO}+q,\uparrow} \hat{c}_{2k_{SO}+q,\uparrow} \quad ,
\end{aligned} \tag{B.14}
$$

where $v_{SO} = \hbar k_{SO}/m^*$. The last line of Eq.(B.14) follows from the fact that, while the spin-$\uparrow$ band is characterized by a low-energy $\hbar v_F q$, the spin-$\downarrow$ band has a large energy $8E_{SO}$ much above the magnetic gap. The weak Zeeman energy $E_Z \ll 2E_{SO}$ cannot couple them, so that in the low energy sector $|E| \ll E_Z$ only the spin-$\uparrow$ states matter. One can proceed in a similar manner near the $-2k_{SO}$ Fermi point, obtaining that only the spin-$\downarrow$ states matter, proving that the states are helical. Repeating the same calculation for $\alpha < 0$ one obtains the opposite helicity. From Eq.(B.14) the massless propagating low energy excitations ($|q| \ll k_{SO}$) are thus described by the set of operators

$$
\begin{cases}
\hat{\xi}_{q\uparrow} &\doteq \hat{c}_{2s_\alpha k_{SO}+q,\uparrow} \\
\\
\hat{\xi}_{q\downarrow} &\doteq \hat{c}_{-2s_\alpha k_{SO}+q,\downarrow}
\end{cases} \tag{B.15}
$$

where s_α is given by Eq.(3.39).

Expansion near $k = 0$. In the low energy range $|E| \ll E_Z$ there are also gapped (i.e. massive) modes, related to the upper and lower bands for $k \sim 0$ (see Fig.3.4). Performing an expansion of Eqs.(B.7) and (B.8) in $q = k$ (with $|q| \ll k_{SO}$) and introducing the new set of operators

$$
\begin{cases}
\hat{\eta}_{q\uparrow} &= \hat{c}_{q\uparrow} \\[2mm]
\hat{\eta}_{q\downarrow} &= \hat{c}_{q\downarrow}
\end{cases} \quad ,
\tag{B.16}
$$

one obtains the low energy expression

$$
\hat{\mathcal{H}}_{NW}\Big|_{k\simeq 0} \simeq -\sum_{|q|\ll k_{SO}} \hbar s_\alpha v_{SO}\, q\, (\hat{\eta}_{q\uparrow}^\dagger\ \hat{\eta}_{q\downarrow}^\dagger)\sigma_z \begin{pmatrix} \hat{\eta}_{q\uparrow} \\ \hat{\eta}_{q\downarrow} \end{pmatrix}
$$
$$
-E_Z \sum_{|q|\ll k_{SO}} (\hat{\eta}_{q\uparrow}^\dagger\ \hat{\eta}_{q\downarrow}^\dagger)\, \sigma_x \begin{pmatrix} \hat{\eta}_{q\uparrow} \\ \hat{\eta}_{q\downarrow} \end{pmatrix} \quad .
\tag{B.17}
$$

Summing up Eqs.(B.14) and (B.17) one obtains a low-energy NW Hamiltonian. Moreover, one can observe that such model shares the same low-energy physics as the Dirac model given in Eq.(3.40), obtained by removing the constraints on wave vector q, which can therefore be regarded to as the effective low energy model for the NW.

B.3 Lattice model

In this Appendix we show that the existence of one single effective massless Dirac mode, i.e. a Weyl mode, inside the magnetic gap of the NW is not an artifact of the continuum model in Eq.(3.36). To this purpose, we consider the following lattice model

$$
\hat{\mathcal{H}} = -t\sum_j \left(\hat{C}_{j+1}^\dagger \hat{C}_j + ia\, \hat{C}_{j+1}^\dagger \sigma_z \hat{C}_j + b\, \hat{C}_j^\dagger \sigma_x \hat{C}_j - \hat{C}_j^\dagger \hat{C}_j \right) + \text{H.c.}
\tag{B.18}
$$

where $\hat{C}_j^\dagger = (c_{j\uparrow}^\dagger,\ c_{j\downarrow}^\dagger)$ and $c_{j\uparrow,\downarrow}^\dagger$ creates a fermion in the site j with spin $\uparrow$ or $\downarrow$, respectively. Here t is the nearest-neighbor hopping amplitude, while a and b are dimensionless parameters related to the strength of the spin-orbit coupling (time reversal preserving) and the external magnetic field (time reversal breaking), respectively. Passing to momentum space operators through $\hat{C}_j = N^{-1/2}\sum_{k\in BZ} e^{ikja_0}\hat{C}_k$, where N denotes the number of lattice
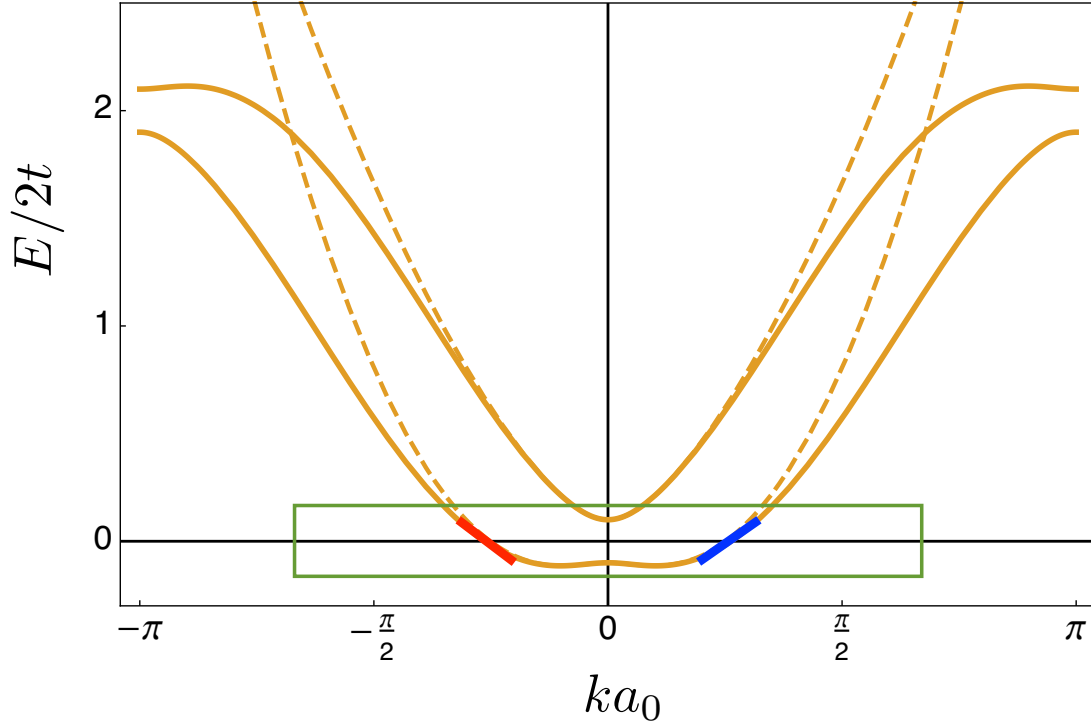
Fig. B.1 Comparison between the spectra of the lattice model Eq.(B.19) (solid curves) and of the continuum model Eq. (3.36)(dashed curves). The latter captures the main features of the former in the low energy sector (green box). In particular only two helical states (red and blue thick lines) are present in the magnetic gap around $E = 0$.

sites, a_0 the lattice spacing and $ka_0 \in [-\pi, \pi]$ the lattice momentum, one gets

$$\hat{\mathcal{H}} = 2t \sum_k \hat{C}_k^\dagger \left\{ [1 - \cos(ka_0)]\, \sigma_0 - a\, \sin(ka_0)\sigma_z - b\, \sigma_x \right\} \hat{C}_k \, . \tag{B.19}$$

It is straightforward to see that Eq.(B.19) can be considered as the lattice regularized version of the continuum model in Eq.(3.36). Indeed in the limit $ka_0 \ll 1$, the former model reduces to the latter upon identifying $t = \hbar^2/2m^*a_0^2$, $a = m^*a_0\alpha/\hbar^2$ and $b = h_x m^*a_0^2/\hbar^2$. The energy spectrum of the lattice model (B.19) is easily obtained

$$E_\pm(k) = 2t\left[1 - \cos(k) \pm \sqrt{a^2 \sin^2(k) + b^2}\right] \quad , \tag{B.20}$$

and is plotted in Fig.B.1 (solid lines), whereas the dashed lines display the spectrum of the continuum model (3.36) for comparison. As one can see, the low energy sector of the lattice model (green box) is perfectly captured by the continuum theory. In particular, the bands of the full lattice model cross the $E = 0$ line in *two and only two points*, namely the ones already found within the continuum model, since a gap is present at $k = 0$. Thus,

inside the magnetic gap, one finds only two massless helical states (red and blue thick lines), i.e. *one* single 1D Weyl mode. Notably, this is consistent with the Nielsen-Ninomiya theorem[457], which implies, in the one dimensional case, that the number of left movers equals the number of right movers at any energy. In pass we note that, at much higher energy (irrelevant to our purposes), a similar situation occurs: The gap opening up at $ka_0 = \pm\pi$ leaves only two massless helical modes at $E = 4t$, giving rise to one single Dirac cone as low energy excitations around that energy. Only when time-reversal symmetry is present, i.e. for $b = 0$ in Eq.(B.19), the two bands touch at $k = 0$ and $k = \pm\pi$, where an additional Weyl mode appears.

B.4   The scattering problem for the inhomogeneous NW with the profile (3.46)

The solution of the scattering problem for the model (3.44) with the piecewise constant profile (3.46) can be obtained from the expression of the electron field operator in the three regions. For an energy E within the magnetic gap ($|E| < E_Z$) one has

$$
\hat{\Phi}_E(x) = \begin{cases}
\hat{a}_{LE} w_{k_E,-} e^{ik_E x} + \hat{b}_{LE} w_{-k_E,-} e^{-ik_E x} + \hat{c}_{LE} \tilde{w}_{\kappa_E, s_E} e^{\kappa_E x} & x < -L/2 \\[2mm]
\dfrac{\hat{h}_E}{\sqrt{2}} \begin{pmatrix} 1 \\ 1 \end{pmatrix} e^{ik_{2,E} x} + \dfrac{\hat{g}_E}{\sqrt{2}} \begin{pmatrix} 1 \\ 1 \end{pmatrix} e^{-ik_{2,E} x} + \dfrac{\hat{d}_E}{\sqrt{2}} \begin{pmatrix} 1 \\ -1 \end{pmatrix} e^{\kappa_{2,E} x} + \dfrac{\hat{f}_E}{\sqrt{2}} \begin{pmatrix} 1 \\ -1 \end{pmatrix} e^{-\kappa_{2,E} x} & |x| < L/2 \\[2mm]
\hat{a}_{RE} w_{-k_E,-} e^{-ik_E x} + \hat{b}_{RE} w_{k_E,-} e^{ik_E x} + \hat{c}_{RE} \tilde{w}_{-\kappa_E, s_E} e^{-\kappa_E x} & x > +L/2
\end{cases}
$$

$$(\text{B.21})$$

where

$$
k_E = \frac{\sqrt{2m^*}}{\hbar} \sqrt{E + 2E_{SO} + \sqrt{4EE_{SO} + 4E_{SO}^2 + E_Z^2}} \tag{B.22}
$$

$$
\kappa_E = \frac{\sqrt{2m^*}}{\hbar} \sqrt{-E - 2E_{SO} + \sqrt{4EE_{SO} + 4E_{SO}^2 + E_Z^2}} \tag{B.23}
$$

$$
s_E = \mathrm{sgn}(E + E_Z^2/4E_{SO}) \tag{B.24}
$$

$$
k_{2,E} = k_Z \sqrt{1 + E/E_Z} \qquad \kappa_{2,E} = k_Z \sqrt{1 - E/E_Z} \quad, \tag{B.25}
$$

while the spinors $w_{\pm k_E,-}$ and $\tilde{w}_{\pm\kappa_E, s_E}$ are given in Eqs.(B.10) and (B.12), respectively.

Imposing the boundary conditions (3.45) to the field (B.21), one expresses the outgoing operators $\hat{b}_{L/R\,E}$ in terms of the operators $\hat{a}_{LE}$ and $\hat{a}_{RE}$ describing the modes incoming from the left and from the right region, respectively. The transmission amplitudes t_E and t'_E are then obtained through the relations $\hat{b}_{RE} = t_E \hat{a}_{LE}$ and $\hat{b}_{LE} = t'_E \hat{a}_{RE}$. The resulting transmission coefficient $T_E = |t_E|^2 = |t'_E|^2$ is numerically exact and is plotted in the solid curves of Fig.3.7 as a function of the spin orbit energy, at the midgap energy $E = 0$ and for different values of the external magnetic field E_Z.

However, as observed in Sec.3.4, an analytical expression for the transmission coefficient can be obtained in the low energy limit (dashed curve in Fig.3.7), where the inhomogeneous NW physics is well captured by the effective massless+massive Dirac theory. Such an expression directly follows from the transfer matrix (3.50) connecting the massless and massive fields of the outer Rashba-dominated regions, which can be obtained as follows. Inserting Eq.(3.49) into the low energy boundary conditions Eqs.(3.47)-(3.48), the latter can be re-expressed in a matrix form as

$$
\mathsf{P} \begin{pmatrix} \hat{\xi}_\uparrow(-L/2) \\ \hat{\xi}_\downarrow(-L/2) \\ \hat{\eta}_\uparrow(-L/2) \\ \hat{\eta}_\downarrow(-L/2) \end{pmatrix} = \mathsf{V}(-L/2) \begin{pmatrix} \hat{h} \\ \hat{g} \\ \hat{d} \\ \hat{f} \end{pmatrix}
\tag{B.26}
$$

$$
\mathsf{V}(L/2) \begin{pmatrix} \hat{h} \\ \hat{g} \\ \hat{d} \\ \hat{f} \end{pmatrix} = \mathsf{Q} \begin{pmatrix} \hat{\xi}_\uparrow(L/2) \\ \hat{\xi}_\downarrow(L/2) \\ \hat{\eta}_\uparrow(L/2) \\ \hat{\eta}_\downarrow(L/2) \end{pmatrix} \quad ,
\tag{B.27}
$$

where the energy dependence of the operators has been dropped to make the notation lighter. Here

$$
\mathsf{P} = \begin{pmatrix} e^{-ik_{SO}L} & 0 & 1 & 0 \\ 0 & e^{ik_{SO}L} & 0 & 1 \\ k_{SO}e^{-ik_{SO}L} & 0 & -k_{SO} & 0 \\ 0 & -k_{SO}e^{ik_{SO}L} & 0 & k_{SO} \end{pmatrix} \quad ,
\tag{B.28}
$$

$$
\mathsf{Q} = \begin{pmatrix} e^{-ik_{SO}L} & 0 & 1 & 0 \\ 0 & e^{ik_{SO}L} & 0 & 1 \\ -k_{SO}e^{-ik_{SO}L} & 0 & k_{SO} & 0 \\ 0 & k_{SO}e^{ik_{SO}L} & 0 & -k_{SO} \end{pmatrix}
\tag{B.29}
$$

and

$$\mathsf{V}(x) = \frac{1}{\sqrt{2}} \begin{pmatrix} e^{ik_{2,E}x} & e^{-ik_{2,E}x} & e^{\kappa_{2,E}x} & e^{-\kappa_{2,E}x} \\ e^{ik_{2,E}x} & e^{-ik_{2,E}x} & -e^{\kappa_{2,E}x} & -e^{-\kappa_{2,E}x} \\ ik_{2,E}e^{ik_{2,E}x} & -ik_{2,E}e^{-ik_{2,E}x} & \kappa_{2,E}e^{\kappa_{2,E}x} & -\kappa_{2,E}e^{-\kappa_{2,E}x} \\ ik_{2,E}e^{ik_{2,E}x} & -ik_{2,E}e^{-ik_{2,E}x} & -\kappa_{2,E}e^{\kappa_{2,E}x} & \kappa_{2,E}e^{-\kappa_{2,E}x} \end{pmatrix} \tag{B.30}$$

The transfer matrix M_E appearing in Eq.(3.50) can thus straightforwardly be obtained as $\mathsf{M}_E = \mathsf{Q}^{-1}\mathsf{V}(L/2)\mathsf{V}^{-1}(-L/2)\mathsf{P}$. In particular, setting the energy to the midgap value $E = 0$ and expanding in the parameter $k_Z L$ one obtains Eq.(3.51), up to $O((k_Z L)^4)$ terms.

Appendix C

C.1 Continuum Spectrum Eigenfunctions of the Post-Quench Hamiltonian

As is well known, since the post-quench Hamiltonian

$$\hat{\mathcal{H}}^{\text{post}} = \int dx \, \hat{\Psi}^\dagger(x) \left(-\hbar^2/2m \, \partial_x^2 \, - \, V_0 \, \theta(a/2 - |x|) \right) \hat{\Psi}(x) \tag{C.1}$$

commutes with the space parity operator, the single-particle eigenfunctions can be classified according to their parity $\eta = \pm = \text{even/odd}$. In particular, within a given parity sector η, the continuum spectrum ($\varepsilon > 0$) wavefunction $\psi_\eta(x)$ *outside* the QW can be written as a linear combination of two wavefunctions, namely the free-particle wavefunction $\varphi_\eta(x)$ and a *singular* wavefunction $\bar{\varphi}_\eta(x)$, both with the same parity η. The weight of such linear combination is determined by an angle θ_η. Explicitly, denoting by $q = \sqrt{2m\varepsilon}/\hbar$ the wavevector outside the QW and by $\tilde{q} = \sqrt{2m(\varepsilon + V_0)}/\hbar$ the wavevector inside the QW, one can label the post-quench unbound eigenfunctions with the discrete-plus-continuum index $\alpha = (\eta, q)$ and compactly write

$$\psi_{\eta,q}(x) = \begin{cases} \cos\theta_{\eta,q} \, \varphi_{\eta,q}(x) - \eta \sin\theta_{\eta,q} \, \bar{\varphi}_{\eta,q}(x) & |x| \geq a/2 \\[2em] \sqrt{\dfrac{1 + \tan^{2\eta}\left(\frac{\tilde{q}a}{2}\right)}{1 + \left(\frac{\tilde{q}}{q}\right)^2 \tan^{2\eta}\left(\frac{\tilde{q}a}{2}\right)}} \, \varphi_{\eta,\tilde{q}}(x) & |x| < a/2 \end{cases} \tag{C.2}$$

where

$$\varphi_{+,q}(x) = \frac{1}{\sqrt{\pi}} \cos(qx) \quad , \quad \varphi_{-,q}(x) = \frac{1}{\sqrt{\pi}} \sin(qx) \tag{C.3}$$

are the pre-quench even/odd eigenfunctions, respectively, and

$$\bar{\varphi}_{+,q}(x) = \frac{1}{\sqrt{\pi}} \sin(q|x|) \quad , \quad \bar{\varphi}_{-,q}(x) = \frac{1}{\sqrt{\pi}} \mathrm{sgn}(x) \cos(qx) \tag{C.4}$$

are their even and odd singular counterparts. Moreover, the angle determining their relative weight in the first line of Equation (C.2) is

$$\theta_{\eta,q} = \arctan\left[\left(\frac{\tilde{q}}{q}\right)^{\eta} \tan\left(\frac{\tilde{q}a}{2}\right)\right] - \frac{qa}{2} + \pi \frac{1 - \mathrm{sgn}\left(\cos\left(\frac{\tilde{q}a}{2}\right)\right)}{2} \quad . \tag{C.5}$$

From the above definitions, one can then verify that the normalization $\langle \psi_{\eta,q} | \psi_{\eta',q'} \rangle = \delta_{\eta,\eta'} \delta(q - q')$ holds.

C.2 Basis Change Coefficients (Continuum Spectrum)

In computing the coefficients of the pre-post basis change appearing in Equation (4.3), we observe that $U_{\eta\eta'}(q, k) = \delta_{\eta\eta'} \langle \psi_{\eta,q} | \varphi_{\eta,k} \rangle$ and

$$
\begin{aligned}
U_{\eta\eta'}(q, k) &= \delta_{\eta\eta'} \left[\underbrace{\int_{|x| \geq \frac{a}{2}} \psi_{\eta,q}^*(x)\, \varphi_{\eta,k}(x)\, dx}_{= C_\eta^{out}(q,k)} + \underbrace{\int_{|x| < \frac{a}{2}} \psi_{\eta,q}^*(x)\, \varphi_{\eta,k}(x)\, dx}_{= C_\eta^{in}(q,k)} \right] \\
&\simeq 2\delta_{\eta\eta'} \left[\cos\theta_{\eta,q} \left(\int_{\frac{a}{2}}^{\infty} \varphi_{\eta,q}(x)\, \varphi_{\eta,k}(x)\, dx \right) \right. \\
&\quad - \left. \eta \sin\theta_{\eta,q} \left(\int_{\frac{a}{2}}^{\infty} \bar{\varphi}_{\eta,q}(x)\, \varphi_{\eta,k}(x)\, dx \right) \right]
\end{aligned}
\tag{C.6}
$$

where in Equation (C.6) we have neglected the second contribution C_η^{in}, which is negligible with respect to the first contribution C_η^{out}, because the space region outside the QW is infinitely long in the thermodynamic limit and because we are focusing on the continuum spectrum wavefunctions. Thus, the $U_{\eta\eta'}(q, k)$ coefficients can be straightforwardly evaluated

by inserting the definitions of φ and $\bar{\varphi}$ into Equation (C.6), and by exploiting the identity

$$\int_{\frac{a}{2}}^{\infty} e^{(ik-k_{min})x}\,dx = e^{(ik-k_{min})\frac{a}{2}} \left(\frac{k_{min}}{k_{min}^2 + k^2} + i\frac{k}{k_{min}^2 + k^2} \right) \sim e^{i\frac{ka}{2}} \left[\pi\delta(k) + i\,\mathrm{P.V.}\left(\frac{1}{k}\right) \right]$$
(C.7)

where

$$\begin{cases} \delta(k) = \dfrac{1}{\pi}\dfrac{k_{min}}{k_{min}^2 + k^2} \\[4mm] \mathrm{P.V.}\left(\dfrac{1}{k}\right) = \dfrac{k}{k_{min}^2 + k^2} \end{cases}$$
(C.8)

are the regularized versions of the δ-function and the Principal Value (P.V.), respectively, while k_{min} is an infrared cut-off controlling the integral divergences and mimicking the inverse total length of the system ($k_{min} \sim 2/L \to 0$ in the thermodynamic limit $L \to \infty$). Within a few algebraic steps, one obtains

$$\begin{aligned} U_{\eta\eta'}(q,k) &= \delta_{\eta\eta'}\left\{ \cos\theta_{\eta,q}\,\delta(q-k) - \frac{\eta}{\pi}\sin\left[(q+k)\frac{a}{2} + \theta_{\eta,q}\right]\mathrm{P.V.}\left(\frac{1}{q+k}\right) \right. \\ &\quad \left. - \frac{1}{\pi}\sin\left[(q-k)\frac{a}{2} + \theta_{\eta,q}\right]\mathrm{P.V.}\left(\frac{1}{q-k}\right) \right\} \end{aligned}$$
(C.9)

C.3 Occupancy of the Continuum Post-Quench Eigenstates

As explained in Section 4.2 (see Equation (4.3)), the continuum–continuum diagonal density matrix entries are given by

$$\rho_{\eta\eta}(q,q) = \langle \hat{\gamma}_{\eta}^{\dagger}(q)\hat{\gamma}_{\eta}(q) \rangle = \int_{0}^{+\infty} dk\,|U_{\eta\eta}(q,k)|^2\,f^{eq}(\varepsilon(k)) \quad .$$
(C.10)

Inserting Equation (C.9) in Equation (C.10), their evaluation can be carried out and leads to

$$\rho_{\eta\eta}(q,q) = \delta(0)\Bigg\{\Bigg[\cos^2\theta_{\eta,q} - \frac{\eta}{\pi}\underbrace{\cos\theta_{\eta,q}\sin\Big(qa + \theta_{\eta,q}\Big)}_{\text{bounded}}\underbrace{\text{P.V.}\left(\frac{1}{q}\right)\frac{1}{\delta(0)}}_{\to 0}\Bigg]f^{eq}(\varepsilon(q)) +$$

$$+\frac{1}{\pi^2}\int_0^\infty dk\ \underbrace{\sin^2\left[\frac{(q+k)a}{2} + \theta_{\eta,q}\right]}_{\text{bounded}}\underbrace{\text{P.V.}^2\left(\frac{1}{q+k}\right)\frac{1}{\delta(0)}}_{\to 0}f^{eq}(\varepsilon(k)) +$$

$$+\frac{1}{\pi^2}\int_0^\infty dk\ \underbrace{\sin^2\left[\frac{(q-k)a}{2} + \theta_{\eta,q}\right]}_{\text{bounded}}\underbrace{\text{P.V.}^2\left(\frac{1}{q-k}\right)\frac{1}{\delta(0)}}_{\to\pi^2\delta(q-k)}f^{eq}(\varepsilon(k)) +$$

$$+\frac{2\eta}{\pi^2}\int_0^\infty dk\ \underbrace{\sin\left[\frac{(q+k)a}{2} + \theta_{\eta,q}\right]\sin\left[\frac{(q-k)a}{2} + \theta_{\eta,q}\right]}_{\text{bounded}}\cdot$$

$$\underbrace{\text{P.V.}\left(\frac{1}{p+k}\right)\text{P.V.}\left(\frac{1}{p-k}\right)\frac{1}{\delta(0)}}_{\to 0}f^{eq}(\varepsilon(k))\Bigg\} \tag{C.11}$$

$$= \delta(0)\Bigg\{\cos^2\theta_{\eta,q}\,f^{eq}(\varepsilon(q)) + \sin^2\theta_{\eta,q}f^{eq}(\varepsilon(q))\Bigg\} \tag{C.12}$$

$$= \delta(0)\,f^{eq}(\varepsilon(q))\,, \tag{C.13}$$

where the regularized δ and P.V. are defined in Equation (C.8). In particular $\delta(0) = \delta(q = 0) = (\pi k_{min})^{-1} \sim L/2\pi \to \infty$, as expected, since the total number of electrons in the continuum should scale extensively with the system size. By singling out a $\delta(0)$ pre-factor, one can see that, apart from the $\cos^2\theta_{\eta,q}$ contribution in the first line of Equation (C.11), the only term yielding a finite contribution is the squared Principal Value appearing on the third line, due to the relation

$$\frac{1}{\delta(0)}\text{P.V.}^2\left(\frac{1}{q-k}\right) \equiv \pi k_{min}\frac{(q-k)^2}{((q-k)^2 + k_{min}^2)^2} = \pi\underbrace{\frac{(q-k)^2}{(q-k)^2 + k_{min}^2}}_{\to 1}\underbrace{\frac{k_{min}}{(q-k)^2 + k_{min}^2}}_{=\pi\delta(q-k)}$$

$$\to \pi^2\delta(q-k)\quad. \tag{C.14}$$

In conclusion, one obtains that the occupancy of the post-quench continuum states equals the equilibrium one.

Appendix D

Here we briefly summarize some aspects of the standard *homogeneous* SSH model, which corresponds to taking $v_j \equiv v \in \mathbb{C}$ and $w_j \equiv w \in \mathbb{C}$ in Eq.(5.2). Let us now recall the cases of a ring and of a chain.

D.1 Ring (periodic boundary conditions) and topological classification

Let M denote the number of cells and by $N = 2M$ the number of lattice sites of a ring-shaped lattice. By re-expressing the site operators as $\hat{c}_{j,s} = M^{-1/2} \sum_k e^{ikja} \hat{c}_{k,s}$, the periodic boundary condition $\hat{c}_{M+1,A} = \hat{c}_{1,A}$ enables one to straightforwardly rewrite the Hamiltonian Eq.(5.2) as a decoupled set of k-dependent Hamiltonians

$$\hat{\mathcal{H}}_{SSH,\chi} = \sum_k \left(\hat{c}_{k,A}^\dagger, \hat{c}_{k,B}^\dagger \right) H(k) \left(\begin{array}{c} \hat{c}_{k,A} \\ \hat{c}_{k,B} \end{array} \right) \quad . \tag{D.1}$$

Here a denotes the cell size, $k = 2\pi n/Ma$ the wavevectors (with $n = -\frac{M}{2}, -\frac{M}{2} + 1, \ldots, \frac{M}{2} - 1$ for even M and $n = -[\frac{M}{2}], -[\frac{M}{2}] + 1, \ldots, +[\frac{M}{2}]$ for odd M), and $\hat{c}_{k,s}$ are the Fourier mode operators[1]. In Eq.(D.1) $H(k) = \boldsymbol{\sigma} \cdot \mathbf{d}(k)$ is the first-quantized SSH Hamiltonian in k-space, with $\boldsymbol{\sigma}$ denoting the set of Pauli matrices and $\mathbf{d}(k) = \left(\text{Re}(v) + \text{Re}(we^{ika}), -\text{Im}(v) + \text{Im}(we^{ika}), 0 \right)$ a vector lying in the plane. The absence of the b_z component is the hallmark of the chiral symmetry, which is expressed by the property $\sigma_z H(k) \sigma_z = -H(k)$ in terms of the first-quantized Hamiltonian. In terms of the tenfold classification scheme[458, 3], the SSH model is in the AIII symmetry class. If $w, v \in \mathbb{R}$ the

---

[1]The k-mode operators $\hat{c}_{k,s}$ (with $s = A, B = \pm$) transform under $\mathcal{C}, \mathcal{S}$ and $\mathcal{T}$ as follows: $\mathcal{C}\hat{c}_{k,s}\mathcal{C}^{-1} = (-1)^s \hat{c}_{-k,s}^\dagger$, $\mathcal{S}\hat{c}_{k,s}\mathcal{S}^{-1} = (-1)^s \hat{c}_{k,s}^\dagger$ and $\mathcal{T}\hat{c}_{k,s}\mathcal{T}^{-1} = \hat{c}_{-k,s}$.

Hamiltonian $H(k)$ also fulfills the properties $H^*(k) = H(-k)$ and $\sigma_z H^*(k)\sigma_z = -H(-k)$ encoding the time-reversal and charge conjugation symmetries, respectively, and the model is in the BDI symmetry class. The spectrum consists of two bands

$$
\begin{aligned}
\varepsilon_\pm(k) &= \pm|\mathbf{d}(k)| = \tag{D.2}\\
&= \pm\sqrt{|w|^2 + |v|^2 + 2|vw|\cos(ka + \arg(v) + \arg(w))} \quad, \tag{D.3}
\end{aligned}
$$

separated by the bandgap $2\varepsilon_g = 2||v| - |w||$. The maximal value of the group velocity $\mathrm{v}(k) = \hbar^{-1}\partial\varepsilon/\partial k$ is $\mathrm{v}_{max} = a\min(|v|, |w|)/\hbar$ and determines the minimal timescale Eq.(5.31) an electron wavepacket takes to travel across the ring length $L = Ma$.

The single-particle eigenvectors related to the two bands $\varepsilon_\pm$ are $|u_-(k)\rangle = (1, -e^{i\varphi(k)})^T/\sqrt{2}$ and $|u_+(k)\rangle = (e^{-i\varphi(k)}, 1)^T/\sqrt{2}$, with $\varphi(k) = -\varphi(-k)$ denoting the polar angle of the $\mathbf{d}(k)$ vector, so that $\tan\varphi(k) = d_y(k)/d_x(k)$. In particular, in the thermodynamic limit, where k becomes a continuous variable spanning the Brillouin zone $[-\pi, +\pi]/a$, $\mathbf{d}(k)$ draws a circle centered at $(\mathrm{Re}(v), -\mathrm{Im}(v))$ and with radius $|w|$. As is well known, this enables one to identify two topological classes of the insulator, depending on whether such circle encloses or not the origin (corresponding to the gap closing). Correspondingly, the winding number of the fully occupied lower band of the insulator

$$
\nu = -\frac{i}{\pi} \oint \langle u_- | \partial_k u_- \rangle \, dk = \frac{1}{2\pi} \oint \frac{d\varphi}{dk} \, dk \tag{D.4}
$$

takes two different integer values $\nu = 1$ (for $|v| < |w|$) and $\nu = 0$ (for $|v| > |w|$). We emphasize that, while the two phases are topologically distinct, labelling one phase as "topological" and the other one as "trivial" is in fact unphysical as long as the model is defined on a ring. This is because the topological classification is defined once the unit cell is identified, which is completely arbitrary in a system with PBCs, though. Indeed the very Hamiltonian $\hat{\mathcal{H}}_{SSH}$, written in Eq.(5.1) by adopting (A, B) as unit cell, could be equivalently rewritten choosing (B, A) as unit cell, which would amount to exchanging the role of intra- and inter-cell hopping amplitudes ($v \leftrightarrow w$), so that the "topological" phase for the choice (A, B) corresponds to the "trivial" phase for the choice (B, A) and viceversa. The emergence of topological edge states, which are perhaps the most striking hallmark distinguishing the topological character of the two phases, requires the breaking of the PBCs.

D.2   Chain (open boundary conditions)

The customary way to break the PBCs is to cut the ring into a finite chain, thereby interfacing the SSH model with vacuum. In turn, this lifts the degeneracy about the choice of the unit cell: If (say) (A, B) is the unit cell of the chain with an even number of sites $N = 2M$, the OBCs of the chain impose $\hat{c}_{M+1,A} = 0 = \hat{c}_{0,B}$, where M again denotes the number of cells. As argued above, in a chain the hopping amplitudes can be taken as real and positive, $v, w \in \mathbb{R}^+$, without loss of generality. The OBCs modify the spectrum and enable one to identify the actual topological and trivial phases. Indeed, besides a continuum spectrum similar to the ring, when $v < w$ the chain also features two additional discrete levels (topological phase), which are absent for $v > w$ (trivial phase) instead. The difference between the two phases becomes apparent in the so called dimerized limit, where one of the two hopping amplitude is set to zero. The SSH chain eigenstates resulting from the OBCc are non-degenerate and can be given an analytic expression[459, 460]. In particular, the continuum eigenstates extend over the entire bulk of the chain and can formally be built by linearly combining the $|u_\pm(k)\rangle$ and $|u_\pm(-k)\rangle$ of the ring

$$|\psi_\pm^{bulk}(k)\rangle = \frac{1}{\sqrt{\mathcal{N}_k}} \sum_{j=1}^M \begin{pmatrix} \sin[kaj - \varphi(k)] \\ \pm \sin[kaj] \end{pmatrix} \tag{D.5}$$

where $\tan \varphi(k) = w \sin(ka)/(v + w \cos(ka))$ and $\mathcal{N}_k = M + v(v + w \cos(ka))/(v^2 + w^2 + 2vw \cos(ka))$ is a a normalization constant. However, the quantization rule of k's differs from the customary $kaM = 2\pi n$ in the ring and fulfill the transcendental equation $ka(M + 1) = \pi n + \varphi(k)$ with $n = 1, 2 \ldots M$. In contrast, the topological edge eigenstates read[459, 460]

$$|\psi_\pm^{edge}\rangle = \frac{1}{\sqrt{\mathcal{N}_0}} \sum_{j=1}^M (-1)^{j+1} \begin{pmatrix} \sinh[\kappa a(M + 1 - j)] \\ \pm \sinh[\kappa aj] \end{pmatrix} \tag{D.6}$$

where κ fulfills $v \sinh[\kappa(M + 1)a] = w \sinh[\kappa Ma]$ and $\mathcal{N}_0 = (w \sinh(2\kappa aM)/2v \sinh(\kappa a)) - (M + 1)$ is a normalization constant. They are localized mainly on A sites on the left edge and on B sites on the right edge. Their energies are $\varepsilon_\pm^{\text{edge}} = \pm w \sinh(\kappa a)/\sinh(\kappa(M + 1)a)$, whose difference decreases exponentially as $\sim \exp[-\kappa Ma]$ with the number of cells.

Appendix E

E.1 State evolution in a quenched two-band system

In this appendix we recall the general state evolution after a sudden quench in a two-band model[390]. Let us suppose that the initial state is the half filled ground state of a two-band Hamiltonian, whose one-body form can be written in momentum space as

$$H_i(k) = \left[d_i^0(k)\sigma_0 + \mathbf{d}_i(k) \cdot \boldsymbol{\sigma} \right] \tag{E.1}$$

The k-th component of the initial state can thus be written as $\rho(k, 0) = \left[\sigma_0 - \hat{\mathbf{d}}_i(k) \cdot \boldsymbol{\sigma} \right]/2$ where $\hat{\mathbf{d}}_i(k) = \mathbf{d}_i(k)/|\mathbf{d}_i(k)|$. The state evolves according to the post-quench Hamiltonian

$$H_f(k) = \left[d_f^0(k)\sigma_0 + \mathbf{d}_f(k) \cdot \boldsymbol{\sigma} \right] \tag{E.2}$$

and, by solving the Liouville-Von Neumann equation for the one-body density matrix, one can write the k-th component of the time evolved state as $\rho(k, t) = \left[\sigma_0 - \hat{\mathbf{d}}(k, t) \cdot \boldsymbol{\sigma} \right]/2$, where the time dependent unit vector can be written as the sum of three orthogonal contributions:

$$\hat{\mathbf{d}}(k, t) = \mathbf{d}_\parallel(k) + \mathbf{d}_\perp(k) \cos\left[2|\mathbf{d}_f(k)|t/\hbar \right] + \mathbf{d}_\times(k) \sin\left[2|\mathbf{d}_f(k)|t/\hbar \right] \tag{E.3}$$

where

$$\mathbf{d}_\parallel(k) = \left[\hat{\mathbf{d}}_i(k) \cdot \hat{\mathbf{d}}_f(k) \right] \hat{\mathbf{d}}_f(k) \tag{E.4}$$

$$\mathbf{d}_\perp(k) = \left[\hat{\mathbf{d}}_i(k) - \mathbf{d}_\parallel(k) \right] \tag{E.5}$$

$$\mathbf{d}_\times(k) = -\left[\hat{\mathbf{d}}_i(k) \times \hat{\mathbf{d}}_f(k) \right] \tag{E.6}$$

Then, by inserting the explicit expression for $\mathbf{d}_i(k)$ and $\mathbf{d}_f(k)$ corresponding to a flux quench in the SSH model, see Eq. (6.3), the expressions in Eqs. (6.8), (6.9), (6.10), (6.12) and (6.13) are recovered.

E.2   Current

In this appendix we briefly outline how to derive the current operators discussed in Sec.6.3. Given the site density operators $\hat{n}_{j,\alpha} = \hat{c}^\dagger_{j\alpha}\hat{c}_{j\alpha}$, with $\alpha = A, B$, and the SSH Hamiltonian with $\phi = 0$ [see Eq.(6.1)], it is straightforward to derive the following Heisenberg equations of motion:

$$\partial_t \hat{n}_{jA} = \hat{J}^{inter}_{j-1} - \hat{J}^{intra}_j \tag{E.7}$$

$$\partial_t \hat{n}_{jB} = \hat{J}^{intra}_j - \hat{J}^{inter}_j \tag{E.8}$$

where, by definition:

$$\hat{J}^{inter}_j = \frac{rv}{\hbar}\left[i\hat{c}^\dagger_{jB}\hat{c}_{j+1A} - i\hat{c}^\dagger_{j+1A}\hat{c}_{jB}\right] \tag{E.9}$$

is the inter-cell current reported in Eq.(6.14), while:

$$\hat{J}^{intra}_j = \frac{v}{\hbar}\left[i\hat{c}^\dagger_{jA}\hat{c}_{jB} - i\hat{c}^\dagger_{jB}\hat{c}_{jA}\right] \tag{E.10}$$

is the intra-cell current reported in Eq.(6.15).

E.3   Drude weight

The Drude weight D characterizing the LRT of the SSH model can be computed following Kohn's approach [398]. In particular, in a 1D ring one has

$$D = -L\frac{d^2 E_0(\Phi)}{d^2\Phi}\bigg|_{\Phi=0} \tag{E.11}$$

where $E_0(\Phi)$ denotes the dependence of the many-body ground state energy on the magnetic flux Φ threading the ring, while L denotes the ring length. For a tight-binding model, we can associate the magnetic flux Φ to a phase ϕ in the hopping amplitudes according to $N\phi = 2\pi\Phi/\Phi_0$, where N is the number of links in the ring and $\Phi_0 = h/e$ is

the magnetic flux quantum. Hence, in a bipartite lattice with two sites per cell, we get:

$$\Phi = L \frac{2}{a} \frac{\hbar}{e} \phi \tag{E.12}$$

where a is the lattice constant. Exploiting the linear relation between ϕ and Φ we can write Kohn's formula as

$$D = -\left(\frac{a}{2}\right)^2 \left(\frac{e}{\hbar}\right)^2 L^{-1} \frac{d^2 E_0(\phi)}{d^2\phi}\bigg|_{\phi=0} \tag{E.13}$$

Moreover, for translation invariant one-body Hamiltonians we can write:

$$D = -\left(\frac{a}{2}\right)^2 \left(\frac{e}{\hbar}\right)^2 L^{-1} \left[\frac{d^2}{d^2\phi} \sum_{(k,b)\in\mathcal{I}} \varepsilon_b(k,\phi)\right]_{\phi=0} \tag{E.14}$$

where $\mathcal{I}$ denotes the set of bands b and wavevectors k that are occupied in the many body ground state without flux, while $\varepsilon_b(k,\phi)$ denotes the band dispersion relations for a finite flux.

Since the single particle energies depend on the phase ϕ only through the combination $ka + 2\phi$, see Eq.(6.4), the many-body ground state energy of a half filled SSH model with dimerization ($r \neq 1$) does not depend on the flux in the thermodynamic limit. Indeed, due to the periodic nature of the lower band over the interval $ka \in [-\pi, \pi]$, one has

$$L^{-1} E_0^{r\neq 1}(\phi) = \frac{1}{2\pi} \frac{1}{a} \int_{-\pi}^{\pi} d(ka)\varepsilon_-(k,\phi) \tag{E.15}$$

$$= \frac{1}{2\pi} \frac{1}{a} \int_{-\pi}^{\pi} d(ka)\varepsilon_-(k,0) = L^{-1} E_0^{r\neq 1}(0) \tag{E.16}$$

and we conclude that the Drude weight (E.13) is identically zero in this case, consistently with Eq.(6.24).

Without dimerization ($r = 1$) the situation is different, since we get

$$L^{-1} E_0^{r=1}(\phi) = -\frac{v}{\pi} \frac{2}{a} \int_{-\frac{\pi}{2}}^{\frac{\pi}{2}} d\left(\frac{ka}{2}\right) \cos\left(\frac{ka}{2} + \phi\right) \tag{E.17}$$

$$= -\frac{2v}{\pi} \frac{2}{a} \cos(\phi) \tag{E.18}$$

and from Eq.(E.13) one obtains

$$D = -\frac{e^2}{\hbar}\frac{2v}{\hbar\pi}\frac{a}{2} = -\frac{e^2}{\hbar}\frac{\mathtt{v}_F}{\pi} \tag{E.19}$$

where $\mathtt{v}_F$ is the Fermi velocity. The finite Drude weight computed in this way coincides with the one obtained in the Ch.6 [see Eq.(6.25)] through its dynamical definition.

Appendix F

In this appendix we summarize some useful results about quenches in two band models and we provide some details about the definition of the Berry phase for a finite size system, its evaluation in the space-time scaling limit, and its connection to the current operator.

F.1 Fictitious Hamiltonian in a quenched two band model

In the quench protocol described in the Ch.7, the single particle eigenstates $|u_\pm^i(k)\rangle$ of the initial Hamiltonian $\hat{\mathcal{H}}^i = \sum_k \hat{c}^\dagger(k)[\mathbf{d}^i(k) \cdot \boldsymbol{\sigma}]\hat{c}(k)$, determined by the unit vector $\hat{\mathbf{d}}^i(k) = \mathbf{d}^i(k)/|\mathbf{d}^i(k)|$ through the eigenvalue problem $[\hat{\mathbf{d}}^i(k) \cdot \boldsymbol{\sigma}]|u_\pm^i(k)\rangle = \pm|u_\pm^i(k)\rangle$, evolve according to the post-quench Hamiltonian $\hat{\mathcal{H}}^f = \sum_k \hat{c}^\dagger(k)[\mathbf{d}^f(k) \cdot \boldsymbol{\sigma}]\hat{c}(k)$ as $|u_\pm(k,t)\rangle = \exp[-i[\mathbf{d}^f(k) \cdot \boldsymbol{\sigma}]t/\hbar]|u_\pm^i(k)\rangle$. In turn, the related projector $\rho_\pm(k,t) = |u_\pm(k,t)\rangle\langle u_\pm(k,t)|$ can always be written as $\rho_\pm(k,t) = [\sigma_0 \pm \hat{\mathbf{d}}(k,t) \cdot \boldsymbol{\sigma}]/2$, where σ_0 denotes the 2×2 identity matrix and $\hat{\mathbf{d}}(k,t)$ is a time-dependent unit vector given by [see Eq.(E.3)]

$$\hat{\mathbf{d}}(k,t) = \mathbf{d}_\parallel(k) + \mathbf{d}_\perp(k)\cos[2|\mathbf{d}^f(k)|t/\hbar] + \mathbf{d}_\times(k)\sin[2|\mathbf{d}^f(k)|t/\hbar] \quad , \tag{F.1}$$

where $\mathbf{d}_\parallel(k) = [\hat{\mathbf{d}}^i(k) \cdot \hat{\mathbf{d}}^f(k)]\hat{\mathbf{d}}^f(k)$, $\mathbf{d}_\perp(k) = \hat{\mathbf{d}}^i(k) - \mathbf{d}_\parallel(k)$ and $\mathbf{d}_\times(k) = -[\hat{\mathbf{d}}^i(k) \times \hat{\mathbf{d}}^f(k)]$, with $\hat{\mathbf{d}}^f(k) = \mathbf{d}^f(k)/|\mathbf{d}^f(k)|$. Because the initial state is the many-body ground state of the initial Hamiltonian $\hat{\mathcal{H}}^i$ at half filling, where the lower band $\epsilon_-^i(k) = -|\mathbf{d}^i(k)|$ is completely filled and the upper band $\epsilon_+^i(k) = +|\mathbf{d}^i(k)|$ is empty, the evolved many-body state can always be regarded to as the half filled ground state of a fictitious (two flat band) Hamiltonian $\hat{\mathcal{H}}(t) = \sum_k \hat{c}^\dagger(k)[\hat{\mathbf{d}}(k,t) \cdot \boldsymbol{\sigma}]\hat{c}(k)$, where time appear as a parameter.

F.2   Discrete Berry phase

On the basis of the previous Section, the Berry phase associated to the many body state of a quenched two band insulator can be formulated in terms of $|u_-(k,t)\rangle$ and $\hat{\mathbf{d}}(k,t)$. We shall now determine some of its general properties that hold independently of the time dependence. In order to lighten the notation, we are thus going to omit the t variable, which will be restored later, when time plays a major role. Yet we will deal with both the lower band Berry phase φ_{B-} and the upper band Berry phase φ_{B+}. In Ch.7, the symbol φ_B was used to denote φ_{B-} while here we explicitly keep both band indexes to highlight the relations between φ_{B-} and φ_{B+}.

When dealing with a finite system, the Berry phase has to be reformulated in terms of finite differences according to $\varphi_{B\pm} = \sum_{k \in BZ} \arg \xi_\pm \mod 2\pi$, where $\xi_\pm = \langle u_\pm(k + \delta k)|u_\pm(k)\rangle$, BZ denotes the Brillouin Zone and $\delta k = 2\pi/L$ [444].

We first note that in the continuum limit $L \to +\infty$, if $|u_\pm(k)\rangle$ is a smooth function of k (as it is usually the case in the time independent framework and for $t \ll L/v^f$), we can approximate $\xi_\pm \approx 1 + i\langle u_\pm(k)|i\partial_k|u_\pm(k)\rangle\delta k$, implying $\arg \xi_\pm \approx \langle u_\pm(k)|i\partial_k|u_\pm(k)\rangle\delta k$, and we recover the standard expression $\varphi_{B\pm} = \int dk A_{B\pm}(k)$, where $A_{B\pm}(k) = \langle u_\pm(k)|i\partial_k|u_\pm(k)\rangle$ is the Berry connection of the upper/lower band.

Then we show that some general properties fulfilled by the Berry phase in the customary continuous formulation are preserved also in the present discrete formulation [375]. Indeed, despite $\xi_\pm$ at each k is gauge dependent, the Berry phase is gauge invariant, as can be seen by rewriting $\varphi_{B\pm}$ as

$$\varphi_{B\pm} \;=\; \operatorname{Im}\ln \prod_{k \in BZ} \langle u_\pm(k + \delta k)|u_\pm(k)\rangle = \arg \operatorname{tr} \prod_{k \in BZ} \rho_\pm(k) \tag{F.2}$$

where tr denotes the trace on a two dimensional space and the projectors $\rho_\pm(k)$ are gauge invariant.

Moreover, Eq.(F.2) also enables one to prove that $\varphi_{B-} + \varphi_{B+} = 0 \mod 2\pi$. Indeed we observe that, for each k, the related projector can be written as $\rho_\pm = \beta^0(\pm\hat{\mathbf{d}})\sigma_0 + \boldsymbol{\beta}(\pm\hat{\mathbf{d}})\cdot\boldsymbol{\sigma}$, where the real parts $\beta_R^0, \boldsymbol{\beta}_R$ and the imaginary parts $\beta_I^0, \boldsymbol{\beta}_I$ of the β-coefficients are functions

of the unit vector $\hat{\mathbf{d}} = \hat{\mathbf{d}}(k)$ satisfying the following parity relations

$$
\begin{cases}
\beta_R^0(\hat{\mathbf{d}}) = +\beta_R^0(-\hat{\mathbf{d}}) \\
\beta_I^0(\hat{\mathbf{d}}) = -\beta_I^0(-\hat{\mathbf{d}}) \\
\boldsymbol{\beta}_R(\hat{\mathbf{d}}) = -\boldsymbol{\beta}_R(-\hat{\mathbf{d}}) \\
\boldsymbol{\beta}_I(\hat{\mathbf{d}}) = +\boldsymbol{\beta}_I(-\hat{\mathbf{d}})
\end{cases}
\tag{F.3}
$$

It is then straightforward to prove by induction that the product $R_\pm = \prod_k \rho_\pm(k)$ of an arbitrary set of projectors $\rho_\pm(k)$ is a matrix $R_\pm = B^0(\{\pm\hat{\mathbf{d}}(k)\})\sigma_0 + \mathbf{B}(\{\pm\hat{\mathbf{d}}(k)\})\cdot\boldsymbol{\sigma}$ whose B-coefficients are functions of the entire set $\{\hat{\mathbf{d}}(k)\}$ of unit vectors and satisfy the parity relations Eq.(F.3) in terms of $\{\hat{\mathbf{d}}(k)\} \leftrightarrow \{-\hat{\mathbf{d}}(k)\}$, implying that

$$
\text{tr} \prod_{k \in BZ} \rho_\pm(k) = B_R^0(\{\pm\hat{\mathbf{d}}(k)\}) + iB_I^0(\{\pm\hat{\mathbf{d}}(k)\}) = B_R^0(\{\hat{\mathbf{d}}(k)\}) \pm iB_I^0(\{\hat{\mathbf{d}}(k)\}) \quad . \tag{F.4}
$$

Thus, in view of Eqs.(F.2) and (F.4), the relation $\varphi_{B-} + \varphi_{B+} = 0 \mod 2\pi$ holds also in the discrete formulation.

Finally, if charge conjugation symmetry is present then the following relations hold true

$$
\begin{aligned}
\hat{d}_x(k) &= \hat{d}_x(-k) \tag{F.5} \\
\hat{d}_{y,z}(k) &= -\hat{d}_{y,z}(-k) \tag{F.6}
\end{aligned}
$$

and one can prove that $\varphi_{B-} = \varphi_{B+} \mod 2\pi$. Together with the general constraint $\varphi_{B-} = -\varphi_{B+} \mod 2\pi$ this implies that, when the system is invariant under charge conjugation, the Berry phase is constrained to be either 0 or π even in the discrete formulation.

F.3 The space-time scaling limit

We can now evaluate the time dependent discrete Berry phase φ_{B-} in the space-time scaling limit (STSL). Given that $\xi_-(k, t, L) = \langle u_-(k + \delta k, t)|u_-(k, t)\rangle$ and $|u_-(k, t)\rangle = \exp[-i\left[\mathbf{d}^f(k)t/\hbar\right] \cdot \boldsymbol{\sigma}]|u_-^i(k)\rangle$ we have to evaluate

$$
e^{i\left[\mathbf{d}^f(k+\delta k)t/\hbar\right]\cdot\boldsymbol{\sigma}} = \cos\left|\mathbf{d}^f(k+\delta k)t/\hbar\right| + i\left[\hat{\mathbf{d}}^f(k+\delta k) \cdot \boldsymbol{\sigma}\right]\sin\left|\mathbf{d}^f(k+\delta k)t/\hbar\right| \tag{F.7}
$$

to order L^{-1}, where $t \sim L$ while $\eta = 2\pi t / L$ is fixed. To make the notation lighter, we suppress the dependence on k and denote $d^f = |\mathbf{d}^f|$. We need to first evaluate the modulus

$$
\begin{aligned}
\left| \mathbf{d}^f (k + \delta k) t \right| &= \left| \mathbf{d}^f t + \partial_k \mathbf{d}^f \eta + \frac{1}{2} \delta k \, \partial_k^2 \mathbf{d}^f \eta + O(L^{-2}) \right| \\
&= |\mathbf{d}^f t| \sqrt{ 1 + 2 \frac{\mathbf{d}^f \cdot \partial_k \mathbf{d}^f}{|\mathbf{d}^f|^2} \delta k + \left(\frac{|\partial_k \mathbf{d}^f|^2}{|\mathbf{d}^f|^2} + \frac{\mathbf{d}^f \cdot \partial_k^2 \mathbf{d}^f}{|\mathbf{d}^f|^2} \right) \delta k^2 + O(L^{-3}) } \\
&= |\mathbf{d}^f t| \sqrt{ 1 + 2 \frac{\mathbf{d}^f \cdot \partial_k \mathbf{d}^f}{|\mathbf{d}^f|^2} \delta k + \frac{\partial_k (\mathbf{d}^f \cdot \partial_k \mathbf{d}^f)}{|\mathbf{d}^f|^2} \delta k^2 + O(L^{-3}) } \\
&= |\mathbf{d}^f t| \left\{ 1 + \frac{\mathbf{d}^f \cdot \partial_k \mathbf{d}^f}{|\mathbf{d}^f|^2} \delta k + \left[\frac{1}{2} \frac{\partial_k (\mathbf{d}^f \cdot \partial_k \mathbf{d}^f)}{|\mathbf{d}^f|^2} - \left(\frac{\mathbf{d}^f \cdot \partial_k \mathbf{d}^f}{|\mathbf{d}^f|^2} \right)^2 \right] \delta k^2 + O(L^{-3}) \right\} \\
&= d^f t \left\{ 1 + \frac{\partial_k d^f}{d^f} \delta k + \frac{1}{2} \left[\frac{d^f \partial_k^2 d^f - (\partial_k d^f)^2}{(d^f)^2} \right] \delta k^2 + O(L^{-3}) \right\} \\
&= d^f t + \partial_k d^f \eta + \frac{1}{2} \delta k \, d_2^f \eta + O(L^{-2})
\end{aligned} \tag{F.8}
$$

where

$$
d_2^f = \partial_k^2 d^f - \frac{(\partial_k d^f)^2}{d^f} \quad . \tag{F.9}
$$

Then the unit vector $\hat{\mathbf{d}}^f$ appearing in Eq.(F.7) is given by

$$
\begin{aligned}
\hat{\mathbf{d}}^f (k + \delta k) &= \frac{\mathbf{d}^f t}{d^f t \left\{ 1 + \frac{\partial_k d^f}{d^f} \delta k + \frac{1}{2} \left[\frac{d^f \partial_k^2 d^f - (\partial_k d^f)^2}{(d^f)^2} \right] \delta k^2 + O(L^{-3}) \right\}} \\
&\quad + \frac{\partial_k \mathbf{d}^f \eta}{d^f t \left\{ 1 + \frac{\partial_k d^f}{d^f} \delta k + \frac{1}{2} \left[\frac{d^f \partial_k^2 d^f - (\partial_k d^f)^2}{(d^f)^2} \right] \delta k^2 + O(L^{-3}) \right\}} + O(L^{-2}) \\
&= \frac{\mathbf{d}^f t}{d^f t} \left\{ 1 - \frac{\partial_k d^f}{d^f} \delta k \right\} + \frac{\partial_k \mathbf{d}^f \eta}{d^f t} + O(L^{-2}) \\
&= \hat{\mathbf{d}}^f + \partial_k \hat{\mathbf{d}}^f \delta k + O(L^{-2})
\end{aligned} \tag{F.10}
$$

whence one obtains

$$
\begin{aligned}
e^{i\left[\mathbf{d}^f(k+\delta k)t/\hbar\right]\cdot\boldsymbol{\sigma}} &= \cos\left[(d^f t + \partial_k d^f \eta + \tfrac{1}{2}\delta k d_2^f \eta)/\hbar\right] \\
&\quad + i\left[(\hat{\mathbf{d}}^f + \partial_k \hat{\mathbf{d}}^f \delta k)\cdot\boldsymbol{\sigma}\right]\sin\left[(d^f t + \partial_k d^f \eta + \tfrac{1}{2}\delta k d_2^f \eta)/\hbar\right] + O(L^{-2}) \\
&= e^{i[(d^f t + \partial_k d^f \eta + \frac{1}{2}\delta k d_2^f \eta)/\hbar]\hat{\mathbf{d}}^f\cdot\boldsymbol{\sigma}} \\
&\quad + i\delta k \sin\left[(d^f t + \partial_k d^f \eta)/\hbar\right][\partial_k \hat{\mathbf{d}}^f \cdot \boldsymbol{\sigma}] + O(L^{-2})
\end{aligned}
\tag{F.11}
$$

and

$$
\begin{aligned}
e^{i\left[\mathbf{d}^f(k+\delta k)t/\hbar\right]\cdot\boldsymbol{\sigma}}&e^{-i\left[\mathbf{d}^f(k)t/\hbar\right]\cdot\boldsymbol{\sigma}} = \\
&= e^{i\left[(\partial_k d^f \eta + \frac{1}{2}\delta k d_2^f \eta)/\hbar\right]\hat{\mathbf{d}}^f\cdot\boldsymbol{\sigma}} + i\delta k \sin\left[(d^f t + \partial_k d^f \eta)/\hbar\right][\partial_k \hat{\mathbf{d}}^f \cdot \boldsymbol{\sigma}]e^{-i\left[\mathbf{d}^f t/\hbar\right]\cdot\boldsymbol{\sigma}} + O(L^{-2}) \\
&= \cos\left[(\partial_k d^f \eta + \tfrac{1}{2}\delta k d_2^f \eta)/\hbar\right] + i\sin\left[(\partial_k d^f \eta + \tfrac{1}{2}\delta k d_2^f \eta)/\hbar\right][\hat{\mathbf{d}}^f \cdot \boldsymbol{\sigma}] \\
&\quad + i\delta k \sin\left[(d^f t + \partial_k d^f \eta)/\hbar\right]\cos\left[d^f t/\hbar\right][\partial_k \hat{\mathbf{d}}^f \cdot \boldsymbol{\sigma}] \\
&\quad + i\delta k \sin\left[(d^f t + \partial_k d^f \eta)/\hbar\right]\sin\left[d^f t/\hbar\right][(\partial_k \hat{\mathbf{d}}^f \times \hat{\mathbf{d}}^f)\cdot\boldsymbol{\sigma}] + O(L^{-2}) \\
&= \cos\left[\partial_k d^f \eta/\hbar\right] - \tfrac{1}{2}\sin\left[\partial_k d^f \eta/\hbar\right][\delta k d_2^f \eta/\hbar] \\
&\quad + i\sin\left[\partial_k d^f \eta/\hbar\right][\hat{\mathbf{d}}^f \cdot \boldsymbol{\sigma}] + \tfrac{i}{2}\cos\left[\partial_k d^f \eta/\hbar\right]\left[\delta k d_2^f \eta/\hbar\right][\hat{\mathbf{d}}^f \cdot \boldsymbol{\sigma}] \\
&\quad + i\delta k \sin\left[(d^f t + \partial_k d^f \eta)/\hbar\right]\cos\left[d^f t/\hbar\right][\partial_k \hat{\mathbf{d}}^f \cdot \boldsymbol{\sigma}] \\
&\quad + i\delta k \sin\left[(d^f t + \partial_k d^f \eta)/\hbar\right]\sin\left[d^f t/\hbar\right][(\partial_k \hat{\mathbf{d}}^f \times \hat{\mathbf{d}}^f)\cdot\boldsymbol{\sigma}] + O(L^{-2}) \\
&= e^{i[\partial_k d^f \eta/\hbar][\hat{\mathbf{d}}^f\cdot\boldsymbol{\sigma}]} - \frac{\delta k}{2}\sin[\partial_k d^f \eta/\hbar][d_2^f \eta/\hbar] + i\frac{\delta k}{2}\cos[\partial_k d^f \eta/\hbar][d_2^f \eta/\hbar][\hat{\mathbf{d}}^f \cdot \boldsymbol{\sigma}] \\
&\quad + i\delta k \cos\left[\partial_k d^f \eta/\hbar\right]\left\{\sin\left[d^f t/\hbar\right]\cos\left[d^f t/\hbar\right][\partial_k \hat{\mathbf{d}}^f \cdot \boldsymbol{\sigma}] + \sin^2\left[d^f t/\hbar\right][(\partial_k \hat{\mathbf{d}}^f \times \hat{\mathbf{d}}^f)\cdot\boldsymbol{\sigma}]\right\} \\
&\quad + i\delta k \sin\left[\partial_k d^f \eta/\hbar\right]\left\{\cos^2\left[d^f t/\hbar\right][\partial_k \hat{\mathbf{d}}^f \cdot \boldsymbol{\sigma}] + \cos\left[d^f t/\hbar\right]\sin\left[d^f t/\hbar\right][(\partial_k \hat{\mathbf{d}}^f \times \hat{\mathbf{d}}^f)\cdot\boldsymbol{\sigma}]\right\} \\
&\quad + O(L^{-2}) \quad .
\end{aligned}
\tag{F.12}
$$

Thus we finally arrive at

$$
\begin{aligned}
\xi_-(k,t,L) = \\
&+\langle u_-^i|e^{i[\partial_k d^f \eta/\hbar][\hat{\mathbf{d}}^f \cdot \boldsymbol{\sigma}]}|u_-^i\rangle + \delta k \langle \partial_k u_-^i|e^{i[\partial_k d^f \eta/\hbar][\hat{\mathbf{d}}^f \cdot \boldsymbol{\sigma}]}|u_-^i\rangle \\
&-\frac{\delta k}{2}\sin[\partial_k d^f \eta/\hbar][d_2^f \eta/\hbar]\langle u_-^i|u_-^i\rangle + i\frac{\delta k}{2}\cos[\partial_k d^f \eta/\hbar][d_2^f \eta/\hbar]\langle u_-^i|[\hat{\mathbf{d}}^f \cdot \boldsymbol{\sigma}]|u_-^i\rangle \\
&+i\delta k \cos\left[\partial_k d^f \eta/\hbar\right]\langle u_-^i|\left\{\frac{1}{2}\sin\left[2d^f t/\hbar\right][\partial_k\hat{\mathbf{d}}^f \cdot \boldsymbol{\sigma}] + \frac{1}{2}\left(1-\cos\left[2d^f t/\hbar\right]\right)[(\partial_k\hat{\mathbf{d}}^f \times \hat{\mathbf{d}}^f)\cdot\boldsymbol{\sigma}]\right\}|u_-^i\rangle \\
&+i\delta k \sin\left[\partial_k d^f \eta/\hbar\right]\langle u_-^i|\left\{\frac{1}{2}\left(1+\cos\left[2d^f t/\hbar\right]\right)[\partial_k\hat{\mathbf{d}}^f \cdot \boldsymbol{\sigma}] + \frac{1}{2}\sin\left[2d^f t/\hbar\right][(\partial_k\hat{\mathbf{d}}^f \times \hat{\mathbf{d}}^f)\cdot\boldsymbol{\sigma}]\right\}|u_-^i\rangle \\
&+O(L^{-2}) \\
&= \xi_-^{(0)}(k,\eta) + \delta k\,\xi_-^{(1)}(k,\eta,t) + O(L^{-2})
\end{aligned}
\tag{F.13}
$$

where

$$
\begin{aligned}
\xi_-^{(0)}(k,\eta) &= \langle u_-^i|e^{i[\partial_k d^f \eta/\hbar][\hat{\mathbf{d}}^f \cdot \boldsymbol{\sigma}]}|u_-^i\rangle = \cos[\partial_k d^f \eta/\hbar] + i\sin[\partial_k d^f \eta/\hbar]\langle u^i|[\hat{\mathbf{d}}^f \cdot \boldsymbol{\sigma}]|u^i\rangle \\
&= \cos[\partial_k d^f \eta/\hbar] + i[\hat{\mathbf{d}}^f \cdot \hat{\mathbf{d}}^i]\sin[\partial_k d^f \eta/\hbar]
\end{aligned}
\tag{F.14}
$$

while $\xi_-^{(1)}(k,\eta,t) = \xi_-^{(1,A)}(k,\eta) + \xi_-^{(1,B)}(k,\eta,t)$ and

$$
\begin{aligned}
\xi_-^{(1,A)}(k,\eta) &= -\frac{1}{2}\sin[\partial_k d^f \eta/\hbar][d_2^f \eta/\hbar] - \sin[\partial_k d^f \eta/\hbar]\mathrm{Im}\{\langle \partial_k u_-^i|[\hat{\mathbf{d}}^f \cdot \boldsymbol{\sigma}]|u_-^i\rangle\} \\
&\quad +\frac{i}{2}\cos[\partial_k d^f \eta/\hbar][d_2^f \eta/\hbar]\langle u_-^i|[\hat{\mathbf{d}}^f \cdot \boldsymbol{\sigma}]|u_-^i\rangle + i\sin[\partial_k d^f \eta/\hbar]\mathrm{Re}\{\langle \partial_k u_-^i|[\hat{\mathbf{d}}^f \cdot \boldsymbol{\sigma}]|u_-^i\rangle\} \\
&\quad +i\cos[\partial_k d^f \eta/\hbar]\langle u_-^i|i\partial_k|u_-^i\rangle + \frac{i}{2}\cos\left[\partial_k d^f \eta/\hbar\right]\langle u_-^i|[(\partial_k\hat{\mathbf{d}}^f \times \hat{\mathbf{d}}^f)\cdot\boldsymbol{\sigma}]|u_-^i\rangle \\
&\quad +\frac{i}{2}\sin\left[\partial_k d^f \eta/\hbar\right]\langle u_-^i|[\partial_k\hat{\mathbf{d}}^f \cdot \boldsymbol{\sigma}]|u_-^i\rangle
\end{aligned}
\tag{F.15}
$$

$$
\begin{aligned}
\xi_-^{(1,B)}(k,\eta,t) = \\
&+\frac{i}{2}\sin\left[2d^f t/\hbar\right]\langle u_-^i|\left\{\cos\left[\partial_k d^f \eta/\hbar\right][\partial_k\hat{\mathbf{d}}^f \cdot \boldsymbol{\sigma}] + \sin\left[\partial_k d^f \eta/\hbar\right][(\partial_k\hat{\mathbf{d}}^f \times \hat{\mathbf{d}}^f)\cdot\boldsymbol{\sigma}]\right\}|u_-^i\rangle \\
&+\frac{i}{2}\cos\left[2d^f t/\hbar\right]\langle u_-^i|\left\{-\cos\left[\partial_k d^f \eta/\hbar\right][(\partial_k\hat{\mathbf{d}}^f \times \hat{\mathbf{d}}^f)\cdot\boldsymbol{\sigma}] + \sin\left[\partial_k d^f \eta/\hbar\right][\partial_k\hat{\mathbf{d}}^f \cdot \boldsymbol{\sigma}]\right\}|u_-^i\rangle.
\end{aligned}
\tag{F.16}
$$

Notice that, since by definition of ξ_- its gauge dependence amounts to corrections of order δk, the zeroth order contribution $\xi_-^{(0)}$ turns out to be *gauge invariant*. Moreover, the modulus of ξ_- is given by

$$|\xi_-| = \sqrt{|\xi_-^{(0)}|^2 + 2\delta k \operatorname{Re}\left\{\xi_-^{(0)}\xi_-^{(1)}\right\} + O(L^{-2})} = |\xi_-^{(0)}| + \delta k \operatorname{Re}\left\{\frac{\xi_-^{(0)}\xi_-^{(1)}}{|\xi_-^{(0)}|}\right\} + O(L^{-2})$$

$$(\text{F.17})$$

while the argument equals

$$\arg\left\{\xi_-\right\} = \operatorname{Im}\left\{\ln\left[\xi_-^{(0)} + \delta k\xi_-^{(1)} + O(L^{-2})\right]\right\} = \arg\left\{\xi_-^{(0)}\right\} + \delta k \operatorname{Im}\left\{\frac{(\xi_-^{(0)})^*\xi_-^{(1)}}{|\xi_-^{(0)}|^2}\right\} + O(L^{-2})$$

$$(\text{F.18})$$

The Berry phase thus acquires the form

$$\begin{aligned}
\varphi_{B-} &= \sum_{k\in BZ}\arg\xi_- = \sum_{k\in BZ}\arg\left\{\xi_-^{(0)}\right\} + \sum_{k\in BZ}\delta k \operatorname{Im}\left\{\frac{(\xi_-^{(0)})^*\xi_-^{(1)}}{|\xi_-^{(0)}|^2}\right\} + O(L^{-1}) \\
&= \varphi_{B-}^{(0)} + \varphi_{B-}^{(1)} + O(L^{-1})
\end{aligned}$$

$$(\text{F.19})$$

where

$$\varphi_{B-}^{(0)} = \sum_{k\in BZ}\arg\left\{\xi_-^{(0)}\right\} \approx \frac{L}{2\pi}\int_{-\pi}^{\pi}dk\,\arg\left\{\xi_-^{(0)}\right\}$$

$$(\text{F.20})$$

while

$$\varphi_{B-}^{(1)} = \sum_{k\in BZ}\delta k \operatorname{Im}\left\{\frac{(\xi_-^{(0)})^*\xi_-^{(1)}}{|\xi_-^{(0)}|^2}\right\} \approx \int_{-\pi}^{\pi}dk\operatorname{Im}\left\{\frac{(\xi_-^{(0)})^*\xi_-^{(1,A)}}{|\xi_-^{(0)}|^2}\right\}\quad.$$

$$(\text{F.21})$$

In Eq.(F.20) the summation over k has been replaced by an integral, according to the usual recipe $\sum_{k\in BZ}\to (L/2\pi)\int_{-\pi}^{\pi}dk$, since the function $\arg\{\xi_-^{(0)}(k,\eta)\}$ varies smoothly in k with respect to δk. The same procedure cannot be straightforwardly applied to the summation in Eq.(F.21) since $\xi_-^{(1)}(k,\eta,t)$ contains terms proportional to $\sin\left[2d^f(k)t/\hbar\right]$ and $\cos\left[2d^f(k)t/\hbar\right]$, which are rapidly oscillatory functions of k for $t\sim L$ [see the contribution $\xi_-^{(1,B)}(k,\eta,t)$ in Eq.(F.16)]. Nonetheless, because of this highly oscillatory behavior, the summation of such terms is negligible in the STSL and $\varphi_{B-}^{(1)}$ in Eq.(F.21) is eventually

recast into an integral involving the contribution $\xi_-^{(1,A)}(k, \eta)$ only.

F.4 Berry phase and current operator

We start this section by showing that, for $\eta \to 0$, which corresponds to the usual thermodynamic limit, one recovers the known relation $\partial_t \varphi_B(t)/2\pi = J^f(t)$ [188]. Indeed, when $\eta \to 0$, Eq.(F.13) reduces to

$$
\begin{aligned}
\xi_-(k, t, L) = {}& 1 + i\delta k (\partial_k d^f t/\hbar)\langle u_-^i|[\hat{\mathbf{d}}^f \cdot \boldsymbol{\sigma}]|u_-^i\rangle + i\delta k\langle u^i|i\partial_k|u^i\rangle \\
& + i\delta k\langle u_-^i| \left\{ \frac{1}{2} \sin\left[2d^f t/\hbar\right] [\partial_k \hat{\mathbf{d}}^f \cdot \boldsymbol{\sigma}] + \frac{1}{2}\left(1 - \cos\left[2d^f t/\hbar\right]\right)[(\partial_k \hat{\mathbf{d}}^f \times \hat{\mathbf{d}}^f) \cdot \boldsymbol{\sigma}] \right\}|u_-^i\rangle \\
& + O(L^{-2})
\end{aligned}
\tag{F.22}
$$

so that

$$
\begin{aligned}
\arg\{\xi_-(k, t, L)\} = {}& \delta k\langle u^i|i\partial_k|u^i\rangle + \delta k(\partial_k d^f t/\hbar)\langle u_-^i|[\hat{\mathbf{d}}^f \cdot \boldsymbol{\sigma}]|u_-^i\rangle \\
& + \delta k\langle u_-^i| \left\{ \frac{1}{2} \sin\left[2d^f t/\hbar\right] [\partial_k \hat{\mathbf{d}}^f \cdot \boldsymbol{\sigma}] + \frac{1}{2}\left(1 - \cos\left[2d^f t/\hbar\right]\right)[(\partial_k \hat{\mathbf{d}}^f \times \hat{\mathbf{d}}^f) \cdot \boldsymbol{\sigma}] \right\}|u_-^i\rangle \\
& + O(L^{-2})
\end{aligned}
\tag{F.23}
$$

and

$$
\begin{aligned}
\frac{\varphi_{B-}(t)}{2\pi} = {}& \frac{1}{2\pi} \sum_k \arg\{\xi_-(k, t, L)\} \\
\approx {}& \frac{1}{2\pi} \int_{-\pi}^{\pi} dk\, A_{B-}^i(k) + \frac{1}{2\pi} \int_{-\pi}^{\pi} dk [\partial_k d^f/\hbar]\langle u_-^i|[\hat{\mathbf{d}}^f \cdot \boldsymbol{\sigma}]|u_-^i\rangle\, t \\
& + \frac{1}{2\pi} \int_{-\pi}^{\pi} dk\langle u_-^i| \left\{ \frac{1}{2} \sin\left[2d^f t/\hbar\right] [\partial_k \hat{\mathbf{d}}^f \cdot \boldsymbol{\sigma}] + \frac{1}{2}\left(1 - \cos\left[2d^f t/\hbar\right]\right)[(\partial_k \hat{\mathbf{d}}^f \times \hat{\mathbf{d}}^f) \cdot \boldsymbol{\sigma}] \right\}|u_-^i\rangle \\
= {}& \frac{\varphi_{B-}(0)}{2\pi} + J_{DC}^f\, t + \int_0^t dt'\, J_{AC}^f(t')
\end{aligned}
\tag{F.24}
$$

where $A_{B-}^i(k)$ is the initial Berry connection, while J_{DC}^f and $J_{AC}^f(t)$ are the integral over the Brillouin zone of the expectation values of the operators $\mathcal{J}_{DC}^f(k) = \hbar^{-1}\partial_k d^f(\hat{\mathbf{d}}^f \cdot \boldsymbol{\sigma})$ and $\mathcal{J}_{AC}^f(k, t) = \hbar^{-1}d^f \{\cos[2d^f t/\hbar][\partial_k \hat{\mathbf{d}}^f \cdot \boldsymbol{\sigma}] + \sin[2d^f t/\hbar][(\hat{\mathbf{d}}^f \times \partial_k \hat{\mathbf{d}}^f) \cdot \boldsymbol{\sigma}]\}$, respectively, which can in turn be interpreted as the DC/AC term of k-component current operator

resulting from its Heisenberg evolution

$$
\begin{aligned}
\hbar \mathcal{J}^f(k,t) &= e^{-i[d^f t/\hbar]\hat{\mathbf{d}}^f \cdot \boldsymbol{\sigma}}[\partial_k \mathbf{d}^f \cdot \boldsymbol{\sigma}]e^{i[d^f t/\hbar]\hat{\mathbf{d}}^f \cdot \boldsymbol{\sigma}} \\
&= e^{-i[d^f t/\hbar]\hat{\mathbf{d}}^f \cdot \boldsymbol{\sigma}}[\partial_k d^f(\hat{\mathbf{d}}^f \cdot \boldsymbol{\sigma}) + d^f(\partial_k \hat{\mathbf{d}}^f \cdot \boldsymbol{\sigma})]e^{i[d^f t/\hbar]\hat{\mathbf{d}}^f \cdot \boldsymbol{\sigma}} \\
&= \partial_k d^f(\hat{\mathbf{d}}^f \cdot \boldsymbol{\sigma}) + d^f\Big(\cos[d^f t/\hbar] - i\sin[d^f t/\hbar][\hat{\mathbf{d}}^f \cdot \boldsymbol{\sigma}]\Big)\cdot \\
&\quad \cdot[\partial_k \hat{\mathbf{d}}^f \cdot \boldsymbol{\sigma}]\Big(\cos[d^f t/\hbar] + i\sin[d^f t/\hbar][\hat{\mathbf{d}}^f \cdot \boldsymbol{\sigma}]\Big) \\
&= \partial_k d^f(\hat{\mathbf{d}}^f \cdot \boldsymbol{\sigma}) + d^f\Big(\cos^2[d^f t/\hbar][\partial_k \hat{\mathbf{d}}^f \cdot \boldsymbol{\sigma}] - i\sin[d^f t/\hbar]\cos[d^f t/\hbar][\hat{\mathbf{d}}^f \cdot \boldsymbol{\sigma}][\partial_k \hat{\mathbf{d}}^f \cdot \boldsymbol{\sigma}] \\
&\quad + i\sin[d^f t/\hbar]\cos[d^f t/\hbar][\partial_k \hat{\mathbf{d}}^f \cdot \boldsymbol{\sigma}][\hat{\mathbf{d}}^f \cdot \boldsymbol{\sigma}] + \sin^2[d^f t/\hbar][\hat{\mathbf{d}}^f \cdot \boldsymbol{\sigma}][\partial_k \hat{\mathbf{d}}^f \cdot \boldsymbol{\sigma}][\hat{\mathbf{d}}^f \cdot \boldsymbol{\sigma}]\Big) \\
&= \partial_k d^f(\hat{\mathbf{d}}^f \cdot \boldsymbol{\sigma}) + d^f\Big(\cos^2[d^f t/\hbar][\partial_k \hat{\mathbf{d}}^f \cdot \boldsymbol{\sigma}] + 2\sin[d^f t/\hbar]\cos[d^f t/\hbar][(\hat{\mathbf{d}}^f \times \partial_k \hat{\mathbf{d}}^f) \cdot \boldsymbol{\sigma}] \\
&\quad - \sin^2[d^f t/\hbar][\hat{\mathbf{d}}^f \times (\partial_k \hat{\mathbf{d}}^f \times \hat{\mathbf{d}}^f)] \cdot \boldsymbol{\sigma}\Big) \\
&= \partial_k d^f(\hat{\mathbf{d}}^f \cdot \boldsymbol{\sigma}) + d^f\Big(\cos^2[d^f t/\hbar][\partial_k \hat{\mathbf{d}}^f \cdot \boldsymbol{\sigma}] + 2\sin[d^f t/\hbar]\cos[d^f t/\hbar][(\hat{\mathbf{d}}^f \times \partial_k \hat{\mathbf{d}}^f) \cdot \boldsymbol{\sigma}] \\
&\quad - \sin^2[d^f t/\hbar][\partial_k \hat{\mathbf{d}}^f \cdot \boldsymbol{\sigma}]\Big) \\
&= \partial_k d^f(\hat{\mathbf{d}}^f \cdot \boldsymbol{\sigma}) + d^f\Big(\cos[2d^f t/\hbar][\partial_k \hat{\mathbf{d}}^f \cdot \boldsymbol{\sigma}] + \sin[2d^f t/\hbar][(\hat{\mathbf{d}}^f \times \partial_k \hat{\mathbf{d}}^f) \cdot \boldsymbol{\sigma}]\Big) \quad \text{(F.25)}
\end{aligned}
$$

Let us now determine the relation between $\varphi_{B-}^{(0)}$ and the current operator in the space-time scaling limit. Starting from $\xi_-^{(0)}(k,\eta) = \langle u_-^i(k)|e^{i\mathcal{J}_{DC}^f(k)\eta}|u_-^i(k)\rangle$ we get

$$
\begin{aligned}
\frac{1}{i}\partial_\eta \xi_-^{(0)}(k,\eta) &= \langle u_-^i(k)|e^{i\mathcal{J}_{DC}^f(k)\eta}\mathcal{J}_{DC}^f(k)\sum_{s=\pm}|u_s^i(k)\rangle\langle u_s^i(k)|u_-^i(k)\rangle = \\
&= \xi_-^{(0)}(k,\eta)\langle u_-^i(k)|\mathcal{J}_{DC}^f(k)|u_-^i(k)\rangle + \chi_-^{(0)}(k,\eta)\langle u_+^i(k)|\mathcal{J}_{DC}^f(k)|u_-^i(k)\rangle
\end{aligned}
$$
$$\text{(F.26)}$$

where $\chi_-^{(0)}(k,\eta) = \langle u_-^i(k)|e^{i\mathcal{J}_{DC}^f(k)\eta}|u_+^i(k)\rangle$. Then, in view of the definition

$$
\varphi_{B-}^{(0)}(\eta) = \frac{L}{2\pi}\int_{-\pi}^{\pi} dk \, \arg\xi_-^{(0)}(k,\eta) = \frac{L}{2\pi}\int_{-\pi}^{\pi} dk \, \mathrm{Im}\ln\xi_-^{(0)}(k,\eta) \qquad \text{(F.27)}
$$

we arrive at

$$
\begin{aligned}
\frac{d}{d\eta}\varphi_{B-}^{(0)}(\eta) &= \frac{L}{2\pi}\int_{-\pi}^{\pi} dk\,\mathrm{Im}\frac{d}{d\eta}\ln\xi_{-}^{(0)}(k,\eta) \\
&= \frac{L}{2\pi}\int_{-\pi}^{\pi} dk\,\mathrm{Im}\frac{i\xi_{-}^{(0)}(k,\eta)\langle u_{-}^{i}(k)|\mathcal{J}_{DC}^{f}(k)|u_{-}^{i}(k)\rangle + i\chi_{-}^{(0)}(k,\eta)\langle u_{+}^{i}(k)|\mathcal{J}_{DC}^{f}(k)|u_{-}^{i}(k)\rangle}{\xi_{-}^{(0)}(k,\eta)} \\
&= \frac{L}{2\pi}\int_{-\pi}^{\pi} dk\,\langle u_{-}^{i}(k)|\mathcal{J}_{DC}^{f}(k)|u_{-}^{i}(k)\rangle + \frac{L}{2\pi}\int_{-\pi}^{\pi} dk\,\mathrm{Re}\left\{\frac{\chi_{-}^{(0)}(k,\eta)}{\xi_{-}^{(0)}(k,\eta)}\langle u_{+}^{i}(k)|\mathcal{J}_{DC}^{f}(k)|u_{-}^{i}(k)\rangle\right\}
\end{aligned}
$$

$$\text{(F.28)}$$

References

[1] M. Z. Hasan and C. L. Kane. "Colloquium: Topological insulators". In: *Rev. Mod. Phys.* 82 (4 Nov. 2010), pp. 3045–3067. DOI: 10.1103/RevModPhys.82.3045. URL: https://link.aps.org/doi/10.1103/RevModPhys.82.3045.

[2] Xiao-Liang Qi and Shou-Cheng Zhang. "Topological insulators and superconductors". In: *Rev. Mod. Phys.* 83 (4 Oct. 2011), pp. 1057–1110. DOI: 10.1103/RevModPhys.83.1057. URL: https://link.aps.org/doi/10.1103/RevModPhys.83.1057.

[3] Ching-Kai Chiu et al. "Classification of topological quantum matter with symmetries". In: *Rev. Mod. Phys.* 88 (3 Aug. 2016), p. 035005. DOI: 10.1103/RevModPhys.88.035005. URL: https://link.aps.org/doi/10.1103/RevModPhys.88.035005.

[4] Xiao-Gang Wen. "Colloquium: Zoo of quantum-topological phases of matter". In: *Rev. Mod. Phys.* 89 (4 Dec. 2017), p. 041004. DOI: 10.1103/RevModPhys.89.041004. URL: https://link.aps.org/doi/10.1103/RevModPhys.89.041004.

[5] Lev Davidovich Landau and Evgenii Mikhailovich Lifshitz. *Statistical Physics: Volume 5.* 3rd ed. Vol. 5. Elsevier, 1980. ISBN: 978-0-08-057046-4. DOI: 10.1016/C2009-0-24487-4.

[6] K. v. Klitzing, G. Dorda, and M. Pepper. "New Method for High-Accuracy Determination of the Fine-Structure Constant Based on Quantized Hall Resistance". In: *Phys. Rev. Lett.* 45 (6 Aug. 1980), pp. 494–497. DOI: 10.1103/PhysRevLett.45.494. URL: https://link.aps.org/doi/10.1103/PhysRevLett.45.494.

[7] David Tong. *Lectures on the Quantum Hall Effect.* 2016. DOI: 10.48550/ARXIV.1606.06687. URL: https://arxiv.org/abs/1606.06687.

[8] Lev Davidovich Landau and Evgenii Mikhailovich Lifshitz. *Quantum mechanics: non-relativistic theory.* 3rd ed. Vol. 3. Pergamon Press, 1977. ISBN: 978-0-08-020940-1. DOI: 10.1016/C2013-0-02793-4.

[9] R. B. Laughlin. "Quantized Hall conductivity in two dimensions". In: *Phys. Rev. B* 23 (10 May 1981), pp. 5632–5633. DOI: 10.1103/PhysRevB.23.5632. URL: https://link.aps.org/doi/10.1103/PhysRevB.23.5632.

[10] D. J. Thouless et al. "Quantized Hall Conductance in a Two-Dimensional Periodic Potential". In: *Phys. Rev. Lett.* 49 (6 Aug. 1982), pp. 405–408. DOI: 10.1103/PhysRevLett.49.405. URL: https://link.aps.org/doi/10.1103/PhysRevLett.49.405.

[11]   Qian Niu, D. J. Thouless, and Yong-Shi Wu. "Quantized Hall conductance as a topological invariant". In: *Phys. Rev. B* 31 (6 Mar. 1985), pp. 3372–3377. DOI: 10.1103/PhysRevB.31.3372. URL: https://link.aps.org/doi/10.1103/PhysRevB.31.3372.

[12]   J. E. Avron, R. Seiler, and B. Simon. "Homotopy and Quantization in Condensed Matter Physics". In: *Phys. Rev. Lett.* 51 (1 July 1983), pp. 51–53. DOI: 10.1103/PhysRevLett.51.51. URL: https://link.aps.org/doi/10.1103/PhysRevLett.51.51.

[13]   D J Thouless. "Localisation and the two-dimensional Hall effect". In: *Journal of Physics C: Solid State Physics* 14.23 (Aug. 1981), p. 3475. DOI: 10.1088/0022-3719/14/23/022. URL: https://dx.doi.org/10.1088/0022-3719/14/23/022.

[14]   B. I. Halperin. "Quantized Hall conductance, current-carrying edge states, and the existence of extended states in a two-dimensional disordered potential". In: *Phys. Rev. B* 25 (4 Feb. 1982), pp. 2185–2190. DOI: 10.1103/PhysRevB.25.2185. URL: https://link.aps.org/doi/10.1103/PhysRevB.25.2185.

[15]   Edward Witten. "Fermion path integrals and topological phases". In: *Rev. Mod. Phys.* 88 (3 July 2016), p. 035001. DOI: 10.1103/RevModPhys.88.035001. URL: https://link.aps.org/doi/10.1103/RevModPhys.88.035001.

[16]   F. D. M. Haldane. "Model for a Quantum Hall Effect without Landau Levels: Condensed-Matter Realization of the "Parity Anomaly"". In: *Phys. Rev. Lett.* 61 (18 Oct. 1988), pp. 2015–2018. DOI: 10.1103/PhysRevLett.61.2015. URL: https://link.aps.org/doi/10.1103/PhysRevLett.61.2015.

[17]   C. L. Kane and E. J. Mele. "Quantum Spin Hall Effect in Graphene". In: *Phys. Rev. Lett.* 95 (22 Nov. 2005), p. 226801. DOI: 10.1103/PhysRevLett.95.226801. URL: https://link.aps.org/doi/10.1103/PhysRevLett.95.226801.

[18]   C. L. Kane and E. J. Mele. "Z_2 Topological Order and the Quantum Spin Hall Effect". In: *Phys. Rev. Lett.* 95 (14 Sept. 2005), p. 146802. DOI: 10.1103/PhysRevLett.95.146802. URL: https://link.aps.org/doi/10.1103/PhysRevLett.95.146802.

[19]   B. Andrei Bernevig and Shou-Cheng Zhang. "Quantum Spin Hall Effect". In: *Phys. Rev. Lett.* 96 (10 Mar. 2006), p. 106802. DOI: 10.1103/PhysRevLett.96.106802. URL: https://link.aps.org/doi/10.1103/PhysRevLett.96.106802.

[20]   Xiao-Liang Qi, Yong-Shi Wu, and Shou-Cheng Zhang. "Topological quantization of the spin Hall effect in two-dimensional paramagnetic semiconductors". In: *Phys. Rev. B* 74 (8 Aug. 2006), p. 085308. DOI: 10.1103/PhysRevB.74.085308. URL: https://link.aps.org/doi/10.1103/PhysRevB.74.085308.

[21]   B. Andrei Bernevig, Taylor L. Hughes, and Shou-Cheng Zhang. "Quantum Spin Hall Effect and Topological Phase Transition in HgTe Quantum Wells". In: *Science* 314.5806 (2006), pp. 1757–1761. DOI: 10.1126/science.1133734. eprint: https://www.science.org/doi/pdf/10.1126/science.1133734. URL: https://www.science.org/doi/abs/10.1126/science.1133734.

[22]   Markus König et al. "Quantum Spin Hall Insulator State in HgTe Quantum Wells". In: *Science* 318.5851 (2007), pp. 766–770. DOI: 10.1126/science.1148047. eprint: https://www.science.org/doi/pdf/10.1126/science.1148047. URL: https://www.science.org/doi/abs/10.1126/science.1148047.

[23] Roland Winkler. *Spin-orbit Coupling Effects in Two-Dimensional Electron and Hole Systems*. Springer Tracts in Modern Physics. Springer Berlin, Heidelberg, 2003. DOI: 10.1007/b13586.

[24] K. S. Novoselov et al. "Room-Temperature Quantum Hall Effect in Graphene". In: *Science* 315.5817 (2007), pp. 1379–1379. DOI: 10.1126/science.1137201. eprint: https://www.science.org/doi/pdf/10.1126/science.1137201. URL: https://www.science.org/doi/abs/10.1126/science.1137201.

[25] Liangzhi Kou et al. "Graphene-Based Topological Insulator with an Intrinsic Bulk Band Gap above Room Temperature". In: *Nano Letters* 13.12 (2013), pp. 6251–6255. DOI: 10.1021/nl4037214. eprint: https://doi.org/10.1021/nl4037214. URL: https://doi.org/10.1021/nl4037214.

[26] Sanfeng Wu et al. "Observation of the quantum spin Hall effect up to 100 kelvin in a monolayer crystal". In: *Science* 359.6371 (2018), pp. 76–79. DOI: 10.1126/science.aan6003. eprint: https://www.science.org/doi/pdf/10.1126/science.aan6003. URL: https://www.science.org/doi/abs/10.1126/science.aan6003.

[27] Liang Fu, C. L. Kane, and E. J. Mele. "Topological Insulators in Three Dimensions". In: *Phys. Rev. Lett.* 98 (10 Mar. 2007), p. 106803. DOI: 10.1103/PhysRevLett.98.106803. URL: https://link.aps.org/doi/10.1103/PhysRevLett.98.106803.

[28] J. E. Moore and L. Balents. "Topological invariants of time-reversal-invariant band structures". In: *Phys. Rev. B* 75 (12 Mar. 2007), p. 121306. DOI: 10.1103/PhysRevB.75.121306. URL: https://link.aps.org/doi/10.1103/PhysRevB.75.121306.

[29] Rahul Roy. "Topological phases and the quantum spin Hall effect in three dimensions". In: *Phys. Rev. B* 79 (19 May 2009), p. 195322. DOI: 10.1103/PhysRevB.79.195322. URL: https://link.aps.org/doi/10.1103/PhysRevB.79.195322.

[30] D. Hsieh et al. "A topological Dirac insulator in a quantum spin Hall phase". In: *Nature* 452.7190 (2008), pp. 970–974. DOI: 10.1038/nature06843. URL: https://doi.org/10.1038/nature06843.

[31] Cui-Zu Chang et al. "Experimental Observation of the Quantum Anomalous Hall Effect in a Magnetic Topological Insulator". In: *Science* 340.6129 (2013), pp. 167–170. DOI: 10.1126/science.1234414. eprint: https://www.science.org/doi/pdf/10.1126/science.1234414. URL: https://www.science.org/doi/abs/10.1126/science.1234414.

[32] D. C. Tsui, H. L. Stormer, and A. C. Gossard. "Two-Dimensional Magnetotransport in the Extreme Quantum Limit". In: *Phys. Rev. Lett.* 48 (22 May 1982), pp. 1559–1562. DOI: 10.1103/PhysRevLett.48.1559. URL: https://link.aps.org/doi/10.1103/PhysRevLett.48.1559.

[33] R. B. Laughlin. "Anomalous Quantum Hall Effect: An Incompressible Quantum Fluid with Fractionally Charged Excitations". In: *Phys. Rev. Lett.* 50 (18 May 1983), pp. 1395–1398. DOI: 10.1103/PhysRevLett.50.1395. URL: https://link.aps.org/doi/10.1103/PhysRevLett.50.1395.

[34] R. de-Picciotto et al. "Direct observation of a fractional charge". In: *Nature* 389.6647 (1997), pp. 162–164. DOI: 10.1038/38241. URL: https://doi.org/10.1038/38241.

[35] L. Saminadayar et al. "Observation of the $e/3$ Fractionally Charged Laughlin Quasiparticle". In: *Phys. Rev. Lett.* 79 (13 Sept. 1997), pp. 2526–2529. DOI: 10.1103/PhysRevLett.79.2526. URL: https://link.aps.org/doi/10.1103/PhysRevLett.79.2526.

[36] B. I. Halperin. "Statistics of Quasiparticles and the Hierarchy of Fractional Quantized Hall States". In: *Phys. Rev. Lett.* 52 (18 Apr. 1984), pp. 1583–1586. DOI: 10.1103/PhysRevLett.52.1583. URL: https://link.aps.org/doi/10.1103/PhysRevLett.52.1583.

[37] Daniel Arovas, J. R. Schrieffer, and Frank Wilczek. "Fractional Statistics and the Quantum Hall Effect". In: *Phys. Rev. Lett.* 53 (7 Aug. 1984), pp. 722–723. DOI: 10.1103/PhysRevLett.53.722. URL: https://link.aps.org/doi/10.1103/PhysRevLett.53.722.

[38] J. M. Leinaas and J. Myrheim. "On the theory of identical particles". In: *Il Nuovo Cimento B (1971-1996)* 37.1 (1977), pp. 1–23. DOI: 10.1007/BF02727953. URL: https://doi.org/10.1007/BF02727953.

[39] Frank Wilczek. "Magnetic Flux, Angular Momentum, and Statistics". In: *Phys. Rev. Lett.* 48 (17 Apr. 1982), pp. 1144–1146. DOI: 10.1103/PhysRevLett.48.1144. URL: https://link.aps.org/doi/10.1103/PhysRevLett.48.1144.

[40] Frank Wilczek. "Quantum Mechanics of Fractional-Spin Particles". In: *Phys. Rev. Lett.* 49 (14 Oct. 1982), pp. 957–959. DOI: 10.1103/PhysRevLett.49.957. URL: https://link.aps.org/doi/10.1103/PhysRevLett.49.957.

[41] J. Nakamura et al. "Direct observation of anyonic braiding statistics". In: *Nature Physics* 16.9 (2020), pp. 931–936. DOI: 10.1038/s41567-020-1019-1. URL: https://doi.org/10.1038/s41567-020-1019-1.

[42] H. Bartolomei et al. "Fractional statistics in anyon collisions". In: *Science* 368.6487 (2020), pp. 173–177. DOI: 10.1126/science.aaz5601. eprint: https://www.science.org/doi/pdf/10.1126/science.aaz5601. URL: https://www.science.org/doi/abs/10.1126/science.aaz5601.

[43] R. Willett et al. "Observation of an even-denominator quantum number in the fractional quantum Hall effect". In: *Phys. Rev. Lett.* 59 (15 Oct. 1987), pp. 1776–1779. DOI: 10.1103/PhysRevLett.59.1776. URL: https://link.aps.org/doi/10.1103/PhysRevLett.59.1776.

[44] Chetan Nayak and Frank Wilczek. "2n-quasihole states realize 2^{n-1}-dimensional spinor braiding statistics in paired quantum Hall states". In: *Nuclear Physics B* 479.3 (1996), pp. 529–553. ISSN: 0550-3213. DOI: https://doi.org/10.1016/0550-3213(96)00430-0. URL: https://www.sciencedirect.com/science/article/pii/055032139600430.

[45] Frank Wilczek and A. Zee. "Appearance of Gauge Structure in Simple Dynamical Systems". In: *Phys. Rev. Lett.* 52 (24 June 1984), pp. 2111–2114. DOI: 10.1103/PhysRevLett.52.2111. URL: https://link.aps.org/doi/10.1103/PhysRevLett.52.2111.

[46] M. Dolev et al. "Observation of a quarter of an electron charge at the $\nu = 5/2$ quantum Hall state". In: *Nature* 452.7189 (2008), pp. 829–834. DOI: 10.1038/nature06855. URL: https://doi.org/10.1038/nature06855.

[47] F. D. M. Haldane and E. H. Rezayi. "Periodic Laughlin-Jastrow wave functions for the fractional quantized Hall effect". In: *Phys. Rev. B* 31 (4 Feb. 1985), pp. 2529–2531. DOI: 10.1103/PhysRevB.31.2529. URL: https://link.aps.org/doi/10.1103/PhysRevB.31.2529.

[48] Alexei Kitaev and John Preskill. "Topological Entanglement Entropy". In: *Phys. Rev. Lett.* 96 (11 Mar. 2006), p. 110404. DOI: 10.1103/PhysRevLett.96.110404. URL: https://link.aps.org/doi/10.1103/PhysRevLett.96.110404.

[49] Michael Levin and Xiao-Gang Wen. "Detecting Topological Order in a Ground State Wave Function". In: *Phys. Rev. Lett.* 96 (11 Mar. 2006), p. 110405. DOI: 10.1103/PhysRevLett.96.110405. URL: https://link.aps.org/doi/10.1103/PhysRevLett.96.110405.

[50] A.Yu. Kitaev. "Fault-tolerant quantum computation by anyons". In: *Annals of Physics* 303.1 (2003), pp. 2–30. ISSN: 0003-4916. DOI: https://doi.org/10.1016/S0003-4916(02)00018-0. URL: https://www.sciencedirect.com/science/article/pii/S0003491602000180.

[51] P.W. Shor. "Algorithms for quantum computation: discrete logarithms and factoring". In: *Proceedings 35th Annual Symposium on Foundations of Computer Science.* 1994, pp. 124–134. DOI: 10.1109/SFCS.1994.365700.

[52] P.W. Shor. "Fault-tolerant quantum computation". In: *Proceedings of 37th Conference on Foundations of Computer Science.* 1996, pp. 56–65. DOI: 10.1109/SFCS.1996.548464.

[53] S. B. Bravyi and A. Yu. Kitaev. *Quantum codes on a lattice with boundary.* 1998. DOI: 10.48550/ARXIV.QUANT-PH/9811052. URL: https://arxiv.org/abs/quant-ph/9811052.

[54] K. J. Satzinger et al. "Realizing topologically ordered states on a quantum processor". In: *Science* 374.6572 (2021), pp. 1237–1241. DOI: 10.1126/science.abi8378. eprint: https://www.science.org/doi/pdf/10.1126/science.abi8378. URL: https://www.science.org/doi/abs/10.1126/science.abi8378.

[55] Dolev Bluvstein et al. "A quantum processor based on coherent transport of entangled atom arrays". In: *Nature* 604.7906 (2022), pp. 451–456. DOI: 10.1038/s41586-022-04592-6. URL: https://doi.org/10.1038/s41586-022-04592-6.

[56] Chetan Nayak et al. "Non-Abelian anyons and topological quantum computation". In: *Rev. Mod. Phys.* 80 (3 Sept. 2008), pp. 1083–1159. DOI: 10.1103/RevModPhys.80.1083. URL: https://link.aps.org/doi/10.1103/RevModPhys.80.1083.

[57] A Yu Kitaev. "Unpaired Majorana fermions in quantum wires". In: *Physics-Uspekhi* 44.10S (Oct. 2001), p. 131. DOI: 10.1070/1063-7869/44/10S/S29. URL: https://dx.doi.org/10.1070/1063-7869/44/10S/S29.

[58] P. G. De Gennes. *Superconductivity Of Metals And Alloys.* CRC Press, 1999. DOI: 10.1201/9780429497032.

[59] Gordon W Semenoff and Pasquale Sodano. "Stretched quantum states emerging from a Majorana medium". In: *Journal of Physics B: Atomic, Molecular and Optical Physics* 40.8 (Mar. 2007), p. 1479. DOI: 10.1088/0953-4075/40/8/002. URL: https://dx.doi.org/10.1088/0953-4075/40/8/002.

[60] G. Goldstein and C. Chamon. "Decay rates for topological memories encoded with Majorana fermions". In: *Phys. Rev. B* 84 (20 Nov. 2011), p. 205109. DOI: 10.1103/PhysRevB.84.205109. URL: https://link.aps.org/doi/10.1103/PhysRevB.84.205109.

[61] Jan Carl Budich, Stefan Walter, and Björn Trauzettel. "Failure of protection of Majorana based qubits against decoherence". In: *Phys. Rev. B* 85 (12 Mar. 2012), p. 121405. DOI: 10.1103/PhysRevB.85.121405. URL: https://link.aps.org/doi/10.1103/PhysRevB.85.121405.

[62] Diego Rainis and Daniel Loss. "Majorana qubit decoherence by quasiparticle poisoning". In: *Phys. Rev. B* 85 (17 May 2012), p. 174533. DOI: 10.1103/PhysRevB.85.174533. URL: https://link.aps.org/doi/10.1103/PhysRevB.85.174533.

[63] Karsten Flensberg. "Non-Abelian Operations on Majorana Fermions via Single-Charge Control". In: *Phys. Rev. Lett.* 106 (9 Mar. 2011), p. 090503. DOI: 10.1103/PhysRevLett.106.090503. URL: https://link.aps.org/doi/10.1103/PhysRevLett.106.090503.

[64] Frank Wilczek. "Majorana returns". In: *Nature Physics* 5.9 (2009), pp. 614–618. DOI: 10.1038/nphys1380. URL: https://doi.org/10.1038/nphys1380.

[65] Roman M. Lutchyn, Jay D. Sau, and S. Das Sarma. "Majorana Fermions and a Topological Phase Transition in Semiconductor-Superconductor Heterostructures". In: *Phys. Rev. Lett.* 105 (7 Aug. 2010), p. 077001. DOI: 10.1103/PhysRevLett.105.077001. URL: https://link.aps.org/doi/10.1103/PhysRevLett.105.077001.

[66] Yuval Oreg, Gil Refael, and Felix von Oppen. "Helical Liquids and Majorana Bound States in Quantum Wires". In: *Phys. Rev. Lett.* 105 (17 Oct. 2010), p. 177002. DOI: 10.1103/PhysRevLett.105.177002. URL: https://link.aps.org/doi/10.1103/PhysRevLett.105.177002.

[67] Jason Alicea et al. "Non-Abelian statistics and topological quantum information processing in 1D wire networks". In: *Nature Physics* 7.5 (2011), pp. 412–417. DOI: 10.1038/nphys1915. URL: https://doi.org/10.1038/nphys1915.

[68] V. Mourik et al. "Signatures of Majorana Fermions in Hybrid Superconductor-Semiconductor Nanowire Devices". In: *Science* 336.6084 (2012), pp. 1003–1007. DOI: 10.1126/science.1222360. eprint: https://www.science.org/doi/pdf/10.1126/science.1222360. URL: https://www.science.org/doi/abs/10.1126/science.1222360.

[69] Allison Linn. *Microsoft doubles down on quantum computing bet.* Nov. 20, 2016. URL: https://blogs.microsoft.com/ai/microsoft-doubles-quantum-computing-bet/.

[70] Torsten Karzig et al. "Scalable designs for quasiparticle-poisoning-protected topological quantum computation with Majorana zero modes". In: *Phys. Rev. B* 95 (23 June 2017), p. 235305. DOI: 10.1103/PhysRevB.95.235305. URL: https://link.aps.org/doi/10.1103/PhysRevB.95.235305.

[71] Ramón Aguado. "Majorana quasiparticles in condensed matter". In: *La Rivista del Nuovo Cimento* 40.11 (2017), pp. 523–593. DOI: 10.1393/ncr/i2017-10141-9. URL: https://doi.org/10.1393/ncr/i2017-10141-9.

[72] M. T. Deng et al. "Majorana bound state in a coupled quantum-dot hybrid-nanowire system". In: *Science* 354.6319 (2016), pp. 1557–1562. DOI: 10.1126/science.aaf3961. eprint: https://www.science.org/doi/pdf/10.1126/science.aaf3961. URL: https://www.science.org/doi/abs/10.1126/science.aaf3961.

[73] S. M. Albrecht et al. "Exponential protection of zero modes in Majorana islands". In: *Nature* 531.7593 (2016), pp. 206–209. DOI: 10.1038/nature17162. URL: https://doi.org/10.1038/nature17162.

[74]   Sasa Gazibegovic et al. "RETRACTED ARTICLE: Epitaxy of advanced nanowire quantum devices". In: *Nature* 548.7668 (2017), pp. 434–438. DOI: 10.1038/nature23468. URL: https://doi.org/10.1038/nature23468.

[75]   Hao Zhang et al. "RETRACTED ARTICLE: Quantized Majorana conductance". In: *Nature* 556.7699 (2018), pp. 74–79. DOI: 10.1038/nature26142. URL: https://doi.org/10.1038/nature26142.

[76]   S. Vaitiekėnas et al. "EDITORIAL CONCERN: Flux-induced topological superconductivity in full-shell nanowires". In: *Science* 367.6485 (2020), eaav3392. DOI: 10.1126/science.aav3392. eprint: https://www.science.org/doi/pdf/10.1126/science.aav3392. URL: https://www.science.org/doi/abs/10.1126/science.aav3392.

[77]   Morteza Aghaee et al. *InAs-Al Hybrid Devices Passing the Topological Gap Protocol*. 2022. DOI: 10.48550/ARXIV.2207.02472. URL: https://arxiv.org/abs/2207.02472.

[78]   Anton Akhmerov. *What can we learn from the reported discovery of Majorana states?* 2022. DOI: 10.36471/JCCM_July_2022_01.

[79]   Anatoli Polkovnikov et al. "Colloquium: Nonequilibrium dynamics of closed interacting quantum systems". In: *Rev. Mod. Phys.* 83 (3 Aug. 2011), pp. 863–883. DOI: 10.1103/RevModPhys.83.863. URL: https://link.aps.org/doi/10.1103/RevModPhys.83.863.

[80]   J. Eisert, M. Friesdorf, and C. Gogolin. "Quantum many-body systems out of equilibrium". In: *Nature Physics* 11.2 (2015), pp. 124–130. DOI: 10.1038/nphys3215. URL: https://doi.org/10.1038/nphys3215.

[81]   Aditi Mitra. "Quantum Quench Dynamics". In: *Annual Review of Condensed Matter Physics* 9.1 (2018), pp. 245–259. DOI: 10.1146/annurev-conmatphys-031016-025451. eprint: https://doi.org/10.1146/annurev-conmatphys-031016-025451. URL: https://doi.org/10.1146/annurev-conmatphys-031016-025451.

[82]   Eytan Barouch, Barry M. McCoy, and Max Dresden. "Statistical Mechanics of the XY Model. I". In: *Phys. Rev. A* 2 (3 Sept. 1970), pp. 1075–1092. DOI: 10.1103/PhysRevA.2.1075. URL: https://link.aps.org/doi/10.1103/PhysRevA.2.1075.

[83]   Eytan Barouch and Barry M. McCoy. "Statistical Mechanics of the *XY* Model. II. Spin-Correlation Functions". In: *Phys. Rev. A* 3 (2 Feb. 1971), pp. 786–804. DOI: 10.1103/PhysRevA.3.786. URL: https://link.aps.org/doi/10.1103/PhysRevA.3.786.

[84]   Eytan Barouch and Barry M. McCoy. "Statistical Mechanics of the XY Model. III". In: *Phys. Rev. A* 3 (6 June 1971), pp. 2137–2140. DOI: 10.1103/PhysRevA.3.2137. URL: https://link.aps.org/doi/10.1103/PhysRevA.3.2137.

[85]   Ferenc Iglói and Heiko Rieger. "Long-Range Correlations in the Nonequilibrium Quantum Relaxation of a Spin Chain". In: *Phys. Rev. Lett.* 85 (15 Oct. 2000), pp. 3233–3236. DOI: 10.1103/PhysRevLett.85.3233. URL: https://link.aps.org/doi/10.1103/PhysRevLett.85.3233.

[86]   K. Sengupta, Stephen Powell, and Subir Sachdev. "Quench dynamics across quantum critical points". In: *Phys. Rev. A* 69 (5 May 2004), p. 053616. DOI: 10.1103/PhysRevA.69.053616. URL: https://link.aps.org/doi/10.1103/PhysRevA.69.053616.

[87] Pasquale Calabrese and John Cardy. "Time Dependence of Correlation Functions Following a Quantum Quench". In: *Phys. Rev. Lett.* 96 (13 Apr. 2006), p. 136801. DOI: 10.1103/PhysRevLett.96.136801. URL: https://link.aps.org/doi/10.1103/PhysRevLett.96.136801.

[88] Immanuel Bloch, Jean Dalibard, and Wilhelm Zwerger. "Many-body physics with ultracold gases". In: *Rev. Mod. Phys.* 80 (3 July 2008), pp. 885–964. DOI: 10.1103/RevModPhys.80.885. URL: https://link.aps.org/doi/10.1103/RevModPhys.80.885.

[89] C. Orzel et al. "Squeezed States in a Bose-Einstein Condensate". In: *Science* 291.5512 (2001), pp. 2386–2389. DOI: 10.1126/science.1058149. eprint: https://www.science.org/doi/pdf/10.1126/science.1058149. URL: https://www.science.org/doi/abs/10.1126/science.1058149.

[90] Markus Greiner et al. "Quantum phase transition from a superfluid to a Mott insulator in a gas of ultracold atoms". In: *Nature* 415.6867 (2002), pp. 39–44. DOI: 10.1038/415039a. URL: https://doi.org/10.1038/415039a.

[91] Markus Greiner et al. "Collapse and revival of the matter wave field of a Bose–Einstein condensate". In: *Nature* 419.6902 (2002), pp. 51–54. DOI: 10.1038/nature00968. URL: https://doi.org/10.1038/nature00968.

[92] Thilo Stöferle et al. "Transition from a Strongly Interacting 1D Superfluid to a Mott Insulator". In: *Phys. Rev. Lett.* 92 (13 Mar. 2004), p. 130403. DOI: 10.1103/PhysRevLett.92.130403. URL: https://link.aps.org/doi/10.1103/PhysRevLett.92.130403.

[93] Cheng Chin et al. "Feshbach resonances in ultracold gases". In: *Rev. Mod. Phys.* 82 (2 Apr. 2010), pp. 1225–1286. DOI: 10.1103/RevModPhys.82.1225. URL: https://link.aps.org/doi/10.1103/RevModPhys.82.1225.

[94] Tim Langen, Remi Geiger, and Jörg Schmiedmayer. "Ultracold Atoms Out of Equilibrium". In: *Annual Review of Condensed Matter Physics* 6.1 (2015), pp. 201–217. DOI: 10.1146/annurev-conmatphys-031214-014548. eprint: https://doi.org/10.1146/annurev-conmatphys-031214-014548. URL: https://doi.org/10.1146/annurev-conmatphys-031214-014548.

[95] Claudio Giannetti et al. "Ultrafast optical spectroscopy of strongly correlated materials and high-temperature superconductors: a non-equilibrium approach". In: *Advances in Physics* 65.2 (2016), pp. 58–238. DOI: 10.1080/00018732.2016.1194044. eprint: https://doi.org/10.1080/00018732.2016.1194044. URL: https://doi.org/10.1080/00018732.2016.1194044.

[96] Alberto de la Torre et al. "Colloquium: Nonthermal pathways to ultrafast control in quantum materials". In: *Rev. Mod. Phys.* 93 (4 Oct. 2021), p. 041002. DOI: 10.1103/RevModPhys.93.041002. URL: https://link.aps.org/doi/10.1103/RevModPhys.93.041002.

[97] L. Perfetti et al. "Time Evolution of the Electronic Structure of $1T-\text{TaS}_2$ through the Insulator-Metal Transition". In: *Phys. Rev. Lett.* 97 (6 Aug. 2006), p. 067402. DOI: 10.1103/PhysRevLett.97.067402. URL: https://link.aps.org/doi/10.1103/PhysRevLett.97.067402.

[98] Martin Eckstein, Marcus Kollar, and Philipp Werner. "Thermalization after an Interaction Quench in the Hubbard Model". In: *Phys. Rev. Lett.* 103 (5 July 2009), p. 056403. DOI: 10.1103/PhysRevLett.103.056403. URL: https://link.aps.org/doi/10.1103/PhysRevLett.103.056403.

[99] M. Mitrano et al. "Possible light-induced superconductivity in K3C60 at high temperature". In: *Nature* 530.7591 (2016), pp. 461–464. DOI: 10.1038/nature16522. URL: https://doi.org/10.1038/nature16522.

[100] M. Budden et al. "Evidence for metastable photo-induced superconductivity in K3C60". In: *Nature Physics* 17.5 (2021), pp. 611–618. DOI: 10.1038/s41567-020-01148-1. URL: https://doi.org/10.1038/s41567-020-01148-1.

[101] S. Hofferberth et al. "Non-equilibrium coherence dynamics in one-dimensional Bose gases". In: *Nature* 449.7160 (2007), pp. 324–327. DOI: 10.1038/nature06149. URL: https://doi.org/10.1038/nature06149.

[102] S. Trotzky et al. "Probing the relaxation towards equilibrium in an isolated strongly correlated one-dimensional Bose gas". In: *Nature Physics* 8.4 (2012), pp. 325–330. DOI: 10.1038/nphys2232. URL: https://doi.org/10.1038/nphys2232.

[103] M. Gring et al. "Relaxation and Prethermalization in an Isolated Quantum System". In: *Science* 337.6100 (2012), pp. 1318–1322. DOI: 10.1126/science.1224953. eprint: https://www.science.org/doi/pdf/10.1126/science.1224953. URL: https://www.science.org/doi/abs/10.1126/science.1224953.

[104] Marc Cheneau et al. "Light-cone-like spreading of correlations in a quantum many-body system". In: *Nature* 481.7382 (2012), pp. 484–487. DOI: 10.1038/nature10748. URL: https://doi.org/10.1038/nature10748.

[105] T. Langen et al. "Local emergence of thermal correlations in an isolated quantum many-body system". In: *Nature Physics* 9.10 (2013), pp. 640–643. DOI: 10.1038/nphys2739. URL: https://doi.org/10.1038/nphys2739.

[106] J. von Neumann. "Proof of the ergodic theorem and the H-theorem in quantum mechanics". In: *The European Physical Journal H* 35.2 (2010), pp. 201–237. DOI: 10.1140/epjh/e2010-00008-5. URL: https://doi.org/10.1140/epjh/e2010-00008-5.

[107] Marcos Rigol, Vanja Dunjko, and Maxim Olshanii. "Thermalization and its mechanism for generic isolated quantum systems". In: *Nature* 452.7189 (2008), pp. 854–858. DOI: 10.1038/nature06838. URL: https://doi.org/10.1038/nature06838.

[108] Luca D'Alessio et al. "From quantum chaos and eigenstate thermalization to statistical mechanics and thermodynamics". In: *Advances in Physics* 65.3 (2016), pp. 239–362. DOI: 10.1080/00018732.2016.1198134. eprint: https://doi.org/10.1080/00018732.2016.1198134. URL: https://doi.org/10.1080/00018732.2016.1198134.

[109] J. M. Deutsch. "Quantum statistical mechanics in a closed system". In: *Phys. Rev. A* 43 (4 Feb. 1991), pp. 2046–2049. DOI: 10.1103/PhysRevA.43.2046. URL: https://link.aps.org/doi/10.1103/PhysRevA.43.2046.

[110] Mark Srednicki. "Chaos and quantum thermalization". In: *Phys. Rev. E* 50 (2 Aug. 1994), pp. 888–901. DOI: 10.1103/PhysRevE.50.888. URL: https://link.aps.org/doi/10.1103/PhysRevE.50.888.

[111] Adam M. Kaufman et al. "Quantum thermalization through entanglement in an isolated many-body system". In: *Science* 353.6301 (2016), pp. 794–800. DOI: 10.1126/science.aaf6725. eprint: https://www.science.org/doi/pdf/10.1126/science.aaf6725. URL: https://www.science.org/doi/abs/10.1126/science.aaf6725.

[112] J. Berges, Sz. Borsányi, and C. Wetterich. "Prethermalization". In: *Phys. Rev. Lett.* 93 (14 Sept. 2004), p. 142002. DOI: 10.1103/PhysRevLett.93.142002. URL: https://link.aps.org/doi/10.1103/PhysRevLett.93.142002.

[113] Marcus Kollar, F. Alexander Wolf, and Martin Eckstein. "Generalized Gibbs ensemble prediction of prethermalization plateaus and their relation to nonthermal steady states in integrable systems". In: *Phys. Rev. B* 84 (5 Aug. 2011), p. 054304. DOI: 10.1103/PhysRevB.84.054304. URL: https://link.aps.org/doi/10.1103/PhysRevB.84.054304.

[114] Matteo Marcuzzi et al. "Prethermalization in a Nonintegrable Quantum Spin Chain after a Quench". In: *Phys. Rev. Lett.* 111 (19 Nov. 2013), p. 197203. DOI: 10.1103/PhysRevLett.111.197203. URL: https://link.aps.org/doi/10.1103/PhysRevLett.111.197203.

[115] Tim Langen, Thomas Gasenzer, and Jörg Schmiedmayer. "Prethermalization and universal dynamics in near-integrable quantum systems". In: *Journal of Statistical Mechanics: Theory and Experiment* 2016.6 (June 2016), p. 064009. DOI: 10.1088/1742-5468/2016/06/064009. URL: https://dx.doi.org/10.1088/1742-5468/2016/06/064009.

[116] Yijun Tang et al. "Thermalization near Integrability in a Dipolar Quantum Newton's Cradle". In: *Phys. Rev. X* 8 (2 May 2018), p. 021030. DOI: 10.1103/PhysRevX.8.021030. URL: https://link.aps.org/doi/10.1103/PhysRevX.8.021030.

[117] Masahito Ueda. "Quantum equilibration, thermalization and prethermalization in ultracold atoms". In: *Nature Reviews Physics* 2.12 (2020), pp. 669–681. DOI: 10.1038/s42254-020-0237-x. URL: https://doi.org/10.1038/s42254-020-0237-x.

[118] Toshiya Kinoshita, Trevor Wenger, and David S. Weiss. "A quantum Newton's cradle". In: *Nature* 440.7086 (2006), pp. 900–903. DOI: 10.1038/nature04693. URL: https://doi.org/10.1038/nature04693.

[119] Jean-Sébastien Caux and Jorn Mossel. "Remarks on the notion of quantum integrability". In: *Journal of Statistical Mechanics: Theory and Experiment* 2011.02 (Feb. 2011), P02023. DOI: 10.1088/1742-5468/2011/02/P02023. URL: https://dx.doi.org/10.1088/1742-5468/2011/02/P02023.

[120] Lev Vidmar and Marcos Rigol. "Generalized Gibbs ensemble in integrable lattice models". In: *Journal of Statistical Mechanics: Theory and Experiment* 2016.6 (June 2016), p. 064007. DOI: 10.1088/1742-5468/2016/06/064007. URL: https://dx.doi.org/10.1088/1742-5468/2016/06/064007.

[121] Fabian H L Essler and Maurizio Fagotti. "Quench dynamics and relaxation in isolated integrable quantum spin chains". In: *Journal of Statistical Mechanics: Theory and Experiment* 2016.6 (June 2016), p. 064002. DOI: 10.1088/1742-5468/2016/06/064002. URL: https://dx.doi.org/10.1088/1742-5468/2016/06/064002.

[122] Marcos Rigol et al. "Relaxation in a Completely Integrable Many-Body Quantum System: An Ab Initio Study of the Dynamics of the Highly Excited States of 1D Lattice Hard-Core Bosons". In: *Phys. Rev. Lett.* 98 (5 Feb. 2007), p. 050405. DOI: 10.1103/PhysRevLett.98.050405. URL: https://link.aps.org/doi/10.1103/PhysRevLett.98.050405.

[123] B. Wouters et al. "Quenching the Anisotropic Heisenberg Chain: Exact Solution and Generalized Gibbs Ensemble Predictions". In: *Phys. Rev. Lett.* 113 (11 Sept. 2014), p. 117202. DOI: 10.1103/PhysRevLett.113.117202. URL: https://link.aps.org/doi/10.1103/PhysRevLett.113.117202.

[124] Marcin Mierzejewski, Peter Prelovšek, and Tomaž Prosen. "Breakdown of the Generalized Gibbs Ensemble for Current-Generating Quenches". In: *Phys. Rev. Lett.* 113 (2 July 2014), p. 020602. DOI: 10.1103/PhysRevLett.113.020602. URL: https://link.aps.org/doi/10.1103/PhysRevLett.113.020602.

[125] Enej Ilievski, Marko Medenjak, and Tomaž Prosen. "Quasilocal Conserved Operators in the Isotropic Heisenberg Spin-1/2 Chain". In: *Phys. Rev. Lett.* 115 (12 Sept. 2015), p. 120601. DOI: 10.1103/PhysRevLett.115.120601. URL: https://link.aps.org/doi/10.1103/PhysRevLett.115.120601.

[126] E. Ilievski et al. "Complete Generalized Gibbs Ensembles in an Interacting Theory". In: *Phys. Rev. Lett.* 115 (15 Oct. 2015), p. 157201. DOI: 10.1103/PhysRevLett.115.157201. URL: https://link.aps.org/doi/10.1103/PhysRevLett.115.157201.

[127] Bruno Bertini et al. "Prethermalization and Thermalization in Models with Weak Integrability Breaking". In: *Phys. Rev. Lett.* 115 (18 Oct. 2015), p. 180601. DOI: 10.1103/PhysRevLett.115.180601. URL: https://link.aps.org/doi/10.1103/PhysRevLett.115.180601.

[128] Tim Langen et al. "Experimental observation of a generalized Gibbs ensemble". In: *Science* 348.6231 (2015), pp. 207–211. DOI: 10.1126/science.1257026. eprint: https://www.science.org/doi/pdf/10.1126/science.1257026. URL: https://www.science.org/doi/abs/10.1126/science.1257026.

[129] Rahul Nandkishore and David A. Huse. "Many-Body Localization and Thermalization in Quantum Statistical Mechanics". In: *Annual Review of Condensed Matter Physics* 6.1 (2015), pp. 15–38. DOI: 10.1146/annurev-conmatphys-031214-014726. eprint: https://doi.org/10.1146/annurev-conmatphys-031214-014726. URL: https://doi.org/10.1146/annurev-conmatphys-031214-014726.

[130] Dmitry A. Abanin et al. "Colloquium: Many-body localization, thermalization, and entanglement". In: *Rev. Mod. Phys.* 91 (2 May 2019), p. 021001. DOI: 10.1103/RevModPhys.91.021001. URL: https://link.aps.org/doi/10.1103/RevModPhys.91.021001.

[131] P. W. Anderson. "Absence of Diffusion in Certain Random Lattices". In: *Phys. Rev.* 109 (5 Mar. 1958), pp. 1492–1505. DOI: 10.1103/PhysRev.109.1492. URL: https://link.aps.org/doi/10.1103/PhysRev.109.1492.

[132] Patrick A. Lee and T. V. Ramakrishnan. "Disordered electronic systems". In: *Rev. Mod. Phys.* 57 (2 Apr. 1985), pp. 287–337. DOI: 10.1103/RevModPhys.57.287. URL: https://link.aps.org/doi/10.1103/RevModPhys.57.287.

[133] B Kramer and A MacKinnon. "Localization: theory and experiment". In: *Reports on Progress in Physics* 56.12 (Dec. 1993), p. 1469. DOI: 10.1088/0034-4885/56/12/001. URL: https://dx.doi.org/10.1088/0034-4885/56/12/001.

[134] Ferdinand Evers and Alexander D. Mirlin. "Anderson transitions". In: *Rev. Mod. Phys.* 80 (4 Oct. 2008), pp. 1355–1417. DOI: 10.1103/RevModPhys.80.1355. URL: https://link.aps.org/doi/10.1103/RevModPhys.80.1355.

[135] I. V. Gornyi, A. D. Mirlin, and D. G. Polyakov. "Interacting Electrons in Disordered Wires: Anderson Localization and Low-T Transport". In: *Phys. Rev. Lett.* 95 (20 Nov. 2005), p. 206603. DOI: 10.1103/PhysRevLett.95.206603. URL: https://link.aps.org/doi/10.1103/PhysRevLett.95.206603.

[136] D.M. Basko, I.L. Aleiner, and B.L. Altshuler. "Metal–insulator transition in a weakly interacting many-electron system with localized single-particle states". In: *Annals of Physics* 321.5 (2006), pp. 1126–1205. ISSN: 0003-4916. DOI: https://doi.org/10.1016/j.aop.2005.11.014. URL: https://www.sciencedirect.com/science/article/pii/S0003491605002630.

[137] Arijeet Pal and David A. Huse. "Many-body localization phase transition". In: *Phys. Rev. B* 82 (17 Nov. 2010), p. 174411. DOI: 10.1103/PhysRevB.82.174411. URL: https://link.aps.org/doi/10.1103/PhysRevB.82.174411.

[138] J. E. Moore. "A perspective on quantum integrability in many-body-localized and Yang–Baxter systems". In: *Phil. Trans. R. Soc. A* 375 (2108 Dec. 2017). DOI: 10.1098/rsta.2016.0429.

[139] Michael Schreiber et al. "Observation of many-body localization of interacting fermions in a quasirandom optical lattice". In: *Science* 349.6250 (2015), pp. 842–845. DOI: 10.1126/science.aaa7432. eprint: https://www.science.org/doi/pdf/10.1126/science.aaa7432. URL: https://www.science.org/doi/abs/10.1126/science.aaa7432.

[140] D.A. Abanin et al. "Distinguishing localization from chaos: Challenges in finite-size systems". In: *Annals of Physics* 427 (2021), p. 168415. ISSN: 0003-4916. DOI: https://doi.org/10.1016/j.aop.2021.168415. URL: https://www.sciencedirect.com/science/article/pii/S000349162100021X.

[141] Marton Kormos et al. "Real-time confinement following a quantum quench to a non-integrable model". In: *Nature Physics* 13.3 (2017), pp. 246–249. DOI: 10.1038/nphys3934. URL: https://doi.org/10.1038/nphys3934.

[142] Titas Chanda et al. "Confinement and Lack of Thermalization after Quenches in the Bosonic Schwinger Model". In: *Phys. Rev. Lett.* 124 (18 May 2020), p. 180602. DOI: 10.1103/PhysRevLett.124.180602. URL: https://link.aps.org/doi/10.1103/PhysRevLett.124.180602.

[143] W. L. Tan et al. "Domain-wall confinement and dynamics in a quantum simulator". In: *Nature Physics* 17.6 (2021), pp. 742–747. DOI: 10.1038/s41567-021-01194-3. URL: https://doi.org/10.1038/s41567-021-01194-3.

[144] Hannes Bernien et al. "Probing many-body dynamics on a 51-atom quantum simulator". In: *Nature* 551.7682 (2017), pp. 579–584. DOI: 10.1038/nature24622. URL: https://doi.org/10.1038/nature24622.

[145]   C. J. Turner et al. "Weak ergodicity breaking from quantum many-body scars". In: *Nature Physics* 14.7 (2018), pp. 745–749. DOI: 10.1038/s41567-018-0137-5. URL: https://doi.org/10.1038/s41567-018-0137-5.

[146]   C. J. Turner et al. "Quantum scarred eigenstates in a Rydberg atom chain: Entanglement, breakdown of thermalization, and stability to perturbations". In: *Phys. Rev. B* 98 (15 Oct. 2018), p. 155134. DOI: 10.1103/PhysRevB.98.155134. URL: https://link.aps.org/doi/10.1103/PhysRevB.98.155134.

[147]   Sanjay Moudgalya et al. "Exact excited states of nonintegrable models". In: *Phys. Rev. B* 98 (23 Dec. 2018), p. 235155. DOI: 10.1103/PhysRevB.98.235155. URL: https://link.aps.org/doi/10.1103/PhysRevB.98.235155.

[148]   Pablo Sala et al. "Ergodicity Breaking Arising from Hilbert Space Fragmentation in Dipole-Conserving Hamiltonians". In: *Phys. Rev. X* 10 (1 Feb. 2020), p. 011047. DOI: 10.1103/PhysRevX.10.011047. URL: https://link.aps.org/doi/10.1103/PhysRevX.10.011047.

[149]   D. Bluvstein et al. "Controlling quantum many-body dynamics in driven Rydberg atom arrays". In: *Science* 371.6536 (2021), pp. 1355–1359. DOI: 10.1126/science.abg2530. eprint: https://www.science.org/doi/pdf/10.1126/science.abg2530. URL: https://www.science.org/doi/abs/10.1126/science.abg2530.

[150]   Maksym Serbyn, Dmitry A. Abanin, and Zlatko Papić. "Quantum many-body scars and weak breaking of ergodicity". In: *Nature Physics* 17.6 (2021), pp. 675–685. DOI: 10.1038/s41567-021-01230-2. URL: https://doi.org/10.1038/s41567-021-01230-2.

[151]   Sanjay Moudgalya, B Andrei Bernevig, and Nicolas Regnault. "Quantum many-body scars and Hilbert space fragmentation: a review of exact results". In: *Reports on Progress in Physics* 85.8 (July 2022), p. 086501. DOI: 10.1088/1361-6633/ac73a0. URL: https://dx.doi.org/10.1088/1361-6633/ac73a0.

[152]   Pengfei Zhang et al. "Many-body Hilbert space scarring on a superconducting processor". In: *Nature Physics* 19.1 (2023), pp. 120–125. DOI: 10.1038/s41567-022-01784-9. URL: https://doi.org/10.1038/s41567-022-01784-9.

[153]   Federica M. Surace et al. "Lattice Gauge Theories and String Dynamics in Rydberg Atom Quantum Simulators". In: *Phys. Rev. X* 10 (2 May 2020), p. 021041. DOI: 10.1103/PhysRevX.10.021041. URL: https://link.aps.org/doi/10.1103/PhysRevX.10.021041.

[154]   Zhihao Lan et al. "Quantum Slow Relaxation and Metastability due to Dynamical Constraints". In: *Phys. Rev. Lett.* 121 (4 July 2018), p. 040603. DOI: 10.1103/PhysRevLett.121.040603. URL: https://link.aps.org/doi/10.1103/PhysRevLett.121.040603.

[155]   Nicola Pancotti et al. "Quantum East Model: Localization, Nonthermal Eigenstates, and Slow Dynamics". In: *Phys. Rev. X* 10 (2 June 2020), p. 021051. DOI: 10.1103/PhysRevX.10.021051. URL: https://link.aps.org/doi/10.1103/PhysRevX.10.021051.

[156]   Sebastian Scherg et al. "Observing non-ergodicity due to kinetic constraints in tilted Fermi-Hubbard chains". In: *Nature Communications* 12.1 (2021), p. 4490. DOI: 10.1038/s41467-021-24726-0. URL: https://doi.org/10.1038/s41467-021-24726-0.

[157] Meng Cheng, Victor Galitski, and S. Das Sarma. "Nonadiabatic effects in the braiding of non-Abelian anyons in topological superconductors". In: *Phys. Rev. B* 84 (10 Sept. 2011), p. 104529. DOI: 10.1103/PhysRevB.84.104529. URL: https://link.aps.org/doi/10.1103/PhysRevB.84.104529.

[158] Torsten Karzig, Gil Refael, and Felix von Oppen. "Boosting Majorana Zero Modes". In: *Phys. Rev. X* 3 (4 Nov. 2013), p. 041017. DOI: 10.1103/PhysRevX.3.041017. URL: https://link.aps.org/doi/10.1103/PhysRevX.3.041017.

[159] M. S. Scheurer and A. Shnirman. "Nonadiabatic processes in Majorana qubit systems". In: *Phys. Rev. B* 88 (6 Aug. 2013), p. 064515. DOI: 10.1103/PhysRevB.88.064515. URL: https://link.aps.org/doi/10.1103/PhysRevB.88.064515.

[160] Torsten Karzig et al. "Shortcuts to non-Abelian braiding". In: *Phys. Rev. B* 91 (20 May 2015), p. 201102. DOI: 10.1103/PhysRevB.91.201102. URL: https://link.aps.org/doi/10.1103/PhysRevB.91.201102.

[161] Torsten Karzig et al. "Optimal control of Majorana zero modes". In: *Phys. Rev. B* 91 (20 May 2015), p. 201404. DOI: 10.1103/PhysRevB.91.201404. URL: https://link.aps.org/doi/10.1103/PhysRevB.91.201404.

[162] Christina Knapp et al. "The Nature and Correction of Diabatic Errors in Anyon Braiding". In: *Phys. Rev. X* 6 (4 Oct. 2016), p. 041003. DOI: 10.1103/PhysRevX.6.041003. URL: https://link.aps.org/doi/10.1103/PhysRevX.6.041003.

[163] Leticia Tarruell et al. "Creating, moving and merging Dirac points with a Fermi gas in a tunable honeycomb lattice". In: *Nature* 483.7389 (2012), pp. 302–305. DOI: 10.1038/nature10871. URL: https://doi.org/10.1038/nature10871.

[164] M. Aidelsburger et al. "Realization of the Hofstadter Hamiltonian with Ultracold Atoms in Optical Lattices". In: *Phys. Rev. Lett.* 111 (18 Oct. 2013), p. 185301. DOI: 10.1103/PhysRevLett.111.185301. URL: https://link.aps.org/doi/10.1103/PhysRevLett.111.185301.

[165] Marcos Atala et al. "Direct measurement of the Zak phase in topological Bloch bands". In: *Nature Physics* 9.12 (2013), pp. 795–800. DOI: 10.1038/nphys2790. URL: https://doi.org/10.1038/nphys2790.

[166] Gregor Jotzu et al. "Experimental realization of the topological Haldane model with ultracold fermions". In: *Nature* 515.7526 (2014), pp. 237–240. DOI: 10.1038/nature13915. URL: https://doi.org/10.1038/nature13915.

[167] L. Duca et al. "An Aharonov-Bohm interferometer for determining Bloch band topology". In: *Science* 347.6219 (2015), pp. 288–292. DOI: 10.1126/science.1259052. eprint: https://www.science.org/doi/pdf/10.1126/science.1259052. URL: https://www.science.org/doi/abs/10.1126/science.1259052.

[168] M. Aidelsburger et al. "Measuring the Chern number of Hofstadter bands with ultracold bosonic atoms". In: *Nature Physics* 11.2 (2015), pp. 162–166. DOI: 10.1038/nphys3171. URL: https://doi.org/10.1038/nphys3171.

[169] C. Schweizer et al. "Spin Pumping and Measurement of Spin Currents in Optical Superlattices". In: *Phys. Rev. Lett.* 117 (17 Oct. 2016), p. 170405. DOI: 10.1103/PhysRevLett.117.170405. URL: https://link.aps.org/doi/10.1103/PhysRevLett.117.170405.

[170] M. Lohse et al. "A Thouless quantum pump with ultracold bosonic atoms in an optical superlattice". In: *Nature Physics* 12.4 (2016), pp. 350–354. DOI: 10.1038/nphys3584. URL: https://doi.org/10.1038/nphys3584.

[171] Shuta Nakajima et al. "Topological Thouless pumping of ultracold fermions". In: *Nature Physics* 12.4 (2016), pp. 296–300. DOI: 10.1038/nphys3622. URL: https://doi.org/10.1038/nphys3622.

[172] Tracy Li et al. "Bloch state tomography using Wilson lines". In: *Science* 352.6289 (2016), pp. 1094–1097. DOI: 10.1126/science.aad5812. eprint: https://www.science.org/doi/pdf/10.1126/science.aad5812. URL: https://www.science.org/doi/abs/10.1126/science.aad5812.

[173] Michael Lohse et al. "Exploring 4D quantum Hall physics with a 2D topological charge pump". In: *Nature* 553.7686 (2018), pp. 55–58. DOI: 10.1038/nature25000. URL: https://doi.org/10.1038/nature25000.

[174] Pimonpan Sompet et al. "Realizing the symmetry-protected Haldane phase in Fermi–Hubbard ladders". In: *Nature* 606.7914 (2022), pp. 484–488. DOI: 10.1038/s41586-022-04688-z. URL: https://doi.org/10.1038/s41586-022-04688-z.

[175] Xie Chen, Zheng-Cheng Gu, and Xiao-Gang Wen. "Local unitary transformation, long-range quantum entanglement, wave function renormalization, and topological order". In: *Phys. Rev. B* 82 (15 Oct. 2010), p. 155138. DOI: 10.1103/PhysRevB.82.155138. URL: https://link.aps.org/doi/10.1103/PhysRevB.82.155138.

[176] Matthew S. Foster et al. "Quantum quench in a $p+ip$ superfluid: Winding numbers and topological states far from equilibrium". In: *Phys. Rev. B* 88 (10 Sept. 2013), p. 104511. DOI: 10.1103/PhysRevB.88.104511. URL: https://link.aps.org/doi/10.1103/PhysRevB.88.104511.

[177] P. D. Sacramento. "Fate of Majorana fermions and Chern numbers after a quantum quench". In: *Phys. Rev. E* 90 (3 Sept. 2014), p. 032138. DOI: 10.1103/PhysRevE.90.032138. URL: https://link.aps.org/doi/10.1103/PhysRevE.90.032138.

[178] M. D. Caio, N. R. Cooper, and M. J. Bhaseen. "Quantum Quenches in Chern Insulators". In: *Phys. Rev. Lett.* 115 (23 Dec. 2015), p. 236403. DOI: 10.1103/PhysRevLett.115.236403. URL: https://link.aps.org/doi/10.1103/PhysRevLett.115.236403.

[179] N. R. Cooper, J. Dalibard, and I. B. Spielman. "Topological bands for ultracold atoms". In: *Rev. Mod. Phys.* 91 (1 Mar. 2019), p. 015005. DOI: 10.1103/RevModPhys.91.015005. URL: https://link.aps.org/doi/10.1103/RevModPhys.91.015005.

[180] Pei Wang, Markus Schmitt, and Stefan Kehrein. "Universal nonanalytic behavior of the Hall conductance in a Chern insulator at the topologically driven nonequilibrium phase transition". In: *Phys. Rev. B* 93 (8 Feb. 2016), p. 085134. DOI: 10.1103/PhysRevB.93.085134. URL: https://link.aps.org/doi/10.1103/PhysRevB.93.085134.

[181] Ying Hu, Peter Zoller, and Jan Carl Budich. "Dynamical Buildup of a Quantized Hall Response from Nontopological States". In: *Phys. Rev. Lett.* 117 (12 Sept. 2016), p. 126803. DOI: 10.1103/PhysRevLett.117.126803. URL: https://link.aps.org/doi/10.1103/PhysRevLett.117.126803.

[182] Justin H. Wilson, Justin C. W. Song, and Gil Refael. "Remnant Geometric Hall Response in a Quantum Quench". In: *Phys. Rev. Lett.* 117 (23 Nov. 2016), p. 235302. DOI: 10.1103/PhysRevLett.117.235302. URL: https://link.aps.org/doi/10.1103/PhysRevLett.117.235302.

[183] F. Nur Ünal, Erich J. Mueller, and M. Ö. Oktel. "Nonequilibrium fractional Hall response after a topological quench". In: *Phys. Rev. A* 94 (5 Nov. 2016), p. 053604. DOI: 10.1103/PhysRevA.94.053604. URL: https://link.aps.org/doi/10.1103/PhysRevA.94.053604.

[184] Atanu Rajak and Amit Dutta. "Survival probability of an edge Majorana in a one-dimensional *p*-wave superconducting chain under sudden quenching of parameters". In: *Phys. Rev. E* 89 (4 Apr. 2014), p. 042125. DOI: 10.1103/PhysRevE.89.042125. URL: https://link.aps.org/doi/10.1103/PhysRevE.89.042125.

[185] P. D. Sacramento. "Edge mode dynamics of quenched topological wires". In: *Phys. Rev. E* 93 (6 June 2016), p. 062117. DOI: 10.1103/PhysRevE.93.062117. URL: https://link.aps.org/doi/10.1103/PhysRevE.93.062117.

[186] Leonardo Mazza et al. "Out-of-equilibrium dynamics and thermalization of string order". In: *Phys. Rev. B* 90 (2 July 2014), p. 020301. DOI: 10.1103/PhysRevB.90.020301. URL: https://link.aps.org/doi/10.1103/PhysRevB.90.020301.

[187] Marcello Calvanese Strinati et al. "Destruction of string order after a quantum quench". In: *Phys. Rev. B* 94 (2 July 2016), p. 024302. DOI: 10.1103/PhysRevB.94.024302. URL: https://link.aps.org/doi/10.1103/PhysRevB.94.024302.

[188] Max McGinley and Nigel R. Cooper. "Topology of One-Dimensional Quantum Systems Out of Equilibrium". In: *Phys. Rev. Lett.* 121 (9 Aug. 2018), p. 090401. DOI: 10.1103/PhysRevLett.121.090401. URL: https://link.aps.org/doi/10.1103/PhysRevLett.121.090401.

[189] Max McGinley and Nigel R. Cooper. "Classification of topological insulators and superconductors out of equilibrium". In: *Phys. Rev. B* 99 (7 Feb. 2019), p. 075148. DOI: 10.1103/PhysRevB.99.075148. URL: https://link.aps.org/doi/10.1103/PhysRevB.99.075148.

[190] G. H. Reid et al. "Dynamically Induced Symmetry Breaking and Out-of-Equilibrium Topology in a 1D Quantum System". In: *Phys. Rev. Lett.* 129 (12 Sept. 2022), p. 123202. DOI: 10.1103/PhysRevLett.129.123202. URL: https://link.aps.org/doi/10.1103/PhysRevLett.129.123202.

[191] O. Klein. "Die Reflexion von Elektronen an einem Potentialsprung nach der relativistischen Dynamik von Dirac". In: *Zeitschrift für Physik* 53.3 (1929), pp. 157–165. DOI: 10.1007/BF01339716. URL: https://doi.org/10.1007/BF01339716.

[192] Walter Greiner. *Relativistic Quantum Mechanics. Wave Equations.* 3rd ed. Springer Berlin, Heidelberg, 2000. DOI: 10.1007/978-3-662-04275-5.

[193] M. I. Katsnelson, K. S. Novoselov, and A. K. Geim. "Chiral tunnelling and the Klein paradox in graphene". In: *Nature Physics* 2.9 (2006), pp. 620–625. DOI: 10.1038/nphys384. URL: https://doi.org/10.1038/nphys384.

[194] Lorenzo Rossi, Fabrizio Dolcini, and Fausto Rossi. "Majorana-like localized spin density without bound states in topologically trivial spin-orbit coupled nanowires". In: *Phys. Rev. B* 101 (19 May 2020), p. 195421. DOI: 10.1103/PhysRevB.101.195421. URL: https://link.aps.org/doi/10.1103/PhysRevB.101.195421.

[195] Lorenzo Rossi, Fabrizio Dolcini, and Fausto Rossi. "Confinement versus interface bound states in spin-orbit coupled nanowires". In: *The European Physical Journal Plus* 135.7 (2020), p. 597. DOI: 10.1140/epjp/s13360-020-00614-2. URL: https://doi.org/10.1140/epjp/s13360-020-00614-2.

[196] Leonid P. Rokhinson, Xinyu Liu, and Jacek K. Furdyna. "The fractional a.c. Josephson effect in a semiconductor–superconductor nanowire as a signature of Majorana particles". In: *Nature Physics* 8.11 (2012), pp. 795–799. DOI: 10.1038/nphys2429. URL: https://doi.org/10.1038/nphys2429.

[197] Anindya Das et al. "Zero-bias peaks and splitting in an Al–InAs nanowire topological superconductor as a signature of Majorana fermions". In: *Nature Physics* 8.12 (2012), pp. 887–895. DOI: 10.1038/nphys2479. URL: https://doi.org/10.1038/nphys2479.

[198] M. T. Deng et al. "Anomalous Zero-Bias Conductance Peak in a Nb–InSb Nanowire–Nb Hybrid Device". In: *Nano Letters* 12.12 (2012). PMID: 23181691, pp. 6414–6419. DOI: 10.1021/nl303758w. eprint: https://doi.org/10.1021/nl303758w. URL: https://doi.org/10.1021/nl303758w.

[199] Eduardo J. H. Lee et al. "Spin-resolved Andreev levels and parity crossings in hybrid superconductor–semiconductor nanostructures". In: *Nature Nanotechnology* 9.1 (2014), pp. 79–84. DOI: 10.1038/nnano.2013.267. URL: https://doi.org/10.1038/nnano.2013.267.

[200] Önder Gül et al. "Ballistic Majorana nanowire devices". In: *Nature Nanotechnology* 13.3 (2018), pp. 192–197. DOI: 10.1038/s41565-017-0032-8. URL: https://doi.org/10.1038/s41565-017-0032-8.

[201] Eduardo J. H. Lee et al. "Zero-Bias Anomaly in a Nanowire Quantum Dot Coupled to Superconductors". In: *Phys. Rev. Lett.* 109 (18 Oct. 2012), p. 186802. DOI: 10.1103/PhysRevLett.109.186802. URL: https://link.aps.org/doi/10.1103/PhysRevLett.109.186802.

[202] Jie Liu et al. "Zero-Bias Peaks in the Tunneling Conductance of Spin-Orbit-Coupled Superconducting Wires with and without Majorana End-States". In: *Phys. Rev. Lett.* 109 (26 Dec. 2012), p. 267002. DOI: 10.1103/PhysRevLett.109.267002. URL: https://link.aps.org/doi/10.1103/PhysRevLett.109.267002.

[203] Haining Pan and S. Das Sarma. "Physical mechanisms for zero-bias conductance peaks in Majorana nanowires". In: *Phys. Rev. Res.* 2 (1 Mar. 2020), p. 013377. DOI: 10.1103/PhysRevResearch.2.013377. URL: https://link.aps.org/doi/10.1103/PhysRevResearch.2.013377.

[204] Chun-Xiao Liu et al. "Andreev bound states versus Majorana bound states in quantum dot-nanowire-superconductor hybrid structures: Trivial versus topological zero-bias conductance peaks". In: *Phys. Rev. B* 96 (7 Aug. 2017), p. 075161. DOI: 10.1103/PhysRevB.96.075161. URL: https://link.aps.org/doi/10.1103/PhysRevB.96.075161.

[205] Jelena Klinovaja and Daniel Loss. "Fermionic and Majorana bound states in hybrid nanowires with non-uniform spin-orbit interaction". In: *The European Physical Journal B* 88.3 (2015), p. 62. DOI: 10.1140/epjb/e2015-50882-2. URL: https://doi.org/10.1140/epjb/e2015-50882-2.

[206] C. Fleckenstein et al. "Decaying spectral oscillations in a Majorana wire with finite coherence length". In: *Phys. Rev. B* 97 (15 Apr. 2018), p. 155425. DOI: 10.1103/PhysRevB.97.155425. URL: https://link.aps.org/doi/10.1103/PhysRevB.97.155425.

[207] J. Chen et al. "Ubiquitous Non-Majorana Zero-Bias Conductance Peaks in Nanowire Devices". In: *Phys. Rev. Lett.* 123 (10 Sept. 2019), p. 107703. DOI: 10.1103/PhysRevLett.123.107703. URL: https://link.aps.org/doi/10.1103/PhysRevLett.123.107703.

[208] L. S. Ricco et al. "Spin-dependent zero-bias peak in a hybrid nanowire-quantum dot system: Distinguishing isolated Majorana fermions from Andreev bound states". In: *Phys. Rev. B* 99 (15 Apr. 2019), p. 155159. DOI: 10.1103/PhysRevB.99.155159. URL: https://link.aps.org/doi/10.1103/PhysRevB.99.155159.

[209] Tudor D. Stanescu and Sumanta Tewari. "Robust low-energy Andreev bound states in semiconductor-superconductor structures: Importance of partial separation of component Majorana bound states". In: *Phys. Rev. B* 100 (15 Oct. 2019), p. 155429. DOI: 10.1103/PhysRevB.100.155429. URL: https://link.aps.org/doi/10.1103/PhysRevB.100.155429.

[210] Elsa Prada et al. "From Andreev to Majorana bound states in hybrid superconductor–semiconductor nanowires". In: *Nature Reviews Physics* 2.10 (2020), pp. 575–594. DOI: 10.1038/s42254-020-0228-y. URL: https://doi.org/10.1038/s42254-020-0228-y.

[211] Flavio Ronetti et al. "Magnetically confined bound states in Rashba systems". In: *Phys. Rev. Res.* 2 (2 June 2020), p. 022052. DOI: 10.1103/PhysRevResearch.2.022052. URL: https://link.aps.org/doi/10.1103/PhysRevResearch.2.022052.

[212] Stevan Nadj-Perge et al. "Observation of Majorana fermions in ferromagnetic atomic chains on a superconductor". In: *Science* 346.6209 (2014), pp. 602–607. DOI: 10.1126/science.1259327. eprint: https://www.science.org/doi/pdf/10.1126/science.1259327. URL: https://www.science.org/doi/abs/10.1126/science.1259327.

[213] Doru Sticlet, Cristina Bena, and Pascal Simon. "Spin and Majorana Polarization in Topological Superconducting Wires". In: *Phys. Rev. Lett.* 108 (9 Mar. 2012), p. 096802. DOI: 10.1103/PhysRevLett.108.096802. URL: https://link.aps.org/doi/10.1103/PhysRevLett.108.096802.

[214] Kristofer Björnson et al. "Spin-polarized edge currents and Majorana fermions in one- and two-dimensional topological superconductors". In: *Phys. Rev. B* 92 (21 Dec. 2015), p. 214501. DOI: 10.1103/PhysRevB.92.214501. URL: https://link.aps.org/doi/10.1103/PhysRevB.92.214501.

[215] Maciej M. Maśka and Tadeusz Domański. "Polarization of the Majorana quasi-particles in the Rashba chain". In: *Scientific Reports* 7.1 (2017), p. 16193. DOI: 10.1038/s41598-017-16323-3. URL: https://doi.org/10.1038/s41598-017-16323-3.

[216] Satoshi Sasaki et al. "Encapsulated gate-all-around InAs nanowire field-effect transistors". In: *Applied Physics Letters* 103.21 (2013), p. 213502. DOI: 10.1063/1.4832058. eprint: https://doi.org/10.1063/1.4832058. URL: https://doi.org/10.1063/1.4832058.

[217]   A. M. Burke et al. "InAs Nanowire Transistors with Multiple, Independent Wrap-Gate Segments". In: *Nano Letters* 15.5 (2015). PMID: 25879492, pp. 2836–2843. DOI: 10.1021/nl5043243. eprint: https://doi.org/10.1021/nl5043243. URL: https://doi.org/10.1021/nl5043243.

[218]   K. Takase et al. "Highly gate-tuneable Rashba spin-orbit interaction in a gate-all-around InAs nanowire metal-oxide-semiconductor field-effect transistor". In: *Scientific Reports* 7.1 (2017), p. 930. DOI: 10.1038/s41598-017-01080-0. URL: https://doi.org/10.1038/s41598-017-01080-0.

[219]   Suprem R. Das. "Chapter 11 - Advances in InSb and InAs Nanowire Based Nanoelectronic Field Effect Transistors". In: *Nanoelectronics*. Ed. by Brajesh Kumar Kaushik. Advanced Nanomaterials. Elsevier, 2019, pp. 355–373. ISBN: 978-0-12-813353-8. DOI: https://doi.org/10.1016/B978-0-12-813353-8.00005-1. URL: https://www.sciencedirect.com/science/article/pii/B9780128133538000051.

[220]   Yiheng Yin et al. "Tellurium Nanowire Gate-All-Around MOSFETs for Sub-5 nm Applications". In: *ACS Applied Materials & Interfaces* 13.2 (2021). PMID: 33404208, pp. 3387–3396. DOI: 10.1021/acsami.0c18767. eprint: https://doi.org/10.1021/acsami.0c18767. URL: https://doi.org/10.1021/acsami.0c18767.

[221]   Keiko Takase, Kouta Tateno, and Satoshi Sasaki. "Electrical tuning of the spin–orbit interaction in nanowire by transparent ZnO gate grown by atomic layer deposition". In: *Applied Physics Letters* 119.1 (2021), p. 013102. DOI: 10.1063/5.0051281. eprint: https://doi.org/10.1063/5.0051281. URL: https://doi.org/10.1063/5.0051281.

[222]   Dong Liang and Xuan P.A. Gao. "Strong Tuning of Rashba Spin–Orbit Interaction in Single InAs Nanowires". In: *Nano Letters* 12.6 (2012). PMID: 22545669, pp. 3263–3267. DOI: 10.1021/nl301325h. eprint: https://doi.org/10.1021/nl301325h. URL: https://doi.org/10.1021/nl301325h.

[223]   Bartosz Slomski et al. "Interband spin–orbit coupling between anti-parallel spin states in Pb quantum well states". In: *New Journal of Physics* 15.12 (Dec. 2013), p. 125031. DOI: 10.1088/1367-2630/15/12/125031. URL: https://dx.doi.org/10.1088/1367-2630/15/12/125031.

[224]   I. van Weperen et al. "Spin-orbit interaction in InSb nanowires". In: *Phys. Rev. B* 91 (20 May 2015), p. 201413. DOI: 10.1103/PhysRevB.91.201413. URL: https://link.aps.org/doi/10.1103/PhysRevB.91.201413.

[225]   Zoltán Scherübl et al. "Electrical tuning of Rashba spin-orbit interaction in multi-gated InAs nanowires". In: *Phys. Rev. B* 94 (3 July 2016), p. 035444. DOI: 10.1103/PhysRevB.94.035444. URL: https://link.aps.org/doi/10.1103/PhysRevB.94.035444.

[226]   Raphael Bindel et al. "Probing variations of the Rashba spin–orbit coupling at the nanometre scale". In: *Nature Physics* 12.10 (2016), pp. 920–925. DOI: 10.1038/nphys3774. URL: https://doi.org/10.1038/nphys3774.

[227]   J. Borge and I. V. Tokatly. "Ballistic spin transport in the presence of interfaces with strong spin-orbit coupling". In: *Phys. Rev. B* 96 (11 Sept. 2017), p. 115445. DOI: 10.1103/PhysRevB.96.115445. URL: https://link.aps.org/doi/10.1103/PhysRevB.96.115445.

[228] Christoph Kloeffel, Marko J. Rančić, and Daniel Loss. "Direct Rashba spin-orbit interaction in Si and Ge nanowires with different growth directions". In: *Phys. Rev. B* 97 (23 June 2018), p. 235422. DOI: 10.1103/PhysRevB.97.235422. URL: https://link.aps.org/doi/10.1103/PhysRevB.97.235422.

[229] Hanshen Tsai et al. "Clear variation of spin splitting by changing electron distribution at non-magnetic metal/Bi2O3 interfaces". In: *Scientific Reports* 8.1 (2018), p. 5564. DOI: 10.1038/s41598-018-23787-4. URL: https://doi.org/10.1038/s41598-018-23787-4.

[230] Paweł Wójcik, Andrea Bertoni, and Guido Goldoni. "Tuning Rashba spin-orbit coupling in homogeneous semiconductor nanowires". In: *Phys. Rev. B* 97 (16 Apr. 2018), p. 165401. DOI: 10.1103/PhysRevB.97.165401. URL: https://link.aps.org/doi/10.1103/PhysRevB.97.165401.

[231] A. Iorio et al. "Vectorial Control of the Spin–Orbit Interaction in Suspended InAs Nanowires". In: *Nano Letters* 19.2 (2019). PMID: 30398889, pp. 652–657. DOI: 10.1021/acs.nanolett.8b02828. eprint: https://doi.org/10.1021/acs.nanolett.8b02828. URL: https://doi.org/10.1021/acs.nanolett.8b02828.

[232] Kasun Premasiri and Xuan P A Gao. "Tuning spin–orbit coupling in 2D materials for spintronics: a topical review". In: *Journal of Physics: Condensed Matter* 31.19 (Mar. 2019), p. 193001. DOI: 10.1088/1361-648X/ab04c7. URL: https://dx.doi.org/10.1088/1361-648X/ab04c7.

[233] Dmitry Shcherbakov et al. "Layer- and gate-tunable spin-orbit coupling in a high-mobility few-layer semiconductor". In: *Science Advances* 7.5 (2021), eabe2892. DOI: 10.1126/sciadv.abe2892. eprint: https://www.science.org/doi/pdf/10.1126/sciadv.abe2892. URL: https://www.science.org/doi/abs/10.1126/sciadv.abe2892.

[234] Fabrizio Dolcini and Fausto Rossi. "Magnetic field effects on a nanowire with inhomogeneous Rashba spin-orbit coupling: Spin properties at equilibrium". In: *Phys. Rev. B* 98 (4 July 2018), p. 045436. DOI: 10.1103/PhysRevB.98.045436. URL: https://link.aps.org/doi/10.1103/PhysRevB.98.045436.

[235] G. Bastard. *Wave mechanics applied to semiconductor heterostructures*. United States: John Wiley and Sons Inc, 1990. ISBN: 0-471-21708-1. URL: http://inis.iaea.org/search/search.aspx?orig_q=RN:23010919.

[236] David Sánchez and Llorenç Serra. "Fano-Rashba effect in a quantum wire". In: *Phys. Rev. B* 74 (15 Oct. 2006), p. 153313. DOI: 10.1103/PhysRevB.74.153313. URL: https://link.aps.org/doi/10.1103/PhysRevB.74.153313.

[237] David Sánchez, Llorenç Serra, and Mahn-Soo Choi. "Strongly modulated transmission of a spin-split quantum wire with local Rashba interaction". In: *Phys. Rev. B* 77 (3 Jan. 2008), p. 035315. DOI: 10.1103/PhysRevB.77.035315. URL: https://link.aps.org/doi/10.1103/PhysRevB.77.035315.

[238] Meng Cheng and Roman M. Lutchyn. "Josephson current through a superconductor / semiconductor-nanowire / superconductor junction: Effects of strong spin-orbit coupling and Zeeman splitting". In: *Phys. Rev. B* 86 (13 Oct. 2012), p. 134522. DOI: 10.1103/PhysRevB.86.134522. URL: https://link.aps.org/doi/10.1103/PhysRevB.86.134522.

[239] Paweł Szumniak et al. "Spin and charge signatures of topological superconductivity in Rashba nanowires". In: *Phys. Rev. B* 96 (4 July 2017), p. 041401. DOI: 10.1103/PhysRevB.96.041401. URL: https://link.aps.org/doi/10.1103/PhysRevB.96.041401.

[240] E.B. Sonin. "Spin currents and spin superfluidity". In: *Advances in Physics* 59.3 (2010), pp. 181–255. DOI: 10.1080/00018731003739943. eprint: https://doi.org/10.1080/00018731003739943. URL: https://doi.org/10.1080/00018731003739943.

[241] Emmanuel I. Rashba. "Spin currents in thermodynamic equilibrium: The challenge of discerning transport currents". In: *Phys. Rev. B* 68 (24 Dec. 2003), p. 241315. DOI: 10.1103/PhysRevB.68.241315. URL: https://link.aps.org/doi/10.1103/PhysRevB.68.241315.

[242] Janine Splettstoesser, Michele Governale, and Ulrich Zülicke. "Persistent current in ballistic mesoscopic rings with Rashba spin-orbit coupling". In: *Phys. Rev. B* 68 (16 Oct. 2003), p. 165341. DOI: 10.1103/PhysRevB.68.165341. URL: https://link.aps.org/doi/10.1103/PhysRevB.68.165341.

[243] G. Usaj and C. A. Balseiro. "Spin accumulation and equilibrium currents at the edge of 2DEGs with spin-orbit coupling". In: *Europhysics Letters* 72.4 (Oct. 2005), p. 631. DOI: 10.1209/epl/i2005-10266-0. URL: https://dx.doi.org/10.1209/epl/i2005-10266-0.

[244] E. B. Sonin. "Equilibrium spin currents in the Rashba medium". In: *Phys. Rev. B* 76 (3 July 2007), p. 033306. DOI: 10.1103/PhysRevB.76.033306. URL: https://link.aps.org/doi/10.1103/PhysRevB.76.033306.

[245] E. B. Sonin. "Proposal for Measuring Mechanically Equilibrium Spin Currents in the Rashba Medium". In: *Phys. Rev. Lett.* 99 (26 Dec. 2007), p. 266602. DOI: 10.1103/PhysRevLett.99.266602. URL: https://link.aps.org/doi/10.1103/PhysRevLett.99.266602.

[246] Qing-feng Sun, X. C. Xie, and Jian Wang. "Persistent Spin Current in a Mesoscopic Hybrid Ring with Spin-Orbit Coupling". In: *Phys. Rev. Lett.* 98 (19 May 2007), p. 196801. DOI: 10.1103/PhysRevLett.98.196801. URL: https://link.aps.org/doi/10.1103/PhysRevLett.98.196801.

[247] Qing-feng Sun, X. C. Xie, and Jian Wang. "Persistent spin current in nanodevices and definition of the spin current". In: *Phys. Rev. B* 77 (3 Jan. 2008), p. 035327. DOI: 10.1103/PhysRevB.77.035327. URL: https://link.aps.org/doi/10.1103/PhysRevB.77.035327.

[248] Vladimir A. Sablikov, Aleksei A. Sukhanov, and Yurii Ya. Tkach. "Equilibrium edge spin currents in two-dimensional electron systems with spin-orbit interaction". In: *Phys. Rev. B* 78 (15 Oct. 2008), p. 153302. DOI: 10.1103/PhysRevB.78.153302. URL: https://link.aps.org/doi/10.1103/PhysRevB.78.153302.

[249] Feng Liang, YaoGuo Shen, and YongHong Yang. "Equilibrium spin current induced by spin–orbital interaction in a quantum dot system". In: *Physics Letters A* 372.25 (2008), pp. 4634–4637. ISSN: 0375-9601. DOI: https://doi.org/10.1016/j.physleta.2008.04.029. URL: https://www.sciencedirect.com/science/article/pii/S0375960108006221.

[250] Bertrand Berche, Christophe Chatelain, and Ernesto Medina. "Mesoscopic rings with spin-orbit interactions". In: *European Journal of Physics* 31.5 (Oct. 2010), p. 1267. DOI: 10.1088/0143-0807/31/5/026. URL: https://dx.doi.org/10.1088/0143-0807/31/5/026.

[251] E. Nakhmedov and O. Alekperov. "Out-of-plane equilibrium spin current in a quasi-two-dimensional electron gas under in-plane magnetic field". In: *Phys. Rev. B* 85 (15 Apr. 2012), p. 153302. DOI: 10.1103/PhysRevB.85.153302. URL: https://link.aps.org/doi/10.1103/PhysRevB.85.153302.

[252] Huan Zhang, Zhongshui Ma, and Jun-Feng Liu. "Equilibrium spin current in graphene with Rashba spin-orbit coupling". In: *Scientific Reports* 4.1 (2014), p. 6464. DOI: 10.1038/srep06464. URL: https://doi.org/10.1038/srep06464.

[253] Feng Liang et al. "Conversion of equilibrium spin current into charge current through a quantum-dot spin valve subject to circularly polarized field". In: *Physics Letters A* 379.47 (2015), pp. 3114–3118. ISSN: 0375-9601. DOI: https://doi.org/10.1016/j.physleta.2015.09.037. URL: https://www.sciencedirect.com/science/article/pii/S0375960115008245.

[254] Tsung-Wei Chen, Chih-Meng Huang, and G. Y. Guo. "Conserved spin and orbital angular momentum Hall current in a two-dimensional electron system with Rashba and Dresselhaus spin-orbit coupling". In: *Phys. Rev. B* 73 (23 June 2006), p. 235309. DOI: 10.1103/PhysRevB.73.235309. URL: https://link.aps.org/doi/10.1103/PhysRevB.73.235309.

[255] Florian Meier and Daniel Loss. "Magnetization Transport and Quantized Spin Conductance". In: *Phys. Rev. Lett.* 90 (16 Apr. 2003), p. 167204. DOI: 10.1103/PhysRevLett.90.167204. URL: https://link.aps.org/doi/10.1103/PhysRevLett.90.167204.

[256] Jürg Fröhlich and Urban M. Studer. "Gauge invariance and current algebra in nonrelativistic many-body theory". In: *Rev. Mod. Phys.* 65 (3 July 1993), pp. 733–802. DOI: 10.1103/RevModPhys.65.733. URL: https://link.aps.org/doi/10.1103/RevModPhys.65.733.

[257] I. V. Tokatly. "Equilibrium Spin Currents: Non-Abelian Gauge Invariance and Color Diamagnetism in Condensed Matter". In: *Phys. Rev. Lett.* 101 (10 Sept. 2008), p. 106601. DOI: 10.1103/PhysRevLett.101.106601. URL: https://link.aps.org/doi/10.1103/PhysRevLett.101.106601.

[258] F. Romeo et al. "Electrical switching and interferometry of massive Dirac particles in topological insulator constrictions". In: *Phys. Rev. B* 86 (16 Oct. 2012), p. 165418. DOI: 10.1103/PhysRevB.86.165418. URL: https://link.aps.org/doi/10.1103/PhysRevB.86.165418.

[259] Pietro Sternativo and Fabrizio Dolcini. "Tunnel junction of helical edge states: Determining and controlling spin-preserving and spin-flipping processes through transconductance". In: *Phys. Rev. B* 89 (3 Jan. 2014), p. 035415. DOI: 10.1103/PhysRevB.89.035415. URL: https://link.aps.org/doi/10.1103/PhysRevB.89.035415.

[260] Jonas Strunz et al. "Interacting topological edge channels". In: *Nature Physics* 16.1 (2020), pp. 83–88. DOI: 10.1038/s41567-019-0692-4. URL: https://doi.org/10.1038/s41567-019-0692-4.

[261] Henrik A. Nilsson et al. "Giant, Level-Dependent g Factors in InSb Nanowire Quantum Dots". In: *Nano Letters* 9.9 (2009). PMID: 19736971, pp. 3151–3156. DOI: 10.1021/nl901333a. eprint: https://doi.org/10.1021/nl901333a. URL: https://doi.org/10.1021/nl901333a.

[262] S. Nadj-Perge et al. "Spectroscopy of Spin-Orbit Quantum Bits in Indium Antimonide Nanowires". In: *Phys. Rev. Lett.* 108 (16 Apr. 2012), p. 166801. DOI: 10.1103/PhysRevLett.108.166801. URL: https://link.aps.org/doi/10.1103/PhysRevLett.108.166801.

[263] Önder Gül et al. "Hard Superconducting Gap in InSb Nanowires". In: *Nano Letters* 17.4 (2017). PMID: 28355877, pp. 2690–2696. DOI: 10.1021/acs.nanolett.7b00540. eprint: https://doi.org/10.1021/acs.nanolett.7b00540. URL: https://doi.org/10.1021/acs.nanolett.7b00540.

[264] P. Roulleau et al. "Suppression of weak antilocalization in InAs nanowires". In: *Phys. Rev. B* 81 (15 Apr. 2010), p. 155449. DOI: 10.1103/PhysRevB.81.155449. URL: https://link.aps.org/doi/10.1103/PhysRevB.81.155449.

[265] Hannah J Joyce et al. "Electronic properties of GaAs, InAs and InP nanowires studied by terahertz spectroscopy". In: *Nanotechnology* 24.21 (Apr. 2013), p. 214006. DOI: 10.1088/0957-4484/24/21/214006. URL: https://dx.doi.org/10.1088/0957-4484/24/21/214006.

[266] S. Heedt et al. "Signatures of interaction-induced helical gaps in nanowire quantum point contacts". In: *Nature Physics* 13.6 (2017), pp. 563–567. DOI: 10.1038/nphys4070. URL: https://doi.org/10.1038/nphys4070.

[267] O. Krupin et al. "Rashba effect at magnetic metal surfaces". In: *Phys. Rev. B* 71 (20 May 2005), p. 201403. DOI: 10.1103/PhysRevB.71.201403. URL: https://link.aps.org/doi/10.1103/PhysRevB.71.201403.

[268] W. Wang, X.M. Li, and J.Y. Fu. "Two distinct regimes for the electrical control of the spin–orbit interaction in GaAs wells". In: *Journal of Magnetism and Magnetic Materials* 411 (2016), pp. 84–90. ISSN: 0304-8853. DOI: https://doi.org/10.1016/j.jmmm.2016.03.053. URL: https://www.sciencedirect.com/science/article/pii/S0304885316302505.

[269] Fumiya Nagasawa et al. "Gate-controlled anisotropy in Aharonov-Casher spin interference: Signatures of Dresselhaus spin-orbit inversion and spin phases". In: *Phys. Rev. B* 98 (24 Dec. 2018), p. 245301. DOI: 10.1103/PhysRevB.98.245301. URL: https://link.aps.org/doi/10.1103/PhysRevB.98.245301.

[270] D. Rugar et al. "Single spin detection by magnetic resonance force microscopy". In: *Nature* 430.6997 (2004), pp. 329–332. DOI: 10.1038/nature02658. URL: https://doi.org/10.1038/nature02658.

[271] Jeremy Cardellino et al. "The effect of spin transport on spin lifetime in nanoscale systems". In: *Nature Nanotechnology* 9.5 (2014), pp. 343–347. DOI: 10.1038/nnano.2014.39. URL: https://doi.org/10.1038/nnano.2014.39.

[272] Kazuyuki Koike et al. "Spin-Polarized Scanning Electron Microscopy". In: *Japanese Journal of Applied Physics* 24.8R (Oct. 1985), p. 1078. DOI: 10.1143/JJAP.24.1078. URL: https://dx.doi.org/10.1143/JJAP.24.1078.

[273] T. Kohashi. "Spin-Polarized Scanning Electron Microscopy (Spin SEM) and its recent progress". In: *Journal of the Magnetics Society of Japan* 39.4 (2015), pp. 131–138. DOI: 10.3379/msjmag.1506R001.

[274] Tomohiro Otsuka et al. "Detection of spin polarization with a side-coupled quantum dot". In: *Phys. Rev. B* 79 (19 May 2009), p. 195313. DOI: 10.1103/PhysRevB.79.195313. URL: https://link.aps.org/doi/10.1103/PhysRevB.79.195313.

[275] Tomohiro Otsuka et al. "Detection of spin polarization utilizing singlet and triplet states in a single-lead quantum dot". In: *Phys. Rev. B* 86 (8 Aug. 2012), p. 081308. DOI: 10.1103/PhysRevB.86.081308. URL: https://link.aps.org/doi/10.1103/PhysRevB.86.081308.

[276] C. H. Li et al. "Electrical detection of charge-current-induced spin polarization due to spin-momentum locking in Bi2Se3". In: *Nature Nanotechnology* 9.3 (2014), pp. 218–224. DOI: 10.1038/nnano.2014.16. URL: https://doi.org/10.1038/nnano.2014.16.

[277] Jianshi Tang et al. "Electrical Detection of Spin-Polarized Surface States Conduction in (Bi0.53Sb0.47)2Te3 Topological Insulator". In: *Nano Letters* 14.9 (2014). PMID: 25158276, pp. 5423–5429. DOI: 10.1021/nl5026198. eprint: https://doi.org/10.1021/nl5026198. URL: https://doi.org/10.1021/nl5026198.

[278] I. V. Tokatly, B. Bujnowski, and F. S. Bergeret. "Universal correspondence between edge spin accumulation and equilibrium spin currents in nanowires with spin-orbit coupling". In: *Phys. Rev. B* 100 (21 Dec. 2019), p. 214422. DOI: 10.1103/PhysRevB.100.214422. URL: https://link.aps.org/doi/10.1103/PhysRevB.100.214422.

[279] Leonid Gogin et al. "The Dirac paradox in $1 + 1$ dimensions and its realization with spin–orbit coupled nanowires". In: *New Journal of Physics* 24.5 (May 2022), p. 053045. DOI: 10.1088/1367-2630/ac6cfe. URL: https://dx.doi.org/10.1088/1367-2630/ac6cfe.

[280] A. K. Geim and K. S. Novoselov. "The rise of graphene". In: *Nature Materials* 6.3 (2007), pp. 183–191. DOI: 10.1038/nmat1849. URL: https://doi.org/10.1038/nmat1849.

[281] A. H. Castro Neto et al. "The electronic properties of graphene". In: *Rev. Mod. Phys.* 81 (1 Jan. 2009), pp. 109–162. DOI: 10.1103/RevModPhys.81.109. URL: https://link.aps.org/doi/10.1103/RevModPhys.81.109.

[282] S. Das Sarma et al. "Electronic transport in two-dimensional graphene". In: *Rev. Mod. Phys.* 83 (2 May 2011), pp. 407–470. DOI: 10.1103/RevModPhys.83.407. URL: https://link.aps.org/doi/10.1103/RevModPhys.83.407.

[283] Shuang Jia, Su-Yang Xu, and M. Zahid Hasan. "Weyl semimetals, Fermi arcs and chiral anomalies". In: *Nature Materials* 15.11 (2016), pp. 1140–1144. DOI: 10.1038/nmat4787. URL: https://doi.org/10.1038/nmat4787.

[284] Shengyuan A. Yang. "Dirac and Weyl Materials: Fundamental Aspects and Some Spintronics Applications". In: *SPIN* 06.02 (2016), p. 1640003. DOI: 10.1142/S2010324716400038. eprint: https://doi.org/10.1142/S2010324716400038. URL: https://doi.org/10.1142/S2010324716400038.

[285] Ryuji Takahashi and Shuichi Murakami. "Gapless Interface States between Topological Insulators with Opposite Dirac Velocities". In: *Phys. Rev. Lett.* 107 (16 Oct. 2011), p. 166805. DOI: 10.1103/PhysRevLett.107.166805. URL: https://link.aps.org/doi/10.1103/PhysRevLett.107.166805.

[286] Diptiman Sen and Oindrila Deb. "Junction between surfaces of two topological insulators". In: *Phys. Rev. B* 85 (24 June 2012), p. 245402. DOI: 10.1103/PhysRevB.85.245402. URL: https://link.aps.org/doi/10.1103/PhysRevB.85.245402.

[287] Christophe De Beule and Bart Partoens. "Gapless interface states at the junction between two topological insulators". In: *Phys. Rev. B* 87 (11 Mar. 2013), p. 115113. DOI: 10.1103/PhysRevB.87.115113. URL: https://link.aps.org/doi/10.1103/PhysRevB.87.115113.

[288] Tetsuro Habe and Yasuhiro Asano. "Robustness of gapless interface states in a junction of two topological insulators". In: *Phys. Rev. B* 88 (15 Oct. 2013), p. 155442. DOI: 10.1103/PhysRevB.88.155442. URL: https://link.aps.org/doi/10.1103/PhysRevB.88.155442.

[289] Chaoxing Liu et al. "Quantum Spin Hall Effect in Inverted Type-II Semiconductors". In: *Phys. Rev. Lett.* 100 (23 June 2008), p. 236601. DOI: 10.1103/PhysRevLett.100.236601. URL: https://link.aps.org/doi/10.1103/PhysRevLett.100.236601.

[290] Markus König et al. "The Quantum Spin Hall Effect: Theory and Experiment". In: *Journal of the Physical Society of Japan* 77.3 (2008), p. 031007. DOI: 10.1143/JPSJ.77.031007. eprint: https://doi.org/10.1143/JPSJ.77.031007. URL: https://doi.org/10.1143/JPSJ.77.031007.

[291] Ivan Knez, Rui-Rui Du, and Gerard Sullivan. "Evidence for Helical Edge Modes in Inverted InAs/GaSb Quantum Wells". In: *Phys. Rev. Lett.* 107 (13 Sept. 2011), p. 136603. DOI: 10.1103/PhysRevLett.107.136603. URL: https://link.aps.org/doi/10.1103/PhysRevLett.107.136603.

[292] Lingjie Du et al. "Robust Helical Edge Transport in Gated InAs/GaSb Bilayers". In: *Phys. Rev. Lett.* 114 (9 Mar. 2015), p. 096802. DOI: 10.1103/PhysRevLett.114.096802. URL: https://link.aps.org/doi/10.1103/PhysRevLett.114.096802.

[293] C. H. L. Quay et al. "Observation of a one-dimensional spin–orbit gap in a quantum wire". In: *Nature Physics* 6.5 (2010), pp. 336–339. DOI: 10.1038/nphys1626. URL: https://doi.org/10.1038/nphys1626.

[294] Ilse van Weperen et al. "Quantized Conductance in an InSb Nanowire". In: *Nano Letters* 13.2 (2013). PMID: 23259576, pp. 387–391. DOI: 10.1021/nl3035256. eprint: https://doi.org/10.1021/nl3035256. URL: https://doi.org/10.1021/nl3035256.

[295] J. Kammhuber et al. "Conductance through a helical state in an Indium antimonide nanowire". In: *Nature Communications* 8.1 (2017), p. 478. DOI: 10.1038/s41467-017-00315-y. URL: https://doi.org/10.1038/s41467-017-00315-y.

[296] P. Středa and P. Šeba. "Antisymmetric Spin Filtering in One-Dimensional Electron Systems with Uniform Spin-Orbit Coupling". In: *Phys. Rev. Lett.* 90 (25 June 2003), p. 256601. DOI: 10.1103/PhysRevLett.90.256601. URL: https://link.aps.org/doi/10.1103/PhysRevLett.90.256601.

[297] Christoph Kloeffel, Mircea Trif, and Daniel Loss. "Strong spin-orbit interaction and helical hole states in Ge/Si nanowires". In: *Phys. Rev. B* 84 (19 Nov. 2011), p. 195314. DOI: 10.1103/PhysRevB.84.195314. URL: https://link.aps.org/doi/10.1103/PhysRevB.84.195314.

[298] Jason Alicea. "New directions in the pursuit of Majorana fermions in solid state systems". In: *Reports on Progress in Physics* 75.7 (June 2012), p. 076501. DOI: 10.1088/0034-4885/75/7/076501. URL: https://dx.doi.org/10.1088/0034-4885/75/7/076501.

[299] Masatoshi Sato and Satoshi Fujimoto. "Majorana Fermions and Topology in Superconductors". In: *Journal of the Physical Society of Japan* 85.7 (2016), p. 072001. DOI: 10.7566/JPSJ.85.072001. eprint: https://doi.org/10.7566/JPSJ.85.072001. URL: https://doi.org/10.7566/JPSJ.85.072001.

[300] N M R Peres. "Scattering in one-dimensional heterostructures described by the Dirac equation". In: *Journal of Physics: Condensed Matter* 21.9 (Jan. 2009), p. 095501. DOI: 10.1088/0953-8984/21/9/095501. URL: https://dx.doi.org/10.1088/0953-8984/21/9/095501.

[301] M. M. Glazov and E. Ya. Sherman. "Theory of Spin Noise in Nanowires". In: *Phys. Rev. Lett.* 107 (15 Oct. 2011), p. 156602. DOI: 10.1103/PhysRevLett.107.156602. URL: https://link.aps.org/doi/10.1103/PhysRevLett.107.156602.

[302] Almas F. Sadreev and E. Ya. Sherman. "Effect of gate-driven spin resonance on the conductance through a one-dimensional quantum wire". In: *Phys. Rev. B* 88 (11 Sept. 2013), p. 115302. DOI: 10.1103/PhysRevB.88.115302. URL: https://link.aps.org/doi/10.1103/PhysRevB.88.115302.

[303] M. Modugno, E. Ya. Sherman, and V. V. Konotop. "Macroscopic random Paschen-Back effect in ultracold atomic gases". In: *Phys. Rev. A* 95 (6 June 2017), p. 063620. DOI: 10.1103/PhysRevA.95.063620. URL: https://link.aps.org/doi/10.1103/PhysRevA.95.063620.

[304] Supriyo Datta. *Electronic Transport in Mesoscopic Systems*. Cambridge Studies in Semiconductor Physics and Microelectronic Engineering. Cambridge University Press, 1995. DOI: 10.1017/CBO9780511805776.

[305] Lorenzo Rossi et al. "Signature of Generalized Gibbs Ensemble Deviation from Equilibrium: Negative Absorption Induced by a Local Quench". In: *Entropy* 23.2 (2021). ISSN: 1099-4300. DOI: 10.3390/e23020220. URL: https://www.mdpi.com/1099-4300/23/2/220.

[306] D. N. Basov, R. D. Averitt, and D. Hsieh. "Towards properties on demand in quantum materials". In: *Nature Materials* 16.11 (2017), pp. 1077–1088. DOI: 10.1038/nmat5017. URL: https://doi.org/10.1038/nmat5017.

[307] J. W. McIver et al. "Light-induced anomalous Hall effect in graphene". In: *Nature Physics* 16.1 (2020), pp. 38–41. DOI: 10.1038/s41567-019-0698-y. URL: https://doi.org/10.1038/s41567-019-0698-y.

[308] M. A. Cazalilla. "Effect of Suddenly Turning on Interactions in the Luttinger Model". In: *Phys. Rev. Lett.* 97 (15 Oct. 2006), p. 156403. DOI: 10.1103/PhysRevLett.97.156403. URL: https://link.aps.org/doi/10.1103/PhysRevLett.97.156403.

[309] A. Iucci and M. A. Cazalilla. "Quantum quench dynamics of the Luttinger model". In: *Phys. Rev. A* 80 (6 Dec. 2009), p. 063619. DOI: 10.1103/PhysRevA.80.063619. URL: https://link.aps.org/doi/10.1103/PhysRevA.80.063619.

[310] Pasquale Calabrese, Fabian H. L. Essler, and Maurizio Fagotti. "Quantum Quench in the Transverse-Field Ising Chain". In: *Phys. Rev. Lett.* 106 (22 June 2011), p. 227203. DOI: 10.1103/PhysRevLett.106.227203. URL: https://link.aps.org/doi/10.1103/PhysRevLett.106.227203.

[311] Aditi Mitra and Thierry Giamarchi. "Mode-Coupling-Induced Dissipative and Thermal Effects at Long Times after a Quantum Quench". In: *Phys. Rev. Lett.* 107 (15 Oct. 2011), p. 150602. DOI: 10.1103/PhysRevLett.107.150602. URL: https://link.aps.org/doi/10.1103/PhysRevLett.107.150602.

[312] M. Heyl, A. Polkovnikov, and S. Kehrein. "Dynamical Quantum Phase Transitions in the Transverse-Field Ising Model". In: *Phys. Rev. Lett.* 110 (13 Mar. 2013), p. 135704. DOI: 10.1103/PhysRevLett.110.135704. URL: https://link.aps.org/doi/10.1103/PhysRevLett.110.135704.

[313] C. Karrasch et al. "Luttinger-liquid universality in the time evolution after an interaction quench". In: *Phys. Rev. Lett.* 109 (12 Sept. 2012), p. 126406. DOI: 10.1103/PhysRevLett.109.126406. URL: https://link.aps.org/doi/10.1103/PhysRevLett.109.126406.

[314] D. M. Kennes and V. Meden. "Luttinger liquid properties of the steady state after a quantum quench". In: *Phys. Rev. B* 88 (16 Oct. 2013), p. 165131. DOI: 10.1103/PhysRevB.88.165131. URL: https://link.aps.org/doi/10.1103/PhysRevB.88.165131.

[315] Mario Collura, Pasquale Calabrese, and Fabian H. L. Essler. "Quantum quench within the gapless phase of the spin $-\frac{1}{2}$ Heisenberg XXZ spin chain". In: *Phys. Rev. B* 92 (12 Sept. 2015), p. 125131. DOI: 10.1103/PhysRevB.92.125131. URL: https://link.aps.org/doi/10.1103/PhysRevB.92.125131.

[316] S. Porta et al. "Out-of-equilibrium density dynamics of a quenched fermionic system". In: *Phys. Rev. B* 94 (8 Aug. 2016), p. 085122. DOI: 10.1103/PhysRevB.94.085122. URL: https://link.aps.org/doi/10.1103/PhysRevB.94.085122.

[317] Alessio Calzona et al. "Quench-induced entanglement and relaxation dynamics in Luttinger liquids". In: *Phys. Rev. B* 96 (8 Aug. 2017), p. 085423. DOI: 10.1103/PhysRevB.96.085423. URL: https://link.aps.org/doi/10.1103/PhysRevB.96.085423.

[318] Simone Ziraldo and Giuseppe E. Santoro. "Relaxation and thermalization after a quantum quench: Why localization is important". In: *Phys. Rev. B* 87 (6 Feb. 2013), p. 064201. DOI: 10.1103/PhysRevB.87.064201. URL: https://link.aps.org/doi/10.1103/PhysRevB.87.064201.

[319] Simone Ziraldo, Alessandro Silva, and Giuseppe E. Santoro. "Relaxation Dynamics of Disordered Spin Chains: Localization and the Existence of a Stationary State". In: *Phys. Rev. Lett.* 109 (24 Dec. 2012), p. 247205. DOI: 10.1103/PhysRevLett.109.247205. URL: https://link.aps.org/doi/10.1103/PhysRevLett.109.247205.

[320] Baoming Tang, Deepak Iyer, and Marcos Rigol. "Quantum quenches and many-body localization in the thermodynamic limit". In: *Phys. Rev. B* 91 (16 Apr. 2015), p. 161109. DOI: 10.1103/PhysRevB.91.161109. URL: https://link.aps.org/doi/10.1103/PhysRevB.91.161109.

[321] Dmitry A. Abanin and Zlatko Papić. "Recent progress in many-body localization". In: *Annalen der Physik* 529.7 (2017), p. 1700169. DOI: https://doi.org/10.1002/andp.201700169. eprint: https://onlinelibrary.wiley.com/doi/pdf/10.1002/andp.201700169. URL: https://onlinelibrary.wiley.com/doi/abs/10.1002/andp.201700169.

[322] Romain Vasseur et al. "Crossover Physics in the Nonequilibrium Dynamics of Quenched Quantum Impurity Systems". In: *Phys. Rev. Lett.* 110 (24 June 2013), p. 240601. DOI: 10.1103/PhysRevLett.110.240601. URL: https://link.aps.org/doi/10.1103/PhysRevLett.110.240601.

[323] Marco Schiró and Aditi Mitra. "Transient Orthogonality Catastrophe in a Time-Dependent Nonequilibrium Environment". In: *Phys. Rev. Lett.* 112 (24 June 2014), p. 246401. DOI: 10.1103/PhysRevLett.112.246401. URL: https://link.aps.org/doi/10.1103/PhysRevLett.112.246401.

[324] D. M. Kennes, V. Meden, and R. Vasseur. "Universal quench dynamics of interacting quantum impurity systems". In: *Phys. Rev. B* 90 (11 Sept. 2014), p. 115101. DOI: 10.1103/PhysRevB.90.115101. URL: https://link.aps.org/doi/10.1103/PhysRevB.90.115101.

[325] Jonas A. Kjäll, Jens H. Bardarson, and Frank Pollmann. "Many-Body Localization in a Disordered Quantum Ising Chain". In: *Phys. Rev. Lett.* 113 (10 Sept. 2014), p. 107204. DOI: 10.1103/PhysRevLett.113.107204. URL: https://link.aps.org/doi/10.1103/PhysRevLett.113.107204.

[326] Ireneusz Weymann, 1 von Delft, and Andreas Weichselbaum. "Thermalization and dynamics in the single-impurity Anderson model". In: *Phys. Rev. B* 92 (15 Oct. 2015), p. 155435. DOI: 10.1103/PhysRevB.92.155435. URL: https://link.aps.org/doi/10.1103/PhysRevB.92.155435.

[327] Kemal Bidzhiev and Grégoire Misguich. "Out-of-equilibrium dynamics in a quantum impurity model: Numerics for particle transport and entanglement entropy". In: *Phys. Rev. B* 96 (19 Nov. 2017), p. 195117. DOI: 10.1103/PhysRevB.96.195117. URL: https://link.aps.org/doi/10.1103/PhysRevB.96.195117.

[328] Yuto Ashida et al. "Solving Quantum Impurity Problems in and out of Equilibrium with the Variational Approach". In: *Phys. Rev. Lett.* 121 (2 July 2018), p. 026805. DOI: 10.1103/PhysRevLett.121.026805. URL: https://link.aps.org/doi/10.1103/PhysRevLett.121.026805.

[329] Nilanjan Bondyopadhaya and Dibyendu Roy. "Dynamics of hybrid junctions of Majorana wires". In: *Phys. Rev. B* 99 (21 June 2019), p. 214514. DOI: 10.1103/PhysRevB.99.214514. URL: https://link.aps.org/doi/10.1103/PhysRevB.99.214514.

[330] F. Cavaliere et al. "Coherent charge and spin oscillations induced by local quenches in nanowires with spin-orbit coupling". In: *Phys. Rev. B* 100 (15 Oct. 2019), p. 155306. DOI: 10.1103/PhysRevB.100.155306. URL: https://link.aps.org/doi/10.1103/PhysRevB.100.155306.

[331] Noa Feldman and Moshe Goldstein. "Dynamics of charge-resolved entanglement after a local quench". In: *Phys. Rev. B* 100 (23 Dec. 2019), p. 235146. DOI: 10.1103/PhysRevB.100.235146. URL: https://link.aps.org/doi/10.1103/PhysRevB.100.235146.

[332] Thomás Fogarty et al. "Orthogonality Catastrophe as a Consequence of the Quantum Speed Limit". In: *Phys. Rev. Lett.* 124 (11 Mar. 2020), p. 110601. DOI: 10.1103/PhysRevLett.124.110601. URL: https://link.aps.org/doi/10.1103/PhysRevLett.124.110601.

[333] Marcos Rigol, Alejandro Muramatsu, and Maxim Olshanii. "Hard-core bosons on optical superlattices: Dynamics and relaxation in the superfluid and insulating regimes". In: *Phys. Rev. A* 74 (5 Nov. 2006), p. 053616. DOI: 10.1103/PhysRevA.74.053616. URL: https://link.aps.org/doi/10.1103/PhysRevA.74.053616.

[334] M. Cramer et al. "Exact Relaxation in a Class of Nonequilibrium Quantum Lattice Systems". In: *Phys. Rev. Lett.* 100 (3 Jan. 2008), p. 030602. DOI: 10.1103/PhysRevLett.100.030602. URL: https://link.aps.org/doi/10.1103/PhysRevLett.100.030602.

[335] S. Porta et al. "Nonmonotonic response and light-cone freezing in fermionic systems under quantum quenches from gapless to gapped or partially gapped states". In: *Phys. Rev. B* 97 (3 Jan. 2018), p. 035433. DOI: 10.1103/PhysRevB.97.035433. URL: https://link.aps.org/doi/10.1103/PhysRevB.97.035433.

[336] S. Porta et al. "Effective metal-insulator nonequilibrium quantum phase transition in the Su-Schrieffer-Heeger model". In: *Phys. Rev. B* 98 (21 Dec. 2018), p. 214306. DOI: 10.1103/PhysRevB.98.214306. URL: https://link.aps.org/doi/10.1103/PhysRevB.98.214306.

[337] Takashi Ishii and Takashi Mori. "Strong eigenstate thermalization within a generalized shell in noninteracting integrable systems". In: *Phys. Rev. E* 100 (1 July 2019), p. 012139. DOI: 10.1103/PhysRevE.100.012139. URL: https://link.aps.org/doi/10.1103/PhysRevE.100.012139.

[338] Sergio Porta et al. "Topological classification of dynamical quantum phase transitions in the xy chain". In: *Scientific Reports* 10.1 (2020), p. 12766. DOI: 10.1038/s41598-020-69621-8. URL: https://doi.org/10.1038/s41598-020-69621-8.

[339] Christian Gramsch and Marcos Rigol. "Quenches in a quasidisordered integrable lattice system: Dynamics and statistical description of observables after relaxation". In: *Phys. Rev. A* 86 (5 Nov. 2012), p. 053615. DOI: 10.1103/PhysRevA.86.053615. URL: https://link.aps.org/doi/10.1103/PhysRevA.86.053615.

[340] Kai He et al. "Single-particle and many-body analyses of a quasiperiodic integrable system after a quench". In: *Phys. Rev. A* 87 (6 June 2013), p. 063637. DOI: 10.1103/PhysRevA.87.063637. URL: https://link.aps.org/doi/10.1103/PhysRevA.87.063637.

[341] Ranjan Modak et al. "Integrals of motion for one-dimensional Anderson localized systems". In: *New Journal of Physics* 18.3 (Mar. 2016), p. 033010. DOI: 10.1088/1367-2630/18/3/033010. URL: https://dx.doi.org/10.1088/1367-2630/18/3/033010.

[342] D. M. Kennes, C. Klöckner, and V. Meden. "Spectral Properties of One-Dimensional Fermi Systems after an Interaction Quench". In: *Phys. Rev. Lett.* 113 (11 Sept. 2014), p. 116401. DOI: 10.1103/PhysRevLett.113.116401. URL: https://link.aps.org/doi/10.1103/PhysRevLett.113.116401.

[343] F. M. Gambetta et al. "Universal transport dynamics in a quenched tunnel-coupled Luttinger liquid". In: *Phys. Rev. B* 94 (4 July 2016), p. 045104. DOI: 10.1103/PhysRevB.94.045104. URL: https://link.aps.org/doi/10.1103/PhysRevB.94.045104.

[344] Marek Gluza, Jens Eisert, and Terry Farrelly. "Equilibration towards generalized Gibbs ensembles in non-interacting theories". In: *SciPost Phys.* 7 (2019), p. 038. DOI: 10.21468/SciPostPhys.7.3.038. URL: https://scipost.org/10.21468/SciPostPhys.7.3.038.

[345] Chaitanya Murthy and Mark Srednicki. "Relaxation to Gaussian and generalized Gibbs states in systems of particles with quadratic Hamiltonians". In: *Phys. Rev. E* 100 (1 July 2019), p. 012146. DOI: 10.1103/PhysRevE.100.012146. URL: https://link.aps.org/doi/10.1103/PhysRevE.100.012146.

[346] Takaaki Monnai, Shohei Morodome, and Kazuya Yuasa. "Relaxation to Gaussian generalized Gibbs ensembles in quadratic bosonic systems in the thermodynamic limit". In: *Phys. Rev. E* 100 (2 Aug. 2019), p. 022105. DOI: 10.1103/PhysRevE.100.022105. URL: https://link.aps.org/doi/10.1103/PhysRevE.100.022105.

[347] P. W. Anderson. "Infrared Catastrophe in Fermi Gases with Local Scattering Potentials". In: *Phys. Rev. Lett.* 18 (24 June 1967), pp. 1049–1051. DOI: 10.1103/PhysRevLett.18.1049. URL: https://link.aps.org/doi/10.1103/PhysRevLett.18.1049.

[348] Wolfgang Münder et al. "Anderson orthogonality in the dynamics after a local quantum quench". In: *Phys. Rev. B* 85 (23 June 2012), p. 235104. DOI: 10.1103/PhysRevB.85.235104. URL: https://link.aps.org/doi/10.1103/PhysRevB.85.235104.

[349] F. Bassani and G. Pastori Parravicini. *Electronic states and optical transitions in solids.* Pergamon Press Ltd., 1975. ISBN: 0-08-016846-9.

[350] Weng W. Chow and Stephan W. Koch. *Semiconductor-Laser Fundamentals. Physics of the Gain Materials.* Springer Berlin, Heidelberg, 1999. ISBN: 978-3-540-64166-7. DOI: 10.1007/978-3-662-03880-2.

[351] Lorenzo Rossi, Fausto Rossi, and Fabrizio Dolcini. "Real-space effects of a quench in the Su–Schrieffer–Heeger model and elusive dynamical appearance of the topological edge states". In: *New Journal of Physics* 24.1 (Jan. 2022), p. 013011. DOI: 10.1088/1367-2630/ac3cf6. URL: https://dx.doi.org/10.1088/1367-2630/ac3cf6.

[352] Biao Lian et al. "Topological quantum computation based on chiral Majorana fermions". In: *Proceedings of the National Academy of Sciences* 115.43 (2018), pp. 10938–10942. DOI: 10.1073/pnas.1810003115. eprint: https://www.pnas.org/doi/pdf/10.1073/pnas.1810003115. URL: https://www.pnas.org/doi/abs/10.1073/pnas.1810003115.

[353] Mengyun He, Huimin Sun, and Qing Lin He. "Topological insulator: Spintronics and quantum computations". In: *Frontiers of Physics* 14.4 (2019), p. 43401. DOI: 10.1007/s11467-019-0893-4. URL: https://doi.org/10.1007/s11467-019-0893-4.

[354] Xin Guo et al. "Quantum information memory based on reconfigurable topological insulators by piezotronic effect". In: *Nano Energy* 60 (2019), pp. 36–42. ISSN: 2211-2855. DOI: https://doi.org/10.1016/j.nanoen.2019.03.035. URL: https://www.sciencedirect.com/science/article/pii/S221128551930223X.

[355] V. W. Scarola and S. Das Sarma. "Emulating non-Abelian topological matter in cold-atom optical lattices". In: *Phys. Rev. A* 77 (2 Feb. 2008), p. 023612. DOI: 10.1103/PhysRevA.77.023612. URL: https://link.aps.org/doi/10.1103/PhysRevA.77.023612.

[356] N. Goldman, D. F. Urban, and D. Bercioux. "Topological phases for fermionic cold atoms on the Lieb lattice". In: *Phys. Rev. A* 83 (6 June 2011), p. 063601. DOI: 10.1103/PhysRevA.83.063601. URL: https://link.aps.org/doi/10.1103/PhysRevA.83.063601.

[357] Feng Mei et al. "Probing a half-odd topological number sequence with cold atoms in a non-Abelian optical lattice". In: *Phys. Rev. A* 84 (2 Aug. 2011), p. 023622. DOI: 10.1103/PhysRevA.84.023622. URL: https://link.aps.org/doi/10.1103/PhysRevA.84.023622.

[358] Feng Mei et al. "Simulating Z_2 topological insulators with cold atoms in a one-dimensional optical lattice". In: *Phys. Rev. A* 85 (1 Jan. 2012), p. 013638. DOI: 10.1103/PhysRevA.85.013638. URL: https://link.aps.org/doi/10.1103/PhysRevA.85.013638.

[359] Xiong-Jun Liu et al. "Detecting Topological Phases in Cold Atoms". In: *Phys. Rev. Lett.* 111 (12 Sept. 2013), p. 120402. DOI: 10.1103/PhysRevLett.111.120402. URL: https://link.aps.org/doi/10.1103/PhysRevLett.111.120402.

[360] H. Nonne et al. "Symmetry-protected topological phases of alkaline-earth cold fermionic atoms in one dimension". In: *Europhysics Letters* 102.3 (May 2013), p. 37008. DOI: 10.1209/0295-5075/102/37008. URL: https://dx.doi.org/10.1209/0295-5075/102/37008.

[361] Xiong-Jun Liu, K. T. Law, and T. K. Ng. "Realization of 2D Spin-Orbit Interaction and Exotic Topological Orders in Cold Atoms". In: *Phys. Rev. Lett.* 112 (8 Feb. 2014), p. 086401. DOI: 10.1103/PhysRevLett.112.086401. URL: https://link.aps.org/doi/10.1103/PhysRevLett.112.086401.

[362] C. Laflamme et al. "Hybrid topological quantum computation with Majorana fermions: A cold-atom setup". In: *Phys. Rev. A* 89 (2 Feb. 2014), p. 022319. DOI: 10.1103/PhysRevA.89.022319. URL: https://link.aps.org/doi/10.1103/PhysRevA.89.022319.

[363] Dong-Ling Deng, Sheng-Tao Wang, and L.-M. Duan. "Direct probe of topological order for cold atoms". In: *Phys. Rev. A* 90 (4 Oct. 2014), p. 041601. DOI: 10.1103/PhysRevA.90.041601. URL: https://link.aps.org/doi/10.1103/PhysRevA.90.041601.

[364] Mathias S. Scheurer, Stephan Rachel, and Peter P. Orth. "Dimensional crossover and cold-atom realization of topological Mott insulators". In: *Scientific Reports* 5.1 (2015), p. 8386. DOI: 10.1038/srep08386. URL: https://doi.org/10.1038/srep08386.

[365] Samuel Mugel et al. "Topological bound states of a quantum walk with cold atoms". In: *Phys. Rev. A* 94 (2 Aug. 2016), p. 023631. DOI: 10.1103/PhysRevA.94.023631. URL: https://link.aps.org/doi/10.1103/PhysRevA.94.023631.

[366] Hui Zhai et al. "Focus on topological physics: from condensed matter to cold atoms and optics". In: *New Journal of Physics* 18.8 (Aug. 2016), p. 080201. DOI: 10.1088/1367-2630/18/8/080201. URL: https://dx.doi.org/10.1088/1367-2630/18/8/080201.

[367] Xue-Ying Mai et al. "Exploring topological double-Weyl semimetals with cold atoms in optical lattices". In: *Phys. Rev. A* 95 (6 June 2017), p. 063616. DOI: 10.1103/PhysRevA.95.063616. URL: https://link.aps.org/doi/10.1103/PhysRevA.95.063616.

[368] I.-D. Potirniche et al. "Floquet Symmetry-Protected Topological Phases in Cold-Atom Systems". In: *Phys. Rev. Lett.* 119 (12 Sept. 2017), p. 123601. DOI: 10.1103/PhysRevLett.119.123601. URL: https://link.aps.org/doi/10.1103/PhysRevLett.119.123601.

[369] Xiao-Shan Ye et al. "Creating single Majorana type topological zero mode in superfluids of cold fermionic atoms". In: *Scientific Reports* 7.1 (2017), p. 13541. DOI: 10.1038/s41598-017-13641-4. URL: https://doi.org/10.1038/s41598-017-13641-4.

[370] Dan-Wei Zhang et al. "Topological quantum matter with cold atoms". In: *Advances in Physics* 67.4 (2018), pp. 253–402. DOI: 10.1080/00018732.2019.1594094. eprint: https://doi.org/10.1080/00018732.2019.1594094. URL: https://doi.org/10.1080/00018732.2019.1594094.

[371] Hui Liu et al. "Floquet engineering of exotic topological phases in systems of cold atoms". In: *Phys. Rev. A* 100 (2 Aug. 2019), p. 023622. DOI: 10.1103/PhysRevA.100.023622. URL: https://link.aps.org/doi/10.1103/PhysRevA.100.023622.

[372] W. P. Su, J. R. Schrieffer, and A. J. Heeger. "Solitons in Polyacetylene". In: *Phys. Rev. Lett.* 42 (25 June 1979), pp. 1698–1701. DOI: 10.1103/PhysRevLett.42.1698. URL: https://link.aps.org/doi/10.1103/PhysRevLett.42.1698.

[373] W. P. Su, J. R. Schrieffer, and A. J. Heeger. "Soliton excitations in polyacetylene". In: *Phys. Rev. B* 22 (4 Aug. 1980), pp. 2099–2111. DOI: 10.1103/PhysRevB.22.2099. URL: https://link.aps.org/doi/10.1103/PhysRevB.22.2099.

[374] William Barford. *Electronic and Optical Properties of Conjugated Polymers*. Oxford University Press, Apr. 2013. ISBN: 9780199677467. DOI: 10.1093/acprof:oso/9780199677467.001.0001. URL: https://doi.org/10.1093/acprof:oso/9780199677467.001.0001.

[375] János K. Asbóth, László Oroszlány, and András Pályi. *A Short Course on Topological Insulators*. Vol. 919. Lecture Notes in Physics. Springer Cham, 2016. DOI: 10.1007/978-3-319-25607-8.

[376] Shun-Qing Shen. *Topological insulators*. Vol. 174. Lecture Notes in Physics. Springer Singapore, 2012. DOI: 10.1007/978-981-10-4606-3.

[377] Eric J. Meier, Fangzhao Alex An, and Bryce Gadway. "Observation of the topological soliton state in the Su–Schrieffer–Heeger model". In: *Nature Communications* 7.1 (2016), p. 13986. DOI: 10.1038/ncomms13986. URL: https://doi.org/10.1038/ncomms13986.

[378] Dizhou Xie et al. "Topological characterizations of an extended Su–Schrieffer–Heeger model". In: *npj Quantum Information* 5.1 (2019), p. 55. DOI: 10.1038/s41534-019-0159-6. URL: https://doi.org/10.1038/s41534-019-0159-6.

[379] Péter Boross et al. "Poor man's topological quantum gate based on the Su-Schrieffer-Heeger model". In: *Phys. Rev. B* 100 (4 July 2019), p. 045414. DOI: 10.1103/PhysRevB.100.045414. URL: https://link.aps.org/doi/10.1103/PhysRevB.100.045414.

[380] V. Dal Lago, M. Atala, and L. E. F. Foa Torres. "Floquet topological transitions in a driven one-dimensional topological insulator". In: *Phys. Rev. A* 92 (2 Aug. 2015), p. 023624. DOI: 10.1103/PhysRevA.92.023624. URL: https://link.aps.org/doi/10.1103/PhysRevA.92.023624.

[381] Souvik Bandyopadhyay, Utso Bhattacharya, and Amit Dutta. "Temporal variation in the winding number due to dynamical symmetry breaking and associated transport in a driven Su-Schrieffer-Heeger chain". In: *Phys. Rev. B* 100 (5 Aug. 2019), p. 054305. DOI: 10.1103/PhysRevB.100.054305. URL: https://link.aps.org/doi/10.1103/PhysRevB.100.054305.

[382] Souvik Bandyopadhyay and Amit Dutta. "Dynamical preparation of a topological state and out-of-equilibrium bulk-boundary correspondence in a Su-Schrieffer-Heeger chain under periodic driving". In: *Phys. Rev. B* 100 (14 Oct. 2019), p. 144302. DOI: 10.1103/PhysRevB.100.144302. URL: https://link.aps.org/doi/10.1103/PhysRevB.100.144302.

[383] Xiao-Long Lü and Hang Xie. "Topological phases and pumps in the Su–Schrieffer–Heeger model periodically modulated in time". In: *Journal of Physics: Condensed Matter* 31.49 (Sept. 2019), p. 495401. DOI: 10.1088/1361-648X/ab3d72. URL: https://dx.doi.org/10.1088/1361-648X/ab3d72.

[384] R. Peierls. "Zur Theorie des Diamagnetismus von Leitungselektronen". In: *Zeitschrift für Physik* 80.11 (1933), pp. 763–791. DOI: 10.1007/BF01342591. URL: https://doi.org/10.1007/BF01342591.

[385] M. Graf and P. Vogl. "Electromagnetic fields and dielectric response in empirical tight-binding theory". In: *Phys. Rev. B* 51 (8 Feb. 1995), pp. 4940–4949. DOI: 10.1103/PhysRevB.51.4940. URL: https://link.aps.org/doi/10.1103/PhysRevB.51.4940.

[386] D J Thouless. "A relation between the density of states and range of localization for one dimensional random systems". In: *Journal of Physics C: Solid State Physics* 5.1 (Jan. 1972), p. 77. DOI: 10.1088/0022-3719/5/1/010. URL: https://dx.doi.org/10.1088/0022-3719/5/1/010.

[387] Yan He and Chih-Chun Chien. "Boundary-induced dynamics in one-dimensional topological systems and memory effects of edge modes". In: *Phys. Rev. B* 94 (2 July 2016), p. 024308. DOI: 10.1103/PhysRevB.94.024308. URL: https://link.aps.org/doi/10.1103/PhysRevB.94.024308.

[388] F. Gebhard et al. "Optical absorption of non-interacting tight-binding electrons in a Peierls-distorted chain at half band-filling". In: *Philosophical Magazine B* 75.1 (1997), pp. 1–12. DOI: 10.1080/13642819708205700. eprint: https://doi.org/10.1080/13642819708205700. URL: https://doi.org/10.1080/13642819708205700.

[389] Szabolcs Vajna and Balázs Dóra. "Topological classification of dynamical phase transitions". In: *Phys. Rev. B* 91 (15 Apr. 2015), p. 155127. DOI: 10.1103/PhysRevB.91.155127. URL: https://link.aps.org/doi/10.1103/PhysRevB.91.155127.

[390] Chao Yang, Linhu Li, and Shu Chen. "Dynamical topological invariant after a quantum quench". In: *Phys. Rev. B* 97 (6 Feb. 2018), p. 060304. DOI: 10.1103/PhysRevB.97.060304. URL: https://link.aps.org/doi/10.1103/PhysRevB.97.060304.

[391] K. Jiménez-García et al. "Peierls Substitution in an Engineered Lattice Potential". In: *Phys. Rev. Lett.* 108 (22 May 2012), p. 225303. DOI: 10.1103/PhysRevLett.108.225303. URL: https://link.aps.org/doi/10.1103/PhysRevLett.108.225303.

[392] J. Struck et al. "Tunable Gauge Potential for Neutral and Spinless Particles in Driven Optical Lattices". In: *Phys. Rev. Lett.* 108 (22 May 2012), p. 225304. DOI: 10.1103/PhysRevLett.108.225304. URL: https://link.aps.org/doi/10.1103/PhysRevLett.108.225304.

[393] Carlos G. Velasco and Belén Paredes. "Realizing and Detecting a Topological Insulator in the AIII Symmetry Class". In: *Phys. Rev. Lett.* 119 (11 Sept. 2017), p. 115301. DOI: 10.1103/PhysRevLett.119.115301. URL: https://link.aps.org/doi/10.1103/PhysRevLett.119.115301.

[394] Lorenzo Rossi and Fabrizio Dolcini. "Nonlinear current and dynamical quantum phase transitions in the flux-quenched Su-Schrieffer-Heeger model". In: *Phys. Rev. B* 106 (4 July 2022), p. 045410. DOI: 10.1103/PhysRevB.106.045410. URL: https://link.aps.org/doi/10.1103/PhysRevB.106.045410.

[395] Ryogo Kubo. "Statistical-Mechanical Theory of Irreversible Processes. I. General Theory and Simple Applications to Magnetic and Conduction Problems". In: *Journal of the Physical Society of Japan* 12.6 (1957), pp. 570–586. DOI: 10.1143/JPSJ.12.570. eprint: https://doi.org/10.1143/JPSJ.12.570. URL: https://doi.org/10.1143/JPSJ.12.570.

[396] Gerald D. Mahan. *Many-Particle Physics*. 3rd ed. Springer New York, NY, Oct. 2000. ISBN: 978-0-306-46338-9. DOI: 10.1007/978-1-4757-5714-9. URL: https://doi.org/10.1007/978-1-4757-5714-9.

[397] Raffaele Resta. "Drude weight and superconducting weight". In: *Journal of Physics: Condensed Matter* 30.41 (Sept. 2018), p. 414001. DOI: 10.1088/1361-648X/aade19. URL: https://dx.doi.org/10.1088/1361-648X/aade19.

[398] Walter Kohn. "Theory of the Insulating State". In: *Phys. Rev.* 133 (1A Jan. 1964), A171–A181. DOI: 10.1103/PhysRev.133.A171. URL: https://link.aps.org/doi/10.1103/PhysRev.133.A171.

[399] B. Sriram Shastry and Bill Sutherland. "Twisted boundary conditions and effective mass in Heisenberg-Ising and Hubbard rings". In: *Phys. Rev. Lett.* 65 (2 July 1990), pp. 243–246. DOI: 10.1103/PhysRevLett.65.243. URL: https://link.aps.org/doi/10.1103/PhysRevLett.65.243.

[400] Norio Kawakami and Sung-Kil Yang. "Conductivity in one-dimensional highly correlated electron systems". In: *Phys. Rev. B* 44 (15 Oct. 1991), pp. 7844–7851. DOI: 10.1103/PhysRevB.44.7844. URL: https://link.aps.org/doi/10.1103/PhysRevB.44.7844.

[401] H. Castella, X. Zotos, and P. Prelovšek. "Integrability and Ideal Conductance at Finite Temperatures". In: *Phys. Rev. Lett.* 74 (6 Feb. 1995), pp. 972–975. DOI: 10.1103/PhysRevLett.74.972. URL: https://link.aps.org/doi/10.1103/PhysRevLett.74.972.

[402] X. Zotos. "Finite Temperature Drude Weight of the One-Dimensional Spin- 1/2 Heisenberg Model". In: *Phys. Rev. Lett.* 82 (8 Feb. 1999), pp. 1764–1767. DOI: 10.1103/PhysRevLett.82.1764. URL: https://link.aps.org/doi/10.1103/PhysRevLett.82.1764.

[403]   J. Benz et al. "On the Finite Temperature Drude Weight of the Anisotropic Heisenberg Chain". In: *Journal of the Physical Society of Japan* 74.Suppl (2005), pp. 181–190. DOI: 10.1143/JPSJS.74S.181. eprint: https://doi.org/10.1143/JPSJS.74S.181. URL: https://doi.org/10.1143/JPSJS.74S.181.

[404]   J. Herbrych, P. Prelovšek, and X. Zotos. "Finite-temperature Drude weight within the anisotropic Heisenberg chain". In: *Phys. Rev. B* 84 (15 Oct. 2011), p. 155125. DOI: 10.1103/PhysRevB.84.155125. URL: https://link.aps.org/doi/10.1103/PhysRevB.84.155125.

[405]   C. Karrasch, J. H. Bardarson, and J. E. Moore. "Finite-Temperature Dynamical Density Matrix Renormalization Group and the Drude Weight of Spin-1/2 Chains". In: *Phys. Rev. Lett.* 108 (22 May 2012), p. 227206. DOI: 10.1103/PhysRevLett.108.227206. URL: https://link.aps.org/doi/10.1103/PhysRevLett.108.227206.

[406]   C. Karrasch, T. Prosen, and F. Heidrich-Meisner. "Proposal for measuring the finite-temperature Drude weight of integrable systems". In: *Phys. Rev. B* 95 (6 Feb. 2017), p. 060406. DOI: 10.1103/PhysRevB.95.060406. URL: https://link.aps.org/doi/10.1103/PhysRevB.95.060406.

[407]   Davide Rossini et al. "Quantum quenches, linear response and superfluidity out of equilibrium". In: *Europhysics Letters* 107.3 (July 2014), p. 30002. DOI: 10.1209/0295-5075/107/30002. URL: https://dx.doi.org/10.1209/0295-5075/107/30002.

[408]   Maciej Lewenstein et al. "Ultracold atomic gases in optical lattices: mimicking condensed matter physics and beyond". In: *Advances in Physics* 56.2 (2007), pp. 243–379. DOI: 10.1080/00018730701223200. eprint: https://doi.org/10.1080/00018730701223200. URL: https://doi.org/10.1080/00018730701223200.

[409]   Jean Dalibard et al. "Colloquium: Artificial gauge potentials for neutral atoms". In: *Rev. Mod. Phys.* 83 (4 Nov. 2011), pp. 1523–1543. DOI: 10.1103/RevModPhys.83.1523. URL: https://link.aps.org/doi/10.1103/RevModPhys.83.1523.

[410]   N. Goldman et al. "Light-induced gauge fields for ultracold atoms". In: *Reports on Progress in Physics* 77.12 (Nov. 2014), p. 126401. DOI: 10.1088/0034-4885/77/12/126401. URL: https://dx.doi.org/10.1088/0034-4885/77/12/126401.

[411]   Yuya O. Nakagawa, Grégoire Misguich, and Masaki Oshikawa. "Flux quench in a system of interacting spinless fermions in one dimension". In: *Phys. Rev. B* 93 (17 May 2016), p. 174310. DOI: 10.1103/PhysRevB.93.174310. URL: https://link.aps.org/doi/10.1103/PhysRevB.93.174310.

[412]   Thierry Giamarchi. *Quantum Physics in One Dimension.* Oxford University Press, Dec. 2003. ISBN: 9780198525004. DOI: 10.1093/acprof:oso/9780198525004.001.0001. URL: https://doi.org/10.1093/acprof:oso/9780198525004.001.0001.

[413]   Rodolfo A. Jalabert and Horacio M. Pastawski. "Environment-Independent Decoherence Rate in Classically Chaotic Systems". In: *Phys. Rev. Lett.* 86 (12 Mar. 2001), pp. 2490–2493. DOI: 10.1103/PhysRevLett.86.2490. URL: https://link.aps.org/doi/10.1103/PhysRevLett.86.2490.

[414]   Zbyszek P. Karkuszewski, Christopher Jarzynski, and Wojciech H. Zurek. "Quantum Chaotic Environments, the Butterfly Effect, and Decoherence". In: *Phys. Rev. Lett.* 89 (17 Oct. 2002), p. 170405. DOI: 10.1103/PhysRevLett.89.170405. URL: https://link.aps.org/doi/10.1103/PhysRevLett.89.170405.

[415]   H. T. Quan et al. "Decay of Loschmidt Echo Enhanced by Quantum Criticality". In: *Phys. Rev. Lett.* 96 (14 Apr. 2006), p. 140604. DOI: 10.1103/PhysRevLett.96.140604. URL: https://link.aps.org/doi/10.1103/PhysRevLett.96.140604.

[416]   Alessandro Silva. "Statistics of the Work Done on a Quantum Critical System by Quenching a Control Parameter". In: *Phys. Rev. Lett.* 101 (12 Sept. 2008), p. 120603. DOI: 10.1103/PhysRevLett.101.120603. URL: https://link.aps.org/doi/10.1103/PhysRevLett.101.120603.

[417]   Andrea De Luca. "Quenching the magnetic flux in a one-dimensional fermionic ring: Loschmidt echo and edge singularity". In: *Phys. Rev. B* 90 (8 Aug. 2014), p. 081403. DOI: 10.1103/PhysRevB.90.081403. URL: https://link.aps.org/doi/10.1103/PhysRevB.90.081403.

[418]   A. Chenu et al. "Quantum work statistics, Loschmidt echo and information scrambling". In: *Scientific Reports* 8.1 (2018), p. 12634. DOI: 10.1038/s41598-018-30982-w. URL: https://doi.org/10.1038/s41598-018-30982-w.

[419]   Szabolcs Vajna and Balázs Dóra. "Disentangling dynamical phase transitions from equilibrium phase transitions". In: *Phys. Rev. B* 89 (16 Apr. 2014), p. 161105. DOI: 10.1103/PhysRevB.89.161105. URL: https://link.aps.org/doi/10.1103/PhysRevB.89.161105.

[420]   F. Andraschko and J. Sirker. "Dynamical quantum phase transitions and the Loschmidt echo: A transfer matrix approach". In: *Phys. Rev. B* 89 (12 Mar. 2014), p. 125120. DOI: 10.1103/PhysRevB.89.125120. URL: https://link.aps.org/doi/10.1103/PhysRevB.89.125120.

[421]   R. Jafari and Henrik Johannesson. "Loschmidt Echo Revivals: Critical and Noncritical". In: *Phys. Rev. Lett.* 118 (1 Jan. 2017), p. 015701. DOI: 10.1103/PhysRevLett.118.015701. URL: https://link.aps.org/doi/10.1103/PhysRevLett.118.015701.

[422]   R. Jafari et al. "Quench dynamics and zero-energy modes: The case of the Creutz model". In: *Phys. Rev. B* 99 (5 Feb. 2019), p. 054302. DOI: 10.1103/PhysRevB.99.054302. URL: https://link.aps.org/doi/10.1103/PhysRevB.99.054302.

[423]   Lorenzo Pastori, Simone Barbarino, and Jan Carl Budich. "Signatures of topology in quantum quench dynamics and their interrelation". In: *Phys. Rev. Res.* 2 (3 Aug. 2020), p. 033259. DOI: 10.1103/PhysRevResearch.2.033259. URL: https://link.aps.org/doi/10.1103/PhysRevResearch.2.033259.

[424]   M. Sadrzadeh, R. Jafari, and A. Langari. "Dynamical topological quantum phase transitions at criticality". In: *Phys. Rev. B* 103 (14 Apr. 2021), p. 144305. DOI: 10.1103/PhysRevB.103.144305. URL: https://link.aps.org/doi/10.1103/PhysRevB.103.144305.

[425]   Jad C. Halimeh and Valentin Zauner-Stauber. "Dynamical phase diagram of quantum spin chains with long-range interactions". In: *Phys. Rev. B* 96 (13 Oct. 2017), p. 134427. DOI: 10.1103/PhysRevB.96.134427. URL: https://link.aps.org/doi/10.1103/PhysRevB.96.134427.

[426]   Ingo Homrighausen et al. "Anomalous dynamical phase in quantum spin chains with long-range interactions". In: *Phys. Rev. B* 96 (10 Sept. 2017), p. 104436. DOI: 10.1103/PhysRevB.96.104436. URL: https://link.aps.org/doi/10.1103/PhysRevB.96.104436.

[427] Johannes Lang, Bernhard Frank, and Jad C. Halimeh. "Concurrence of dynamical phase transitions at finite temperature in the fully connected transverse-field Ising model". In: *Phys. Rev. B* 97 (17 May 2018), p. 174401. DOI: 10.1103/PhysRevB.97.174401. URL: https://link.aps.org/doi/10.1103/PhysRevB.97.174401.

[428] Bojan Žunkovič et al. "Dynamical Quantum Phase Transitions in Spin Chains with Long-Range Interactions: Merging Different Concepts of Nonequilibrium Criticality". In: *Phys. Rev. Lett.* 120 (13 Mar. 2018), p. 130601. DOI: 10.1103/PhysRevLett.120.130601. URL: https://link.aps.org/doi/10.1103/PhysRevLett.120.130601.

[429] Nicolò Defenu, Tilman Enss, and Jad C. Halimeh. "Dynamical criticality and domain-wall coupling in long-range Hamiltonians". In: *Phys. Rev. B* 100 (1 July 2019), p. 014434. DOI: 10.1103/PhysRevB.100.014434. URL: https://link.aps.org/doi/10.1103/PhysRevB.100.014434.

[430] Jan Carl Budich and Markus Heyl. "Dynamical topological order parameters far from equilibrium". In: *Phys. Rev. B* 93 (8 Feb. 2016), p. 085416. DOI: 10.1103/PhysRevB.93.085416. URL: https://link.aps.org/doi/10.1103/PhysRevB.93.085416.

[431] N. Fläschner et al. "Observation of dynamical vortices after quenches in a system with topology". In: *Nature Physics* 14.3 (2018), pp. 265–268. DOI: 10.1038/s41567-017-0013-8. URL: https://doi.org/10.1038/s41567-017-0013-8.

[432] Haruki Watanabe and Masaki Oshikawa. "Generalized f-sum rules and Kohn formulas on nonlinear conductivities". In: *Phys. Rev. B* 102 (16 Oct. 2020), p. 165137. DOI: 10.1103/PhysRevB.102.165137. URL: https://link.aps.org/doi/10.1103/PhysRevB.102.165137.

[433] Haruki Watanabe, Yankang Liu, and Masaki Oshikawa. "On the General Properties of Non-linear Optical Conductivities". In: *Journal of Statistical Physics* 181.6 (2020), pp. 2050–2070. DOI: 10.1007/s10955-020-02654-5. URL: https://doi.org/10.1007/s10955-020-02654-5.

[434] Raffaele Resta. *Theory of nonlinear dc conductivity, longitudinal and transverse.* 2021. DOI: 10.48550/ARXIV.2111.12617. URL: https://arxiv.org/abs/2111.12617.

[435] Lorenzo Rossi, Jan Carl Budich, and Fabrizio Dolcini. *Topology in the space-time scaling limit of quantum dynamics.* 2023. DOI: 10.48550/ARXIV.2301.07752. URL: https://arxiv.org/abs/2301.07752.

[436] Markus König et al. "Quantum Spin Hall Insulator State in HgTe Quantum Wells". In: *Science* 318.5851 (2007), pp. 766–770. DOI: 10.1126/science.1148047. eprint: https://www.science.org/doi/pdf/10.1126/science.1148047. URL: https://www.science.org/doi/abs/10.1126/science.1148047.

[437] N. Goldman, J. C. Budich, and P. Zoller. "Topological quantum matter with ultracold gases in optical lattices". In: *Nature Physics* 12.7 (2016), pp. 639–645. DOI: 10.1038/nphys3803. URL: https://doi.org/10.1038/nphys3803.

[438] Zhoushen Huang and Alexander V. Balatsky. "Dynamical Quantum Phase Transitions: Role of Topological Nodes in Wave Function Overlaps". In: *Phys. Rev. Lett.* 117 (8 Aug. 2016), p. 086802. DOI: 10.1103/PhysRevLett.117.086802. URL: https://link.aps.org/doi/10.1103/PhysRevLett.117.086802.

[439] Ce Wang et al. "Scheme to Measure the Topological Number of a Chern Insulator from Quench Dynamics". In: *Phys. Rev. Lett.* 118 (18 May 2017), p. 185701. DOI: 10.1103/PhysRevLett.118.185701. URL: https://link.aps.org/doi/10.1103/PhysRevLett.118.185701.

[440] Matthias Tarnowski et al. "Measuring topology from dynamics by obtaining the Chern number from a linking number". In: *Nature Communications* 10.1 (2019), p. 1728. DOI: 10.1038/s41467-019-09668-y. URL: https://doi.org/10.1038/s41467-019-09668-y.

[441] Matthew S. Foster et al. "Quench-Induced Floquet Topological p-Wave Superfluids". In: *Phys. Rev. Lett.* 113 (7 Aug. 2014), p. 076403. DOI: 10.1103/PhysRevLett.113.076403. URL: https://link.aps.org/doi/10.1103/PhysRevLett.113.076403.

[442] Michael Victor Berry. "Quantal phase factors accompanying adiabatic changes". In: *Proceedings of the Royal Society of London. A. Mathematical and Physical Sciences* 392.1802 (1984), pp. 45–57. DOI: 10.1098/rspa.1984.0023. eprint: https://royalsocietypublishing.org/doi/pdf/10.1098/rspa.1984.0023. URL: https://royalsocietypublishing.org/doi/abs/10.1098/rspa.1984.0023.

[443] Barry Simon. "Holonomy, the Quantum Adiabatic Theorem, and Berry's Phase". In: *Phys. Rev. Lett.* 51 (24 Dec. 1983), pp. 2167–2170. DOI: 10.1103/PhysRevLett.51.2167. URL: https://link.aps.org/doi/10.1103/PhysRevLett.51.2167.

[444] Takahiro Fukui, Yasuhiro Hatsugai, and Hiroshi Suzuki. "Chern Numbers in Discretized Brillouin Zone: Efficient Method of Computing (Spin) Hall Conductances". In: *Journal of the Physical Society of Japan* 74.6 (2005), pp. 1674–1677. DOI: 10.1143/JPSJ.74.1674. eprint: https://doi.org/10.1143/JPSJ.74.1674. URL: https://doi.org/10.1143/JPSJ.74.1674.

[445] M. J. Rice and E. J. Mele. "Elementary Excitations of a Linearly Conjugated Diatomic Polymer". In: *Phys. Rev. Lett.* 49 (19 Nov. 1982), pp. 1455–1459. DOI: 10.1103/PhysRevLett.49.1455. URL: https://link.aps.org/doi/10.1103/PhysRevLett.49.1455.

[446] Nicola Marzari and David Vanderbilt. "Maximally localized generalized Wannier functions for composite energy bands". In: *Phys. Rev. B* 56 (20 Nov. 1997), pp. 12847–12865. DOI: 10.1103/PhysRevB.56.12847. URL: https://link.aps.org/doi/10.1103/PhysRevB.56.12847.

[447] Walter Kohn. "Theory of the Insulating State". In: *Phys. Rev.* 133 (1A Jan. 1964), A171–A181. DOI: 10.1103/PhysRev.133.A171. URL: https://link.aps.org/doi/10.1103/PhysRev.133.A171.

[448] Yang Ge and Marcos Rigol. "Topological phase transitions in finite-size periodically driven translationally invariant systems". In: *Phys. Rev. A* 96 (2 Aug. 2017), p. 023610. DOI: 10.1103/PhysRevA.96.023610. URL: https://link.aps.org/doi/10.1103/PhysRevA.96.023610.

[449] Johannes Motruk and Frank Pollmann. "Phase transitions and adiabatic preparation of a fractional Chern insulator in a boson cold-atom model". In: *Phys. Rev. B* 96 (16 Oct. 2017), p. 165107. DOI: 10.1103/PhysRevB.96.165107. URL: https://link.aps.org/doi/10.1103/PhysRevB.96.165107.

[450] Yin-Chen He et al. "Realizing and adiabatically preparing bosonic integer and fractional quantum Hall states in optical lattices". In: *Phys. Rev. B* 96 (20 Nov. 2017), p. 201103. DOI: 10.1103/PhysRevB.96.201103. URL: https://link.aps.org/doi/10.1103/PhysRevB.96.201103.

[451] Alexander Keesling et al. "Quantum Kibble–Zurek mechanism and critical dynamics on a programmable Rydberg simulator". In: *Nature* 568.7751 (2019), pp. 207–211. DOI: 10.1038/s41586-019-1070-1. URL: https://doi.org/10.1038/s41586-019-1070-1.

[452] S. Barbarino et al. "Preparing Atomic Topological Quantum Matter by Adiabatic Nonunitary Dynamics". In: *Phys. Rev. Lett.* 124 (1 Jan. 2020), p. 010401. DOI: 10.1103/PhysRevLett.124.010401. URL: https://link.aps.org/doi/10.1103/PhysRevLett.124.010401.

[453] Filippo Cardano et al. "Detection of Zak phases and topological invariants in a chiral quantum walk of twisted photons". In: *Nature Communications* 8, 15516 (June 2017), p. 15516. DOI: 10.1038/ncomms15516. arXiv: 1610.06322 [cond-mat.mes-hall].

[454] Xiao-Ye Xu et al. "Measuring a dynamical topological order parameter in quantum walks". In: *Light: Science & Applications* 9.1 (2020), p. 7. DOI: 10.1038/s41377-019-0237-8. URL: https://doi.org/10.1038/s41377-019-0237-8.

[455] Supriyo Datta and Biswajit Das. "Electronic analog of the electro-optic modulator". In: *Applied Physics Letters* 56.7 (1990), pp. 665–667. DOI: 10.1063/1.102730. eprint: https://doi.org/10.1063/1.102730. URL: https://doi.org/10.1063/1.102730.

[456] Dario Bercioux and Procolo Lucignano. "Quantum transport in Rashba spin–orbit materials: a review". In: *Reports on Progress in Physics* 78.10 (Sept. 2015), p. 106001. DOI: 10.1088/0034-4885/78/10/106001. URL: https://dx.doi.org/10.1088/0034-4885/78/10/106001.

[457] H.B. Nielsen and M. Ninomiya. "Absence of neutrinos on a lattice: (II). Intuitive topological proof". In: *Nuclear Physics B* 193.1 (1981), pp. 173–194. ISSN: 0550-3213. DOI: https://doi.org/10.1016/0550-3213(81)90524-1. URL: https://www.sciencedirect.com/science/article/pii/0550321381905241.

[458] Shinsei Ryu et al. "Topological insulators and superconductors: tenfold way and dimensional hierarchy". In: *New Journal of Physics* 12.6 (June 2010), p. 065010. DOI: 10.1088/1367-2630/12/6/065010. URL: https://dx.doi.org/10.1088/1367-2630/12/6/065010.

[459] P. Delplace, D. Ullmo, and G. Montambaux. "Zak phase and the existence of edge states in graphene". In: *Phys. Rev. B* 84 (19 Nov. 2011), p. 195452. DOI: 10.1103/PhysRevB.84.195452. URL: https://link.aps.org/doi/10.1103/PhysRevB.84.195452.

[460] Meri Zaimi et al. "Detecting topological edge states with the dynamics of a qubit". In: *Physics Letters A* 388 (2021), p. 127035. ISSN: 0375-9601. DOI: https://doi.org/10.1016/j.physleta.2020.127035. URL: https://www.sciencedirect.com/science/article/pii/S0375960120309026.